Dissertation

SUBMITTED TO THE

Combined Faculties of the Natural Sciences and Mathematics
of the Ruperto-Carola-University of Heidelberg, Germany

FOR THE DEGREE OF

Doctor of Natural Sciences

Put forward by

Michael Mayle

born in: Ansbach, Germany

Oral examination: December 9th, 2009

Ultracold Rydberg Atoms in a Ioffe-Pritchard Trap

* * *

Creating One-Dimensional Rydberg Gases and Exploiting their Composite Character

Referees:

Prof. Dr. Peter Schmelcher
Dr. Rosario González-Férez

Ultrakalte Rydberg Atome in einer Ioffe-Pritchard Falle: Bildung von eindimensionalen Rydberg Gasen und Ausnutzung ihres Zweiteilchencharakters – Gegenstand dieser Arbeit ist die theoretische Untersuchung der Quanteneigenschaften von ultrakalten Rydberg Atomen in Anwesenheit inhomogener äußerer Felder. Wir betrachten die Ioffe-Pritchard Konfiguration und überlagern diese mit einem homogenen elektrischen Feld um zu zeigen, dass gefangene Rydberg Atome in langlebigen *zirkularen* Zuständen erzeugt werden können und dabei ein permanentes elektrisches Dipolmoment von einigen hundert Debye aufweisen. Die daraus resultierende Dipol-Dipol Wechsewirkung in Verbindung mit der radialen Einsperrung führt zu einem effektiv eindimensionalen Rydberg Gas mit makroskopischen Teilchenabständen. Unsere Untersuchungen auf *Niedrigdrehimpulszustände* verlagernd zeigen wir, dass – im Vergleich zu Punktteilchen mit identischen magnetischen Moment – der Zweiteilchencharkter von Rydberg Atomen maßgeblich ihre Falleneigenschaften beeinflußt. Analytische Ausdrücke für die resultierenden Fallenpotentiale werden hergeleitet und ihre Gültigkeit wird durch den Vergleich mit den numerischen Lösungen der zugrunde liegenden Schrödingergleichung bestätigt. Die Schwerpunktsbewegung wird mittels eines adiabatischen Ansatzes untersucht und Implikationen für Quanteninformations-Protokolle, die magnetisch gefangene Rydberg Atome involvieren, werden diskutiert. Abschließend zeigen wir, wie die spezifischen Merkmale des Rydberg Fallenpotentials mit Hilfe von Grundzustandsatomen geprobt werden können, welche mit dem Rydberg Zustand mittels eines nichtresonanten Zweiphotonenübergangs verkoppelt sind.

Ultracold Rydberg Atoms in a Ioffe-Pritchard Trap: Creating One-Dimensional Rydberg Gases and Exploiting their Composite Character – Subject of this thesis is the theoretical study of the quantum properties of ultracold Rydberg atoms in the presence of inhomogeneous external fields. Using the Ioffe-Pritchard configuration as a key ingredient superimposed by a homogeneous electric field, we demonstrate that trapped Rydberg atoms can be created in long-lived *circular* states exhibiting a permanent electric dipole moment of several hundred Debye. The resulting dipole-dipole interaction in conjunction with the radial confinement is demonstrated to entail an effectively one-dimensional Rydberg gas with a macroscopic interparticle distance. Turning our investigations to the *low angular momentum* electronic states, we demonstrate that the two-body character of Rydberg atoms significantly alters their trapping properties opposed to point-like particles with identical magnetic moment. Analytical expressions describing the resulting trapping potentials are derived and their validity is confirmed by comparison with the numerical solutions of the underlying Schrödinger equation. The center of mass dynamics are studied by means of an adiabatic approach and implications for quantum information protocols involving magnetically trapped Rydberg atoms are discussed. We conclude by demonstrating how the specific signatures of the Rydberg trapping potential can be probed by means of ground state atoms that are off-resonantly coupled to the Rydberg state via a two-photon laser transition.

Contents

Chapter 1

Introduction

During the past two decades, powerful cooling techniques enabled remarkable experiments with ultracold atomic gases revealing a plethora of intriguing phenomena. Laser and evaporative cooling allow nowadays the routine production of ultracold samples of ground state atoms in the temperature regime below one micro-Kelvin. The first highlight in the (at this time still new) field of ultracold atomic physics was in the year 1995: Bose-Einstein Condensation (BEC) was achieved for an ultracold gas of rubidium atoms [1] – an effect that has been predicted theoretically already in the early years of the twentieth century [2–4]. Independently, in the same year a BEC of sodium was obtained [5]. These pioneering experiments established the field of ultracold physics, which ought to expand rapidly in the years to come. Just to pick an example, only four years later the first gas of fermionic species was brought to degeneracy [6]. Also from a theoretical point of view, great effort was put into understanding the properties of degenerate quantum gases. The so-called Gross-Pitaevski equation proved to be a very useful concept in this direction [7–10]. It affords an excellent description of the newly-found condensates of alkali atoms [11]. Many physical properties have been derived and interesting physical features have been predicted for the novel systems [12]. Nowadays, degenerate quantum gases of many different species can be routinely achieved in many laboratories around the globe. Quantum gases of mixed species are not uncommon and even a BEC of ground state polar molecules is about to be achieved [13]. The ultimate goals of the pursued research projects are numerous: They range from technical applications such as extraordinarily sensitive magnetic field detection [14] to state-sensitive controlled chemistry [15]. Other, even more ambitious applications include quantum computation and quantum information [16].

Due to their widely tunable properties, ultracold atomic gases provide the ideal playground to model and study complex many body systems. The interatomic interaction can be tailored using Feshbach resonances and magnetic, optical, and electric fields can be applied in order to generate virtually any external potential. Famous examples for the versatility are the demonstration of the Mott-Insulator to superfluid phase-transition of ultracold atoms in an optical lattice [17], the BEC-BCS crossover in a gas of ^{6}Li [18], or the Kosterlitz-Thouless phase transition studied within a two-dimensional Bose-Einstein condensate [19]. In one dimension and in the limit of an infinitely strong interparticle interaction strength, a so-called Tonks-Girardeau gas emerges [20] in which the bosons behave like spin-less non-interacting fermions piled up in the single-particle eigenstates of the one-dimensional potential. Experimentally, such a gas has been realized in a ^{87}Rb Bose-Einstein condensate of very low density in a tight optical potential using an optical lattice to manipulate the atoms' effective mass [21].

Common to all ultracold experiments is the vast usage of external fields to control and manipulate the internal as well as external degrees of freedoms of ultracold atoms and molecules. For example, static electric fields are used to align ultracold polar heteronuclear molecules by mixing their field-free rotational states in order to exploit their intrinsic electric dipole moment for dipolar interactions [22–27]. In a similar vein, magnetic fields are employed to manipulate ultracold atoms possessing large magnetic dipole moments, such as chromium [28]. Moreover, they are widely used to tailor the interatomic interaction using Feshbach resonances, allowing – amongst others – the almost 100% efficient conversion from atoms to molecules and back [29]. Inhomogeneous magnetic fields are the basis of controlling the external degree of freedom as well. In combination with counterpropagating laser beams of well-defined polarization, they are encountered in virtually any ultracold experiment: the magneto-optical trap [30]. The latter offers efficient cooling of a large number of atoms and at the same time provides stable and strongly confining trapping. However, the magneto-optical trap allows only cooling until the Doppler limit is reached. This issue is overcome in purely magnetic traps where the temperature of the atomic sample is further reduced by evaporative cooling; in the evaporative cooling scheme only the hottest atoms escape the trap, thereby effectively reducing the temperature of the whole sample [31].

Rydberg Atoms

Among the many fascinating systems encountered in modern ultracold atomic and molecular physics are Rydberg atoms. Rydberg atoms are (in the framework of ultracold physics almost exclusively alkali-)atoms in states of high principal quantum number n. Their size can easily exceed that of ground state atoms by several orders of magnitude. Already a state with principal quantum number $n \approx 40$ has an electronic orbit that measures ~ 200 nm in diameter and thus is more than thousand times larger than the ground state [32]. The associated displacement of the atomic charges makes Rydberg atoms highly susceptible to external fields and at the same time is the origin of their strong mutual interaction. Combining such extraordinary properties with the plethora of techniques known from the preparation and manipulation of ultracold gases enables remarkable observations. In ultracold gases, the strong dipole-dipole interaction has been shown theoretically [33, 34] and experimentally [35–39] to entail a blockade mechanism thereby effectuating a collective excitation process of Rydberg atoms [40–42]. Moreover, two recent experiments demonstrated the blockade between two single atoms a few micrometers apart [43, 44]. The strong dipole-dipole interaction renders Rydberg atoms also promising candidates for the implementation of protocols realizing two-qubit quantum gates [33, 34] or efficient multiparticle entanglement [45]. The extraordinary size of Rydberg atoms furthermore gives rise to a novel binding mechanism for a system of one Rydberg and one ground state atom. The negative scattering length between the Rydberg electron and the ground state atom entails an attractive potential for the latter at the position of the Rydberg electron. Consequently, the appearance of such giant Rydberg molecules is determined by the Rydberg electron wave function, giving rise to so-called *trilobite* or *butterfly* molecular states [46–49]. Only recently, signatures of such extraordinary molecules have been observed experimentally using an ultracold gas of rubidium atoms in a magnetic Ioffe-Pritchard trap [50].

Owed to their large size, Rydberg atoms do not only interact much stronger than their ground state counterparts but also behave quite differently when placed in electric and/or

magnetic field configurations that provide trapping for ground state atoms. Several works have focused on the issue of trapping Rydberg atoms based on electric [51,52], optical [53], or strong magnetic fields [54]. Being omnipresent in experiments dealing with ultracold atoms, inhomogeneous magnetic fields seem predestined for trapping Rydberg atoms (even a two-dimensional permanent magnetic lattice of Ioffe-Pritchard microtraps for ultracold atoms has been realized experimentally [55, 56]). Similar to ground state atoms, the magnetic trapping of Rydberg atoms originates from the interaction of their magnetic moment with the magnetic field. In particular, this allows to utilize trap geometries which are well-known from ground state atoms. However, due to the high level density and the strong spectral fluctuations with spatially varying fields, trapping or manipulation in general is a more delicate task than for ground state atoms. This holds particularly for the case where both the center of mass and internal motion are of quantum nature and inhomogeneous external fields lead to an inherent coupling of these motions.

In a first attempt to understand the quantum properties of a Rydberg atom placed in a three-dimensional magnetic quadrupole field, Lesanovsky and Schmelcher exploited a one-body approach assuming an infinite nuclear mass. As they showed, the delicate interplay between the Coulomb and magnetic interactions in the inhomogeneous field leads to, e.g., intriguing spin polarization patterns of individual Rydberg states and magnetic field induced electric-dipole moments [57–60]. Providing such a promising starting point, more involved studies incorporating the fully coupled center of mass and electronic dynamics were not long to follow [61,62]. The essential step of these studies is the introduction of an adiabatic approach of Born-Oppenheimer kind: The fast electronic dynamics is assumed to adapt instantaneously to any change in the local magnetic field structure while the center of mass is slowly moving through the external field. Hence, at each point in space the electronic structure of the Rydberg atom yields a different energy, providing after all an electronic potential energy surface for the center of mass dynamics. By determining in this manner the quantum states of the center of mass motion, it has been demonstrated that trapping can be achieved if the *total*, i.e., combined center of mass and electronic angular momentum of the atom is sufficiently large. This holds even for very tight traps or high principal quantum numbers when the extension of the electronic Rydberg state becomes equal to or even exceeds that of the ultracold center of mass motion.

Although being omnipresent in ultracold atomic physics experiments, the three-dimensional magnetic quadrupole field configuration has a serious drawback, namely, its lack of a finite field strength at its minimum. Consequently, spin flips that lead to particle losses become possible at the trap center [63]. As mentioned above, this issue can be alleviated, e.g., by imposing a large center of mass angular momentum such that – pictorially speaking –the Rydberg atom circles around the point of zero field at sufficiently large distance. For practical purposes, however, it is desirable to provide trapping at small or even vanishing center of mass angular momentum: usually, ultracold atoms are prepared in such states. Hezel and co-workers tackled this issue by considering the Ioffe-Pritchard magnetic field configuration, for which an additional offset field removes the degeneracy of the trapped and anti-trapped states at the trap center and thereby greatly reduces the undesirable spin flips. Addressing the regime of inherently coupled center of mass and electronic motions, they demonstrated in their theoretical studies that Rydberg atoms can be tightly confined and prepared in long-lived *circular* electronic states, i.e., in states of maximal electronic angular momentum and projection, $l = m_l = n - 1$ [64, 65]. Interestingly, despite the strong localization of the center

of mass, the electronic structure of the Rydberg atom is barely changed compared to the field-free case. As it turned out, however, only the adiabatic energy surface of the circular state proved to be very robust with respect to changes in the magnetic field parameters. The lower lying angular momentum states, in contrast, are subject to numerous avoided crossings and non-adiabatic transitions, rendering stable trapping impossible. Hence, the trapping mechanism relies in these studies on high angular momentum electronic states that have not been realized yet in experiments with ultracold atoms.

Objective of this Work

In this thesis, we continue and expand the studies of Hezel and co-workers of investigating the quantum properties of Rydberg atoms in a Ioffe-Pritchard trap. As pointed out above, Refs. [64,65] focused on Rydberg states of high electronic angular momentum. This particular choice allowed to employ a very useful approximation: The interaction between the Rydberg electron and the remaining ionic core can be considered in such cases as purely Coulombic. Consequently, in the field-free case the high degree of degeneracy known from the hydrogen atom is yielded. In the presence of the Ioffe-Pritchard field, this degeneracy gives rise to the multitude of non-adiabatic avoided crossings; at the same time the trapping of non-circular Rydberg states is rendered practically impossible. When going to very low electronic angular momenta $l \lesssim 3$, however, the situation changes dramatically. The core-penetration and scattering effects of the valence electron splits the low angular momentum states energetically apart from the degenerate hydrogenic manifold by means of the so-called *quantum defect* [32], providing a separate submanifold for each l. Hence, quite naturally the question arises if stable trapping becomes again possible in such low angular momentum Rydberg states. Investigating this issue is of particular relevance for current experiments since ultracold Rydberg atoms are usually prepared in low angular momentum nS or nD states by a two-photon laser excitation of trapped ultracold ground state atoms.

The investigation of ultracold Rydberg atoms in low angular momentum electronic states differs quite substantially from the high angular momentum ones. As indicated above, the core-scattering and polarization effects, that lead to the quantum defect of the energy levels, must be accounted for. Moreover, the spin-orbit interaction of the valence electron is much stronger for small angular momenta. Accordingly, fine-structure effects must not be neglected. We start in **Chapter 2** by providing a brief introduction to Rydberg atoms in general and highlighting the peculiar properties of low angular momentum states of alkali atoms. In **Chapter 3** we lay the foundations of this thesis, namely, the working Hamiltonian of an alkali Rydberg atom in a magnetic Ioffe-Pritchard trap is derived. For this reason, a two-particle picture (Rydberg electron and remaining ionic core) is employed. The initial Hamiltonian in the minimal coupling scheme is presented, including a thorough examination of all ingredients necessary to adequately describe the low angular momentum Rydberg states of an alkali atom. Introducing relative coordinates and a suitable unitary transformation allows us to simplify the initial Hamiltonian considerably. An adiabatic approach reminiscent of the Born-Oppenheimer separation in molecular dynamics finally treats the remaining couplings between the relative and center of mass motion.

The adiabatic approach relies on finding the solutions to the electronic part of the previously derived Hamiltonian parametrically as a function of the center of mass position of the Rydberg atom. In **Chapter 4** we tackle this issue by introducing a spatially dependent unitary

transformation that 'homogenizes' the magnetic field by rotating the magnetic field vector into the z-direction of the laboratory frame of reference. The drawback of this method is, however, that it relies on further approximations and that certain terms can only be included in a perturbative manner. In **Chapter 5**, we present our computational approach for determining the solutions of the electronic Schrödinger equation numerically, based on the *linear variational principle*. Opposed to the analytical solutions of Chapter 4, this approach does not require further approximations and yields in principle arbitrarily exact solutions. While for the investigations of high angular momentum Rydberg states hydrogenic eigenfunctions are very suitable as underlying basis set, we need to construct adapted eigenfunctions for the low angular momentum Rydberg states of alkali atoms. The method used for gaining the latter – the so-called *Discrete Variable Representation* – is discussed in Chapter 5 as well.

Before turning to the discussion of our results concerning Rydberg atoms in low angular momentum electronic states, in **Chapter 6** of this thesis we use the Ioffe-Pritchard configuration as a key ingredient in order to prepare and study a one-dimensional Rydberg gas consisting of long lived *circular* states. Specifically, we propose a modified Ioffe-Pritchard trap, a magneto-electric trap, that offers tightly confining potential energy surfaces for the atomic center of mass motion; at the same time, the Rydberg atom possesses an oriented permanent electric dipole moment in this kind of trap. The resulting strong repulsion between neighboring Rydberg atoms in conjunction with the tight transverse confinement is demonstrated to give rise to an effectively one-dimensional Rydberg gas with macroscopic interparticle distances. Moreover, we are going to derive analytical expressions for the electric dipole moment and the required linear density of Rydberg atoms below which a one-dimensional Rydberg gas is expected to form.

In **Chapter 7** we finally switch to the investigation of low angular momentum states of Rydberg atoms. Specifically, we analyze the quantum properties of nS, nP, and nD Rydberg atoms in a magnetic Ioffe-Pritchard trap. It is demonstrated that the two-body character of Rydberg atoms, i.e., the fact that they consists of an outer electron far away from a compact ionic core significantly alters their trapping properties opposed to point-like particles with identical magnetic moment. As we are going to show, the resulting trapping potentials possess a reduced azimuthal symmetry and a finite trap depth, which can be a few vibrational quanta only or less. Choosing the magnetic field parameters appropriately, on the other hand, stable trapping can be achieved with trap depths in the micro-Kelvin regime. In addition to the electronic properties, the center of mass dynamics of trapped Rydberg atoms are studied. In particular, we analyze the influence of a short-time Rydberg excitation on the center of mass motion of trapped ground state atoms. A corresponding heating rate is derived and the implications for quantum information protocols involving magnetically trapped Rydberg atoms are discussed.

One major drawback of Rydberg atoms is their finite lifetimes due to spontaneous radiative decays. Although being denoted as long-lived for the purpose of many experiments, lifetimes in the range of microseconds up to milliseconds can still be insufficient. For example, the atomic motion in the ultracold regime is hard to resolve within this timescale. Also in the context of quantum information, coherence times exceeding the typical lifetime of Rydberg atoms are desirable. A remedy of this issue is to combine the huge amount of control known from ultracold physics with the exceptional properties of Rydberg atoms by *dressing* ground state atoms with Rydberg states. This can be achieved by off-resonantly coupling the ground and Rydberg state by an appropriate laser transition (which is usually of two-photon char-

acter), resulting in dressed states where the Rydberg level becomes weakly admixed to the ground state and vice versa. In **Chapter 8** we illuminate the question of how the external, i.e., center of mass motion of magnetically trapped ^{87}Rb ground state atoms is affected by such a dressing with the Rydberg state. We thoroughly discuss the two-photon laser coupling scheme that maps the features of the Rydberg trapping potential onto the dressed ground state atom. The resulting dressed trapping potentials are systematically studied. In particular, we demonstrate how the delicate interplay between the spatially varying quantization axis of the Ioffe-Pritchard field and the fixed polarizations of the laser transitions determines the actual shape of the trapping potentials.

In **Chapter 9** we conclude this thesis by briefly summarizing our findings and providing an outlook on further perspectives in this intriguing field of research.

Unless stated differently, atomic units are used throughout this thesis, cf. Appendix A. We remark that Chapters 6-8 contain each a brief summary of the theoretical background necessary to comprehend the argumentation and results presented in the respective chapters by its own.

Chapter 2

Rydberg Atoms

The main subject of this thesis are Rydberg atoms and their properties in (in-)homogeneous external fields. For this reason, we provide in this chapter an introduction to Rydberg atoms in general, highlighting their remarkable properties. We start in Section 2.1 by short historical remarks, including the first appearance of Rydberg atoms in atomic physics. Being omnipresent in modern ultracold atomic physics, alkali atoms gained huge attention during the last decades. As a paradigm example for the latter, we outline in Section 2.2 the particular properties of rubidium Rydberg atoms. In Section 2.3 we set the stage of this thesis by summarizing the energy scales that are encountered for a Rydberg atom in a magnetic field. For a comprehensive review of the physics of Rydberg atoms, including experimental and theoretical methods, we refer the reader to the monograph by T. F. Gallagher [32].

2.1 Historical Remarks

Rydberg atoms are atoms in states of high principal quantum number n. Although the concept of a quantum number has not yet been around at this time, the first appearance of Rydberg atoms was already in the year 1885 in the Balmer series of atomic hydrogen [66]. Balmer's formula for the wavelengths of the visible series of atomic hydrogen is given by

$$\lambda = \frac{bn^2}{n^2 - 4}$$

where $b = 3645.6\,\text{Å}$. Rewriting Balmer's formula in terms of the wavenumber of the observed lines instead of the wavelength,

$$\nu = \frac{1}{4b}\left(\frac{1}{4} - \frac{1}{n^2}\right),$$

we nowadays recognize that it describes the series of transitions from the $n = 2$ states to higher lying levels. In the 1890s Rydberg began to classify the spectra of other atoms into *sharp*, *principal*, and *diffuse* series of lines [67].[1] He realized that the wavenumbers of the observed lines could be expressed as

$$\nu_l = \nu_{\infty l} - \frac{Ry}{(n - \delta_l)^2},$$

[1] Note that this classification survived in the labeling s, p, $d\ldots$ of the electronic angular momentum l.

Table 2.1: Properties of Rydberg atoms and their dependence on the principal quantum number n. Adapted from Ref. [32].

Property	n dependence
Binding energy	n^{-2}
Energy between adjacent n states	n^{-3}
Orbital radius	n^2
Dipole moment $\langle nd\|er\|nf\rangle$	n^2
Polarizability	n^7
Radiative lifetime	n^3
Fine-structure interval	n^{-3}

where l stands for the s, p, and d series. The constants $\nu_{\infty l}$ are the series limits and δ_l we would call nowadays the quantum defect of the corresponding series. Ry is the so-called *Rydberg constant*, $Ry = 109721.6\,\mathrm{cm}^{-1}$, which is universal and can be used to describe the transition wavenumbers, not only for different series of an atom but also for different atoms.

The physical significance of n as the principal quantum number did not become clear until Bohr proposed his theory of the hydrogen atom in 1913. Bohr employed the picture of an electron classically orbiting the ionic core. While we know today that the Bohr model is not valid entirely, it nevertheless successfully introduced the properties of Rydberg atoms which make them interesting. In particular, it gives the connection of the orbital radius of the electron around the ionic core and the principal quantum number n,

$$r = \frac{4\pi\varepsilon_0\hbar^2}{e^2 m_e}\, n^2 = a_0 n^2\,,$$

where $a_0 = 0.529177208\,\text{Å}$ is the size of the ground state atom and is called the *Bohr radius*. In other words, the size of the orbit increases as the square of the principal quantum number. Consequently, Rydberg states (which are states of high n) have very large orbits. The binding energy of such a state, on the other hand, quadratically decreases with increasing n:

$$W = -\frac{1}{(4\pi\varepsilon_0)^2}\frac{e^4 m_e}{2n^2\hbar^2} = -\frac{Ry}{n^2}\,.$$

Hence, the Bohr atom physically defines our understanding of Rydberg atoms: In a Rydberg atom, the valence electron is in a large, loosely bound orbit that is characterized by the principal quantum number n.

Nowadays, we know that the Bohr model gives an intuitive picture of a Rydberg atom but a correct description must be derived from quantum mechanics. The properties of a Rydberg atom are therefore determined by its wave function ψ. In developing the latter, we begin with the Schrödinger equation for the hydrogen atom in its simplest form, i.e., neglecting all relativistic effects such as spin-orbit coupling or hyperfine structure [68]:

$$\left(-\frac{\nabla^2}{2} - \frac{1}{r}\right)\psi = W\psi\,. \tag{2.1}$$

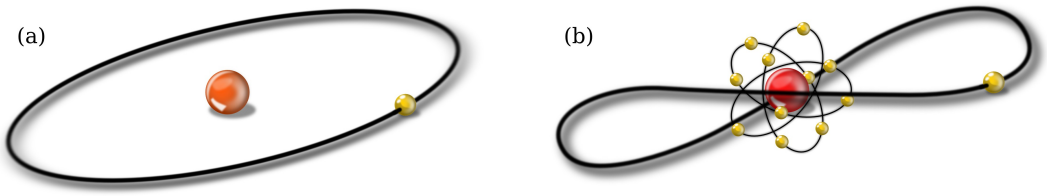

Figure 2.1: Sketch of a high angular momentum alkali Rydberg atom (a) compared to its low angular momentum counterpart (b). For the latter, the interaction of the valence electron with the closed-shell electrons of the finite-size ionic core leads to core-scattering and polarization effects. In case of the high angular momentum state, the internal structure of the ionic core is not resolved.

r denotes the distance of the electron from the proton, which is assumed to be infinitely heavy, and W its energy. As for the rest of this thesis, Eq. (2.1) is given in atomic units, cf. Appendix A. In this chapter we do not aim to solve the Schrödinger equation (2.1). We rather acknowledge that its solutions are well-known and are introduced in Section 5.3. From the wave functions we can infer the n scaling of many properties of Rydberg atoms; Tab. 2.1 shows a short list of the most representative ones. Most notably – although being highly excited – the lifetime of Rydberg atoms increases rapidly as n^3. A further example of the extraordinary properties of Rydberg atoms is their huge polarizability. It is proportional to the sum of of squares of electric dipole matrix elements divided by energy denominator, resulting in a n^7 scaling. Consequently, Rydberg atoms are expected to be extremely sensitive to external fields.

2.2 Rydberg States of Alkali Atoms

In this work, we are interested in Rydberg states of alkali atoms rather than the hydrogen atom. Conceptually, electronically excited alkali atoms are very similar to the simple hydrogen Rydberg atom: both possess one valence electron orbiting around an ionic core of charge +1. However, for the alkali atoms this charge is not of point-like nature as the proton in the hydrogen atom but is rather due to the shielding of a nucleus of charge $Z > 1$ by the remaining (non-excited) $Z - 1$ electrons. The latter form a closed-shell ionic core (Li^+, Na^+, Ka^+, Rb^+, etc.) such that electronic excitations of the positively charged ion are strongly suppressed and the single valence electron picture can be maintained. If the structure of the ionic core is not resolved – as it is the case for high angular momentum electronic states with $l \gtrsim 4$ – alkali Rydberg atoms are well described by considering point-like charges as for the hydrogen atom. If the Rydberg atom resides in a low angular momentum electronic state ($l \leq 3$), on the other hand, the precise charge distribution of the alkali ionic core matters. In particular, the valence electron penetrates and polarizes the finite-size ionic core of the alkali atom, changing the wave functions and energies of alkali Rydberg states from their hydrogenic counterparts. In Figure 2.1, the conceptual differences between the high and low angular momentum Rydberg states of an alkali atom are illustrated. These differences can be quantified by introducing the so-called *quantum defect* δ_{njl} that depends on the quantum numbers n, j, and l of the Rydberg atom:

$$E_{njl}^{el} = -\frac{Ry}{(n - \delta_{njl})^2} \,. \tag{2.2}$$

Table 2.2: Modified Rydberg-Ritz parameters of the rubidium atom for the calculation of the quantum defect according to Eq. (2.3). The presented data are taken from Ref. [70] for $l \leq 2$ (δ_0, δ_2 only) and from Ref. [69] otherwise.

State	δ_0	δ_2	δ_4	δ_6	δ_8
$nS_{1/2}$	3.131 180 4	0.178 4	−1.8	–	–
$nP_{1/2}$	2.654 884 9	0.290 0	−7.904 0	116.437 3	−405.907
$nP_{3/2}$	2.641 673 7	0.295 0	−0.974 95	14.600 1	−44.726 5
$nD_{3/2}$	1.348 091 71	−0.602 86	−1.505 17	−2.420 6	19.736
$nD_{5/2}$	1.346 465 72	−0.596 00	−1.505 17	−2.420 6	19.736
nF_j	0.016 312	−0.064 007	−0.360 05	3.239 0	–

The quantum defect can be determined via the modified Rydberg-Ritz expression [69]

$$\delta_{njl} = \delta_0 + \frac{\delta_2}{(n-\delta_0)^2} + \frac{\delta_4}{(n-\delta_0)^4} + \frac{\delta_6}{(n-\delta_0)^6} + \frac{\delta_8}{(n-\delta_0)^8} + \cdots . \tag{2.3}$$

The parameters δ_0, $\delta_2, \ldots$ are specific for each element; in Tab. 2.2 we give the corresponding values for rubidium, on which we focus throughout this thesis. We remark that for high-n states the first two terms of Eq. (2.3) are often sufficient. Figure 2.2 illustrates the energy levels of rubidium for various angular momentum states l and principal quantum numbers n; for comparison, the hydrogen level scheme is included additionally. As expected from Eq. (2.2), the low angular momentum states ($l \leq 3$) are lowered in energy due to the quantum defect. States with higher angular momenta are degenerate and coincide with the hydrogen manifold. For these states, the core penetration and polarization effects obviously are of minor importance, leading to a vanishing quantum defect. From a mathematical point of view, they are thus identical to their hydrogenic counterparts.

From the obvious difference between the rubidium and hydrogen energy levels for low angular momentum states, it is clear that the corresponding wave functions must differ as well. Because of the penetration and polarization effects, the pure Coulomb potential $-1/r$ employed in the Schrödinger equation (2.1) is not valid for alkali atoms. Nevertheless, the one-particle picture can be sustained by replacing the Coulomb potential by a model potential of the form

$$V_l(r) = -\frac{Z_l(r)}{r} - \frac{\alpha_c}{2r^4}\left[1 - e^{-(r/r_c)^6}\right],$$

where $Z_l(r)$ is an effective charge and α_c the static dipole polarizability of the positive-ion core [72].[2] Solving the Schrödinger equation employing such a potential yields the correct wave functions of the low angular momentum states of alkali atoms. Figure 2.3 shows the probability density distribution of some exemplary radial wave functions that have been calculated numerically by means of a discrete variable representation technique based on generalized Laguerre polynomials, cf. Section 5.4.2. For comparison, the corresponding hydrogenic eigenfunctions are provided in Fig. 2.3 as well. The difference caused by the quantum defect is clearly visible. For small r the potential seen by the rubidium valence electron is lowered

[2] For a more detailed description of the model potential, including actual values of the parameters a_i for the rubidium atom, we refer the reader to Section 3.1

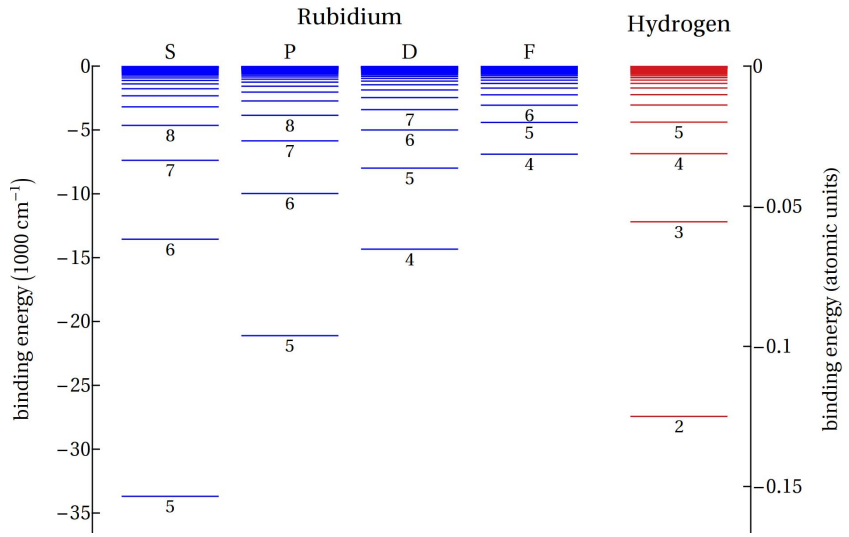

Figure 2.2: Energy levels of rubidium and hydrogen. The numbers below the level indicate the principal quantum number n. The depression of the low angular momentum ($l \leq 3$) energies due to the quantum defect is obvious. For $n > 7$, the energy levels are yielded according to Eq. (2.2). The low-n values are adapted from the NIST Atomic Spectra Database [71].

compared to the pure Coulomb potential of the hydrogen atom. Consequently, the kinetic energy of the rubidium valence electron is increased, leading to a decrease of the wavelength of the radial oscillations relative to the hydrogen atom. As a result, in rubidium all the nodes of the radial wave function are pulled closer to the origin than in hydrogen.

Radiative Lifetimes

Because Rydberg atoms are highly excited quantum objects, they possess only a finite lifetime due to spontaneous radiative decays. The transition rate for the radiative decay from an initial state $|i\rangle$ to a final state $|f\rangle$ reads [73]

$$\Gamma_{f\leftarrow i} = \frac{4}{3}\alpha^3 \Delta E^3 |\langle f|\mathbf{r}|i\rangle|^2 \,,$$

where α is the fine structure constant and $\Delta E = E_i - E_f$ the energy difference between the initial and final state. The lifetime of the initial state accordingly reads $\tau = (\sum_f \Gamma_{f\leftarrow i})^{-1}$. Hence, any variation in the radial matrix element produced by a non-zero quantum defect effectively alters the lifetime known from the hydrogen atom. The perhaps most distinct example for such a situation occurs in the nP states of alkali atoms: In hydrogen, they have a very short lifetime while in an alkali atom the lifetime is very long due to their small oscillator strengths to the ground state [32].

The lifetimes of alkali Rydberg states are well known and can be calculated accurately [74]. As already mentioned in Section 2.1, we expect the lifetime of Rydberg atoms to increase rapidly as n^3.[3] The most compact and consistent way of presenting the alkali lifetimes is thus

[3]Note that for high angular momentum states we get a different scaling behavior. For example, the circular state ($l = m_l = n - 1$) possesses only a single decay channel, namely, $l' = m_l' = n' - 1$ with $n' = n - 1$.

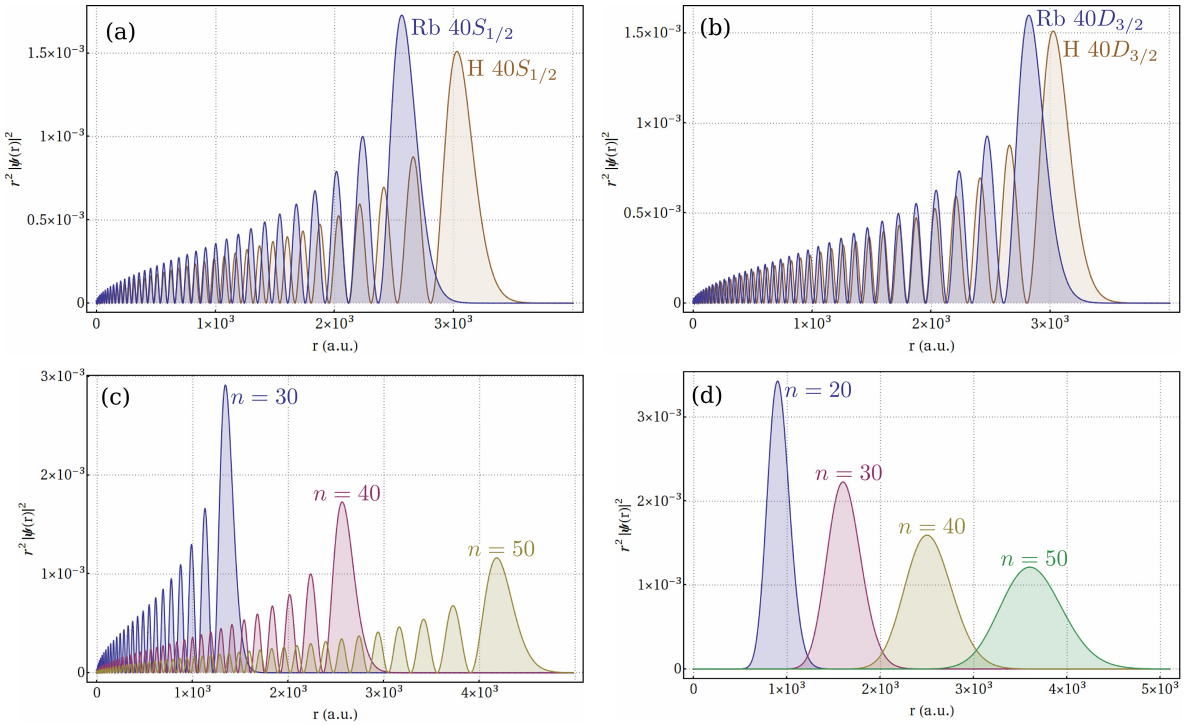

Figure 2.3: Radial probability density distributions $r^2|\psi(r)|^2$ of different Rydberg states of rubidium and hydrogen. (a) The $40S_{1/2}$ state; (b) the $40D_{3/2}$ state. As expected, the influence of the quantum defect is less pronounced for the state with a higher electronic angular momentum, i.e., the $40D_{3/2}$ state. (c) and (d): Scaling of the wave functions with the principal quantum number n. Panel (c) illustrates the low angular momentum nS states that show strong core penetration and polarization effects. In contrast, the circular states ($l = m_l = n - 1$) have a vanishing probability density for small r, cf. panel (d).

by a fit of the calculated values to the form

$$\tau_0 = \tau'(n - \delta)^\gamma \,. \tag{2.4}$$

The actual values of τ' and γ resulting from a fit for the rubidium atom are presented in Tab. 2.3; in this table, we also included fitted parameters from recent experimental data using cold trapped atoms [75,76]. Equation (2.4) denotes the lifetime of an isolated Rydberg atom. Considering in addition stimulated emission and absorption due to black body radiation, we get an increased decay rate according to

$$\frac{1}{\tau} = \frac{1}{\tau_0} + \frac{1}{\tau_{bb}} \,.$$

The black body induced decay rate can be written as [32]

$$\frac{1}{\tau_{bb}} = \frac{4\alpha^3 kT}{3n^2} \,.$$

Interestingly, it only depends on the principal quantum number n rather than on l. As a

The corresponding lifetime evaluates to $\tau_0 = \frac{3}{2}\alpha^{-3}n^5$, cf. Eq. (6.21).

Table 2.3: Lifetime parameters for rubidium, according to Eq. (2.4). The theoretical values τ'_{th} and γ_{th} are adapted from Ref. [77]; the parameters τ'_{exp} and γ_{exp}, that are gained from experimental data using cold trapped atoms, are taken from Refs. [75, 76].

	τ'_{th}(ns)	γ_{th}	τ'_{exp}(ns)	γ_{exp}
nS	1.43	2.94	1.43	2.94
nP	2.76	3.02	2.80	3.01
nD	2.09	2.85	1.90	2.83
nF	0.76	2.95	–	–

Table 2.4: Parameters for calculating the fine structure intervals of rubidium according to Eq. (2.5). The given values are adapted from Ref. [32].

	A	B
nP	85.865 THz	–
nD	10.800 THz	−84.87 THz
nF	−152 GHz	1.82 THz

consequence, for high l states the black body induced decay rate is often much larger than the spontaneous emission rate since the latter usually decreases rapidly with increasing l. Moreover, for high enough n the black body radiation rate exceeds the spontaneous emission rate even for low angular momentum states: the latter scales as n^{-3} compared to the n^{-2} scaling of τ_{bb}^{-1}.

2.3 Emergent Energy Scales in a Ioffe-Pritchard Trap

As we have seen in the previous section, the finite size of the ionic core of alkali atoms significantly influences the valence electron energies and wave functions. In this section, we give a brief preview on further interactions that are going to be introduced in the course of this thesis. To set the stage for the chapters to follow, we provide the hierarchy of the emergent energy scales already at this point of the thesis.

The largest energy scales encountered in our system are – as outlined in the previous section – the splitting between n-manifolds and the quantum defects of low angular momentum states. If we consider a given quantum defect splitted state, i.e., fixing the principal and angular momentum quantum numbers n and l, respectively, the next important interaction is the spin-orbit coupling of the valence electron. The resulting fine structure intervals of alkali atoms can be parameterized as [32]

$$\Delta W_{\mathrm{fs}} = \frac{A}{(n-\delta_{nlj})^3} + \frac{B}{(n-\delta_{nlj})^5}\,. \tag{2.5}$$

The fine structure parameters A and B for rubidium are summarized in Tab. 2.4. Because of the spin-orbit interaction, the orbital angular momentum $\mathbf{L}$ and the spin $\mathbf{S}$ of the valence electron couple to the total electronic angular momentum $\mathbf{J} = \mathbf{L} + \mathbf{S}$. The latter then interacts with the nuclear spin I, giving rise to the total angular momentum $\mathbf{F} = \mathbf{J} + \mathbf{I}$ and the

Table 2.5: Energy scales emerging for a rubidium Rydberg atom in a Ioffe-Pritchard trap. The n-splitting refers to nS states, i.e, is given by $E^{el}_{nS} - E^{el}_{n-1S}$. The values denoted as nS quantum defect are the shifts from the degenerate hydrogenic manifold, $E^{el}_{nl>3} - E^{el}_{nS}$. The hyperfine structure splitting also refers to the nS state. For the Zeeman splitting we assumed a field strength of $B = 1\,\mathrm{G}$ and for the trap frequency additionally a gradient field of $G = 2.5\,\mathrm{Tm}^{-1}$; both are given for the $nS_{1/2}, m_j = 1/2$ state.

n	n-splitting	nS quantum defect	$nS - nP$ splitting	nP fine structure	hyperfine structure	Zeeman splitting	trap frequency
30	359 GHz	−902 GHz	158 GHz	4199 MHz	1737 kHz		
40	137 GHz	−364 GHz	61 GHz	1648 MHz	672 kHz	2.8 MHz	319 Hz
50	66 GHz	−182 GHz	30 GHz	809 MHz	327 kHz		

accompanying hyperfine structure splitting between different hyperfine eigenstates F and F':

$$\Delta W_{\mathrm{hfs}} = \frac{hA}{2}\left[F(F+1) - F'(F'+1)\right], \tag{2.6}$$

see Eq. (3.12) in Section 3.1. Like for the fine structure intervals, the hyperfine structure constant A scales with the principal quantum number n, $A(n) = A_0/(n - \delta_{njl})^3$. Specific values of $A(n)$ and A_0 for the rubidium atom can be found in Tab. 3.2 of Section 3.1.

The scope of this thesis is to investigate the properties of Rydberg atoms in a magnetic Ioffe-Pritchard trap. That is, we are going to encounter yet another energy scale, namely, the Zeeman splitting of formerly degenerate magnetic substates. Assuming a constant magnetic field for the moment, the magnetic field interaction becomes $W_{\mathrm{zee}} = \frac{1}{2} g_j m_j B$, where g_j is the Landé-factor splitting factor, m_j the magnetic quantum number of a given state, and B the magnetic field strength. For our Ioffe-Pritchard trap, we can derive an analogous expression, cf. Eq. (4.17) in Section 4.3. The splitting between adjacent magnetic sublevels accordingly reads

$$\Delta W_{\mathrm{zee}} = \tfrac{1}{2} g_j B\,. \tag{2.7}$$

Finally, we are interested in the external dynamics of the Rydberg atom, i.e., its center of mass motion. The latter is determined by the adiabatic potentials that arise from the electronic structure of the Rydberg atom in the magnetic field. As we are going to show in Section 4.3, the Ioffe-Pritchard configuration yields in first order a harmonic potential whose trap frequency is given by

$$\omega = G\sqrt{\frac{g_j m_j}{2MB}}\,, \tag{2.8}$$

which is at the same time the energy splitting between adjacent center of mass eigenstates. Actual values of the various energy scales presented in this section are provided in Tab. 2.5.

Chapter 3

The Hamiltonian

In this chapter, the working Hamiltonian of an alkali Rydberg atom in a magnetic Ioffe-Pritchard trap is derived. For this reason, a two-particle picture (Rydberg electron and remaining ionic core) is employed. In Section 3.1 the initial Hamiltonian in the minimal coupling scheme is presented, including a thorough examination of all ingredients necessary to adequately describe the low angular momentum Rydberg states of an alkali atom. Introducing relative coordinates and a suitable unitary transformation in Sections 3.2 and 3.3, respectively, allows us to simplify the initial Hamiltonian considerably. An adiabatic approach reminiscent of the Born-Oppenheimer separation in molecular dynamics finally removes in Section 3.4 the remaining couplings between the relative and center of mass motion.

The derivations presented in this chapter focus on the case of low electronic angular momentum Rydberg states. In Chapter 6, however, circular states with maximal electronic angular momentum are considered. For such a case, not all interactions discussed in this chapter are of relevance, simplifying the derivation of the working Hamiltonian considerably. For more details on the arising changes, we refer the reader to Section 6.1.

3.1 Two Particle Hamiltonian in Minimal Coupling Scheme

Throughout this thesis, an alkali Rydberg atom is considered as a two particle system consisting of the Rydberg valence electron loosely bound to the remaining closed-shell ionic core. The coupling of the charged particles to the external magnetic field is introduced via the minimal coupling, $\mathbf{p}_i \rightarrow \mathbf{p}_i - q_i\mathbf{A}(\mathbf{r}_i)$, with $i \in \{e, c\}$ denoting the valence electron or the remaining ionic core of a Rydberg atom, respectively; q_i is the charge of the particle and $\mathbf{A}(\mathbf{x})$ is the vector potential belonging to the magnetic field $\mathbf{B}(\mathbf{x})$. Employing $q_e = -1$ and $q_c = 1$, our initial Hamiltonian reads

$$\begin{aligned} H &= \frac{1}{2m_e}[\mathbf{p}_e - q_e\mathbf{A}(\mathbf{r}_e)]^2 + \frac{1}{2M_c}[\mathbf{p}_c - q_c\mathbf{A}(\mathbf{r}_c)]^2 + V(|\mathbf{r}_e - \mathbf{r}_c|) + V_{so}(\mathbf{L}, \mathbf{S}) \\ &\quad - \boldsymbol{\mu}_e \cdot \mathbf{B}(\mathbf{r}_e) - \boldsymbol{\mu}_c \cdot \mathbf{B}(\mathbf{r}_c) \qquad (3.1) \\ &= \frac{\mathbf{p}_e^2}{2m_e} + \frac{\mathbf{p}_c^2}{2M_c} + \frac{1}{m_e}\mathbf{A}(\mathbf{r}_e) \cdot \mathbf{p}_e - \frac{1}{M_c}\mathbf{A}(\mathbf{r}_c) \cdot \mathbf{p}_c + \frac{1}{2m_e}\mathbf{A}(\mathbf{r}_e)^2 + \frac{1}{2M_c}\mathbf{A}(\mathbf{r}_c)^2 \\ &\quad + V(|\mathbf{r}_e - \mathbf{r}_c|) + V_{so}(\mathbf{L}, \mathbf{S}) - \boldsymbol{\mu}_e \cdot \mathbf{B}(\mathbf{r}_e) - \boldsymbol{\mu}_c \cdot \mathbf{B}(\mathbf{r}_c) \qquad (3.2) \end{aligned}$$

with m_e and M_c being the mass of the Rydberg electron and the ionic core, respectively. The magnetic moments are connected to the electronic spin $\mathbf{S}$ and the nuclear spin $\boldsymbol{I}$ according

to $\boldsymbol{\mu}_e = -\mu_B g_S \mathbf{S}/\hbar$ and $\boldsymbol{\mu}_c = -\mu_B g_I \boldsymbol{I}/\hbar$ with g_S and g_I being the electronic and nuclear g-factors, respectively. The terms involving $\boldsymbol{\mu}_c$ usually can be neglected due to the large mass of the ionic core which entails a small nuclear g-factor[1]. Unless stated differently, atomic units are used throughout this thesis[2], yielding $\mu_S = -\mathbf{S}$.

Magnetic Field Configuration

Two widely spread magnetic field configurations that serve as key ingredients for the trapping of ultracold atoms are the Ioffe-Pritchard and the three-dimensional quadrupole configuration. A serious drawback of the latter is its lack of a finite field strength at its minimum. Consequently, spin flips that lead to particle losses become possible at the trap center [63]. For the Ioffe-Pritchard field configuration, this issue is resolved by an additional offset field that removes the degeneracy of the trapped and anti-trapped states at the trap center and thereby greatly reduces the undesirable spin flips [79]. In this thesis, we consider the Ioffe-Pritchard configuration as a paradigm for the magnetic trapping of ultracold (Rydberg-) atoms.

The magnetic field configuration of the Ioffe-Pritchard trap is given by a two-dimensional quadrupole field in the x_1, x_2-plane together with a perpendicular offset (Ioffe-) field in the x_3-direction. It can be created by several means. The "traditional" macroscopic realization uses four parallel current carrying Ioffe bars which generate the two-dimensional quadrupole field. Encompassing Helmholtz coils create the additional constant field [80]. More recent implementations are for example the QUIC [81] and the clover-leaf configuration [82]. On a microscopic scale, the Ioffe-Pritchard trap has been implemented on atom chips by a Z-shaped wire [83]. The Ioffe-Pritchard configuration can be parameterized as

$$\mathbf{B}(\mathbf{x}) = \underbrace{\begin{pmatrix} 0 \\ 0 \\ B \end{pmatrix}}_{\equiv \mathbf{B}_c} + \underbrace{G \begin{pmatrix} x_1 \\ -x_2 \\ 0 \end{pmatrix}}_{\equiv \mathbf{B}_l(\mathbf{x})} \tag{3.3}$$

where B denotes the strength of the Ioffe field and G the field gradient of the two-dimensional quadrupole field[3]. The magnitude of the magnetic field at a certain position $\mathbf{x}$ in space is given by

$$|\mathbf{B}(\mathbf{x})| = \sqrt{B^2 + G^2(x_1^2 + x_2^2)}\,, \tag{3.4}$$

which yields a linear asymptote $|\mathbf{B}(\mathbf{x})| \to G\rho$ for large coordinates ($\rho = \sqrt{x_1^2 + x_2^2} \gg B/G$) and a harmonic behavior $|\mathbf{B}(\mathbf{x})| \approx B + \frac{1}{2}G^2\rho^2$ close to the origin ($\rho \ll B/G$). The Ioffe-Pritchard magnetic field configuration for a typical parameter set B and G is illustrated in Fig. 3.1.

The vector potential corresponding to the magnetic field $\mathbf{B}(\mathbf{x})$ is only determined up to some gauge transformation[4]. For the constant part of the magnetic field, $\mathbf{B}_c$, a sensible choice of the vector potential is $\mathbf{A}_c(\mathbf{x}) = \frac{B}{2}\left[x_1\mathbf{e}_2 - x_2\mathbf{e}_1\right]$ giving rise to $\mathbf{A}_c(\mathbf{x}) = \frac{1}{2}\mathbf{B}_c \times \mathbf{x}$. For the linear

[1] For ^{87}Rb one finds $g_I = -0.0009951414$ [78].

[2] In particular, $m_e = \hbar = 1$ and $\mu_B = 1/2$, cf. Appendix A. Furthermore, we approximate $g_S = 2$.

[3] The quadratic term that usually arises for a Ioffe-Pritchard configuration can be exactly zeroed by geometry. For simplicity, we consider this case throughout this thesis.

[4] Since the Hamiltonian depends explicitly on the vector potential $\mathbf{A}$, it will be changed under a gauge

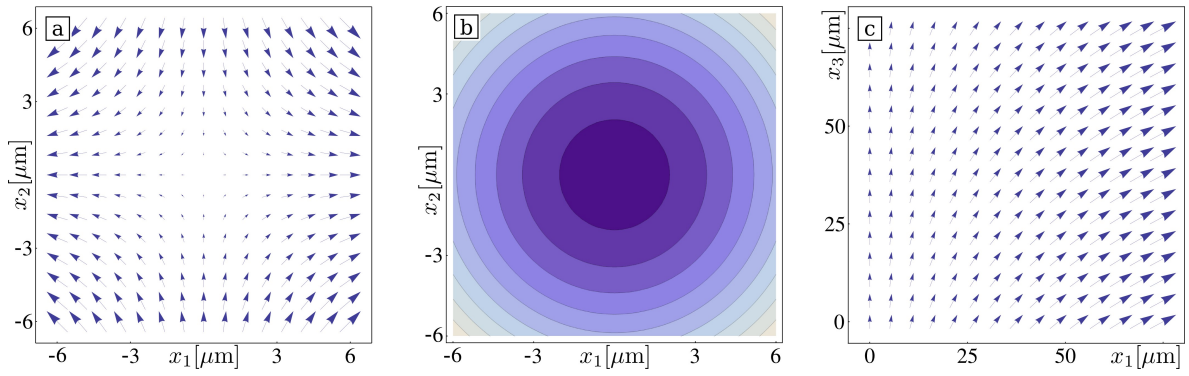

Figure 3.1: Sketch of the Ioffe-Pritchard magnetic field configuration Eq. (3.3) for $B = 1\,\mathrm{G}$ and $G = 2.5\,\mathrm{Tm}^{-1}$. (a) Vectorial plot of the two-dimensional quadrupole field $\mathbf{B}_l(\mathbf{x})$ in the x_1, x_2-plane. (b) Magnitude of the magnetic field in the x_1, x_2-plane. The azimuthal symmetry as expected from Eq. (3.4) is clearly visible. Moreover, the transition from a quadratic increase of the field strength to a linear behavior can be observed. The magnetic field is translational invariant in the x_3-direction, as can be observed in panel (c) where the intersection for $x_2 = 0$ is illustrated. In this subfigure we chose a larger spatial range such that the variation of the magnetic field direction within the trap becomes evident.

part of the magnetic field, $\mathbf{B}_l(\mathbf{x})$, the situation is not as obvious. A rather simple form is given by $\mathbf{A}_l(\mathbf{x}) = Gx_1x_2\mathbf{e}_3$. However, in this case the connection to the magnetic field becomes a bit more involved, namely, $\frac{1}{3}\mathbf{B}_l(\mathbf{x}) \times \mathbf{x} = \mathbf{A}_l(\mathbf{x}) + \mathbf{A}_{add}(\mathbf{x})$ where $\mathbf{A}_{add}(\mathbf{x}) = -\frac{G}{3}(yz, xz, xy)^T$. If we define $\mathbf{A}'_l(\mathbf{x}) = \mathbf{A}_l(\mathbf{x}) + \mathbf{A}_{add}(\mathbf{x})$, on the other hand, the complexity of the vector potential is increased in favor of a simple relation between the magnetic field and its vector potential: $\mathbf{A}'_l(\mathbf{x}) = \frac{1}{3}\mathbf{B}_l(\mathbf{x}) \times \mathbf{x}$. $\mathbf{A}_{add}(\mathbf{x})$ can be written as $\mathbf{A}_{add}(\mathbf{x}) = \boldsymbol{\nabla}\chi(\mathbf{x})$ with $\chi(\mathbf{x}) = -\frac{G}{3}xyz$. That is, both potentials are connected by a gauge transformation and they both satisfy the Coulomb gauge $\boldsymbol{\nabla}\mathbf{A} = 0$. For the purpose of this thesis, we chose $\mathbf{A}_l(\mathbf{x})$ as vector potential because of its simplicity. Hence, the vector potential of the Ioffe-Pritchard configuration reads

$$\mathbf{A}(\mathbf{x}) = \mathbf{A}_c(\mathbf{x}) + \mathbf{A}_l(\mathbf{x}) = \frac{B}{2}\begin{pmatrix} -x_2 \\ x_1 \\ 0 \end{pmatrix} + G\begin{pmatrix} 0 \\ 0 \\ x_1x_2 \end{pmatrix}. \tag{3.6}$$

Model Potential

The mutual interaction of the highly excited Rydberg valence electron and the remaining closed-shell ionic core is modeled by an effective potential which is assumed to be a function of the distance of the two particles only. The actual appearance of the model potential largely depends on the electronic states investigated. For high angular momentum Rydberg states of alkali atoms (i.e., $l \gtrsim 4$), the probability of finding the Rydberg electron in the vicinity of the ionic core is negligible. Consequently, the finite size and the internal structure of the closed-shell ionic core is not resolved and a simple Coulomb potential of the form $V(r) = -1/r$ can be

transformation

$$\mathbf{A} \longrightarrow \mathbf{A}' = \mathbf{A} + \boldsymbol{\nabla}\chi\,, \quad \phi \longrightarrow \phi' = \phi - \frac{1}{c}\frac{\partial\chi}{\partial t}\,. \tag{3.5}$$

However, the physics do not change: If ψ is a solution of the Schrödinger equation in $\mathbf{A}$, then $\psi' = \exp(\frac{ie}{\hbar c}\chi)\psi$ is a solution of the Schrödinger equation in $\mathbf{A}'$ [84].

employed. In particular, this is an excellent approximation for circular states with maximal angular momentum ($l = m = n - 1$) which are investigated, e.g., in Refs. [61, 64, 65, 85] and in Chapter 6 of this thesis. The low angular momentum states of alkali atoms, on the other hand, penetrate the ionic core and hence differ significantly from the hydrogenic ones. The resulting core penetration, scattering, and polarization effects can be accounted for by employing a model potential of the form

$$V(r) \equiv V_l(r) = -\frac{Z_l(r)}{r} - \frac{\alpha_c}{2r^4}\left[1 - e^{-(r/r_c)^6}\right] \tag{3.7}$$

with α_c being the static dipole polarizability of the positive-ion core. The radial charge $Z_l(r)$ is given by

$$Z_l(r) = 1 + (z-1)e^{-a_1 r} - r(a_3 + a_4 r)e^{-a_2 r}\,, \tag{3.8}$$

where z is the nuclear charge of the neutral atom and r_c is the cutoff radius introduced to truncate the unphysical short-range behavior of the polarization potential near the origin [72]. Note that $V_l(r)$ depends on the orbital angular momentum l via its parameters, i.e., $a_i \equiv a_i(l)$ and $r_c \equiv r_c(l)$. The actual values of $a_i(l)$, $r_c(l)$, and α_c are listed in Tab. 3.1. The resulting binding energies are related to the effective quantum number n^* and the quantum defect δ_{njl} by $W = -\frac{1}{2n^{*2}} = -\frac{1}{2(n-\delta_{njl})^2}$ [32]. For a qualitative introduction to the low angular momentum Rydberg states of alkali atoms – including the illustration of some exemplary radial wave functions – we refer the reader to Chapter 2.

Spin-Orbit Interaction

Similar to the question on which model potential to use, the inclusion of the spin-orbit interaction depends on the angular momentum states investigated. For high angular momentum states, the resulting fine-structure splittings scale as $\alpha^2/2n^5$ [68] and it turns out that the spin-orbit effects are negligible compared to the Zeeman splittings due to the magnetic field interaction [65]. For low angular momentum states, the story is again quite different. In this case, one encounters a scaling of the fine-structure intervals as $\sim 1/n^{*3}$. For the regime investigated in thesis, the spin-orbit effects consequently dominate over the Zeeman splittings (see Section 2.3 for an overview of the energy scales encountered in our system). Hence, the introduction of the total electronic angular momentum $\mathbf{J} = \mathbf{L} + \mathbf{S}$ and the inclusion of the spin-orbit interaction is indispensable for investigating low angular momentum Rydberg states of alkali atoms. In particular, up to first order it even suffices to investigate the effect of the magnetic field within a single fine structure manifold with fixed total electronic angular momentum j. However – as shall be shown within this thesis – the two-body character of Rydberg atoms necessitates the inclusion of higher order effects resulting in the coupling of j- as well as n-manifolds.

The spin-orbit interaction of the valence electron is given by

$$V_{so}(\mathbf{L}, \mathbf{S}) = \frac{\alpha^2}{2}\frac{1}{r}\frac{\mathrm{d}V_l(r)}{\mathrm{d}r}\mathbf{L}\cdot\mathbf{S}\,, \tag{3.9}$$

α being the fine-structure constant. $\mathbf{L} = \mathbf{r} \times \mathbf{p}$ denotes the orbital angular momentum of the valence electron and $r = |\mathbf{r}_e - \mathbf{r}_c|$ its distance from the nucleus. However, for a Coulomb potential $V(r) = -Z/r$, Eq. (3.9) leads to a nonphysical $1/r^3$ singularity near the origin [86].

Table 3.1: Optimized parameters $a_i(l)$, $r_c(l)$, and α_c for the l-dependent model potential Eq. (3.7) as given in Ref. [72].

	$l=0$	$l=1$	$l=2$	$l\geq 3$
a_1	3.696 284 74	4.440 889 78	3.787 173 63	2.398 489 33
a_2	1.649 152 55	1.928 288 31	1.570 278 64	1.768 105 44
a_3	−9.860 691 96	−16.795 977 70	−11.655 889 70	−12.071 067 80
a_4	0.195 799 87	−0.816 333 14	0.529 428 35	0.772 565 89
r_c	1.662 421 17	1.501 951 24	4.868 519 38	4.798 313 27
α_c		9.0760		

If the spin-orbit interaction is treated perturbatively, this singularity does not cause any problems: Because the radial wave function behaves as r^l near the origin, the expectation value of the interaction (3.9) is not divergent for $l > 0$; for $l = 0$ it can be shown that the spin-orbit interaction term vanishes. A more rigorous treatment based on the Dirac equation suggests that the interaction Eq. (3.9) can be regularized using either the factor $[1-\alpha^2 V(r)/2]^{-1}$ [68] or $[1-\alpha^2 V(r)/2]^{-2}$ [87]. This ambiguity stems from the ambiguity in defining a hermitian energy-independent Hamiltonian for the Pauli equation when going from first-order Dirac equations for the large and small components of the relativistic wave function to one second-order Schrödinger-Pauli equation [86]. In our calculations, we choose the second alternative, yielding the following spin-orbit interaction term:

$$V_{so}(\mathbf{L},\mathbf{S}) = \frac{\alpha^2}{2}\left[1-\tfrac{\alpha^2}{2}V_l(r)\right]^{-2}\frac{1}{r}\frac{\mathrm{d}V_l(r)}{\mathrm{d}r}\mathbf{L}\cdot\mathbf{S}\,. \tag{3.10}$$

Digression: Hyperfine Structure

So far, we omitted the interaction of the total electronic angular momentum $\mathbf{J}=\mathbf{L}+\mathbf{S}$ with the nuclear spin $\mathbf{I}$, which leads to the hyperfine structure of the atomic energy spectrum. For high angular momentum states this is apparently a sensible approximation since already the fine-structure could be neglected. In the case of Rydberg atoms in low angular momentum electronic states, however, it is *a priori* not clear if the hyperfine structure can be neglected. In the next few paragraphs, we are going to motivate why the hyperfine structure can indeed be omitted in our theoretical description. In doing so, we make use of a simplified picture, namely, that the Rydberg atom couples to the magnetic field either via $g_j m_j B$ or $g_F m_F B$ depending on the involved field strength and the resulting coupling scheme [68].[5]

The hyperfine Hamiltonian can be written as [78]

$$H_{\mathrm{hfs}} = \underbrace{hA\mathbf{I}\cdot\mathbf{J}}_{\text{magnetic dipole interaction}} + \underbrace{hB\frac{6(\mathbf{I}\cdot\mathbf{J})^2+3(\mathbf{I}\cdot\mathbf{J})-2I(I+1)J(J+1)}{2I(2I-1)2J(2J-1)}}_{\text{electric quadrupole interaction}} \tag{3.11}$$

where A is the so-called magnetic hyperfine constant. Since the fine structure splitting of low

[5] This basically corresponds to assuming a constant magnetic field in z-direction. Indeed, we show in Chapter 4 that our Hamiltonian can be reformulated to yield such a simple form. However, this only holds up to first order and the two-body character of Rydberg atoms will introduce further effects.

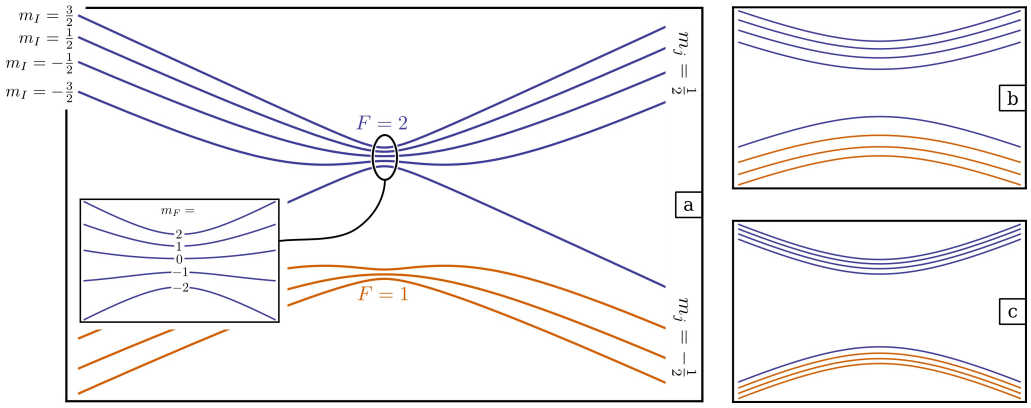

Figure 3.2: Schematics of the $nS_{1/2}$ Rydberg trapping potentials in a magnetic Ioffe-Pritchard trap including the hyperfine interaction for (a)-(b) $n = 30$ and (c) $n = 40$. The Ioffe field B is chosen as (a) 0.1 G, and (b)+(c) 1 G, respectively. For all subfigures the magnetic field gradient is $G = 10\,\mathrm{Tm}^{-1}$ and the spatial range displayed corresponds to 30 μm. Subfigure (a) represents a typical example where two different coupling schemes are encountered. For large coordinates, the Zeeman splitting of the $m_j = \pm 1/2$ states dominates the energy spectrum. The splitting on top of this level structure is due to the hyperfine interaction, giving rise to $2I + 1$ sublevels defined by the magnetic quantum number m_I of the nuclear spin. Coming closer to the origin, the magnitude of the magnetic field is gradually decreased until the value of the Ioffe field B, which is chosen rather small in subfigure (a). Consequently, the hyperfine splitting of the $F = 1$ and $F = 2$ components dominates the level structure at this point. The magnetic field then splits each of these states into $2F + 1$ sublevels characterized by the magnetic quantum number m_F. For stronger Ioffe fields, the m_j splitting prevails not only for large coordinates but also at the origin, cf. subfigures (b) and (c). In case of subfigure (c), the hyperfine structure leads merely to a small splitting of the trapping potentials.

angular momentum states of rubidium atoms is quite large, we can restrict ourselves here to a single j-manifold even in the presence of a magnetic field. Considering only the magnetic dipole interaction and introducing the total angular momentum $\mathbf{F} = \mathbf{I} + \mathbf{J}$, one yields for the hyperfine splitting of two adjacent levels ($F' = F - 1$)

$$\Delta W_{\mathrm{hfs}}^{(0)} = \frac{hA}{2}\left[F(F+1) - F'(F'+1)\right] = 2F\frac{hA}{2}. \tag{3.12}$$

Including a weak magnetic field B, each hyperfine level is then splitted into $2F + 1$ magnetic sublevels according to $\frac{1}{2}g_F m_F B$. However, we are interested in the regime of stronger magnetic fields, where hyperfine structure effects are small and the dominant level structure is consequently given by the coupling of the total electronic magnetic moment to the magnetic field according to $\frac{1}{2}g_j m_j B$. In this case, the resulting trapping potentials are characterized by the magnetic quantum number m_j of the total electronic angular momentum $\mathbf{J}$. The hyperfine interaction can then be treated perturbatively, resulting in a $(2I + 1)$-fold splitting of a given m_j sublevel according to

$$H_{\mathrm{hfs}} = hAm_I m_j\,, \tag{3.13}$$

i.e., the magnitude of the hyperfine splitting $\Delta W_{\mathrm{hfs}} = hAm_j$ depends on the magnetic quantum number m_j of the electronic state [88].

In a Ioffe-Pritchard trap with a weak offset field B, one can encounter both of the above

Table 3.2: Zeeman splittings ΔW_{zee} of the low angular momentum states for a field strength of $B = 1\,\text{G}$ and hyperfine constants $A(n)$ of the ^{87}Rb atom for various principal quantum numbers n. The latter are obtained by an extrapolation of the hyperfine constants provided in Ref. [78] for $n \lesssim 10$ according to $A(n) = A_0/n^{*3}$. For the $nS_{1/2}$ state, experimental values of the hyperfine splittings for $28 \leq n \leq 33$ are available from Ref. [70]. Correspondingly, the $nS_{1/2}$ values presented here are extrapolated from this data.

	$S_{1/2}$	$P_{1/2}$	$P_{3/2}$	$D_{3/2}$	$D_{5/2}$
g_J	2	2/3	4/3	4/5	6/5
ΔW_{zee} [MHz]	2.8	0.9	1.9	1.1	1.7
A_0 [MHz]	16846	4469	1050	963	-405
$A(30)$ [MHz]	0.869	0.222	0.051	0.040	-0.017
$A(40)$ [MHz]	0.336	0.087	0.020	0.016	-0.007
$A(50)$ [MHz]	0.164	0.042	0.010	0.008	-0.003

described coupling schemes at the same time: In such a case, the hyperfine splitting dominates at the origin, whereas far from it the gradient field eventually overcomes the weak field limit. Exactly this situation is illustrated in Fig. 3.2(a) for the $30S_{1/2}$ state of ^{87}Rb with $F \in \{1, 2\}$ and $j = 1/2$. At the origin, one observe first of all the splitting of the $F = 1$ and $F = 2$ component according to Eq. (3.12). Each of these hyperfine levels is then split by the magnetic field into $2F+1$ sublevels that show either trapping or antitrapping behavior when going away from the origin, depending on the sign of the magnetic quantum number m_F. For even larger coordinates, the m_j coupling scheme is recovered. However, for Ioffe-Pritchard configurations with larger offset fields – as can be seen in Fig. 3.2(b) and (c) – already at the origin the m_j splitting prevails. In this case, the trapping potentials are well described by the electronic properties alone and the inclusion of the hyperfine interaction merely leads to a splitting into various subsurfaces without changing their actual shape. This is exactly the regime we are aiming at.

To get a feeling where the above mentioned desirable regime is valid, we compare in Tab. 3.2 actual values of the hyperfine constant A (that determines the magnitude of the hyperfine structure splitting) with the Zeeman splitting of m_j states. The latter is given by[6] $\Delta W_{\text{zee}} = \frac{g_J}{2} B \approx 1.4\,\text{MHz} \cdot g_J B[\text{G}]$ with $g_j = \frac{3}{2} + \frac{s(s+1)-l(l+1)}{2j(j+1)}$ being the Landé g-factor and B being given in units of Gauss. As desired, one recognizes that ΔW_{hfs} is smaller than the Zeeman splitting ΔW_{zee} for $B = 1\,\text{G}$. That is, the hyperfine structure acts as a perturbation on the Zeeman levels and lifts the degeneracy of the states. Generally, we will consider configurations where the hyperfine interaction can be omitted.

3.2 Center of Mass and Relative Coordinates

After identifying all ingredients necessary for a sensible description of our system, we continue by simplifying Hamiltonian (3.2). The first, most natural step to achieve this is to introduce

[6] At this point, we are only interested in the magnitude of the splittings. For this reason, we consider a constant magnetic field of strength B pointing along the z-direction. In the regime of sufficiently small field strengths where no mixing between states of different j occurs, the interaction with the magnetic field can be written as $H^0_{\text{zee}} = \frac{B}{2}\left[L_z + 2S_z\right] = \frac{g_J}{2} J_z B$ by projecting onto the subspace $\mathcal{H}(n, j, l, s)$ [89]. As will be shown in Chapter 4, also in a Ioffe-Pritchard trap the interaction can be written in this form.

a center of mass coordinate $\mathbf{R} = \frac{m_e\mathbf{r}_e + M_c\mathbf{r}_c}{m_e+M_c}$ and a relative coordinate $\mathbf{r} = \mathbf{r}_e - \mathbf{r}_c$. As known from the theory of the hydrogen atom, this choice decouples the field-free Hamiltonian,

$$\frac{\mathbf{p}_e^2}{2m_e} + \frac{\mathbf{p}_c^2}{2M_c} + V(|\mathbf{r}_e - \mathbf{r}_c|) + V_{so}(\mathbf{L},\mathbf{S}) = \frac{\mathbf{P^2}}{2M} + \frac{\mathbf{p}^2}{2m} + V(r) + V_{so}(\mathbf{L},\mathbf{S})\,, \tag{3.14}$$

where $M = m_e + M_c$ is the total and $m = \frac{m_e M_c}{m_e+M_c}$ the reduced mass, respectively. Since the mass of the ionic core M_c exceeds the electronic mass m_e by more than a factor 10^3, it is often a good approximation to identify the center of mass with the ionic core itself and the relative motion with the motion of the Rydberg electron about the core.[7] In this manner, we are going to approximate $m = \frac{m_e}{1+m_e/M_c} = m_e(1 - \frac{m_e}{M_c} + (\frac{m_e}{M_c})^2 + \cdots) \approx m_e$ when necessary. The center of mass and relative momentum are given by $\mathbf{P} = \mathbf{p}_e + \mathbf{p}_c$ and $\mathbf{p} = \frac{M_c\mathbf{p}_e - m_e\mathbf{p}_c}{m_e+M_c}$, respectively. Hamiltonian (3.14) contains no couplings between the relative and center of mass motion; its solutions can thus be separated exactly in a center of mass and relative part.

Introducing the new coordinates for the terms of Hamiltonian (3.2) that contain the vector potential $\mathbf{A}(\mathbf{x})$ becomes somehow more involved. The lengthy calculation can be found in Appendix B and results in

$$\begin{aligned}
\frac{\mathbf{A}_c(\mathbf{r}_e)\cdot\mathbf{p}_e}{m_e} - \frac{\mathbf{A}_c(\mathbf{r}_c)\cdot\mathbf{p}_c}{M_c} &= \frac{1}{m}\mathbf{A}_c(\mathbf{R})\cdot\mathbf{p} + \Big(\frac{1}{m} - \frac{2}{M_c}\Big)\mathbf{A}_c(\mathbf{r})\cdot\mathbf{p} + \frac{1}{M}\mathbf{A}_c(\mathbf{r})\cdot\mathbf{P}\,,\\
\frac{\mathbf{A}_l(\mathbf{r}_e)\cdot\mathbf{p}_e}{m_e} - \frac{\mathbf{A}_l(\mathbf{r}_c)\cdot\mathbf{p}_c}{M_c} &\approx \frac{1}{m}\mathbf{A}_l(\mathbf{R}+\mathbf{r})\cdot\mathbf{p}\,,\\
\frac{\mathbf{A}(\mathbf{r}_e)^2}{2m_e} + \frac{\mathbf{A}(\mathbf{r}_c)^2}{2M_c} &\approx \frac{1}{2m}\mathbf{A}_c(\mathbf{R})^2 + \Big(\frac{1}{m} - \frac{2}{M_c}\Big)\mathbf{A}_c(\mathbf{R})\cdot\mathbf{A}_c(\mathbf{r})\\
&\quad + \frac{1}{2}\Big(\frac{1}{m} - \frac{3}{M}\Big)\mathbf{A}_c(\mathbf{r})^2 + \frac{1}{2m}\mathbf{A}_l(\mathbf{R}+\mathbf{r})^2\,.
\end{aligned}$$

Note that the approximations above only concern terms including $\mathbf{A}_l(\mathbf{x})$ and are performed at this point already, anticipating that the unitary transformation, which we are going to introduce in the next section, does not affect these terms. The interactions of the magnetic moments with the magnetic field are correspondingly given by

$$\begin{aligned}
\boldsymbol{\mu}_e\cdot\mathbf{B}(\mathbf{r}_e) &= \boldsymbol{\mu}_e\cdot\big[\mathbf{B}_c + \mathbf{B}_l(\mathbf{R} + \tfrac{\mathbf{M_c}}{\mathbf{M}}\mathbf{r})\big] \approx \boldsymbol{\mu}_e\cdot\big[\mathbf{B}_c + \mathbf{B}_l(\mathbf{R}+\mathbf{r})\big]\,,\\
\boldsymbol{\mu}_c\cdot\mathbf{B}(\mathbf{r}_c) &= \boldsymbol{\mu}_c\cdot\big[\mathbf{B}_c + \mathbf{B}_l(\mathbf{R} - \tfrac{m_e}{M}\mathbf{r})\big] \approx \boldsymbol{\mu}_c\cdot\big[\mathbf{B}_c + \mathbf{B}_l(\mathbf{R})\big]\,.
\end{aligned}$$

As pointed out in the previous section, the terms involving $\boldsymbol{\mu}_c$ usually can be neglected due to the large mass of the ionic core. In fact, we will do so in the rest of this thesis. After all, we are left with the following Hamiltonian,

$$\begin{aligned}
H = \frac{\mathbf{P}^2}{2M} + H_A - \boldsymbol{\mu}_e\cdot\big[\mathbf{B}_c + \mathbf{B}_l(\mathbf{R}+\mathbf{r})\big] + \frac{1}{m}\mathbf{A}_c(\mathbf{R})\cdot\mathbf{p} + \Big(\frac{1}{m} - \frac{2}{M_c}\Big)\mathbf{A}_c(\mathbf{r})\cdot\mathbf{p} + \frac{1}{M}\mathbf{A}_c(\mathbf{r})\cdot\mathbf{P}\\
+ \frac{1}{2m}\mathbf{A}_c(\mathbf{R})^2 + \Big(\frac{1}{m} - \frac{2}{M_c}\Big)\mathbf{A}_c(\mathbf{R})\cdot\mathbf{A}_c(\mathbf{r}) + \frac{1}{2}\Big(\frac{1}{m} - \frac{3}{M}\Big)\mathbf{A}_c(\mathbf{r})^2\\
+ \frac{1}{m}\mathbf{A}_l(\mathbf{R}+\mathbf{r})\cdot\mathbf{p} + \frac{1}{2m}\mathbf{A}_l(\mathbf{R}+\mathbf{r})^2\,,
\end{aligned} \tag{3.15}$$

[7] When speaking about the position of the Rydberg atom, we thus refer to the center of mass coordinate $\mathbf{R}$.

where $H_A = \mathbf{p}^2/2m + V_l(r) + V_{so}(\mathbf{L}, \mathbf{S})$ is the field-free electronic Hamiltonian of the Rydberg atom.

3.3 Unitary Transformation

As pointed out in the previous section, the introduction of center of mass and relative coordinates decouples the Hamiltonian in the field-free case. However, this thesis focuses explicitly on including (even inhomogeneous) magnetic fields. Inspecting Hamiltonian (3.15), it thus comes with no surprise that field-induced couplings of the relative and center of mass motion are encountered. It is therefore desirable to find a means to reduce the amount of such couplings in our theoretical description. In case of neutral systems in a homogeneous magnetic field, a pseudo momentum can be defined that constitutes a conserved quantity [90,91]. Based on the latter a wave function can be constructed that is a simultaneous eigenfunction of every component of this pseudo momentum [92]. Inspired by these early findings, we apply a unitary transformation [64,65] that allows us to partially remove the field-induced couplings of the relative and center of mass motion:

$$U = \exp\left\{ i\frac{e}{2}(\mathbf{B}_c \times \mathbf{r}) \cdot \mathbf{R} \right\}. \tag{3.16}$$

The behavior of a given operator O under such a unitary transformation can be calculated using the so-called *Baker-Campbell-Hausdorff* formula,

$$e^X O e^{-X} = \sum_{n=0}^{\infty} \frac{1}{n!}[X, O]_n \,, \tag{3.17}$$

with $[X, O]_n = [X, [X, O]_{n-1}]$, $[X, O]_0 = B$, and $X = -i\frac{e}{2}(\mathbf{B}_c \times \mathbf{r}) \cdot \mathbf{R}$ in our case. Consequently, any operator that commutes with $\mathbf{R}$ and $\mathbf{r}$ is invariant under the transformation (3.16). The derivation of the transformation properties of the various ingredients of Hamiltonian (3.15) is provided in Appendix C. We find

$$U^\dagger \mathbf{p}^2 U = \mathbf{p}^2 - 2\mathbf{A}_c(\mathbf{R}) \cdot \mathbf{p} + \mathbf{A}_c(\mathbf{R})^2 \,, \tag{3.18a}$$

$$U^\dagger \mathbf{P}^2 U = \mathbf{P}^2 + 2\mathbf{A}_c(\mathbf{r}) \cdot \mathbf{P} + \mathbf{A}_c(\mathbf{r})^2 \,, \tag{3.18b}$$

$$U^\dagger V_{so}(\mathbf{L}, \mathbf{S}) U = V_{so}(\mathbf{L}, \mathbf{S}) - \frac{\alpha^2}{2r}\frac{\mathrm{d}V_l(r)}{\mathrm{d}r}\big[\mathbf{r} \times \mathbf{A}_c(\mathbf{R})\big] \cdot \mathbf{S} \,, \tag{3.18c}$$

$$U^\dagger \big[\mathbf{A}_c(\mathbf{r}) \cdot \mathbf{P}\big] U = \mathbf{A}_c(\mathbf{r}) \cdot \mathbf{P} + \mathbf{A}_c(\mathbf{r})^2 \,, \tag{3.18d}$$

$$U^\dagger \big[\mathbf{A}_c(\mathbf{R}) \cdot \mathbf{p}\big] U = \mathbf{A}_c(\mathbf{R}) \cdot \mathbf{p} - \mathbf{A}_c(\mathbf{R})^2 \,, \tag{3.18e}$$

$$U^\dagger \big[\mathbf{A}_c(\mathbf{r}) \cdot \mathbf{p}\big] U = \mathbf{A}_c(\mathbf{r}) \cdot \mathbf{p} - \mathbf{A}_c(\mathbf{R}) \cdot \mathbf{A}_c(\mathbf{r}) \,, \tag{3.18f}$$

where all quantities are given in atomic units. Because of the particular choice of the vector potential, the terms involving the linear part $\mathbf{A}_l(\mathbf{x})$ are invariant. Note that $V_l(r)$ depends on the angular momentum $\mathbf{L}$ and therefore does not commute with the unitary transformation (3.16). However, it turns out that the transformation of $V_l(r)$ leads to minor corrections that

can be neglected for our purposes[8]. Incorporating these results, our transformed Hamiltonian reads (in atomic units, see Appendix C for more details)

$$\begin{aligned} U^\dagger H U = &\frac{\mathbf{P}^2}{2M} + \frac{\mathbf{p}^2}{2} + V_l(r) + V_{so}(\mathbf{L},\mathbf{S}) + \tfrac{1}{2}[\mathbf{L}+2\mathbf{S}]\cdot\mathbf{B}_c - \boldsymbol{\mu}_e\cdot\mathbf{B}_l(\mathbf{R}+\mathbf{r}) \\ &+ \mathbf{A}_l(\mathbf{R}+\mathbf{r})\cdot\mathbf{p} + \frac{1}{2m}\big[\mathbf{A}_c(\mathbf{r})^2 + \mathbf{A}_l(\mathbf{R}+\mathbf{r})^2\big] \\ &+ \frac{1}{M}\mathbf{B}_c\cdot\big[\mathbf{r}\times\mathbf{P}\big] - \frac{\alpha^2}{2r}\frac{\mathrm{d}V_l(r)}{\mathrm{d}r}\big[\mathbf{r}\times\mathbf{A}_c(\mathbf{R})\big]\cdot\mathbf{S}\,. \end{aligned} \tag{3.20}$$

3.4 Adiabatic Approach

Inspecting our final Hamiltonian (3.20) from above, we notice that the center of mass and relative motion are by far not decoupled completely. However, the arising coupling terms – except the term $\frac{1}{M}\mathbf{B}_c\cdot[\mathbf{r}\times\mathbf{P}]$ – only show a dependence on the center of mass coordinate $\mathbf{R}$ rather than the corresponding momentum $\mathbf{P}$. Having additionally in mind that for ultracold temperatures the motion of the Rydberg electron occurs on much faster timescales than the external, i.e., center of mass motion, this allows us to employ an adiabatic approach reminiscent of the well-known *Born-Oppenheimer approximation* for the decoupling of the electronic and nuclear motion in molecular dynamics. Figuratively speaking, we assume that the electronic dynamics instantaneously adapts to the surrounding magnetic field while the center of mass (which we can identify with the Rydberg atom itself) is slowly moving through the inhomogeneous field. In doing so, the energy of the electronic dynamics can be considered to be a function of the position of our Rydberg atom. Computing the electronic energy spectrum for fixed center of mass positions therefore provides us adiabatic electronic potentials for the external motion.[9]

To put the above described concept on firm mathematical grounds, we rewrite Hamiltonian

[8] Since the model potential $V_l(r)$ depends only implicitly on the electronic angular momentum $\mathbf{L}$, the necessary commutator $[ie\mathbf{A}_c(\mathbf{R})\cdot\mathbf{r}, V_l(r)]_n$ cannot be calculated straightforwardly. Nevertheless, we can estimate its relevance for the Hamiltonian by anticipating the matrix representation that will be used for solving the underlying Schrödinger equation. That is, we have to relate the matrix elements $i\mathbf{A}_c(\mathbf{R})\cdot\langle n'l'j'm_j'|[\mathbf{r},\hat{V}]|nljm_j\rangle$ to other energy scales emerging for our Hamiltonian. Note that we write $\hat{V}$ emphasizing that the model potential is an operator that is sensitive to the angular part of the basis functions (although being diagonal). We get

$$\langle n'l'j'm_j'|[\mathbf{r},\hat{V}]|nljm_j\rangle = \langle n'l'j'm_j'||r(V_l(r)-V_{l'}(r))||nljm_j\rangle\cdot\langle n'l'j'm_j'|\hat{\mathbf{r}}|nljm_j\rangle \tag{3.19}$$

where we assumed $\hat{V}$ to be hermitian, $\hat{\mathbf{r}} = \mathbf{r}/r$, and $\langle||\ldots||\rangle$ denotes the reduced matrix element, i.e., only the radial integration remains. For the transformation of the derivative $\frac{\mathrm{d}V_l(r)}{\mathrm{d}r}$, which appears in the spin-orbit coupling term, an analog treatment is necessary. An estimation of the order of magnitude of the matrix elements Eq. (3.19) reveals that they can become as large as the spatially dependent magnetic field interaction terms. However, they are only non-vanishing for $\Delta l = \pm 1$. The effect on the energy surfaces is therefore suppressed by the large energy difference between adjacent l-levels due to the quantum defect (for higher angular momentum, these states become degenerate and the model potential commutes with U). This has been confirmed by calculations of the energy surfaces including the transformed part of the potential. Higher orders of the commutator $[ie\mathbf{A}_c(\mathbf{R})\cdot\mathbf{r}, V_l(r)]_n$ are suppressed by additional factors of B.

[9] Note that each eigenvalue of the electronic Hamiltonian corresponds to a separate potential. Hence we get multiple adiabatic potentials, each corresponding to a certain internal, i.e., electronic state of the Rydberg atom.

(3.20) as

$$H = \frac{\mathbf{P}^2}{2M} + \frac{1}{M}\mathbf{B}_c \cdot [\mathbf{r} \times \mathbf{P}] + H_r(\mathbf{r}, \mathbf{p}, \mathbf{L}, \mathbf{S}; \mathbf{R}) \,, \tag{3.21}$$

where

$$\begin{aligned} H_r(\mathbf{r}, \mathbf{p}, \mathbf{L}, \mathbf{S}; \mathbf{R}) = H_A + \tfrac{1}{2}[\mathbf{L} + 2\mathbf{S}] \cdot \mathbf{B}_c - \boldsymbol{\mu}_e \cdot \mathbf{B}_l(\mathbf{R} + \mathbf{r}) + \mathbf{A}_l(\mathbf{R} + \mathbf{r}) \cdot \mathbf{p} \\ + \frac{1}{2m}\big[\mathbf{A}_c(\mathbf{r})^2 + \mathbf{A}_l(\mathbf{R} + \mathbf{r})^2\big] - \frac{\alpha^2}{2r}\frac{\mathrm{d}V_l(r)}{\mathrm{d}r}\big[\mathbf{r} \times \mathbf{A}_c(\mathbf{R})\big] \cdot \mathbf{S} \end{aligned} \tag{3.22}$$

designates the electronic part of the Hamiltonian. The adiabatic approximation is introduced by employing the limit of vanishing center of mass kinetic energy, i.e., setting $\mathbf{P} = 0$. A parametric dependence of the electronic wave function on the position $\mathbf{R}$ of the atom then allows us to solve the stationary Schrödinger equation belonging to the electronic Hamiltonian:

$$H_r|\varphi_\kappa(\mathbf{r}; \mathbf{R})\rangle = E_\kappa(\mathbf{R})|\varphi_\kappa(\mathbf{r}; \mathbf{R})\rangle \,.$$

Note that the eigenvalues $E_\kappa(\mathbf{R})$ themselves depend on the position of the atom and therefore constitute the adiabatic electronic potential surfaces for the center of mass motion. Within the adiabatic approximation, the Schrödinger equation for the center of mass wave function thus reads

$$\big[T + E_\kappa(\mathbf{R})\big]|\chi_\nu(\mathbf{R})\rangle = E_\nu|\chi_\nu(\mathbf{R})\rangle \tag{3.23}$$

with $|\chi_\nu(\mathbf{R})\rangle$ being the eigenfunctions of the quantized center of mass motion and ν labeling the possible eigenstates for a given adiabatic electronic potential surface $E_\kappa(\mathbf{R})$. Note that in Eq. (3.23) we omitted the term $\frac{1}{M}\mathbf{B}_c \cdot [\mathbf{r} \times \mathbf{P}] = 2\mathbf{A}_c(\mathbf{r}) \cdot \mathbf{P}/M$ opposed to the contribution $\frac{1}{2}\mathbf{L} \cdot \mathbf{B}_c = \mathbf{A}_c(\mathbf{r}) \cdot \mathbf{p}/m$ incorporated in H_r since for ultracold temperatures $\langle \mathbf{P}/M \rangle$ becomes negligible compared to the relative motion $\langle \mathbf{p}/m \rangle$. We will continue to do so throughout this thesis.

As the name suggests, the Born-Oppenheimer kind of approximation that we just applied is not exact. Diagonalizing solely the electronic Hamiltonian H_r without considering the center of mass kinetic energy $T = \mathbf{P}^2/2m$ corresponds to applying a suitable spatially dependent unitary transformation U_r to the Hamiltonian (3.21). Because of its spatial dependence, U_r does not commute with the kinetic energy operator T,

$$U_r^\dagger H U_r = U_r^\dagger H_r U_r + U_r^\dagger T U_r = E_\kappa(\mathbf{R}) + T + \Delta T \,,$$

giving rise to nonadiabatic couplings ΔT [65]:

$$\Delta T = -\frac{1}{2M}\Big[U_r^\dagger(\partial_X^2 U_r) + U_r^\dagger(\partial_Y^2 U_r) + 2U_r^\dagger(\partial_X U_r)\partial_X + 2U_r^\dagger(\partial_Y U_r)\partial_Y\Big] \,, \tag{3.24}$$

These couplings have been neglected in Eq. (3.23) which is reasonable if the conditions

$$\begin{aligned} \left|\frac{\langle\varphi_{\kappa'}|\partial_X H|\varphi_\kappa\rangle}{E_{\kappa'} - E_\kappa}\right| \ll 1, \qquad \left|\frac{\langle\varphi_{\kappa'}|\partial_Y H|\varphi_\kappa\rangle}{E_{\kappa'} - E_\kappa}\right| \ll 1, \\ \left|\frac{\langle\varphi_{\kappa'}|\partial_X^2 H|\varphi_\kappa\rangle}{E_{\kappa'} - E_\kappa}\right| \ll 1, \qquad \left|\frac{\langle\varphi_{\kappa'}|\partial_Y^2 H|\varphi_\kappa\rangle}{E_{\kappa'} - E_\kappa}\right| \ll 1 \end{aligned} \tag{3.25}$$

are fulfilled [62, 65]. Provided that the above matrix elements are well-behaved, the energy denominator in Eqs. (3.25) thus suppresses couplings between the adiabatic energy surfaces. Nevertheless, we have to keep in mind that transitions between these surfaces can become relevant in the vicinity of avoided crossings, i.e., if they become very close in energy.

An alternative approach to calculate the nonadiabatic couplings is presented in Ref. [79] by Sukumar and Brink. They rewrite the transformed center of mass momentum as

$$\mathbf{P}' = U_r^\dagger \mathbf{P} U_r = \mathbf{P} + \mathbf{A}(\mathbf{R}) \tag{3.26}$$

where the Hermitian matrix operator $\mathbf{A}(\mathbf{R})$ is defined by[10]

$$\mathbf{A}(\mathbf{R}) = -i\hbar U_r^\dagger (\boldsymbol{\nabla} U_r)\,.$$

The transformed center of mass kinetic energy reads correspondingly

$$T' = \frac{[\mathbf{P} + \mathbf{A}(\mathbf{R})]^2}{2M}$$

and the nonadiabatic couplings can be written in compact form as

$$\Delta T = \frac{1}{2M}\Big[\mathbf{A}(\mathbf{R})\cdot\mathbf{P} + \mathbf{P}\cdot\mathbf{A}(\mathbf{R}) + \mathbf{A}(\mathbf{R})^2\Big]\,. \tag{3.27}$$

Note the striking similarity of expressions (3.26) and (3.27) with the minimal coupling scheme as employed in Section 3.1. Sukumar and Brink calculated in Ref. [79] the nonadiabatic spin-flip transition rate Γ in a Ioffe-Pritchard trap. For a $S_{1/2}$ ground state atom residing in the ground state of the trapping potential $E_\kappa(\mathbf{R})$, they yield a transition rate of

$$\Gamma \approx \frac{\pi\omega}{2} e^{-E_0/2\hbar\omega} \tag{3.28}$$

with ω denoting the trap frequency and $E_0 = 2\mu_b B + \hbar\omega$ being the final kinetic energy of the atom after the spin flip. Since $2\mu_B B$ corresponds to the separation of the adjacent surfaces, we come to the same conclusions as deduced from Eqs. (3.25): The suppression of nonadiabatic transitions increases with the separation of the involved energy surfaces. Note that Eq. (3.28) holds if the transition occurs to an untrapped state while Eqs. (3.25) provide an estimation of the nonadiabatic transitions between arbitrary surfaces.

In order to calculate the adiabatic electronic energy surfaces $E_\kappa(\mathbf{R})$ and the nonadiabatic couplings ΔT, the unitary transformation U_r must be determined. In the next two chapters, we are going to present two different approaches to this end. The first one provides an analytical expression for U_r,

$$U_r = e^{-i\gamma(L_x+S_x)} e^{-i\beta(L_y+S_y)}\,,$$

which basically rotates the magnetic field into the z-direction. In this manner, a Hamiltonian is obtained that shows a well-defined quantization axis along the z-direction for all center of mass coordinates $\mathbf{R}$. The drawback of this method is, however, that it relies on further

[10] Not incidentally the same notation as for the vector potential of the magnetic field is used here. Since $\mathbf{A}(\mathbf{R})$ refers to the nonadiabatic couplings only in this paragraph, this should not bear any confusions.

approximations and that certain terms can only be included in a perturbative manner. The second method of determining U_r is based on the numerical diagonalization of H_r employing a basis-set approach. This method is not in need of further approximations but necessitates the repeated diagonalization of the Hamiltonian matrix for a whole set of center of mass coordinates $\mathbf{R}$ in order to yield the adiabatic energy surfaces. U_r is then composed of the normalized vector representations of the electronic eigenfunctions $|\varphi_\kappa(\mathbf{r};\mathbf{R})\rangle$ for a fixed center of mass position $\mathbf{R}$. The matrix representation of U_r correspondingly reads

$$(U_r)_{\alpha\kappa} = \langle\alpha|\varphi_\kappa(\mathbf{r};\mathbf{R})\rangle$$

where $|\alpha\rangle$ denote the underlying basis functions, i.e., the eigenfunctions $|\varphi_\kappa(\mathbf{r};\mathbf{R})\rangle$ constitute the column vectors of U_r.

Chapter 4

Analytical Diagonalization

In the previous chapter, we derived the Hamiltonian for a Rydberg atom in a Ioffe-Pritchard trap and introduced an adiabatic approach that decouples the internal and external degrees of freedom. The latter relies on finding the solutions to the electronic part of Hamiltonian (3.20) parametrically as a function of the center of mass position of the Rydberg atom. In this chapter, we tackle this problem by introducing the spatially dependent unitary transformation U_r. The basic idea of this transformation is quite intuitive: It simply rotates the magnetic field vector $\mathbf{B}(\mathbf{x})$ into the direction of the z-axis and thereby 'homogenizes' the magnetic field by means of a well-defined quantization axis. In Section 4.1, we start this chapter with a short digression about rotations in quantum mechanics and the different conventions used in the literature. In order to successfully diagonalize the electronic part of Hamiltonian (3.20) by means of the envisaged unitary transformation, we need to introduce some further simplifications in Section 4.2. In Section 4.3, the transformation U_r is specified and analytical expressions for the adiabatic electronic energy surfaces are derived. Relevant terms that cannot be diagonalized using U_r are finally treated in Section 4.4 in a perturbation theoretical approach.

4.1 Digression: Rotations in Quantum Mechanics

When dealing with rotation operators in quantum mechanics, one has to take great care about the convention used: either active or passive rotations can be considered [93, 94]. In the active point of view, an object is rotated about the fixed origin, i.e., every point will acquire a new position in space: $\mathbf{x}' = A\mathbf{x}$ where A denotes the *active* rotation matrix. In the passive point of view, the object is kept fixed in space but the frame of reference is rotated about the origin, i.e., every point will be represented in the rotated frame of reference by new coordinates: $\mathbf{x}'' = P\mathbf{x}$ where P denotes the *passive* rotation matrix. That is, $\mathbf{x}''$ is the coordinate vector of a point in the rotated system while $\mathbf{x}'$ is the rotated coordinate vector of a point in the fixed system. For the scope of this thesis, we will stick with the active point of view.

In the active point of view, the rotation operator of a spinless particle about the ith coordinate axis by an angle α is given by

$$U_r = \mathrm{e}^{-\mathrm{i}\alpha L_i} \,. \tag{4.1}$$

An arbitrary operator O (and therefore also our Hamiltonian) transforms under this unitary

transformation like[1] $O' = U_r O U_r^\dagger$. We should note that for passive rotations one yields $U_r = \mathrm{e}^{\mathrm{i}\alpha L_i}$. The rotation matrices corresponding to rotations about the x-, $y-$, and z-axes are given by (again in the active viewpoint)

$$\mathcal{R}_x(\alpha) = \begin{pmatrix} 1 & 0 & 0 \\ 0 & \cos\alpha & -\sin\alpha \\ 0 & \sin\alpha & \cos\alpha \end{pmatrix}, \tag{4.2}$$

$$\mathcal{R}_y(\beta) = \begin{pmatrix} \cos\beta & 0 & \sin\beta \\ 0 & 1 & 0 \\ -\sin\beta & 0 & \cos\beta \end{pmatrix}, \text{ and} \tag{4.3}$$

$$\mathcal{R}_z(\gamma) = \begin{pmatrix} \cos\gamma & -\sin\gamma & 0 \\ \sin\gamma & \cos\gamma & 0 \\ 0 & 0 & 1 \end{pmatrix}, \tag{4.4}$$

respectively. One important property of *vector operators* is that their components transform in the rotation U_r like those of a vector in the rotation $\mathcal{R}^{-1} = \mathcal{R}^T$ [95]. Hence, the transformation law for the Cartesian components of a vector operator $\mathbf{O}$ is

$$O_i' = U_r O_i U_r^\dagger = \mathcal{R}_{ij}^{-1} O_j \,. \tag{4.5}$$

In particular, this holds for the position operator $\mathbf{r}$ as well as the electronic orbital angular momentum $\mathbf{L}$:

$$U_r \mathbf{r} U_r^\dagger = \mathcal{R}^{-1}\mathbf{r} \tag{4.6}$$

$$U_r \mathbf{L} U_r^\dagger = \mathcal{R}^{-1}\mathbf{L} \,. \tag{4.7}$$

Following the same line of reasoning for the spin degree of freedom, we get similarly

$$U_r \mathbf{S} U_r^\dagger = \mathcal{R}^{-1}\mathbf{S} \tag{4.8}$$

with $U_r = \mathrm{e}^{-\mathrm{i}\alpha S_i}$.

4.2 Preparing the Hamiltonian

Within the adiabatic approach, our aim is to determine the spatially dependent unitary transformation U_r that diagonalizes the electronic Hamiltonian

$$\begin{aligned} H_r(\mathbf{r},\mathbf{p},\mathbf{L},\mathbf{S};\mathbf{R}) = H_A + \tfrac{1}{2}[\mathbf{L}+2\mathbf{S}]\cdot\mathbf{B}_c - \boldsymbol{\mu}_e\cdot\mathbf{B}_l(\mathbf{R}+\mathbf{r}) + \mathbf{A}_l(\mathbf{R}+\mathbf{r})\cdot\mathbf{p} \\ + \frac{1}{2m}\big[\mathbf{A}_c(\mathbf{r})^2 + \mathbf{A}_l(\mathbf{R}+\mathbf{r})^2\big] - \frac{\alpha^2}{2r}\frac{\mathrm{d}V_l(r)}{\mathrm{d}r}\big[\mathbf{r}\times\mathbf{A}_c(\mathbf{R})\big]\cdot\mathbf{S}\,, \end{aligned} \tag{4.9}$$

cf. Section 3.4. The scope of the present chapter is to provide reasonably simple expressions for the adiabatic electronic potentials and the underlying unitary transformation U_r. To this end,

[1] Note that we use the convention $U_r O U_r^\dagger$ instead of $U_r^\dagger O U_r$ as used in Chapter 3. As the former is more common in the context of rotations, this hopefully prevents confusions regarding the rotation angles when comparing with literature.

we "prepare" in this section the above Hamiltonian by introducing further approximations that provide a more simple structure of the Hamiltonian. We are then able to exploit the fact that the field-free Hamiltonian H_A determines the energy spectrum, which allows us to consider the effect of the magnetic field within a given submanifold of fixed total electronic angular momentum j. By employing the latter restriction, we yield our final Hamiltonian that can be diagonalized analytically by the unitary transformation U_r that rotates the magnetic field vector $\mathbf{B}(\mathbf{x})$ into the direction of the z-axis.

We start by rewriting Hamiltonian (4.9) as

$$H_r = H_A + \tfrac{1}{2}B[L_z + 2S_z] + G(Xy + xY)p_z + G(XS_x - YS_y) + H' + H''\,.$$

The contribution

$$H'' = \mathbf{A}_l(\mathbf{r})\cdot\mathbf{p} - \boldsymbol{\mu}_e\cdot\mathbf{B}_l(\mathbf{r}) + \frac{1}{2m}\big[\mathbf{A}_c(\mathbf{r})^2 + \mathbf{A}_l(\mathbf{R}+\mathbf{r})^2\big] - \frac{\alpha^2}{2r}\frac{\mathrm{d}V_l(r)}{\mathrm{d}r}\big[\mathbf{r}\times\mathbf{A}_c(\mathbf{R})\big]\cdot\mathbf{S}$$

contains the diamagnetic terms, the transformed part of the spin-orbit coupling, and terms not showing an explicit spatial dependence, i.e., only depending on the relative coordinate $\mathbf{r}$. For the purpose of this chapter, we neglect H'' in the following.[2] The validity of this approach will be confirmed in Chapter 7 by comparison with the numerically calculated results. $H' = GXYp_z$ has a strong spatial dependence and is going to be treated perturbatively in Section 4.4. That is, our Hamiltonian gains the form $H_r = H_0 + H'$ and our initial problem is reduced to finding a unitary transformation that diagonalizes

$$H_0 = H_A + \tfrac{1}{2}B[L_z + 2S_z] + G(Xy + xY)p_z + G(XS_x - YS_y)\,. \tag{4.10}$$

As in Chapter 3, $H_A = \mathbf{p}^2/2m + V_l(r) + V_{so}(\mathbf{L},\mathbf{S})$ denotes the field-free electronic Hamiltonian of the Rydberg atom. In particular, H_A yields field-free eigenfunctions $|\kappa\rangle = |njm_jls\rangle$ that are defined by the principal quantum number n, the total and orbital angular momentum quantum numbers j and l, the magnetic quantum number m_j, as well as the spin s. The spin and angular part of the latter are given by the spin-orbit coupled generalized spherical harmonics $\mathcal{Y}_{j,m_j,l}$ [73] while for the radial degree of freedom numerically computed eigenfunctions must be employed, see Chapter 5. As outlined in Section 2.3, we are considering the regime of field strengths where the fine structure dominates over the Zeeman splitting. It is therefore reasonable to consider the effect of the magnetic field interaction only within a single fine structure manifold, i.e., fixing the total angular momentum j for given l. Within this regime, the contribution $G(Xy + xY)p_z$ of Hamiltonian (4.10) can be simplified as follows. Noting

$$[yz, H_A] = [yz, \tfrac{1}{2}\mathbf{p}^2 + V_l(r) + V_{so}(\mathbf{L},\mathbf{S})] = i(yp_z + zp_y) + [yz, V_l(r) + V_{so}(\mathbf{L},\mathbf{S})]\,,$$

we rewrite

$$yp_z = \frac{1}{2}(yp_z - zp_y) - \frac{i}{2}[yz, H_A] + \frac{i}{2}[yz, V_l(r) + V_{so}(\mathbf{L},\mathbf{S})] \tag{4.11}$$

bearing in mind that only the action of any involved operator within a single j-manifold is considered. The first commutator in the above equation then vanishes due to the field-free

[2] Note that *a priori* the contribution $\mathbf{A}_l(\mathbf{r})\cdot\mathbf{p} - \boldsymbol{\mu}_e\cdot\mathbf{B}_l(\mathbf{r})$ is not small in magnitude. However, the lack of a center of mass dependence of these terms allows us to treat them as a mere energy offset to the adiabatic electronic potentials. Consequently, they are not expected to be relevant for the actual shape of the latter.

energetic degeneracy of the m_j states and since no coupling to different n-, l-, or j-states is considered. Likewise, the second commutator in Eq. (4.11) vanishes since neither $V_l(r)$ nor $V_{so}(\mathbf{L},\mathbf{S})$ depend on the magnetic quantum number m_j.[3] Consequently, we can substitute $yp_z \to \frac{1}{2}(yp_z - zp_y) = \frac{1}{2}L_x$ and $xp_z \to \frac{1}{2}(xp_z - zp_x) = -\frac{1}{2}L_y$ in Eq. (4.10), yielding

$$H_0 = H_A + \frac{1}{2}\left[\mathbf{L} + 2\mathbf{S}\right] \cdot \mathbf{B}(\mathbf{R})\,. \tag{4.12}$$

Applying the same argumentation as above for the remaining term $H' = GXYp_z$, we see that it vanishes within one j-manifold since $p_z \sim [H_A, z]$. However, this term has a strong dependence on the center of mass position $\mathbf{R}$. For large center of mass coordinates X and Y, it can generate non-negligible couplings to others than the considered fine structure level, thereby producing significant contributions to the Hamiltonian. Thus neglecting this term is only a valid approximation for a restricted range of center of mass positions. In Section 4.4, a perturbative approach to include this term is presented.

4.3 Adiabatic Electronic Potentials

After preparing our Hamiltonian in the previous section, Eq. (4.12) represents now the coupling of a point-like particle to the spatially dependent magnetic field $\mathbf{B}(\mathbf{R})$ via its magnetic moment $\boldsymbol{\mu} = \frac{1}{2}\mathbf{L} + \mathbf{S}$. Such a Hamiltonian can be diagonalized by applying the unitary transformation U_r that rotates the magnetic field vector $\mathbf{B}(\mathbf{R})$ into the z-direction of the laboratory frame. In this manner, the quantization axis is well defined along the z-axis for all positions $\mathbf{R}$ of the atom and m_j stays a valid quantum number. Hence, in a sense the magnetic field gets homogenized by the unitary transformation U_r. The only spatial dependence remaining is then in the magnitude of the magnetic field, $|\mathbf{B}(\mathbf{R})| = \sqrt{B^2 + G^2(X^2+Y^2)}$.

As pointed out above, we start by applying a combination of successive rotations such that at each point in space the magnetic field vector points into the z-direction of the fixed frame of reference (active point of view!). This can be achieved in two steps, namely,

(a) first rotate about the y-axis such that $B'_x = 0$ (yielding $B'_y = B_y$ and $B'_z = \sqrt{B^2 + G^2X^2}$) and

(b) then rotate about the x-axis such that $B''_y = 0$ (yielding $B''_x = B'_x = 0$ and $B''_z = |\mathbf{B}(\mathbf{R})|$).

That is, including the spin degree of freedom our spatially dependent unitary transformation reads

$$U_r = e^{-i\gamma(L_x+S_x)}e^{-i\beta(L_y+S_y)}\,, \tag{4.13}$$

[3] As shown in Section 3.3, the commutator $[\mathbf{r}, V_l(r)]$ is proportional to the radial matrix element $\langle\kappa||r[V_{l'}(r) - V_l(r)]||\kappa'\rangle$; the latter vanishes since we restrict ourselves to a single l, i.e., $l = l'$. The same argumentation holds for the commutator $[\mathbf{r}, V_{so}(\mathbf{L},\mathbf{S})]$ including the spin-orbit coupling. In this case we end up with the matrix element

$$\langle\kappa|[yz, V_{so}(\mathbf{L},\mathbf{S})]|\kappa'\rangle = \langle\kappa||\big[\tfrac{1}{2}\big(j'(j'+1) - l'(l'+1) - \frac{3}{4}\big)r^2\frac{\alpha^2}{2r}\frac{\mathrm{d}V_{l'}(r)}{\mathrm{d}r} - \tfrac{1}{2}\big(j(j+1) - l(l+1) - \frac{3}{4}\big)r^2\frac{\alpha^2}{2r}\frac{\mathrm{d}V_l(r)}{\mathrm{d}r}\big]||\kappa'\rangle \times \langle\kappa|\hat{y}\hat{z}|\kappa'\rangle = 0$$

since $\mathbf{L}\cdot\mathbf{S}|njm_jls\rangle = \frac{1}{2}\big[j(j+1) - l(l+1) - s(s+1)\big]|njm_jls\rangle$ and $l = l'$, $j = j'$. We used $\hat{x}_i \equiv x_i/r$.

where γ and β denote the rotation angles:

$$\begin{aligned} \sin\gamma &= \frac{-GY}{\sqrt{B^2+G^2(X^2+Y^2)}}\,, & \sin\beta &= \frac{-GX}{\sqrt{B^2+G^2X^2}}\,, \\ \cos\gamma &= \frac{\sqrt{B^2+G^2X^2}}{\sqrt{B^2+G^2(X^2+Y^2)}}\,, & \cos\beta &= \frac{B}{\sqrt{B^2+G^2X^2}}\,. \end{aligned} \tag{4.14}$$

The rotation matrix $\mathcal{R}$ associated with the unitary transformation (4.13) correspondingly reads $\mathcal{R} = \mathcal{R}_x(\gamma).\mathcal{R}_y(\beta)$. As noted in Section 4.1, the components of both the angular momentum $\mathbf{L}$ and the spin $\mathbf{S}$ transform in the rotation U_r like those of a vector in the rotation $\mathcal{R}^{-1} = \mathcal{R}^T$. With the rotation matrices as given in Eqs. (4.2)-(4.4), the transformed vector operator $\mathbf{r}$ reads

$$U_r\mathbf{r}U_r^\dagger = \mathcal{R}^{-1}\mathbf{r} = \begin{pmatrix} x\cos\beta + y\sin\beta\,\sin\gamma - z\cos\gamma\,\sin\beta \\ y\cos\gamma + z\sin\gamma \\ x\sin\beta - y\cos\beta\,\sin\gamma + z\cos\beta\,\cos\gamma \end{pmatrix} \tag{4.15}$$

and similarly for $\mathbf{L}$ and $\mathbf{S}$. Making use of the relations Eqs. (4.14), the field interaction terms of Hamiltonian (4.12) eventually become

$$\begin{aligned} \mathbf{B}(\mathbf{R})\cdot U_r\mathbf{L}U_r^\dagger &= \mathbf{B}(\mathbf{R})\cdot\mathcal{R}^{-1}\mathbf{L} = \sqrt{B^2+G^2(X^2+Y^2)}\,L_z\,, \\ \mathbf{B}(\mathbf{R})\cdot U_r\mathbf{S}U_r^\dagger &= \mathbf{B}(\mathbf{R})\cdot\mathcal{R}^{-1}\mathbf{S} = \sqrt{B^2+G^2(X^2+Y^2)}\,S_z\,. \end{aligned}$$

Employing the *Baker-Campbell-Hausdorff* formula, cf. Eq. (3.17), and considering the fact that the orbital angular momentum $\mathbf{L}$ commutes with scalar operators[4], moreover provides us

$$\begin{aligned} U_r\mathbf{p}^2U_r^\dagger &= \mathbf{p}^2\,, \\ U_rV_{so}(\mathbf{L},\mathbf{S})U_r^\dagger \propto U_r\mathbf{L}\cdot\mathbf{S}U_r^\dagger &= \mathbf{L}\cdot\mathbf{S}\,, \\ U_r\mathbf{L}^2U_r^\dagger &= \mathbf{L}^2\,. \end{aligned}$$

Having additionally in mind that the model potential $V_l(r)$ transforms as $\mathbf{L}^2$, we see that the field-free Hamiltonian H_A is invariant, $U_rH_AU_r^\dagger = H_A$. Putting all together, the transformed Hamiltonian reads

$$U_rH_0U_r^\dagger = H_A + \tfrac{1}{2}(L_z+2S_z)\sqrt{B^2+G^2(X^2+Y^2)}\,. \tag{4.16}$$

Like Eq. (4.12), the above Hamiltonian describes a point-like particle with magnetic moment $\boldsymbol{\mu} = \frac{1}{2}\mathbf{L}+\mathbf{S}$. The crucial difference is, however, that the magnetic field $\mathbf{B}(\mathbf{R}) = \sqrt{B^2+G^2(X^2+Y^2)}\,\mathbf{e}_z$ now points along the z-direction at each point in space.

Given its simple form, the adiabatic electronic potential energy surfaces originating from Hamiltonian (4.16) can be deduced straightforwardly. In the regime of weak magnetic fields – on which we are focusing throughout this thesis – the magnetic field interaction can be considered as a small perturbation compared to spin-orbit effects.[5] The eigenvalues of Hamil-

[4] In particular, $[\mathbf{J},\mathbf{p}^2] = [\mathbf{L},\mathbf{p}^2] = 0$, $[\mathbf{J},\mathbf{L}\cdot\mathbf{S}] = \frac{1}{2}[\mathbf{L},\mathbf{J^2}-\mathbf{L^2}-\mathbf{S^2}] = 0$, and $[\mathbf{J},\mathbf{L}^2] = 0$.

[5] This is consistent with deriving Eq. (4.16) for fixed j.

tonian (4.16) can then be calculated in first order perturbation theory, taking the field-free electronic states $|\kappa\rangle = |njm_jls\rangle$ as eigenfunctions[6]. We get

$$E_\kappa^{(0)}(\mathbf{R}) = E_\kappa^{el} + \tfrac{1}{2} g_j m_j \sqrt{B^2 + G^2(X^2+Y^2)} \tag{4.17}$$

where

$$g_j = \frac{3}{2} + \frac{s(s+1) - l(l+1)}{2j(j+1)} \tag{4.18}$$

is the *Landé splitting factor* [68] and E_κ^{el} the field-free energy of a given state $|\kappa\rangle$, i.e., $H_A|\kappa\rangle = E_\kappa^{el}|\kappa\rangle$.

The adiabatic energy surfaces Eq. (4.17) are rotationally symmetric around the Z-axis and confining for $m_j > 0$. For small radii ($\rho = \sqrt{X^2+Y^2} \ll B/G$) an expansion up to second order yields a harmonic potential

$$E_\kappa^{(0)}(\rho) \approx E_\kappa^{el} + \tfrac{1}{2} g_j m_j B + \frac{1}{2} M\omega^2 \rho^2 \tag{4.19}$$

with the trap frequency defined by

$$\omega = G\sqrt{\frac{g_j m_j}{2MB}}\,. \tag{4.20}$$

On the contrary, when the center of mass is far from the Z-axis ($\rho \gg B/G$) we find a linear behavior, $E_\kappa^{(0)}(\rho) \approx E_\kappa^{el} + \frac{1}{2} g_j m_j G\rho$.

At this point, let us give a short preview on the properties of the center of mass eigenstates arising for such an adiabatic electronic potential. For a more detailed discussion, we refer the reader to Section 7.4. In the harmonic part of the potential, the center of mass eigenfunctions can be written as a superposition of two independent harmonics oscillators in the X- and Y-direction. The center of mass energies correspondingly read

$$E_{\kappa,\nu}^{cm} = E_\kappa^{(0)}(0) + (\nu+1)\omega$$

with $\nu = \nu_x + \nu_y \in \mathbb{N}$ being the sum of the individual harmonic oscillator quantum numbers. Accordingly, the splitting between adjacent center of mass states is determined by ω. The separation between adjacent electronic energy surfaces at the origin, on the other hand, is given by $\Delta E_\kappa = \frac{1}{2} g_j B$. The size of the center of mass ground state ($\nu = 0$) in such a harmonic potential evaluates to $\langle\rho\rangle = \sqrt{\pi}/2\sqrt{M\omega}$ [65].

4.4 Perturbation Theory for H'

In the above results for the adiabatic electronic potentials, Eq. (4.17), the contribution $H' = GXYp_z$ has been omitted. However, because of its strong spatial dependence it might render important for our adiabatic potentials by mixing different fine structure levels and n-manifolds. In this section, we tackle this issue by including H' in second order perturbation theory.

[6] Note that such a state now refers to the transformed Hamiltonian, i.e., it is defined in the *rotated* frame of reference. In the laboratory frame, the eigenfunctions correspondingly read $|\kappa\rangle_{\text{lab}} = U_r|\kappa\rangle$.

In the previous section, we derived particularly simple expressions for the adiabatic potentials by transforming to a rotated frame of reference in which Hamiltonian (4.16) becomes diagonal. Since we want to keep this simple structure, we remain in the rotated frame of reference and therefore apply the unitary transformation (4.13) to H' as well:

$$U_r H' U_r^\dagger = GXYU_r p_z U_r^\dagger = GXY\left[p_x \sin\beta - p_y \sin\gamma\cos\beta + p_z \cos\gamma\cos\beta\right].$$

As in Section 4.2, we can rewrite $p_i = i[H_A, x_i] - i[V_l(r) + V_{so}(\mathbf{L},\mathbf{S}), x_i]$ and see that H' vanishes in first order perturbation theory, $\langle njm_jls|U_rH'U_r^\dagger|njm_jls\rangle = 0$. In second order we get

$$\begin{aligned} E_\kappa^{(2)}(\mathbf{R}) &= G^2X^2Y^2 \sum_{\kappa'\neq\kappa} \frac{\left|\langle\kappa|U_r p_z U_r^\dagger|\kappa'\rangle\right|^2}{E_\kappa^{el} - E_{\kappa'}^{el}} \\ &= G^2X^2Y^2 \sum_{\kappa'\neq\kappa} \frac{\left|\langle\kappa|p_x\sin\beta - p_y\sin\gamma\cos\beta + p_z\cos\gamma\cos\beta|\kappa'\rangle\right|^2}{E_\kappa - E_{\kappa'}}, \end{aligned}$$

where the summation excludes all states within the desired manifold, i.e., $|n'j'm_j'l's'\rangle \notin \{|njm_jls\rangle, -j \le m_j \le j\}$. Omitting the terms arising from $V_l(r)$ and $V_{so}(\mathbf{L},\mathbf{S})$[7], we can approximate

$$\langle\kappa|p_i|\kappa'\rangle \approx i(E_\kappa^{el} - E_{\kappa'}^{el}) \times \langle\kappa|x_i|\kappa'\rangle,$$

yielding

$$E_\kappa^{(2)}(\mathbf{R}) \approx G^2X^2Y^2 \sum_{\kappa'\neq\kappa} (E_\kappa^{el} - E_{\kappa'}^{el}) \times \left|\langle\kappa|U_r z U_r^\dagger|\kappa'\rangle\right|^2. \tag{4.21}$$

Since $E_\kappa^{(0)}(\mathbf{R})$ resembles the confinement of a ground state atom, we are going to attribute $E_\kappa^{(2)}(\mathbf{R})$ to the *composite* nature of the Rydberg atom, i.e., the fact that it consists of a Rydberg electron far apart from its ionic core. Expanding the modulus square in Eq. (4.21), one obtains mixed terms of the form $\langle\kappa|x|\kappa'\rangle^*\langle\kappa|y|\kappa'\rangle + \langle\kappa|x|\kappa'\rangle\langle\kappa|y|\kappa'\rangle^*$. Employing the standard basis of spherical harmonics and consequently using $\langle\kappa|x|\kappa'\rangle \in \mathbb{R}$ as well as $\langle\kappa|y|\kappa'\rangle = -\langle\kappa|y|\kappa'\rangle^*$, this sum vanishes. The matrix element of z obeys a different selection rule, namely $\Delta m_l = 0$ opposed to $\Delta m_l = \pm 1$ of x and y; hence mixed terms involving $\langle\kappa|z|\kappa'\rangle$ vanish as well. Consequently, only the matrix elements $|\langle\kappa|x|\kappa'\rangle|^2$, $|\langle\kappa|y|\kappa'\rangle|^2$, and $|\langle\kappa|z|\kappa'\rangle|^2$ remain and the second order energy contribution Eq. (4.21) can be parameterized as

$$E_\kappa^{(2)}(\mathbf{R}) = G^2X^2Y^2\left(C_x\sin^2\beta + C_y\sin^2\gamma\cos^2\beta + C_z\cos^2\gamma\cos^2\beta\right).$$

The parameters C_i are calculated via

$$C_i = \sum_{\kappa'\neq\kappa} (E_\kappa^{el} - E_{\kappa'}^{el}) |\langle\kappa|x_i|\kappa'\rangle|^2 \tag{4.22}$$

and obey $C_x = C_y$ since $|\langle\kappa|x|\kappa'\rangle| = |\langle\kappa|y|\kappa'\rangle|$. The latter relation simplifies the second order

[7] Their magnitude is determined by $|\langle\kappa|[V_l(r), x_i]|\kappa'\rangle|^2/(E_\kappa^{el} - E_{\kappa'}^{el})$ and $|\langle\kappa|[V_{so}(\mathbf{L},\mathbf{S}), x_i]|\kappa'\rangle|^2/(E_\kappa^{el} - E_{\kappa'}^{el})$ compared to the leading contribution of $(E_\kappa^{el} - E_{\kappa'}^{el}) \times |\langle\kappa|x_i|\kappa'\rangle|^2$.

contribution $E_\kappa^{(2)}(\mathbf{R})$ further, yielding

$$E_\kappa^{(2)}(\mathbf{R}) = C_z G^2 X^2 Y^2 \left[1 + \frac{C_x - C_z}{C_z}\left(\sin^2\beta + \sin^2\gamma\cos^2\beta\right)\right]. \tag{4.23}$$

For $nS_{1/2}$ Rydberg states we even find $C_x = C_y = C_z \equiv C$, which leaves us with a single parameter describing the contribution of H', $E_{nS_{1/2}}^{(2)}(\mathbf{R}) = C \cdot G^2 X^2 Y^2$.

Note that the parameters C_i depend on the state κ under investigation. Since $E_\kappa^{el} - E_{\kappa'}^{el} \propto n^{-3}$ and $|\langle\kappa|x_i|\kappa'\rangle|^2 \propto n^4$, a linear scaling of $E_\kappa^{(2)}(\mathbf{R})$ with the quantum number n is anticipated. For quantitative results, both the energies E_κ^{el} and the matrix elements $\langle\kappa|x_i|\kappa'\rangle$ must be known. In the next chapter, we present our computational approach on how they can be determined numerically. For a thorough investigation of the resulting adiabatic potentials including the effects of H', we refer the reader to Chapter 7.

Chapter 5

Numerical Methods

The investigations in this thesis necessitate – like myriads of other quantum mechanical problems – the solution of the stationary Schrödinger equation

$$H|\Psi\rangle = E|\Psi\rangle \tag{5.1}$$

associated with the Hamiltonian H of interest. In the previous chapter, we tackled this problem by introducing a unitary transformation U_r that reduces the Schrödinger equation to a form for which the solutions $|\Psi\rangle$ are well known. However, this came with a price, namely, the introduction of further approximations and the use of perturbation theory for selected terms of the Hamiltonian. Consequently, the solutions that we determined in the previous chapter can only be regarded approximative.

In this chapter, we present our computational approach for determining the solutions of the Schrödinger equation numerically. Opposed to the analytical solutions of Chapter 4, this approach does not rely on introducing further approximations to our electronic Hamiltonian (3.20) and yields in principle arbitrarily exact solutions. However, the latter are only gained on a numerical basis, i.e., an analytical form of the wave function cannot be provided. A powerful tool that allows for solving in general infinitely dimensional eigenvalue problems is the so-called *linear variational principle* and is introduced in Section 5.1. It is based on a basis set expansion of a trial wave function and the subsequent matrix representation of the Hamiltonian in this basis. The underlying basis functions are discussed in the Sections 5.3 and 5.4. While for the investigations of circular Rydberg states hydrogenic eigenfunctions (Section 5.3) are very suitable, we need to construct adapted eigenfunctions for the low angular momentum Rydberg states of alkali atoms (Section 5.4). The method used for gaining the latter – the so-called *Discrete Variable Representation* – is discussed in Section 5.4 as well.

5.1 The Linear Variational Principle

In this section, we provide a short introduction to the *Linear Variational Method* for finding the best possible approximative solutions to the eigenvalue problem Eq. (5.1). This method has become a standard technique in quantum mechanics and can be found in basically every textbook on this subject. For the concise review presented here, we are going to stick to the description given by Szabo and Ostlund, cf. Ref. [96].

In an attempt to solve Eq. (5.1), we introduce a set of basis functions $\{|\varphi_j\rangle\}$ and write $|\Psi\rangle$

as

$$|\Psi\rangle = \sum_j c_j |\varphi_j\rangle \,. \tag{5.2}$$

For the scope of this thesis, we assume an orthonormal basis, i.e., $\langle\varphi_i|\varphi_j\rangle = \delta_{ij}$. Substituting expansion (5.2) into Eq. (5.1),

$$\sum_j c_j H|\varphi_j\rangle = E \sum_j c_j |\varphi_j\rangle$$

and multiplying by $\langle\varphi_i|$ on the left, yields

$$\sum_j c_j \langle\varphi_i|H|\varphi_j\rangle = E \sum_j c_j \langle\varphi_i|\varphi_j\rangle = E c_i$$

or equivalently

$$\sum_j H_{ij} c_j = E c_i \tag{5.3}$$

where $H_{ij} = \langle\varphi_i|H|\varphi_j\rangle$ denotes the matrix elements of the Hamiltonian H for the given basis. Equation (5.3) is a matrix eigenvalue problem whose solutions determine the coefficients c_i of the expansion Eq. (5.2) for the solution of our initial quantum mechanical problem. Note that if we use a *complete* orthonormal basis, we would obtain a infinite matrix (H_{ij}) whose eigenvalues are exactly equal to the eigenvalues of the operator H itself. In practice, however, we are restricted to a finite basis and the corresponding eigenvalues are only approximations to the exact solution. Thus the linear variational method is equivalent to solving the eigenvalue equation (5.1) in a finite subspace spanned by $\{|\varphi_j\rangle, i = 1, 2, \cdots, N\}$. By increasing the basis size until convergence is achieved, *numerically exact* solutions can be obtained.

Solving the Eigenvalue Problem

The main computational task is to solve the eigenvalue problem Eq. (5.3), i.e., to diagonalize the Hamiltonian matrix $\mathcal{H} = (H_{ij})$. Hence, by employing the variational principle, the initial differential equation is reduced to a symmetric eigenvalue problem. The associated matrices are usually of large dimension but sparsely occupied. Standard matrix diagonalization methods – like the popular LAPACK subroutines [97] – are therefore not suitable. Instead, we employ the implicitly restarted Lanczos method [98] implemented in the package ARPACK [99, 100]. The quintessence of this method is to reduce the large-scale eigenvalue problem to a lower dimensional one that can be solved with comparatively little effort. Moreover, in combination with the so-called *shift and invert* method the calculation of energies lying in almost arbitrary regions of the energy spectrum becomes possible without the need of computing the entire spectrum bottom up or top down.

The ARPACK software package requires an external routine for solving – as efficiently as possible – a linear system of equation. In our implementation, we utilize the SUPERLU software package that accomplishes this task by a triangular factorization of the matrix $\mathcal{H}$ into a lower triangular matrix L and an upper triangular matrix U [101]. A major advantage of this choice is the usage of the column-compressed format (often referred to as the *Harwell-Boeing* format) for the storage of matrices. The latter only stores nonzero matrix elements and is therefore especially suited for our sparse Hamiltonian matrix.

5.2 Spherical Coordinates

Before presenting the basis sets that underly our variational method, we note that the electronic part of our Hamiltonian (3.20) can be most conveniently written in spherical coordinates (r, θ, ϕ). Accordingly, the basis functions that we are going to introduce in the next two sections are expressed in these coordinates. The Cartesian coordinates (x, y, z) are related to the spherical ones via

$$\begin{aligned} x &= r \sin\theta \, \cos\phi \,, \\ y &= r \sin\theta \, \sin\phi \,, \\ z &= r \cos\theta \,. \end{aligned}$$

For the components of the momentum operator $\mathbf{p}$ we find

$$\begin{aligned} p_x = -i\hbar\partial_x &= -i\hbar\Big[\sin\theta \, \cos\phi \, \partial_r + \cos\theta \, \cos\phi \, r^{-1}\partial_\theta - \frac{\sin\phi}{r\sin\theta}\partial_\phi \Big] \,, \\ p_y = -i\hbar\partial_y &= -i\hbar\Big[\sin\theta \, \sin\phi \, \partial_r + \cos\theta \, \sin\phi \, r^{-1}\partial_\theta + \frac{\cos\phi}{r\sin\theta}\partial_\phi \Big] \,, \\ p_z = -i\hbar\partial_z &= -i\hbar\Big[\cos\theta \, \partial_r - \sin\theta \, r^{-1}\partial_\theta \Big] \,, \end{aligned}$$

and accordingly

$$\mathbf{p}^2 = -\hbar^2 r^{-2}\partial_r(r^2\partial_r) + \frac{\mathbf{L}^2}{r^2}$$

since

$$\mathbf{L}^2 = -\hbar^2\left[\frac{1}{\sin\theta} \, \partial_\theta \left(\sin\theta \, \partial_\theta \right) + \frac{1}{\sin^2\theta} \, \partial_\phi^2 \right] .$$

Note that $\hbar = 1$ in atomic units, which we are going to employ in the following.

5.3 Hydrogen Eigenfunctions

In this section, we are going to discuss the electronic eigenfunctions of the hydrogen atom. They are employed as basis functions when considering high angular momentum Rydberg states like the circular one. In such a case, the hydrogen eigenfunctions are solutions to the field-free Rydberg Hamiltonian H_A as well. They can be decomposed in a radial and an angular part according to [68]

$$\psi_{nlm}(r, \theta, \phi) = R_{nl}(r) \, Y_{lm}(\theta, \phi) \,.$$

The radial part $R_{nl}(r)$ is characterized by the *generalized Laguerre polynomials*[1] $L_\nu^\alpha(x)$ and reads

$$R_{nl}(r) = -\sqrt{\frac{(n-l-1)!}{2n[(n+l)!]^3}} \left(\frac{2}{na_0} \right)^{l+3/2} r^l e^{-\frac{r}{na_0}} \, L_{n+l}^{2l+1}(\tfrac{2r}{na_0}) \,. \tag{5.4}$$

[1] A discussion of the generalized Laguerre polynomials will be given in the next section. They constitute the underlying basis functions for the discrete variable representation employed there.

Note that $a_0 = 1$ in atomic units. The angular eigenfunctions $Y_{lm}(\theta, \phi)$ are the *spherical harmonics*. They are given by

$$Y_{lm}(\theta,\phi) = (-1)^m \sqrt{\frac{2l+1}{4\pi}\frac{(l-m)!}{(l+m)!}}\, P_l^m(\cos\theta)\, e^{im\phi}$$

where $P_l^m(\cos\theta)$ denotes the *associated Legendre functions*. The spherical harmonics for negative magnetic quantum numbers $m < 0$ are obtained via

$$Y_{l-|m|}(\theta,\phi) = (-1)^m\, Y_{l|m|}^*(\theta,\phi)\,.$$

The spherical harmonics $Y_{lm}(\theta, \phi)$ are eigenfunctions of the squared angular momentum operator $\mathbf{L}^2$ and its z-component L_z:

$$\begin{aligned}\mathbf{L}^2 Y_{lm}(\theta,\phi) &= \hbar^2 l(l+1)\, Y_{lm}(\theta,\phi)\,,\\ L_z Y_{lm}(\theta,\phi) &= \hbar m\, Y_{lm}(\theta,\phi)\,.\end{aligned}$$

Both the radial and angular eigenfunctions are orthonormal systems, i.e.,

$$\int_0^\infty R_{n'l}^*(r) R_{nl}(r)\, r^2 \mathrm{d}r = \delta_{nn'} \quad \text{and}$$
$$\int_0^{2\pi}\int_0^{\pi} Y_{l'm'}^*(\theta,\phi) Y_{lm}(\theta,\phi)\sin\theta\,\mathrm{d}\theta\,\mathrm{d}\phi = \delta_{ll'}\delta_{mm'}\,,$$

yielding the well-known orthonormality of the hydrogen wave functions, $\langle\psi_{n'l'm'}|\psi_{nlm}\rangle = \delta_{nn'}\delta_{ll'}\delta_{mm'}$.

As discussed in the previous section, we require the matrix representation $\mathcal{H} = (H_{ij})$ of our Hamiltonian in order to numerically determine its eigenvalues and eigenfunctions. That is, we need to compute matrix elements $\langle\psi_{n'l'm'}|O|\psi_{nlm}\rangle$ of all operators O occurring in the Hamiltonian H of interest. There are basically two ways of achieving this: either perform a numerical integration or find an analytical expression for the matrix element. In the framework of this thesis, we pursued both approaches. The angular matrix elements, i.e., $\langle Y_{l'm'}(\theta,\phi)|O(\theta,\phi)|Y_{lm}(\theta,\phi)\rangle$, can often be determined analytically by employing the recurrence relations of the associated Legendre functions:

$$\begin{aligned}(2l+1)\cos\theta\, P_l^m(\cos\theta) &= (l+m)P_{l-1}^m(\cos\theta) + (l-m+1)P_{l+1}^m(\cos\theta)\,,\\ (2l+1)\sin\theta\, P_l^m(\cos\theta) &= P_{l+1}^{m+1}(\cos\theta) - P_{l-1}^{m+1}(\cos\theta)\\ &= (l+m)(l+m-1)P_{l-1}^{m-1}(\cos\theta)\\ &\quad + (l-m+1)(l-m+2)P_{l+1}^{m-1}(\cos\theta)\,,\\ \sin\theta\,\partial_\theta P_l^m(\cos\theta) &= \Big[\frac{l(l+m)}{2l+1} - (l+m)\Big]P_{l-1}^m(\cos\theta) + l(l-m+1)P_{l+1}^m(\cos\theta)\,.\end{aligned}$$

Whenever possible, we thus implemented the analytical expressions in our code. The radial matrix elements, $\langle R_{n'l'}(r)|O(r)|R_{nl}(r)\rangle$, on the other hand have been exclusively treated numerically.[2]

[2]There exist also recurrence relations for the generalized Laguerre polynomials. However, the matrix elements

The spin degree of freedom of the hydrogen atom can be conveniently expressed using two-component spinors [73]

$$\varphi = \begin{pmatrix} \varphi_+(\mathbf{r}) \\ \varphi_-(\mathbf{r}) \end{pmatrix} = \begin{pmatrix} \varphi(\mathbf{r}, m_s = +\frac{1}{2}) \\ \varphi(\mathbf{r}, m_s = -\frac{1}{2}) \end{pmatrix}.$$

If we introduce the two basis spinors

$$\chi_+ = \begin{pmatrix} 1 \\ 0 \end{pmatrix} \quad \text{and} \quad \chi_- = \begin{pmatrix} 0 \\ 1 \end{pmatrix}$$

corresponding to the spin quantum numbers $m_s = \frac{1}{2}$ and $-\frac{1}{2}$, respectively, the matrix representation of the spin operators are – as usual – related to the Pauli matrices

$$\sigma_x = \begin{pmatrix} 0 & 1 \\ 1 & 0 \end{pmatrix}, \quad \sigma_y = \begin{pmatrix} 0 & -i \\ i & 0 \end{pmatrix}, \quad \sigma_z = \begin{pmatrix} 1 & 0 \\ 0 & -1 \end{pmatrix}$$

via $\mathbf{S} = \frac{\hbar}{2}\boldsymbol{\sigma}$. As we are going to argument in Chapter 6, the spin-orbit interaction can be neglected for high angular momentum Rydberg states. Consequently, our basis functions are a direct product of the spatial part $|\psi_{nlm_l}(\mathbf{r})\rangle$ and the spin part $|m_s\rangle$, $|nlm_l; m_s\rangle \equiv |\psi_{nlm_l}(\mathbf{r})\rangle \otimes |m_s\rangle$. The basis set expansion of our trial wave function consequently reads

$$|\Psi\rangle = \sum_{n,l,m_l,m_s} c_{nlm_lm_s} |nlm_l; m_s\rangle$$

providing a matrix representation of our Hamiltonian with matrix elements

$$H_{n'l'm_l'm_s',nlm_lm_s} = \langle n'l'm_l'; m_s'|H|nlm_l; m_s\rangle .$$

5.4 Low Angular Momentum Rydberg States

As already pointed out in Chapter 2, the low angular momentum Rydberg states of alkali atoms largely differ from their hydrogen counterparts due to the strong quantum defect. For our numerical calculations we therefore constructed new basis states that are eigenfunctions to the field-free Hamiltonian $H_A = p^2/2m + V_l(r) + V_{so}(\mathbf{L}, \mathbf{S})$,

$$H_A|njm_jls\rangle = E^{el}_{nljm_jls}|njm_jls\rangle .$$

As for the hydrogen problem, we made an ansatz $\psi_{njm_jls}(\mathbf{r}) = R_{njl}(r)\mathcal{Y}_{j,m_j,l}$ separating the radial and angular degree of freedom. Note that for these states the spin-orbit coupling $V_{so}(\mathbf{L}, \mathbf{S})$ must be included. The spin and angular part of the eigenfunctions is therefore given by the spin-orbit coupled generalized spherical harmonics $\mathcal{Y}_{j,m_j,l}$ [73]. They are related to the spherical harmonics via the *Clebsch-Gordan coefficients* $\langle lm_lsm_s|jm_j\rangle$,

$$|jm_jls\rangle = \sum_{m_l,m_s} \langle lm_lsm_s|jm_j\rangle\, Y_{lm_l}(\theta,\phi)\, \chi_{m_s} . \tag{5.5}$$

often involve various combinations of derivative operators, which makes them hard to tackle analytically.

The quantum number s is of course always $1/2$, resulting in two possible values of j for each value of l larger than zero, namely, $j = l + 1/2$ and $j = l - 1/2$. For $l = 0$ only $j = 1/2$ is possible. The generalized spherical harmonics are thus essentially two-component spinors of spherical harmonics, given by

$$\mathcal{Y}_{j,m_j,l} = \frac{1}{\sqrt{2j}} \begin{pmatrix} \sqrt{j+m}\, Y_{lm_j-\frac{1}{2}}(\theta,\phi) \\ \sqrt{j-m}\, Y_{lm_j+\frac{1}{2}}(\theta,\phi) \end{pmatrix}, \quad j = l + \tfrac{1}{2}\,,$$
$$\mathcal{Y}_{j,m_j,l} = \frac{1}{\sqrt{2j+2}} \begin{pmatrix} -\sqrt{j-m+1}\, Y_{lm_j-\frac{1}{2}}(\theta,\phi) \\ \sqrt{j+m+1}\, Y_{lm_j+\frac{1}{2}}(\theta,\phi) \end{pmatrix}, \quad j = l - \tfrac{1}{2}\,.$$

Consequently, the spin and angular part of the Hamiltonian matrix elements can be largely deduced from the corresponding hydrogenic ones, cf. Section 5.3.

Because of the intricate form of the model potential $V_l(r)$, the radial part $R_{njl}(r)$ of the eigenfunctions are not obtained as easily. The scope of this section is thus to illuminate two issues regarding this problem, namely, (a) what is the numerical method for computing the radial eigenfunctions of H_A and (b) how can finally the radial matrix elements of our field-interaction Hamiltonian (3.20) be obtained using the numerically determined eigenfunctions. The answer to basically both questions is the use of the *Discrete Variable Representation* (DVR) technique that represents the radial part of the wave function on a grid. Because of the equivalence to a Gaussian quadrature rule, the numerical evaluation of integrals becomes particularly feasible within this scheme. A brief outline of the DVR technique in general is given in Section 5.4.1. Section 5.4.2 then introduces the Laguerre DVR that is used for our numerical treatment. We conclude this section by providing an exemplary wave function that is computed by means of the below discussed technique.

5.4.1 The Discrete Variable Representation Technique

The discrete variable representation is a powerful method for representing wave functions and operators. A comprehensive review of the DVR technique can be found in Appendix B of Ref. [102]. Here we present a brief summary of its basic properties, which should provide the reader sufficient background knowledge for the scope of this thesis.

We consider a one-dimensional problem and choose a complete square integrable basis set $\{\phi_n(r)\}$, the derivatives $\phi_n'(r)$ and $r\phi_n(r)$ also being square integrable. We can then introduce the position operator matrix $\mathcal{Q}$ that is defined by

$$\mathcal{Q}_{nm} = \langle \phi_n | r | \phi_m \rangle\,.$$

Its diagonalization provides the grid points r_α and the transformation matrix $\mathcal{U}$, i.e.,

$$(\mathcal{U}^\dagger \mathcal{Q} \mathcal{U})_{\alpha\beta} = r_\alpha \delta_{\alpha\beta}\,.^{3}$$

With this knowledge, we can define the so-called *Finite Basis Representation* (FBR) of the

[3] Note that the basis functions are numbered by Latin letters $n, m, \ldots$ while we label the grid points by Greek letters $\alpha, \beta, \ldots$

potential energy operator $V(r)$:

$$V_{nm}^{\mathrm{FBR}} = \sum_{\alpha=1}^{N} U_{n\alpha} V(r_\alpha) U_{m\alpha}^{*} \,. \tag{5.6}$$

Note that the FBR approach is an approximation since the basis set has been truncated to N basis functions. The FBR allows us to evaluate the potential matrix elements very efficiently on the grid $\{r_\alpha\}$. Moreover, the knowledge of the eigenvalues r_α and the unitary eigenvector matrix $\mathcal{U}$ of the position operator permits us to perform a conceptually new step: The matrix $\mathcal{U}$ is used to unitarily transform the FBR to the DVR via the DVR functions

$$\chi_\alpha(r) = \sum_{n=1}^{N} \phi_n(r) U_{n\alpha} \,.$$

These functions are orthonormal, $\langle \chi_\alpha | \chi_\beta \rangle = \delta_{\alpha\beta}$, and diagonalize by construction the position operator, $\langle \chi_\alpha | r | \chi_\beta \rangle = r_\alpha \delta_{\alpha\beta}$. In order to treat a quantum mechanical problem by means of the DVR, we need to transform both the kinetic energy T and the potential V to the DVR:

$$\begin{aligned} \mathcal{T}^{\mathrm{DVR}} &= \mathcal{U}^{\dagger} \mathcal{T} \mathcal{U} \,, \\ \mathcal{V}^{\mathrm{DVR}} &= \mathcal{U}^{\dagger} \mathcal{V}^{\mathrm{FBR}} \mathcal{U} \,. \end{aligned} \tag{5.7}$$

As usual, the kinetic energy matrix $\mathcal{T}$ is defined as $T_{nm} = \langle \phi_n | T | \phi_m \rangle$. Note that $T_{\alpha\beta}^{\mathrm{DVR}} = \langle \chi_\alpha | T | \chi_\beta \rangle$ is an exact expression, while $V_{\alpha\beta}^{\mathrm{DVR}} = \langle \chi_\alpha | V | \chi_\beta \rangle$ holds only approximatively because of the FBR approximation. The attractiveness of the DVR finally arises from the particularly simple evaluation of the potential matrix elements:

$$V_{\alpha\beta}^{\mathrm{DVR}} = V(r_\alpha) \delta_{\alpha\beta} \,. \tag{5.8}$$

Hence, the potential is represented by a diagonal matrix whose entries are given by the values of the potential at the grid positions. Recalling our model potential $V_l(r)$, Eqs. (3.7-3.8), the advantage is obvious: Computing $V_l(r_\alpha)$ at the grid points r_α is straightforward whereas actually evaluating the integral $\langle \phi_n | V_l(r) | \phi_m \rangle$ would require more elaborate methods.

If the representation $\mathcal{Q}$ of the position operator is tridiagonal, we speak of a *proper* DVR. A proper DVR has the intriguing property that it is very closely related to a Gaussian quadrature. The overlap integrals as well as the matrix elements of the position operator are then given exactly by quadrature,

$$\begin{aligned} \sum_{\alpha=1}^{N} w_\alpha \phi_n^{*}(r_\alpha) \phi_m(r_\alpha) &= \langle \phi_n | \phi_m \rangle = \delta_{nm} \,, \\ \sum_{\alpha=1}^{N} w_\alpha \phi_n^{*}(r_\alpha) r_\alpha \phi_m(r_\alpha) &= \langle \phi_n | r | \phi_m \rangle = Q_{nm} \,, \end{aligned}$$

where the weights w_α are determined by

$$w_\alpha^{1/2} = U_{n\alpha}^{*} / \phi_n(r_\alpha) \,. \tag{5.9}$$

Note that Eq. (5.9) holds independently of n for a proper DVR.[4] The relation

$$\langle \chi_\alpha | R \rangle = w_\alpha^{1/2} R(r_\alpha)$$

finally turns a proper DVR into a collocation method: The wave function $R(r)$ is no longer represented by its overlaps with basis functions but rather by its values on the grid points r_α, i.e.,

$$R(r) \to \mathbf{R}(r) = \begin{pmatrix} w_1^{1/2} R(r_1) \\ w_2^{1/2} R(r_2) \\ \vdots \\ w_N^{1/2} R(r_N) \end{pmatrix}.$$

Going back to our initial problem of finding the solutions of H_A, we now see that – after the diagonalization of the Hamiltonian in the DVR scheme – its radial eigenfunctions $R_{njl}(r)$ are represented on the grid $\{r_\alpha\}$. Their actual values at the grid points r_α can then be deduced from the eigenvectors $\mathbf{c}_{njl}$ of H_A,

$$R_{nlj}(r_\alpha) = (\mathbf{c}_{njl})_\alpha / \sqrt{w_\alpha}\,,$$

i.e., the components of the eigenvectors read $(\mathbf{c}_{njl})_\alpha = \langle \chi_\alpha | R_{njl} \rangle = w_\alpha^{1/2} R_{njl}(r_\alpha)$.

The above described method successfully and efficiently provides us the radial eigenfunctions of H_A, which serve within our computational scheme as basis functions for representing the electronic Hamiltonian *including* the magnetic field interaction. Hence the advantages of the DVR are passed on to the determination of the more general matrix elements of Hamiltonian (3.20). In practice, we first need to calculate the DVR matrix representation $\mathcal{O}^{\mathrm{DVR}}$ of a given operator O. The matrix elements of O with respect to the new basis of the radial eigenfunctions $R_{nlj}(r)$ are then gained by simple matrix multiplication:

$$\langle R_{n'j'l'} | O | R_{njl} \rangle = \mathbf{R}_{n'j'l'}^T \mathcal{O}\, \mathbf{R}_{njl}\,.$$

While for operators only involving the position operator r the determination of $\mathcal{O}$ is straightforward, cf. Eq. (5.8), the representation of derivative operators becomes somehow more involved. In the next section, we therefore introduce our particular underlying basis $\{\phi_n(r)\}$ and determine the resulting matrix representations of all operators needed for Hamiltonian (3.20).

[4] In general, the Gaussian quadrature rule states that the expression

$$\int w(r) f(r)\, \mathrm{d}r = \sum_{\alpha=1}^{N} w_\alpha f(r_\alpha)$$

is exact if $f(r)$ is a polynomial of degree lower or equal to $2N-1$ [103]. For the above equation we assumed that there are a non-negative weight function $w(r)$ and polynomials $p_n(r)$ of degree n that are orthogonal to each other with respect to the weight function $w(r)$. Defining basis functions ϕ_n as

$$\phi_n(r) = A_n \sqrt{w(r)}\, p_{n-1}(r)\,, \quad n = 1, \ldots N$$

one can show that a DVR derived from such a quadrature rule (therefore usually referred to as *quadrature DVR*) is equivalent to a proper DVR [102]. A_n is a normalization constant.

5.4.2 Laguerre DVR

Inspired by the hydrogen eigenfunctions, Eq. (5.4), we use the scaled functions

$$\phi_n^a(r) = r_0^{-1/2} \sqrt{\frac{(n-1)!}{(n+a-1)!}} \left(\frac{r}{r_0}\right)^{\frac{a}{2}} e^{-\frac{r}{2r_0}} L_{n-1}^a(\tfrac{r}{r_0}) \tag{5.10}$$

as finite basis set representation underlying the DVR; r_0 serves as a scaling factor and

$$L_n^a(z) = \frac{1}{n!} e^z z^{-a} \frac{\mathrm{d}^n}{\mathrm{d}z^n} \left(e^{-z} z^{n+a}\right)$$

are the generalized Laguerre polynomials with $a = 1, 2, \ldots$ and $n = 1, 2, \ldots, N$. This choice of the basis functions is known as the so-called *Laguerre DVR*. A brief review of the latter – although for the unscaled version – can be found in the Appendix of Ref. [104]. We favor the DVR based on generalized Laguerre polynomials because of its inhomogeneous distribution of grid points with a higher density at small radii. This characteristic is ideal for the treatment of the employed model potentials since deviations from the hydrogenic $1/r$ potential occur at small distances from the nucleus.

For fixed a, the basis functions Eq. (5.10) are orthonormal on the interval $[0, \infty)$,

$$\int_0^\infty \phi_n^{a\,*}(r) \phi_m^a(r)\, \mathrm{d}r = \langle \phi_n^a | \phi_m^a \rangle = \delta_{nm}$$

and satisfy the recurrence relation

$$\tfrac{r}{r_0} \phi_m^a(r) = -\sqrt{(m-1)(m+a-1)}\, \phi_{m-1}^a(r) + (2m+a-1) \phi_m^a(r) - \sqrt{m(m+a)}\, \phi_{m+1}^a(r)\,.$$

As desired for a proper DVR, the resulting matrix representation of the position operator is tridiagonal:

$$\langle \phi_n^a | r | \phi_m^a \rangle = r_0 \Big[-\sqrt{(m-1)(m+a-1)}\, \delta_{nm-1} + (2m+a-1)\, \delta_{nm} - \sqrt{m(m+a)}\, \delta_{nm+1} \Big]\,. \tag{5.11}$$

Diagonalization of the position operator matrix produces the DVR grid points r_α, which are given by the eigenvalues. The corresponding eigenvectors define the FBR/DVR transformation matrix $\mathcal{U}$. As described in the previous section, the DVR matrix representation of operators only involving the position operator r is determined by their evaluation at the grid points, cf. Eq. (5.8). For operators D involving derivatives, on the other hand, we have to calculate

$$\mathcal{D}^{\mathrm{DVR}} = \mathcal{U}^\dagger \mathcal{D}\, \mathcal{U}$$

with $\mathcal{D} = \langle \phi_n^a | D | \phi_m^a \rangle$ being the FBR representation of the operator D.

Some basic matrix elements in the FBR representation are provided in the Appendix of Ref. [104]. Incorporating our scaling factor r_0, they read

$$\langle \phi_n^a | r^{-1} | \phi_m^a \rangle = \frac{1}{a r_0} w(n, m, a)\,, \tag{5.12}$$

$$\langle\phi_n^a|r^{-2}|\phi_m^a\rangle = \frac{1}{r_0^2}\frac{(a-2)!}{(a-1)!}\big[(a+1)n_> - (a-1)(n_<-1)\big]w(n,m,a)\,, \tag{5.13}$$

$$\langle\phi_n^a|\partial_r|\phi_m^a\rangle = \frac{1}{2r_0}v_{nm}w(n,m,a)\,, \tag{5.14}$$

$$\langle\phi_n^a|\partial_r^2 - cr^{-2}|\phi_m^a\rangle = \frac{1}{r_0^2}\Big[-\frac{2n_<+a-1}{2(a+1)}w(n,m,a) + \frac{1}{4}\delta_{nm}\Big]\,, \tag{5.15}$$

where

$$v_{nm} = \begin{cases} -1 & \text{if } n<m, \\ 0 & \text{if } n=m, \\ 1 & \text{if } n>m \end{cases}$$

and

$$w_{nm}(n,m,a) = \sqrt{\frac{(n_<+a-1)!(n_>-1)!}{(n_<-1)!(n_>+a-1)!}}\,,$$

with $n_< = \min(n,m)$ and $n_> = \max(n,m)$, as well as

$$c = \begin{cases} K^2-1/4 & \text{with } K=(a-1)/2 \text{ if } a=\text{odd}, \\ j(j+1) & \text{with } j=(a-2)/2 \text{ if } a=\text{even}. \end{cases}$$

Equation (5.13) is valid for $a \geq 2$ only. In principle, the matrices (5.12) and (5.13) are not required because potential terms are usually evaluated by the DVR approximation Eq. (5.8). As noted before, the latter is equivalent to evaluating Eqs. (5.12) and (5.13) by a particular Gaussian quadrature where the DVR points are the quadrature points, cf. Eq. (5.6). When high precision is desired, however, one may revert to Eqs. (5.12) and (5.13), or their DVR-transformed versions, respectively. Equations (5.12) and (5.13) are also needed for the derivation of further matrix elements that are required for the representation of Hamiltonian (3.20). Employing in addition the recursion relations

$$\begin{aligned} r\partial_r L_n^a(r) &= nL_n^a(r) - (n+a)L_{n-1}^a(r)\,, \\ rL_n^a(r) &= (2n+a+1)L_n^a(r) - (n+a)L_{n-1}^a(r) - (n+1)L_{n+1}^a(r) \end{aligned}$$

of the generalized Laguerre polynomials, after a considerable amount of algebra one yields

$$\langle\phi_n^a|r\partial_r|\phi_m^a\rangle = -\frac{1}{2}\delta_{nm} - \frac{1}{2}\sqrt{(m-1)(m+a-1)}\,\delta_{nm-1} + \frac{1}{2}\sqrt{m(m+a)}\,\delta_{nm+1}\,, \tag{5.16}$$

$$\begin{aligned} \langle\phi_n^a|r^2\partial_r|\phi_m^a\rangle = r_0\Big[&\frac{1}{2}\sqrt{(m-1)(m-2)(m+a-1)(m+a-2)}\,\delta_{nm-2} \\ &- \frac{1}{2}(2m+a-4)\sqrt{(m-1)(m+a-1)}\,\delta_{nm-1} - (2m+a-1)\delta_{nm} \\ &+ \frac{1}{2}(2m+a+2)\sqrt{m(m+a)}\,\delta_{nm+1} \\ &- \frac{1}{2}\sqrt{m(m+1)(m+a)(m+a+1)}\,\delta_{nm+2}\Big]\,. \end{aligned} \tag{5.17}$$

Table 5.1: DVR matrix representation of various operators including the scaling factor r_0 and our ansatz $R(r) = \rho(r)/r$. For the FBR representation $\langle\phi_n^a|.|\phi_m^a\rangle$ of the given operators, see Eqs. (5.12)-(5.17). $\mathcal{U}$ denotes the FBR/DVR transformation matrix and is obtained by the diagonalization of the position operator $\mathcal{Q}$, cf. Eq. (5.11). r_α are the DVR grid points that are given by the eigenvalues of $\mathcal{Q}$.

Operator	Matrix Representation
r	$r_\alpha \delta_{\alpha\beta}$
$V(r)$	$V(r_\alpha)\,\delta_{\alpha\beta}$
∂_r	$r_0^{-1}\,\mathcal{U}^\dagger\langle\phi_n^a|\partial_r - \frac{1}{r}|\phi_m^a\rangle\,\mathcal{U}$
$r\partial_r$	$\mathcal{U}^\dagger\langle\phi_n^a|r\partial_r - 1|\phi_m^a\rangle\,\mathcal{U}$
$r^2\partial_r$	$r_0\,\mathcal{U}^\dagger\langle\phi_n^a|r^2\partial_r - r|\phi_m^a\rangle\,\mathcal{U}$
$r^{-2}\partial_r(r^2\partial_r)$	$r_0^{-2}\,\mathcal{U}^\dagger\langle\phi_n^a|\partial_r^2|\phi_m^a\rangle\,\mathcal{U}$

Solving the Three-Dimensional Schrödinger Equation

In the framework of this thesis, we solve the three-dimensional Schrödinger equation, i.e., our kinetic energy operator reads

$$T = \frac{\mathbf{p}^2}{2m} = \frac{1}{2m}\Big[-r^{-2}\partial_r(r^2\partial_r) + \frac{\mathbf{L}^2}{r^2}\Big]\,. \tag{5.18}$$

Because the matrix representation of the derivative operator in Eq. (5.18) is fairly hard to determine, we make the ansatz

$$R(r) = \rho(r)/r \tag{5.19}$$

for the radial wave function $R(r)$, well-known from the treatment of the hydrogen problem [68]. We find

$$r^{-2}\partial_r\,[r^2\partial_r\,\rho(r)/r] = r^{-1}\,\partial_r^2\rho(r)$$

and our field-free Schrödinger equation becomes

$$\tilde{H}_A\,\rho_{njl}(r)\mathcal{Y}_{j,m_j,l} = E_{njm_jl}\,\rho_{njl}(r)\mathcal{Y}_{j,m_j,l} \tag{5.20}$$

with

$$\tilde{H}_A = \frac{1}{2m}\big[-\partial_r^2 + r^{-2}\mathbf{L}^2\big] + V_l(r) + V_{so}(\mathbf{L},\mathbf{S})\,.$$

Within our numerical approach, we solve the more simple Schrödinger equation (5.20) instead of the one incorporating the kinetic energy operator as given by Eq. (5.18). Thus, we determine $\rho_{njl}(r)$ rather than $R_{njl}(r)$. Since the newly gained eigenfunctions $\rho_{njl}(r)$ are used for the calculation of the matrix representation of Hamiltonian (3.20), ansatz (5.19) has to be kept in mind for this purpose as well. For the radial matrix element $\langle||.||\rangle$ of a given operator D, we find

$$\begin{aligned}
\langle\tfrac{1}{r}\rho_{n'j'l'}||D||\tfrac{1}{r}\rho_{njl}\rangle &= \int_0^\infty \tfrac{1}{r}\rho_{n'j'l'}(D\tfrac{1}{r}\rho_{njl})\,r^2\mathrm{d}r \\
&= \int_0^\infty \rho_{n'j'l'}D\rho_{njl}\,\mathrm{d}r + \int_0^\infty \rho_{n'j'l'}\,r[D,\tfrac{1}{r}]\,\rho_{njl}\,\mathrm{d}r \\
&= \boldsymbol{\rho}^T_{n'j'l'}\mathcal{D}^{\mathrm{DVR}}\boldsymbol{\rho}_{njl} + \boldsymbol{\rho}^T_{n'j'l'}\left(r[D,\tfrac{1}{r}]\right)^{\mathrm{DVR}}\boldsymbol{\rho}_{njl}\,,
\end{aligned}$$

where $\boldsymbol{\rho_{nlj}}$ denotes the DVR vector representation of the radial wave function $\rho_{nlj}(r)$. In Table 5.1 the matrix representations of all operators relevant for this thesis are summarized.

Radial Wave Functions

Let us conclude this chapter by presenting an exemplary radial wave function calculated by means of the above discussed DVR technique. In Fig. 5.1(a) the computed radial wave function of the $40S_{1/2}$ Rydberg state of ^{87}Rb is illustrated. For comparison and to highlight their differences, the hydrogenic eigenfunction according to Eq. (5.4) for the same quantum numbers is displayed as well. Employing the same computational technique, in part (b) of Fig. 5.1 the numerically determined *hydrogenic* wave function is compared with the exact solution. An excellent agreement is found, emphasizing the applicability of our numerical approach. For both calculations, a grid size of $N = 4000$ and a scaling factor $r_0 = 0.5$ has been employed; the parameter a was set to two.

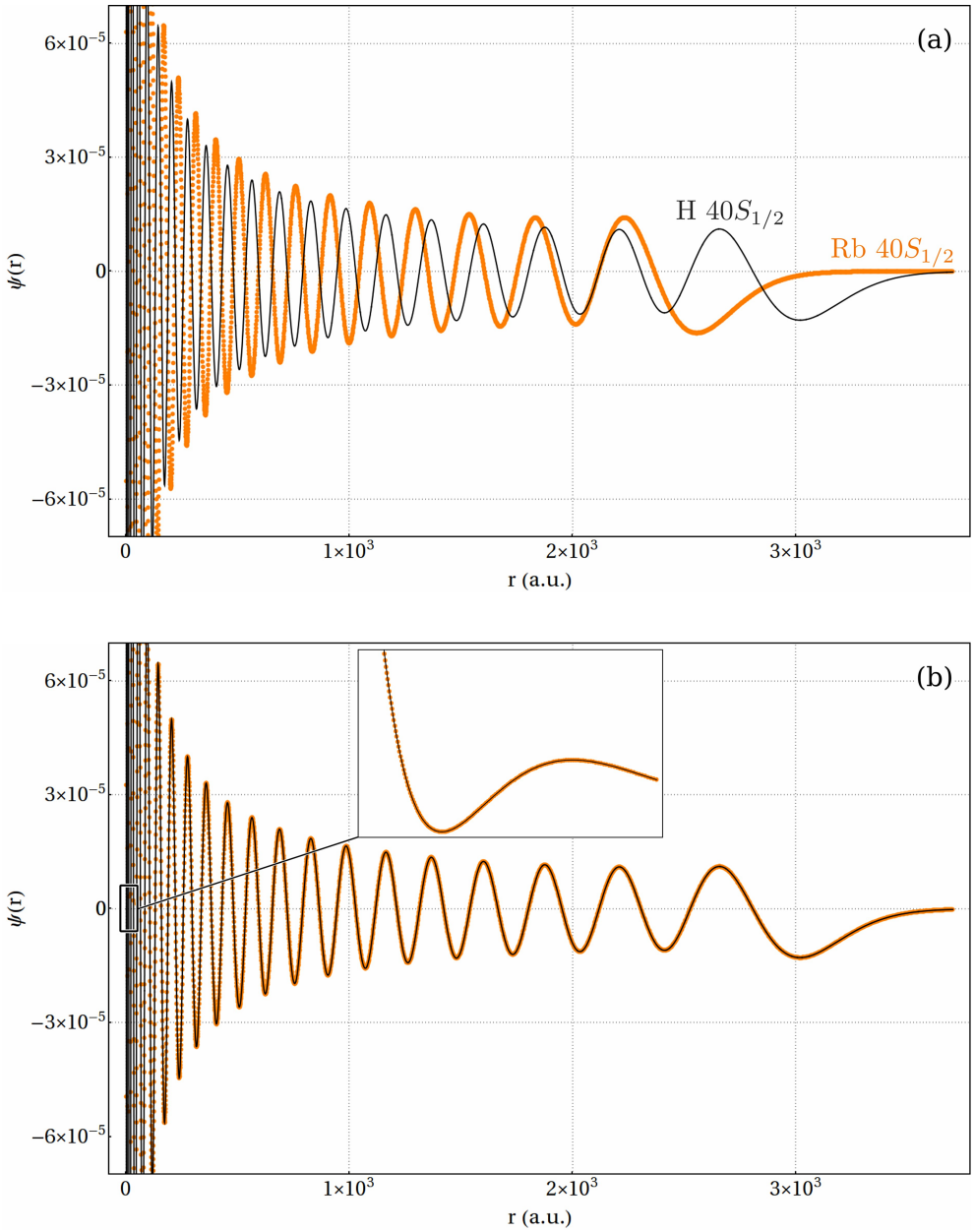

Figure 5.1: (a) Radial wave function of the $40S_{1/2}$ state of rubidium, determined by means of the Laguerre DVR technique with $N = 4000$, $r_0 = 0.5$, and $a = 2$. Because of the core penetration and polarization effects it clearly differs from the corresponding hydrogenic wave function, which is illustrated as well (solid line). To demonstrate the accuracy of our approach, in subfigure (b) the numerically determined hydrogen $40S_{1/2}$ wave function [dots; same parameters as in (a)] is compared to the analytical solution (solid line). The inset shows the data close to the origin.

Chapter 6

One-Dimensional Rydberg Gas in a Magnetoelectric Ioffe-Pritchard Trap

Traditionally, there is a great interest in studying systems with reduced spatial dimensions. This is rooted in the fact that reducing the dimension usually considerably simplifies the theoretical treatment but at the same time also leads to new physics. One paradigm is constituted by the work of Lieb and Liniger who were the first to solve the system of arbitrary many interacting bosons in one dimension using Bethe's ansatz [105, 106]. In the limit of an infinitely strong interparticle interaction strength, a so-called Tonks-Girardeau gas emerges [20] in which the bosons behave like spin-less non-interacting fermions piled up in the single-particle eigenstates of the one-dimensional potential. Experimentally, such a gas has been realized in a ^{87}Rb Bose-Einstein condensate of very low density in a tight optical potential using an optical lattice to manipulate the atoms' effective mass [21].

Besides gases of ground state atoms, particularly Rydberg gases represent excellent systems to study the influence of a strong interparticle interaction on the dynamics of many-particle systems. Due to the large displacement of the ionic core and the valence electron, Rydberg atoms can develop a large electric dipole moment leading to a strong and long-ranged dipole-dipole interaction among them [32]. In this chapter, we use the Ioffe-Pritchard configuration as a key ingredient in order to 'prepare' and study a one-dimensional Rydberg gas consisting of long lived circular states. Specifically, we propose a modified Ioffe-Pritchard trap, a magneto-electric trap, that offers tightly confining potential energy surfaces for the atomic center of mass motion; at the same time, the Rydberg atom possesses an oriented permanent electric dipole moment in this kind of trap. The resulting strong repulsion between neighboring Rydberg atoms in conjunction with the tight transverse confinement then gives rise to an effectively one-dimensional Rydberg gas with macroscopic interparticle distances.

In detail, we proceed as follows. In Section 6.1 we present the working Hamiltonian for our Ioffe-Pritchard trap that is superimposed by a homogeneous electric field. Since we are considering high-angular momentum Rydberg states in this chapter, the differences to Hamiltonian (3.20), that is derived in Chapter 3 for low angular momentum Rydberg states, are outlined in this section as well. In Section 6.3 we present the resulting adiabatic trapping potentials for the center of mass motion. Analytical expressions for the dipole-dipole interaction among trapped Rydberg atoms are derived and we estimate below which Rydberg atom density a one-dimensional Rydberg gas is expected to form. Moreover, the lifetime of such a gas is estimated. We conclude by brief outline how the envisaged one-dimensional Rydberg gas can be realized experimentally.

Most of the result presented in this chapter are published in Ref. [85].

6.1 Hamiltonian

Proceeding along the lines of Chapter 3, we derive in this section the Hamiltonian for a Rydberg atom in magnetic Ioffe-Pritchard trap that is superimposed by a homogeneous electric field. Serving as a paradigm, we specifically chose the ^{87}Rb atom in its $n = 30$ Rydberg state. Since we are particularly interested in circular states, i.e., states of maximal electronic angular momentum and projection $l = m_l = n - 1$, the single valence electron and the ionic core are assumed to interact via a pure Coulomb potential. Consequently, $V(r) = -1/r$ independently of the electronic angular momentum l, instead of the more elaborate model potential of Chapter 3, cf. Eq. (3.7). Moreover, while the inclusion of the fine structure can be readily done as presented in Chapter 3, it turns out not to be necessary in the regime we are focusing on: For high angular momentum electronic states the fine structure splittings scale as $\Delta W_{\mathrm{fs}} = \alpha^2/2n^5$ and are therefore strongly suppressed.[1] Similarly, diamagnetic effects can be neglected [65].

As discussed in Section 3.1, the Ioffe-Pritchard field configuration $\mathbf{B}(\mathbf{x})$ and the associated vector potential $\mathbf{A}(\mathbf{x})$ read

$$\mathbf{B}(\mathbf{x}) = \mathbf{B}_c + \mathbf{B}_l(\mathbf{x}) \quad \text{and} \quad \mathbf{A}(\mathbf{x}) = \mathbf{A}_c(\mathbf{x}) + \mathbf{A}_l(\mathbf{x})\,,$$

with $\mathbf{B}_c = B\mathbf{e}_3$, $\mathbf{B}_l(\mathbf{x}) = G\,[x_1\mathbf{e}_1 - x_2\mathbf{e}_2]$, $\mathbf{A}_c(\mathbf{x}) = \frac{B}{2}\,[x_1\mathbf{e}_2 - x_2\mathbf{e}_1]$, and $\mathbf{A}_l(\mathbf{x}) = Gx_1x_2\mathbf{e}_3$. B and G are the Ioffe field strength and the gradient, respectively. For our modified electromagnetic Ioffe Pritchard trap, we apply in addition to these inhomogeneous magnetic fields a homogeneous electric field pointing in the x_1-direction of the laboratory frame, $\mathbf{F} = F\mathbf{e}_1$. The corresponding scalar potential reads

$$\Phi = -Fx_1\,.$$

The interaction of the electric field with the Rydberg atom is then given by

$$H_F = \sum_{i\,\in\{e,c\}} q_i\Phi \tag{6.1}$$

where q_i denotes the charge of the interacting particle, i.e., $q_e = -1$ and $q_c = 1$ for the Rydberg electron and the ionic core, respectively. After introducing relative and center of mass coordinates $\mathbf{r}$ and $\mathbf{R}$ (see Section 3.2), Eq. (6.1) becomes

$$H_F = Fx = \mathbf{F}\cdot\mathbf{r}\,. \tag{6.2}$$

Moreover, – as in Section 3.3 – we apply the unitary transformation $U = \exp\left\{\frac{i}{2}(\mathbf{B}_c\times\mathbf{r})\cdot\mathbf{R}\right\}$ in order to partially remove the coupling between the relative and center of mass motion. The electric field interaction term H_F is invariant under this transformation of the Hamiltonian since it commutes with U.

Accounting for all considerations from above, the Hamiltonian describing the Rydberg atom

[1] In contrast, for low angular momentum states the fine structure splitting scales as n^{-3}. Consequently, in theses cases the spin-orbit coupling effects the energy spectrum significantly, cf. Section 2.3.

in our modified Ioffe-Pritchard trap finally reads

$$H = \frac{\mathbf{P}^2}{2M} + H_A + \tfrac{1}{2}[\mathbf{L} + 2\mathbf{S}] \cdot \mathbf{B}_c - \boldsymbol{\mu}_e \cdot \mathbf{B}_l(\mathbf{R} + \mathbf{r}) + \mathbf{A}_l(\mathbf{R} + \mathbf{r}) \cdot \mathbf{p} + \mathbf{F} \cdot \mathbf{r}\,. \tag{6.3}$$

Here, $H_A = \frac{\mathbf{p}^2}{2} - \frac{1}{r}$ is the Hamiltonian of a hydrogen atom possessing the energies $E_n = -\frac{1}{2}n^{-2}$. As in Chapter 3 the direct coupling of the nuclear spin to the magnetic field, $-\boldsymbol{\mu}_c \cdot \mathbf{B}(\mathbf{R})$, is omitted due to the large nuclear mass and the resulting small nuclear magnetic moment. The Schrödinger equation associated with Hamiltonian (6.3) is solved by means of the adiabatic approach presented in Section 3.4. The non-adiabatic (off-diagonal) coupling terms ΔT that arise within this procedure in the transformed kinetic energy term, cf. Eqs. (3.24) and (3.27), can be neglected in our parameter regime. They are suppressed by the splitting between adjacent energy surfaces which is proportional to powers of $1/B$. We remark that the Z-component of the center of mass momentum $\mathbf{P}$ commutes with Hamiltonian (3.20); hence the longitudinal motion can be integrated out by employing plane waves $|K_Z\rangle = \exp(-iK_Z Z)$.

Within our adiabatic approach, we are consequently left with solving the electronic Hamiltonian

$$H_r = H_A + \tfrac{1}{2}[\mathbf{L} + 2\mathbf{S}] \cdot \mathbf{B}_c - \boldsymbol{\mu}_e \cdot \mathbf{B}_l(\mathbf{R} + \mathbf{r}) + \mathbf{A}_l(\mathbf{R} + \mathbf{r}) \cdot \mathbf{p} + \mathbf{F} \cdot \mathbf{r} \equiv H_0 + H_F \tag{6.4}$$

where

$$H_0 = H_A + \tfrac{1}{2}[\mathbf{L} + 2\mathbf{S}] \cdot \mathbf{B}_c - \boldsymbol{\mu}_e \cdot \mathbf{B}_l(\mathbf{R} + \mathbf{r}) + \mathbf{A}_l(\mathbf{R} + \mathbf{r}) \cdot \mathbf{p}$$

is the Hamiltonian of a purely magnetic Ioffe-Pritchard trap. For a thorough discussion of H_0 including the resulting trapping potentials of high angular momentum Rydberg states, we refer the reader to Refs. [64, 65]. In order to find the stationary states of Hamiltonian (6.4), we assume that neither the magnetic nor the electric field causes couplings between electronic states with different principal quantum number n. In this case we can consider each n-manifold separately and may represent Hamiltonian (6.4) in the space of the $2n^2$ states which span the n-manifold under investigation.[2] For our numerical treatment (see Chapter 5), this means that our basis consists of the 2^n hydrogen eigenfunctions for a given principal quantum number n, i.e., all states $|nlm_l; m_s\rangle$ with $l < n$, $|m_l| \leq l$, and $m_s = \pm 1/2$. Hence, the restriction to a single n-manifold reduces the dimensionality of the resulting matrix representation and therefore the computational effort.

6.2 Analytical Diagonalization and Perturbed Wave Functions

Besides the technical reason of saving computation time, the reduction of the full Hilbert space to a single n-manifold allows us to gain analytical solutions for the Schrödinger equation associated with H_0. We pursue an approach analogous to Chapter 4, where we considered the action of any involved operator only within a given fine structure manifold. The degeneracy

[2] The parameter range in which this approximation is valid – including, of course, the one investigated here – has been examined in Refs. [65, 107].

of the field-free states within such a submanifold allowed us to substitute

$$\begin{aligned} yp_z &\to \frac{1}{2}L_x\,, \\ xp_z &\to -\frac{1}{2}L_x\,, \\ p_z &\to 0\,. \end{aligned} \tag{6.5}$$

Since we are neglecting spin orbit and quantum defect effects for the investigation of the high angular momentum states, here the same reasoning holds not only for a given fine structure submanifold but for the whole n-manifold, yielding

$$H_0 = H_A + \frac{1}{2}\left[\mathbf{L} + 2\mathbf{S}\right] \cdot \mathbf{B}(\mathbf{R})\,. \tag{6.6}$$

As in Chapter 4, we omitted terms not showing an explicit spatial dependence,

$$H'' = \mathbf{A}_l(\mathbf{r}) \cdot \mathbf{p} - \boldsymbol{\mu}_e \cdot \mathbf{B}_l(\mathbf{r})\,. \tag{6.7}$$

To first order, H'' merely represents an energy offset to the $\mathbf{R}$-dependent adiabatic energy surfaces determined by Hamiltonian (6.6).

Similar to Eq. (4.12), Hamiltonian (6.6) represents now the coupling of a point-like particle to the spatially dependent magnetic field $\mathbf{B}(\mathbf{R})$ via its magnetic moment $\boldsymbol{\mu} = \frac{1}{2}\mathbf{L} + \mathbf{S}$. Such a Hamiltonian can be diagonalized by applying the spatially dependent unitary transformation $U_r = e^{-i\gamma(L_x+S_x)}e^{-i\beta(L_y+S_y)}$, cf. Eq. 4.13, that rotates the magnetic field vector $\mathbf{B}(\mathbf{R})$ into the z-direction of the laboratory frame. In this manner, the quantization axis is well defined along the z-axis for all positions $\mathbf{R}$ of the atom and m_j stays a valid quantum number. With the rotation angles as defined in Eq. (4.14), the transformed Hamiltonian H_0 becomes

$$U_r H_0 U_r^\dagger = H_A + \tfrac{1}{2}(L_z + 2S_z)\sqrt{B^2 + G^2(X^2+Y^2)}\,. \tag{6.8}$$

This Hamiltonian is diagonal in the basis of the hydrogen eigenfunctions $|nlm_l; m_s\rangle$ and the resulting adiabatic electronic energy potentials consequently read

$$E^{(0)}_{nlm_lm_s}(\mathbf{R}) = -\frac{1}{2n^2} + \frac{1}{2}(m_l + 2m_s)\sqrt{B^2 + G^2(X^2+Y^2)}\,. \tag{6.9}$$

The adiabatic energy surfaces Eq. (6.9) are rotationally symmetric around the Z-axis and confining for $m_j > 0$. For small radii ($\rho = \sqrt{X^2+Y^2} \ll B/G$) an expansion up to second order yields a harmonic potential

$$E^{(0)}_\kappa(\rho) \approx E^{el}_\kappa + \tfrac{1}{2}g_j m_j B + \frac{1}{2}M\omega^2\rho^2$$

with the trap frequency defined by

$$\omega = G\sqrt{\frac{m_l + 2m_s}{2MB}}\,.$$

On the contrary, when the center of mass is far from the Z-axis ($\rho \gg B/G$) we find a linear

behavior, $E_\kappa^{(0)}(\rho) \approx E_\kappa^{el} + \frac{1}{2} g_j m_j G \rho$. For a more thorough discussion of the energy surfaces Eq. (6.9), we refer the reader once more to Refs. [64, 65]. The possible combinations of m_l and m_s result in $2n+1$ energy surfaces, each of which shows a degree of degeneracy given by $2n - |m_l + 2m_s + 1| - |m_l + 2m_s - 1|$ [65]. At the origin, these manifolds of surfaces are energetically separated by $\Delta E = B/2$. Here, we are interested in the uppermost surface, which is non-degenerate and is constituted by the *circular* state

$$|\text{circ}\rangle \equiv |n, l = m_l = n-1; m_s = 1/2\rangle \,. \tag{6.10}$$

The energetically next lower surface (that we need for the determination of the perturbed eigenfunctions due to H_F) shows a two-fold degeneracy and is determined by

$$\begin{aligned} |2\rangle &\equiv |n, l = n-1, m_l = n-2; m_s = 1/2\rangle \text{ and} \\ |3\rangle &\equiv |n, l = m_l = n-2; m_s = 1/2\rangle \,. \end{aligned} \tag{6.11}$$

The influence of the electric field $\mathbf{F}$ on the circular state $|\text{circ}\rangle$ can be calculated in second order perturbation theory. The perturbed wave function reads

$$|\psi\rangle = |\text{circ}\rangle + \sum_{\kappa \neq \text{circ}} \frac{\langle \kappa | U_r H_F U_r^\dagger | \text{circ}\rangle}{E_\text{circ} - E_\kappa} |\kappa\rangle \tag{6.12}$$

$$= |\text{circ}\rangle + c_3 |3\rangle \tag{6.13}$$

with

$$c_3 = \frac{\langle 3 | U_r H_F U_r^\dagger | \text{circ}\rangle}{E_\text{circ} - E_3} = \frac{3}{\sqrt{2}} \frac{F}{B} n\sqrt{n-1} \left(\cos\beta + i \sin\beta \, \sin\gamma\right). \tag{6.14}$$

Equation (6.13) is yielded due to the selection rules $\Delta l = \pm 1$ and $\Delta m_l \in \{0, \pm 1\}$ of the transformed field interaction $U_r H_F U_r^\dagger = F \cdot (x \cos\beta + y \sin\beta \, \sin\gamma - z \cos\gamma \, \sin\beta)$. That is, the electric field $\mathbf{F}$ admixes solely state $|3\rangle$ to the circular state.[3] For the calculation of the corresponding coefficient c_3 we employed $\langle 3|y|\text{circ}\rangle = i\langle 3|x|\text{circ}\rangle$, $\langle 3|z|\text{circ}\rangle = 0$ as well as $\langle 3|x|\text{circ}\rangle = \frac{3}{2\sqrt{2}} n\sqrt{n-1}$, see Appendix D.

6.3 Energy Surfaces and One-Dimensional Rydberg Gas

In this section, we discuss the solutions of the electronic Hamiltonian (6.4), focusing on the circular state. In particular, a comparison to the purely magnetic Ioffe-Pritchard trap is provided. We show that trapped Rydberg atoms can be created in long-lived electronic states exhibiting an electric dipole moment of several hundred Debye. The resulting dipole-dipole

[3] Note that the electric field lifts the degeneracy of the submanifold $\{|2\rangle, |3\rangle\}$ resulting in the field-dressed states $|\pm\rangle = \frac{1}{\sqrt{2}}\big[|2\rangle \pm |3\rangle\big]$. Consequently, the sum in Eq. (6.12) should include these states rather than the non-dressed states $|2\rangle$ and $|3\rangle$. We would get

$$|\psi\rangle = |\text{circ}\rangle + \frac{c_+}{\sqrt{2}}\Big(1 - \frac{\Delta E_+}{\Delta E_-}\Big)|2\rangle + \frac{c_+}{\sqrt{2}}\Big(1 + \frac{\Delta E_+}{\Delta E_-}\Big)|3\rangle$$

with $\Delta E_\pm = E_\text{circ} - E_\pm$ and $c_+ = \langle + | U_r H_F U_r^\dagger | \text{circ}\rangle / \Delta E_+$. However, we are considering the perturbative regime where the electric field effects are much smaller than the magnetic field interaction. Thus employing $\Delta E_+ \approx \Delta E_- \approx \Delta E$ yields Eq. (6.14) for the coefficient.

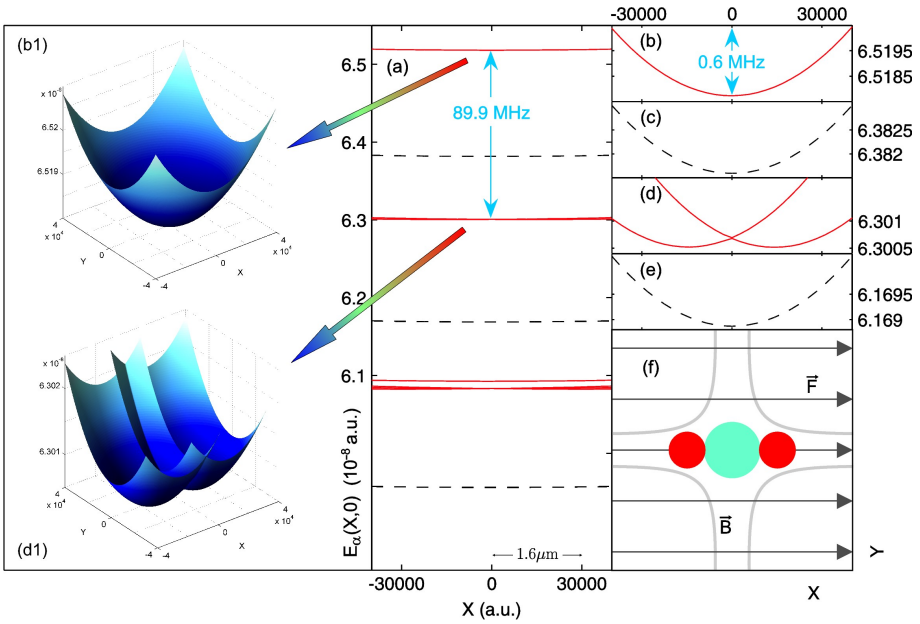

Figure 6.1: Potential energy surfaces for the center of mass motion of a ^{87}Rb Rydberg atom ($n = 30$) in a Ioffe-Pritchard trap with $B = 10\,\mathrm{G}$, $G = 10\,\mathrm{Tm}^{-1}$. Dashed lines: $F = 0$, solid lines: $F = 5.14\,\mathrm{Vm}^{-1}$. An overview of the seven energetically highest potential curves ($Y = 0$) is shown in panel (a). Magnified views of the uppermost (b,c) and next lower ones (d,e) are also provided while for (b) and (d) the two-dimensional surfaces are shown additionally in (b1) and (d1), respectively. The range of the X-coordinate, corresponding to 2.1μm, is the same for each subfigure (a)-(e). The total field configuration is sketched in panel (f) where the circles depict the locations of the minima of the uppermost (big circle) and the two adjacent lower-lying (small circles) adiabatic surfaces. The magnetic field lines are indicated in gray while the electric field is sketched by black arrows.

interaction of Rydberg atoms in conjunction with the radial confinement provided by the Ioffe-Pritchard trap is demonstrated to give rise to an effectively one-dimensional ultracold Rydberg gas with a macroscopic interparticle distance. We derive analytical expressions for the electric dipole moment and the required linear density of Rydberg atoms.

Adiabatic Electronic Potential Surfaces

Within our adiabatic approach, the diagonalization of Hamiltonian (6.4) yields a set of $2n^2$ decoupled differential equations governing the adiabatic center of mass motion within the individual two-dimensional energy surfaces $E_\kappa(\mathbf{R})$, i.e., the surfaces $E_\kappa(\mathbf{R})$ serve as potentials for the center of mass motion of the Rydberg atom. In Figure 6.1 we present intersections along the X-direction of such potential surfaces for $B = 10\,\mathrm{G}$, $G = 10\,\mathrm{Tm}^{-1}$, and $n = 30$ in the case of ^{87}Rb. As outlined in Section 6.2, for zero electric field strength (dashed lines) the potential curves are organized in groups that are energetically well-separated by a gap of $\Delta E = B/2 = 87.9$ MHz. The uppermost surface originates from the circular state, $l = m_l = n-1$, is non-degenerate, and provides an approximately harmonic confinement with a trap frequency of $\omega = G\sqrt{n/2MB} = 13.9\,\mathrm{kHz}$, corresponding to $0.1\,\mu\mathrm{K}$. The two adjacent lower surfaces are degenerate and also approximately harmonic, possessing a trap frequency of $\omega = G\sqrt{(n-1)/2MB}$.

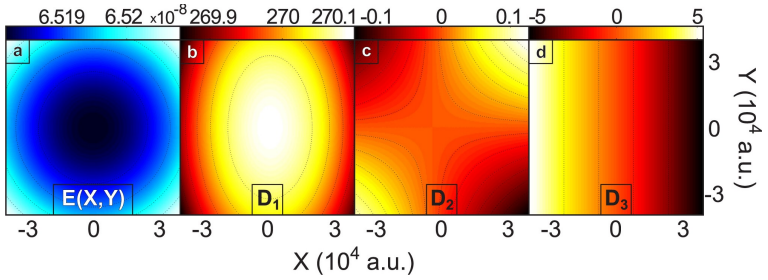

Figure 6.2: (a) Uppermost electronic potential surface for the center of mass motion of ^{87}Rb in the $n = 30$ multiplet and the parameters used in Fig. 6.1. (b-d) Components of the electric dipole moment $\mathbf{D}(\mathbf{R})$ in atomic units. One recognizes the clear alignment of the electric dipole moment along the electric field vector. The numerically calculated values of $\mathbf{D}(\mathbf{R})$ are to a good accuracy reproduced by Eq. (6.15).

As soon as an electric field is applied, all surfaces are shifted considerably in energy. This is visible from the solid curves in Fig. 6.1 for which an electric field of strength $F = 5.14\,\mathrm{Vm}^{-1}$ is applied. The shapes of the potentials are barely affected by the electric field such that Rydberg states that are trapped in a pure Ioffe-Pritchard configuration remain confined also in the magneto-electric trap. Moreover, adding the electric field leads to non-trivial effects: The second and third surface, that are degenerate in the absence of the electric field, are now shifted in opposite ways along the X-direction. All surfaces shown provide a harmonic confinement with a trap frequency ω also in the Y-direction. The corresponding two-dimensional trapping potentials are illustrated in Fig. 6.1(b1) and (d1). We remark that the chosen parameter set does not generate an extreme constellation; hence an even stronger confinement can be achieved without invalidating the applied approximations [65].

Electric Dipole Moment

Let us now investigate the electronic properties of a Rydberg atom being trapped in the uppermost potential surface. For $F = 0$ and sufficiently large values of B, this surface is formed almost exclusively by the highest possible electronic angular momentum state, i.e., $l = m_l = n - 1$.[4] If F is increased, electronic states with smaller l will be inevitably admixed to the electronic state belonging to this energy surface. An interesting property to investigate is hence the electric dipole moment of trapped Rydberg atoms: While for $F = 0$ the electronic states are approximately pure parity eigenstates and therefore exhibit almost no electric dipole, the admixture of lower l states to the uppermost surface in the presence of the electric field is expected to give rise to a non-vanishing expectation value of the dipole operator. Indeed, this becomes evident in Fig. 6.2 where the uppermost potential surface and the three components of the expectation value of the electric dipole operator $\mathbf{D}(\mathbf{R}) = \langle \mathbf{r} \rangle (\mathbf{R})$ are shown (same parameters as in Fig. 6.1). It can be clearly seen that a permanent dipole moment is established whose dominant contribution points along the electric field vector, i.e., $D_2(\mathbf{R}) \ll D_1(\mathbf{R})$ and $D_3(\mathbf{R}) \ll D_1(\mathbf{R})$.

In order to study the dependence of $\mathbf{D}(\mathbf{R})$ on the field strengths F and B as well as on the degree of electronic excitation, we use expression (6.13) for the perturbed wave function. In

[4] In Section 6.2 we derived analytical expressions for the adiabatic potentials and assigned the uppermost surface *exclusively* to the circular state. However, we neglected the contribution H'', cf. Eq. 6.7, that is non-diagonal and therefore weakly couples to lower lying states.

second order perturbation theory, the electric dipole moment is consequently given by

$$\mathbf{D}(\mathbf{R}) = \langle\psi|U_r\mathbf{r}U_r^\dagger|\psi\rangle\,.$$

Employing the same relations as in Section 6.2 for the transition matrix elements $\langle 3|x_i|\mathrm{circ}\rangle$ yields

$$\mathbf{D}(\mathbf{R}) = 2\,\mathrm{Re}(c_3^*\langle 3|U_r\mathbf{r}U_r^\dagger|\mathrm{circ}\rangle)\,.$$

Inserting the expression for the transformed position operator (see Eq. (4.15)),

$$U_r\mathbf{r}U_r^\dagger = \begin{pmatrix} x\cos\beta + y\sin\beta\,\sin\gamma - z\cos\gamma\,\sin\beta \\ y\cos\gamma + z\sin\gamma \\ x\sin\beta - y\cos\beta\,\sin\gamma + z\cos\beta\,\cos\gamma \end{pmatrix},$$

finally provides us an analytic expression for the electric dipole moment:

$$\mathbf{D}(\mathbf{R}) = \frac{9}{2}\frac{F}{B}n^2(n-1)\begin{pmatrix} \cos^2\beta + \sin^2\gamma\,\sin^2\beta \\ \cos\beta\,\sin\beta\,\sin\gamma \\ \cos\beta\,\sin\beta - \sin\beta\,\sin\gamma\,\cos\gamma \end{pmatrix}. \tag{6.15}$$

We note that $\mathbf{D}(\mathbf{R})$ scales proportional to the third power of the principal quantum number and can therefore gain a significant magnitude even if the ratio F/B is small. Although the chosen field configuration already constitutes an extreme example for the perturbative approach, good agreement of Eq. (6.15) with the numerically obtained data presented in Fig. 6.2 is found. For example, in the vicinity of the minimum of the potential surface ($X = Y = 0$) we find an exact value of $D_x^{\mathrm{exact}}(0) = 270$ whereas the expression (6.15) yields $D_x(0) = 276$. The remaining components vanish at the origin: $D_y(0) = D_x(0) = 0$. This is again in good agreement with the numerically calculated results, which yield $D_y^{\mathrm{exact}}(0) = 8.0 \times 10^{-11}$ and $D_z(0)^{\mathrm{exact}} = -0.024$, respectively. The arising residual dipole moment of the exact results is due to the contribution of H'' that has been neglected for deriving the analytical expression Eq. (6.15). For smaller ratios of F/B, even better agreement can be achieved.

One-Dimensional Rydberg Gas

Due to the dependence on the angles γ and β, the dipole moment weakly depends on the quantum state of the center of mass motion. However, the electric dipole moment is independent of the Z-position of the Rydberg atoms in the trap since the field configuration is translational symmetric. If we now consider two transversally confined atoms in the same trap at the longitudinal positions Z_A and Z_B, we can write for their dipole-dipole interaction

$$\begin{aligned} V_{\mathrm{D}}(\mathbf{R}_A, \mathbf{R}_B) &= \frac{1}{|\mathbf{R}_A - \mathbf{R}_B|^3}\Big\{\mathbf{D}(\mathbf{R}_A)\cdot\mathbf{D}(\mathbf{R}_B) - 3\,[\mathbf{D}(\mathbf{R}_A)\cdot\mathbf{e}]\,[\mathbf{D}(\mathbf{R}_B)\cdot\mathbf{e}]\Big\} \\ &\approx \frac{\mathbf{D}(\mathbf{R}_A)\cdot\mathbf{D}(\mathbf{R}_B)}{|Z_A - Z_B|^3} \end{aligned} \tag{6.16}$$

where $\mathbf{e} = (\mathbf{R}_A - \mathbf{R}_B)/R$ denotes the interparticle unit vector. The approximation in Eq. (6.16) holds due to the orientation of the dipoles and the assumption that $|Z_A - Z_B|$

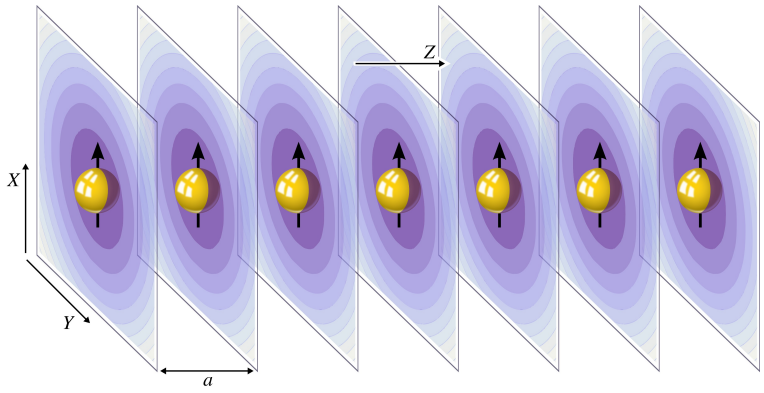

Figure 6.3: Schematics of a one-dimensional Rydberg gas in an electric-field-enhanced Ioffe-Pritchard trap. The arrows represent the dipole moments of the Rydberg atoms oriented along the external homogeneous electric field in X-direction. The interparticle spacing a belongs to the critical density N_{1D} that is given by Eq. (6.18).

is large compared to the transversal oscillator length of the trap. These conditions moreover ensure a minimal coupling of the transversal and longitudinal motion.

Using the above approximation, one can estimate the interaction energy of one atom being part of an infinite atomic chain with an interparticle spacing a. One finds

$$E_{\text{int}} = 2\frac{\mathbf{D}^2(0)}{a^3}\sum_{k=1}^{\infty} k^{-3} = \frac{81}{2a^3}\frac{F^2}{B^2}n^4(n-1)^2\zeta(3) \tag{6.17}$$

with the Riemann zeta function $\zeta(3) = 1.202\,06$. Here we have approximated $\mathbf{D}^2(\mathbf{R}) \approx \mathbf{D}^2(0)$ since the dipole moment barely varies in the vicinity of the origin $X = Y = 0$. If the interaction energy E_{int} is smaller than the transversal trap frequency ω, we can assume that the interacting atoms remain in the transversal ground state: This is considered the one-dimensional regime, see Fig. 6.3 for a sketch. The linear density below which a one-dimensional Rydberg gas is expected to form is then given by

$$N_{1D} = \frac{\sqrt{B}}{3}\left[3\sqrt{\frac{M_c}{2}}\frac{F^2}{G}\,\zeta(3)\,n^{7/2}(n-1)^2\right]^{-\frac{1}{3}}. \tag{6.18}$$

Above this density, excited transversal center of mass states might be populated, resulting in a quasi one-dimensional Rydberg gas (that is certainly of interest on its own). For our parameter set, we obtain a minimal interparticle spacing $a = 43\,\mu$m; hence a chain of 1 mm in length contains 23 particles. This density can be further increased by either increasing the magnetic field gradient and/or decreasing the electric field strength: At $B = 10\,$G, $G = 100\,\text{Tm}^{-1}$, and $F = 0.514\,\text{Vm}^{-1}$ a chain of the same length would contain 230 Rydberg atoms.

Radiative Decay

Rydberg atoms are highly excited quantum object that possess only a finite lifetime due to spontaneous decays. Since one might be interested in observing the external dynamics of the

above proposed one-dimensional Rydberg gas, we need to understand the radiative properties of a Rydberg atom that is exposed to our modified Ioffe-Pritchard trap. After integrating over all directions of the emitted photon and summing over all possible polarizations, the transition rate for the radiative decay from an initial state $|i\rangle$ to a final state $|f\rangle$ reads [73]

$$\Gamma_{f\leftarrow i} = \frac{4}{3}\alpha^3 \Delta E^3 |\langle f|\mathbf{r}|i\rangle|^2 \,, \tag{6.19}$$

where α is the fine structure constant and $\Delta E = E_i - E_f$ the energy difference between the initial and final state. Note that the states in Eq. (6.19) include the external motion, i.e., within our adiabatic approach we need to calculate the center of mass matrix element $|\langle f|\mathbf{r}|i\rangle| = |\langle \chi_f|\mathbf{r}_{fi}(\mathbf{R})|\chi_i\rangle|$ with $\mathbf{r}_{fi}(\mathbf{R})$ being the spatially dependent electronic matrix element and $|\chi\rangle$ denoting the center of mass states.

In order to estimate the changes in the field-free decay rates due to the electromagnetic trapping fields, we neglect the center of mass dependence of the decay rate and simply evaluate Eq. (6.19) at the origin. This is motivated by the fact that $\mathbf{r}_{fi}(\mathbf{R})$ only varies slightly throughout the support of the center of mass wave function. Consequently, the center of mass integration transforms into a simple overlap integral with $\langle \chi_f|\chi_i\rangle \approx \delta_{fi}$.[5] Adopting this approximation, the possible single channel decay rates of the dressed circular state[6] $|\psi_n\rangle = |\mathrm{circ}_n\rangle + c_{3,n}|3_n\rangle$ evaluate to[7]

$$\begin{aligned}
\Gamma_{\mathrm{circ}_{n-1}\leftarrow\mathrm{circ}_n} &= \frac{8}{3}\alpha^3 \Delta E_{n,n-1}^3 \Big[\big|\langle \mathrm{circ}_{n-1}|x|\mathrm{circ}_n\rangle\big|^2 + |c_{3,n-1}|^2 |c_{3,n}|^2 \big|\langle 3_{n-1}|x|3_n\rangle\big|^2 \\
&\qquad + 2\,\mathrm{Re}(c_{3,n}c_{3,n-1}^*)\langle 3_{n-1}|x|3_n\rangle\langle \mathrm{circ}_{n-1}|x|\mathrm{circ}_n\rangle \Big] \,, \\
\Gamma_{3_{n-1}\leftarrow\mathrm{circ}_n} &= \frac{8}{3}\alpha^3 \Delta E_{n,n-1}^3 |c_{3,n}|^2 \big|\langle 3_{n-1}|x|3_n\rangle\big|^2 \,, \\
\Gamma_{\mathrm{circ}_{n-2}\leftarrow\mathrm{circ}_n} &= \frac{8}{3}\alpha^3 \Delta E_{n,n-2}^3 |c_{3,n}|^2 \big|\langle \mathrm{circ}_{n-2}|x|3_n\rangle\big|^2 \,.
\end{aligned} \tag{6.20}$$

Analytical expressions of the matrix elements emerging in Eq. (6.20) are listed in Tab. 6.1. Note that we did not consider transitions within one n-manifold since the Zeeman splitting $\Delta E_{n,n} \propto B$ of the surfaces within one n-manifold is much smaller than the energetical separation of adjacent n-manifolds, $\Delta E_{n,n-1} \propto n^{-3}$ (e.g., the magnetic field $B = 1\,\mathrm{T}$ yields $\Delta E_{n,n-1}^3/\Delta E_{n,n}^3 \sim 10^3$). Because the matrix elements for both kinds of transitions are of the same order of magnitude, the intra-n decay rates are negligible compared to the inter-n ones.

Employing the approximate expressions as given in Tab. 6.1, the total decay rate $\Gamma_{\mathrm{circ}_n} = \sum_f \Gamma_{f\leftarrow\mathrm{circ}_n}$ reads

$$\Gamma_{\mathrm{circ}_n} = \frac{2}{3}\alpha^3 n^{-5}\Big[1 + |c_{3,n}|^2 + 2\,\mathrm{Re}(c_{3,n}c_{3,n-1}^*) + |c_{3,n}|^2|c_{3,n-1}|^2 + \frac{4}{n}\,|c_{3,n}|^2\Big] \tag{6.21}$$

[5] Strictly speaking, the orthonormality of the center of mass wave functions is only exact within one surface. However, for the decay of the circular state this orthonormality also approximately holds between adjacent surfaces due to their almost identical trap frequencies.

[6] We introduced the index n here to distinguish between different n-manifolds.

[7] In general, we would encounter the matrix element $|\langle f|\mathbf{r}|i\rangle|$ rather than $|\langle f|x|i\rangle|$, cf. Eq. (6.19). Here, we exploited the fact that $|\langle f|z|i\rangle|$ does not contribute for the decay of our dressed circular state $|\psi\rangle$ and that $|\langle f|x|i\rangle| = |\langle f|y|i\rangle|$.

Table 6.1: Transition matrix elements necessary for the calculation of the radiative lifetime of the dressed circular state $|\psi_n\rangle = |\mathrm{circ}_n\rangle + c_{3,n}|3_n\rangle$, cf. Eq. (6.13). The resulting single channel decay rates – approximated for large n – are also provided. The states $|\mathrm{circ}\rangle$ and $|3\rangle$ are defined in Eqs. (6.10) and (6.11), respectively; the indices denote the corresponding principal quantum number. For a general analytic expression of the transition matrix elements, see Appendix D.

Matrix Element	Exact	Approximate Decay Rate
$\Delta E^3 \left\lvert\langle \mathrm{circ}_{n-1}\lvert x\rvert \mathrm{circ}_n\rangle\right\rvert^2$	$\frac{1}{4n^5}\left[\frac{n^{2n+1}(n-1)^{2n-2}}{(n-1/2)^{4n-1}}\right]$	$\frac{2}{3}\alpha^3 n^{-5}$
$\Delta E^3 \left\lvert\langle 3_{n-1}\lvert x\rvert 3_n\rangle\right\rvert^2$	$\frac{1}{4n^5}\left[\frac{n^{2n-1}(n-1)^{2n-3}(n-2)}{(n-1/2)^{4n-3}}\right]$	$\frac{2}{3}\alpha^3 n^{-5}$
$\Delta E^3 \langle 3_{n-1}\lvert x\rvert 3_n\rangle\langle \mathrm{circ}_{n-1}\lvert x\rvert \mathrm{circ}_n\rangle$	$\frac{1}{4n^5}\left[\frac{n^{2n}(n-1)^{2n-5/2}(n-2)^{1/2}}{(n-1/2)^{4n-2}}\right]$	$\frac{2}{3}\alpha^3 n^{-5}$
$\Delta E^3 \left\lvert\langle \mathrm{circ}_{n-2}\lvert x\rvert 3_n\rangle\right\rvert^2$	$\frac{1}{n^6}\left[\frac{n^{2n}(n-2)^{2n-4}}{(n-1)^{4n-4}}\right]$	$\frac{8}{3}\alpha^3 n^{-6}$

and the lifetime evaluates to $\tau_{\mathrm{circ}_n} = \Gamma^{-1}_{\mathrm{circ}_n}$. Hence, corrections to the bare decay rate of the field-free circular state, $\tau_0 = 3n^5/2\alpha^3$, are found to be of the order of $|c_{3,n}|^2 \sim (F/B)^2 n^3$. For an atom being confined to the energy surface that is shown in Fig. 6.2, we have calculated a lifetime of $\tau_{\mathrm{circ}_n} = 2.109\,\mathrm{ms}$, which basically corresponds to the field-free result $\tau_0 = 2.194\,\mathrm{ms}$. We remark that τ_{circ_n} has been determined utilizing the numerically calculated electronic eigenstates rather than Eq. (6.21). For the chosen field configuration, the perturbative approach has to be taken with a grain of salt; indeed Eq. (6.21) deviates considerably with $\tau_{\mathrm{circ}_n} = 0.677\,\mathrm{ms}$. For the alternative field configuration mention earlier ($B = 10\,\mathrm{G}$, $G = 100\,\mathrm{Tm}^{-1}$, and $F = 0.514\,\mathrm{Vm}^{-1}$), on the other hand, Eq. (6.21) yields $\tau_{\mathrm{circ}_n} = 2.153\,\mathrm{ms}$, which is in good agreement with the numerically calculated lifetime of $2.192\,\mathrm{ms}$.[8]

The lifetime of the one-dimensional Rydberg gas is determined by the decay rate of a single Rydberg atom.[9] If we want to resolve the external dynamics of the proposed one-dimensional Rydberg chain, the Rydberg lifetime thus must exceed the time scale of the envisaged dynamics. Assuming only next-neighbor dipole-dipole interactions, the potential experienced by a single Rydberg atom at position $\mathbf{R} = 0$ is given by

$$V_{\mathrm{dd}}(Z) = \frac{\mathbf{D}^2(0)}{(a+Z)^3} + \frac{\mathbf{D}^2(0)}{(a-Z)^3} = \frac{2\,\mathbf{D}^2(0)}{a^3} + \frac{12\,\mathbf{D}^2(0)}{a^5}\,Z^2 + \ldots \tag{6.22}$$

where we assumed once more $\mathbf{D}^2(\mathbf{R}) \approx \mathbf{D}^2(0)$. A sketch of the exemplary situation of three Rydberg atoms is provided in Fig. 6.4. Note that at this point we are only interested in the longitudinal dynamics, i.e., along the untrapped x_3 direction. Equating $V_{\mathrm{dd}}(Z) \equiv \frac{1}{2}M\omega_{\mathrm{dd}}^2 Z^2 + \mathrm{const}$, we can define a one-particle oscillator frequency ω_{dd} as

$$\omega_{\mathrm{dd}} = \sqrt{\frac{24\,\mathbf{D}^2(0)}{Ma^5}}\,, \tag{6.23}$$

[8] Note that the numbers given in this paragraph have been calculated employing the exact expressions given in Tab. 6.1 rather than the approximate ones.

[9] We remark, however, that a single decay $|\mathrm{circ}_n\rangle \to |\mathrm{circ}_{n-1}\rangle$ does not destroy the Rydberg chain entirely since the $|\mathrm{circ}_{n-1}\rangle$ state possesses very similar properties to its non-decayed counterpart.

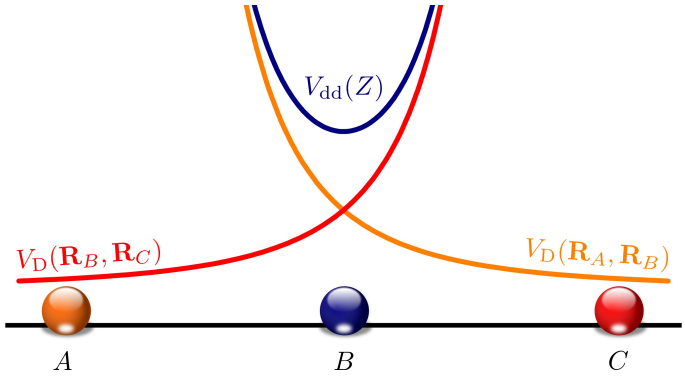

Figure 6.4: Sketch of three Rydberg atoms interacting via $V_{\mathrm{D}}(\mathbf{R}_A, \mathbf{R}_B)$, cf. Eq. 6.16. For the atom in the middle, this results in an approximately harmonic potential $V_{\mathrm{dd}}(Z)$ as given by Eq. (6.22).

giving rise to the time scale $\tau_{\mathrm{dd}} = \omega_{\mathrm{dd}}^{-1}$. As an example, the field configuration $B = 10\,\mathrm{G}$, $G = 100\,\mathrm{Tm}^{-1}$, and $F = 0.514\,\mathrm{Vm}^{-1}$ yields a time scale of less than one millisecond.

Finally, let us remark that – because of the scaling proportional to n^5 – the lifetime of a Rydberg atom can be significantly enhanced by exciting to a higher principal quantum number n. In addition, it can be further prolonged by establishing an adapted experimental setup which inhibits the electromagnetic field mode at the dominant transition frequency [108]. At the same time, a cryogenic environment will diminish the undesirable effect of stimulated (de-)excitation by blackbody radiation.

Preparation of the One-Dimensional Rydberg Gas

We conclude this chapter by briefly commenting on the realization of such a Rydberg gas, which is certainly a challenging experimental task. One could start from an extremely dilute ultracold atomic gas prepared in an elongated Ioffe-Pritchard trap. For transferring ground state atoms to high angular momentum Rydberg states, techniques such as crossed electric and magnetic fields or rotating microwave fields can be employed, see Ref. [109] and references therein. During the preparation, the excitation lasers have to be focused such that Rydberg atoms emerge only at positions separated by the interparticle spacing a that is required to meet the criterion (6.18). Since a is in the order of several μm, which can be resolved optically, this should be feasible. The large value of a moreover ensures that the mutual ionization due to the overlap of the electronic clouds of two atoms does not occur. For our circular states with $n = 30$, the atomic extension can be estimated by $\langle r \rangle \approx n^2 = 48$ nm and is thus orders of magnitude smaller than the corresponding value of a for our field configuration. In order to probe the dynamics of the resultant Rydberg chain, one can field-ionize the atoms: From the spatially resolved electron signal a direct mapping to the positions of the Rydberg atoms should be possible.

Chapter 7

Magnetic Trapping of Ultracold Rydberg Atoms in Low Angular Momentum States

Being omnipresent in experiments dealing with ultracold atoms, inhomogeneous magnetic fields seem predestined for trapping Rydberg atoms. Similar to ground state atoms, the magnetic trapping of Rydberg atoms originates from the interaction of their magnetic moment with the magnetic field. In particular, this facilitates the utilization of trap geometries that are well-known from ground state atoms. In this spirit, theoretical studies recently demonstrated that Rydberg atoms can be tightly confined in a magnetic Ioffe-Pritchard trap [64, 65] and that one-dimensional Rydberg gases can be created and stabilized by means of an additional electric field, see Chapter 6 of this thesis and Ref. [85]. However, the trapping mechanism relies in these studies on high angular momentum electronic states that have not been realized yet in experiments with ultracold atoms. In this chapter, we explore the trapping potentials arising for the low angular momentum nS, nP, and nD Rydberg states of ^{87}Rb. In particular, we illuminate the question of how the composite character of Rydberg atoms, i.e., the fact that they consist of an outer electron far away from a compact ionic core becomes manifest in a standard Ioffe-Pritchard magnetic trap. As we are going to show, the resulting trapping potentials possess a reduced azimuthal symmetry and a finite trap depth, which can be a few vibrational quanta only or less. Choosing the magnetic field parameters appropriately, on the other hand, stable trapping can be achieved with trap depths in the micro-Kelvin regime. Implications for quantum information protocols involving magnetically trapped Rydberg atoms are discussed.

In detail we proceed as follows. Section 7.1 summarizes the derivation of our working Hamiltonian for low angular momentum Rydberg atoms in a Ioffe-Pritchard trap as given in Chapter 3. Section 7.2 then introduces reasonable approximations which allow us to gain analytical solutions for the stationary Schrödinger equation and hence for the trapping potentials. In Section 7.3 we analyze the resulting energy surfaces which serve as trapping potentials for the center of mass motion of the Rydberg atom. The range of validity of our analytical approach is discussed. Section 7.4 is dedicated to the center of mass dynamics within the adiabatic potential surfaces. The question how the center of mass state of a ground state atom is altered due to its short-time excitation to a Rydberg state is illuminated in Section 7.5. A heating rate associated with this process is derived. In Section 7.6, the effect of the same process on the purity of the density matrix of a qubit which is encoded in the hyperfine states of a ground state atom is discussed.

The results presented in this chapter are published in Refs. [110, 111].

7.1 Hamiltonian

Along the lines of Chapter 3 we model the mutual interaction of the highly excited valence electron and the remaining closed-shell ionic core of an alkali Rydberg atom by an effective potential which is assumed to depend only on the distance of the two particles. In the previous chapter, this potential could be considered to be purely Coulombic since solely circular states with maximum electronic angular momentum were investigated. The low angular momentum states of alkali atoms, on the other hand, significantly differ from the hydrogenic ones because of the finite size and the electronic structure of the ionic core. The resulting core penetration, scattering, and polarization effects can be accounted for by employing a model potential of the form

$$V(r) \equiv V_l(r) = -\frac{Z_l(r)}{r} - \frac{\alpha_c}{2r^4}\left[1 - e^{-(r/r_c)^6}\right]$$

where $Z(r)$ is an effective radial charge and α_c the static dipole polarizability of the positive-ion core, see Section 3.1 and Eqs. (3.8) for more details.

The coupling of the charged particles to the external magnetic field is introduced via the minimal coupling, $\mathbf{p}_i \to \mathbf{p}_i - q_i\mathbf{A}(\mathbf{r}_i)$, with $i \in \{e, c\}$ denoting the valence electron and the remaining ionic core of a Rydberg atom, respectively; q_i is the charge of the i-th particle and $\mathbf{A}(\mathbf{x})$ is the vector potential belonging to the magnetic field $\mathbf{B}(\mathbf{x})$. Including the coupling of the magnetic moments to the external field ($\boldsymbol{\mu}_e$ and $\boldsymbol{\mu}_c$ originate from the electronic and nuclear spin, respectively), our initial Hamiltonian in the laboratory frame reads (employing $q_e = -1$, $q_c = 1$)

$$H = \frac{1}{2}[\mathbf{p}_e + \mathbf{A}(\mathbf{r}_e)]^2 + \frac{1}{2M}[\mathbf{p}_c - \mathbf{A}(\mathbf{r}_c)]^2 + V_l(r) + V_{so}(\mathbf{L}, \mathbf{S}) - \boldsymbol{\mu}_e \cdot \mathbf{B}(\mathbf{r}_e) - \boldsymbol{\mu}_c \cdot \mathbf{B}(\mathbf{r}_c)$$

with $r = |\mathbf{r}_e - \mathbf{r}_c|$ and M being the mass of the ionic core, cf. Eq.(3.2). As pointed out already in Chapter 2 and in contrast to our previous studies of high angular momentum states, one has to take the fine structure of the atomic energy levels into account: For the magnetic field strengths investigated in this work, the spin-orbit interaction will lead to splittings larger than any Zeeman splitting encountered; it is given by

$$V_{so}(\mathbf{L}, \mathbf{S}) = \frac{\alpha^2}{2}\left[1 - \frac{\alpha^2}{2}V_l(r)\right]^{-2}\frac{1}{r}\frac{\mathrm{d}V_l(r)}{\mathrm{d}r}\mathbf{L} \cdot \mathbf{S} \tag{7.1}$$

where $\mathbf{L}$ and $\mathbf{S}$ denote the angular momentum and spin of the valence electron, respectively. The term $[1 - \alpha^2 V_l(r)/2]^{-2}$ has been introduced to regularize the nonphysical divergence near the origin, see Section 3.1 for more details. As usual, we will label the field-free electronic eigenstates by the total electronic angular momentum $\mathbf{J} = \mathbf{L} + \mathbf{S}$. We remark that the model potential $V_l(r)$ has been developed ignoring the fine structure; let us therefore briefly comment on the accuracy of Eq. (7.1) in reproducing the fine structure intervals. For the $40P$ state of rubidium, our approach yields a fine structure splitting of 1.641 GHz, which is in good agreement with the measured value of 1.649 GHz, cf. Eq. (2.5). This accuracy decreases for higher angular momenta; for the $40D$ state a qualitative agreement between the calculated value (586 MHz) and the measured one (187 MHz) is found.

The Ioffe-Pritchard field configuration is given by $\mathbf{B}(\mathbf{x}) = \mathbf{B}_c + \mathbf{B}_l(\mathbf{x})$ with $\mathbf{B}_c = B\mathbf{e}_3$, $\mathbf{B}_l(\mathbf{x}) = G\,[x_1\mathbf{e}_1 - x_2\mathbf{e}_2]$ and the vector potential reads $\mathbf{A}(\mathbf{x}) = \mathbf{A}_c(\mathbf{x}) + \mathbf{A}_l(\mathbf{x})$ with $\mathbf{A}_c(\mathbf{x}) =$

$\frac{B}{2}[x_1\mathbf{e}_2 - x_2\mathbf{e}_1]$ and $\mathbf{A}_l(\mathbf{x}) = Gx_1x_2\mathbf{e}_3$, where B and G are the Ioffe field strength and the gradient, respectively. After introducing relative and center of mass coordinates ($\mathbf{r}$ and $\mathbf{R}$) and employing the unitary transformation $U = \exp\left\{\frac{i}{2}(\mathbf{B}_c \times \mathbf{r}) \cdot \mathbf{R}\right\}$, the Hamiltonian describing the Rydberg atom becomes[1]

$$\begin{aligned} U^\dagger H U = \frac{\mathbf{P}^2}{2M} + H_A + \tfrac{1}{2}[\mathbf{L} + 2\mathbf{S}] \cdot \mathbf{B}_c - \boldsymbol{\mu}_e \cdot \mathbf{B}_l(\mathbf{R}+\mathbf{r}) - \boldsymbol{\mu}_c \cdot \mathbf{B}(\mathbf{R}) \\ + \mathbf{A}_l(\mathbf{R}+\mathbf{r}) \cdot \mathbf{p} + \tfrac{1}{2}\mathbf{A}_c(\mathbf{r})^2 + H_{\mathrm{corr}}\,. \end{aligned} \tag{7.2}$$

Here, $H_A = \mathbf{p}^2/2 + V_l(r) + V_{so}(\mathbf{L},\mathbf{S})$ is the Hamiltonian of an alkali atom possessing the energies $E^{el}_{nlj} = -\frac{1}{2}(n-\delta_{nlj})^{-2}$. $H_{\mathrm{corr}} = \frac{1}{2}\mathbf{A}_l(\mathbf{R}+\mathbf{r})^2 + \frac{1}{M}\mathbf{B}_c\cdot(\mathbf{r}\times\mathbf{P}) + U^\dagger[V_l(r)+V_{so}(\mathbf{L},\mathbf{S})]U - [V_l(r)+V_{so}(\mathbf{L},\mathbf{S})]$ are small corrections which can be neglected because of the following reasons: In the parameter regime we are focusing on, the diamagnetic contribution of the gradient field, $\mathbf{A}_l(\mathbf{R}+\mathbf{r})^2$, is small compared to the one of the constant Ioffe field, $\mathbf{A}_c(\mathbf{r})^2$. The second contribution of H_{corr} is negligible within our adiabatic approach since $\langle\mathbf{P}/M\rangle$ becomes negligible for ultracold temperatures compared to the relative motion $\langle\mathbf{p}/m\rangle$. Finally, the remaining terms couple to remote electronic states only and are therefore irrelevant, cf. Section 3.3.

The magnetic moments of the particles are connected to the electronic spin $\mathbf{S}$ and the nuclear spin $\mathbf{I}$ according to $\boldsymbol{\mu}_e = -\mathbf{S}$ and $\boldsymbol{\mu}_c = -\frac{1}{2}g_I\mathbf{I}$, with g_I being the nuclear g-factor; because of the large nuclear mass and the resulting small nuclear magnetic moment, the term involving $\boldsymbol{\mu}_c$ is neglected in the following. We remark that the Z-component of the center of mass momentum commutes with Hamiltonian (7.2); hence the longitudinal motion can be integrated out by employing plane waves $|K_Z\rangle = \exp(-iK_Z Z)$. In order to solve the remaining coupled Schrödinger equation, we employ a Born-Oppenheimer separation of the center motion and the electronic degrees of freedom by projecting Eq. (7.2) on the electronic eigenfunctions $\psi_\kappa(\mathbf{r};\mathbf{R})$ that parametrically depend on the center of mass coordinates. We are thereby led to a set of decoupled differential equations governing the adiabatic center of mass motion within the individual two-dimensional energy surfaces $E_\kappa(\mathbf{R})$, i.e., the surfaces $E_\kappa(\mathbf{R})$ serve as potentials for the center of mass dynamics of the atom. The non-adiabatic (off-diagonal) coupling terms ΔT that arise within this procedure in the kinetic energy term can be neglected in our parameter regime since they are suppressed by the splitting between adjacent energy surfaces, cf. Eq. (3.25). As will be shown in Section 7.2, the latter is proportional to the Ioffe field strength B, i.e., the non-adiabatic couplings are proportional to powers of $1/B$. For a more detailed description of the adiabatic approach, we refer the reader to Section 3.4.

The electronic eigenfunctions and energies are found by the basis set method discussed in Chapter 5 of this thesis. It utilizes the field-free eigenfunctions $|\kappa\rangle = |njm_jls\rangle$ of H_A whose spin and angular parts $|jm_jls\rangle$ are given by the spin-orbit coupled generalized spherical harmonics $\mathcal{Y}_{j,m_j,l}$. For the radial degree of freedom, a discrete variable representation (DVR) based on generalized Laguerre polynomials is employed. The latter provides a non-uniform grid for the radial coordinate which is more dense close to the origin and hence especially suited for representing radial Rydberg wave functions. Since in the DVR scheme the potential matrix element evaluation is equivalent to a Gaussian quadrature rule, representing the Hamiltonian (7.2) – especially $V_l(r)$ and the derivative terms arising from the momentum

[1] see Chapter 3 for a thorough derivation

operator $\mathbf{p}$ – becomes particularly efficient. The numerical diagonalization of the resulting Hamiltonian matrix (in the limit $\mathbf{P} \to 0$) then yields the electronic eigenfunctions $\psi_\kappa(\mathbf{r};\mathbf{R})$ and energies $E_\kappa(\mathbf{R})$ which both parametrically depend on the center of mass coordinates $\mathbf{R}$. Convergence is ensured by appropriately choosing the size of the field-free basis as well as the underlying DVR grid size.

7.2 Analytical Approach

While the above described numerical treatment of the electronic Hamiltonian offers accurate results, the analytical but approximate expressions for the adiabatic energy surfaces derived in Chapter 4 are able to provide us with a profound understanding of the underlying physics. In this section, we summarize the findings of Chapter 4 specifically for the low angular momentum Rydberg states of ^{87}Rb.

For our analytical approach, we only consider a single fine structure manifold, i.e., fixed total angular momentum j for given l. Such an assumption is motivated by the fact that the fine structure dominates over the Zeeman splitting for the field strengths we are interested in. Figure 7.1 visualizes this specific situation along with the hierarchy of the various interactions encountered for our system. As derived in Chapter 4, within a given j-manifold the electronic part of Hamiltonian (7.2) can be approximated by

$$H_r = H_A + \frac{1}{2}\left[\mathbf{L} + 2\mathbf{S}\right] \cdot \mathbf{B}(\mathbf{R}) + H' + H'' \,. \tag{7.3}$$

with $H' = GXYp_z$ and $H'' = \mathbf{A}_l(\mathbf{r}) \cdot \mathbf{p} + \mathbf{B}_l(\mathbf{r}) \cdot \mathbf{S} + \frac{1}{2}\mathbf{A}_c(\mathbf{r})^2$. The latter contribution only depends on the relative coordinate and – as we will show later – for a wide range of field strengths can approximately be regarded as a mere energy offset to the electronic energy surfaces; we will restrict ourselves to this regime and hence omit H'' in the following.

The first two terms of Hamiltonian (7.3) can be diagonalized analytically by applying the spatially dependent transformation

$$U_r = e^{-i\gamma(L_x+S_x)} e^{-i\beta(L_y+S_y)}$$

that rotates the local magnetic field vector at each point in space into the z-direction of the laboratory frame of reference. γ and β denote the rotation angles as given in Eqs. (4.14). The transformed Hamiltonian becomes

$$U_r H_r U_r^\dagger = H_A + \tfrac{1}{2} g_j J_z \sqrt{B^2 + G^2(X^2+Y^2)} + U_r H' U_r^\dagger \tag{7.4}$$

with $g_j = \frac{3}{2} + \frac{s(s+1)-l(l+1)}{2j(j+1)}$ and $U_r H_A U_r^\dagger = H_A$; see Section 4.3 for a thorough derivation. Like for ground state atoms, the second term of Eq. (7.4) represents the coupling of a point-like particle to the magnetic field via its magnetic moment $\boldsymbol{\mu} = \frac{1}{2}\mathbf{L} + \mathbf{S}$.

As depicted in Fig. 7.1, H' only couples to different n, l, and j and hence vanishes within one j-manifold. The first two terms of Eq. (7.4), on the other hand, are diagonal, giving rise to the electronic potential energy surface

$$E_\kappa^{(0)}(\mathbf{R}) = E_\kappa^{el} + \tfrac{1}{2} g_j m_j \sqrt{B^2 + G^2(X^2+Y^2)} \tag{7.5}$$

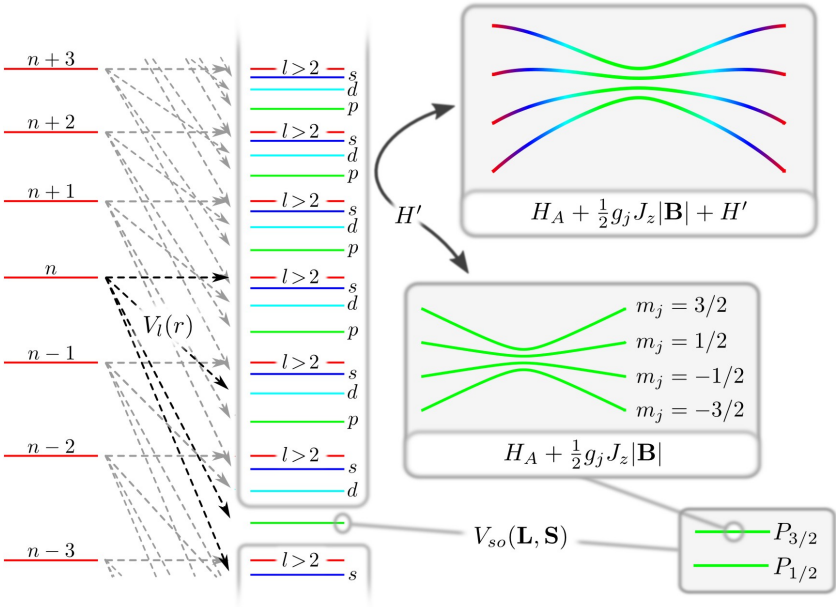

Figure 7.1: Schematic overview of the energy scales and coupling terms involved. Starting from the degenerate Hydrogen energy spectrum on the left, it is shown how the quantum defect – modeled by the potential $V_l(r)$ – separates the low angular momentum states. The spin-orbit coupling $V_{so}(\mathbf{L}, \mathbf{S})$ then yields the fine structure splitting for fixed l. Within a given j-manifold, the simplified Ioffe-Pritchard Hamiltonian $H_A + \frac{1}{2} g_j m_j |\mathbf{B}|$ resembles the coupling of a point-like particle to the magnetic field $\mathbf{B}(\mathbf{R})$. The two-body character of the Rydberg atom, which is represented by H', only contributes if energetically remote levels are considered as well: it admixes states of different n, l, j, and m_j thereby qualitatively changing the shape of the surfaces.

for a given electronic state $|\kappa\rangle = |n j m_j l s\rangle$. Note that such a state refers to the *rotated* frame of reference. Only there, m_j constitutes a good quantum number; in the laboratory frame of reference m_j is not conserved. The surfaces Eq. (7.5) are rotationally symmetric around the Z-axis and confining for $m_j > 0$. For small radii ($\rho = \sqrt{X^2 + Y^2} \ll B/G$) an expansion up to second order yields a harmonic potential

$$E_\kappa^{(0)}(\rho) \approx E_\kappa^{el} + \tfrac{1}{2} g_j m_j B + \frac{1}{2} M \omega^2 \rho^2 \tag{7.6}$$

with the trap frequency defined by $\omega = G\sqrt{\frac{g_j m_j}{2MB}}$ while we find a linear behavior $E_\kappa^{(0)}(\rho) \approx E_\kappa^{el} + \frac{1}{2} g_j m_j G \rho$ when the center of mass is far from the Z-axis ($\rho \gg B/G$). In the harmonic part of the potential, the center of mass energies are thus given by

$$E_{\kappa,\nu}^{cm} = E_\kappa^{(0)}(0) + (\nu + 1)\omega \,, \; \nu = \nu_x + \nu_y \in \mathbb{N}$$

with a splitting of ω between adjacent center of mass eigenstates; see Section 7.4 for a more detailed discussion. The separation between adjacent electronic energy surfaces at the origin, on the other hand, is given by $\Delta E_\kappa = \frac{1}{2} g_j B$. The size of the center of mass ground state ($\nu = 0$) in such a harmonic potential evaluates to $\langle \rho \rangle = \sqrt{\pi}/2\sqrt{M\omega}$ [65].

Table 7.1: Coefficients of the linear fit of $C_i(n) = C_i^{(0)} + C_i^{(1)} n$ in the range $35 \leq n \leq 45$ for the nS, nP, and nD states of the ^{87}Rb atom. Note that negative magnetic quantum numbers m_j yield the same results as their positive counterparts and are consequently omitted. The fitted C_i are calculated using Eq. (7.8) with $n' \in [n-10, n+10]$.

State	$C_x^{(0)}$	$C_x^{(1)}$	$C_z^{(0)}$	$C_z^{(1)}$
$S_{1/2}, m_j = 1/2$	-0.4813	-0.00027	-0.4813	-0.00027
$P_{1/2}, m_j = 1/2$	-0.4484	-0.00148	-0.4484	-0.00148
$P_{3/2}, m_j = 1/2$	-0.4541	-0.00152	-0.4316	-0.00164
$P_{3/2}, m_j = 3/2$	-0.4391	-0.00160	-0.4616	-0.00149
$D_{3/2}, m_j = 1/2$	-0.4570	-0.00069	-0.4326	-0.00011
$D_{3/2}, m_j = 3/2$	-0.4407	-0.00030	-0.4652	-0.00088
$D_{5/2}, m_j = 1/2$	-0.4570	-0.00073	-0.4287	-0.00006
$D_{5/2}, m_j = 3/2$	-0.4500	-0.00057	-0.4429	-0.00040
$D_{5/2}, m_j = 5/2$	-0.4358	-0.00023	-0.4712	-0.00107

Perturbation Theory for H'

The remaining term $U_r H' U_r^\dagger$ of Hamiltonian (7.4) can be treated perturbatively. While it vanishes in first order, second order perturbation theory yields[2]

$$\begin{aligned} E_\kappa^{(2)}(\mathbf{R}) &= G^2 X^2 Y^2 \sum_{\kappa' \neq \kappa} \frac{\left|\langle \kappa | U_r p_z U_r^\dagger | \kappa' \rangle\right|^2}{E_\kappa^{el} - E_{\kappa'}^{el}} \\ &\approx C_z G^2 X^2 Y^2 \Big[1 + \frac{C_x - C_z}{C_z} \left(\sin^2\beta + \sin^2\gamma \cos^2\beta \right) \Big] . \end{aligned} \tag{7.7}$$

Since $E_\kappa^{(0)}(\mathbf{R})$ resembles the confinement of a ground state atom, we attribute $E_\kappa^{(2)}(\mathbf{R})$ to the composite nature of the Rydberg atom, i.e., the fact that it consists of a Rydberg electron far apart from its ionic core. Like the magnetic field itself, $E_\kappa^{(2)}(\mathbf{R})$ shows no continuous azimuthal symmetry but rather a discrete one. This can be understood as follows. In the absence of H', the atomic orbitals and hence the magnetic moments align perfectly with the magnetic field vector. The inclusion of H' admixes different angular momentum states such that the relative angles between the involved atomic orbitals and the magnetic field direction matters. The contribution $E_\kappa^{(2)}(\mathbf{R})$ consequently reflects the discrete azimuthal symmetry of the vector field $\mathbf{B}(\mathbf{R})$ rather than the continuous one of its magnitude $|\mathbf{B}(\mathbf{R})|$. The parameters C_i are calculated via

$$C_i = \sum_{\kappa' \neq \kappa} (E_\kappa^{el} - E_{\kappa'}^{el}) |\langle \kappa | x_i | \kappa' \rangle|^2 \tag{7.8}$$

and obey $C_x = C_y$ in general as well as $C_x = C_y = C_z \equiv C$ more specifically for $l = 0$. Note that the parameters C_i depend on the state κ under investigation.

Since $E_\kappa^{el} - E_{\kappa'}^{el} \propto n^{-3}$ and $|\langle \kappa | x_i | \kappa' \rangle|^2 \propto n^4$, a linear scaling of $E_\kappa^{(2)}(\mathbf{R})$ with the quantum number n is anticipated, i.e., $C_i(n) = C_i^{(0)} + C_i^{(1)} n$. Resulting from a fit of calculated C_i

[2] see Section 4.4 for more details.

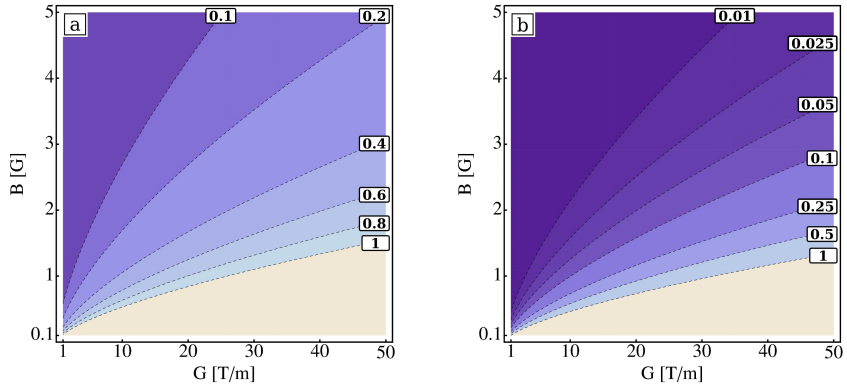

Figure 7.2: Range of validity for deriving Eq. (7.11). (a) $2G^2X^2/B^2 \ll 1$ resulting in $X \ll B/\sqrt{2}G$. In the figure, the value $X_+/(B/\sqrt{2}G)$ is shown which should be $\ll 1$. Figure (b) shows $G^2X_0^2/B^2$ which should be $\ll 1$ as well. In both cases $l = 2, j = m_j = 5/2$ is used.

values within the range $35 \leq n \leq 45$, in Tab. 7.1 the coefficients $C_i^{(j)}$ are tabulated for the nS, nP, and nD states of the ^{87}Rb atom. All considered states show a similar behavior: The magnitude of C_i is close to $-1/2$ and shows a rather weak n-dependence. In particular, $C_x \approx C_z$ and therefore

$$E_\kappa^{(2)}(\mathbf{R}) \approx C_z \cdot G^2X^2Y^2\,. \tag{7.9}$$

We remark that for smaller n $C_i(n)$ deviates from the linear behavior in favor of a more rapid decrease.

Final Surfaces

In the last part of this section, let us reconsider the adiabatic energy surfaces for the center of mass motion, including now the contribution of $U_r H' U_r^\dagger$. That is, we investigate the approximate, but analytical solutions

$$E_\kappa(\mathbf{R}) \equiv E_\kappa^{(0)}(\mathbf{R}) + E_\kappa^{(2)}(\mathbf{R}) - E_\kappa^{el}, \tag{7.10}$$

of Hamiltonian (7.3). In particular, we concentrate on the diagonal of the surfaces ($X = Y$) where $E_\kappa^{(2)}(\mathbf{R})$ is maximal. The approximation $C_x = C_z$ (which is exact for $nS_{1/2}$ states) then yields

$$E_\kappa(X = Y) = \frac{1}{2} g_j m_j \sqrt{B^2 + 2G^2X^2} + C_z G^2 X^4\,,$$

which shows only a *local* minimum at the origin since the surface drops off for large center of mass coordinates when $E_\kappa^{(2)}(\mathbf{R})$ dominates (note that $C_z < 0$), see also Fig. 7.3. The positions of the maxima which enclose the minimum are approximately given by

$$X_\pm \approx \pm\left(\frac{G^2}{B^2} - \frac{4BC_z}{g_j m_j}\right)^{-1/2} \approx \pm X_0\left(1 - \frac{G^2}{2B^2}X_0^2\right) \tag{7.11}$$

with the length scale $X_0 = \sqrt{\frac{g_j m_j}{4B|C_z|}}$ only depending on the Ioffe field strength. The depth of the potential well associated with the minimum correspondingly evaluates to

$$\begin{aligned}\Delta E_\kappa &= E_\kappa(X = Y = X_+) - E_\kappa(0) \\ &\approx \frac{1}{2} g_j m_j \frac{G^2 X_0^2}{B} \left(1 - \frac{G^2 X_0^2}{B^2})\right) + C_z G^2 X_0^4 \left(1 - 2\frac{G^2 X_0^2}{B^2}\right).\end{aligned} \tag{7.12}$$

Note that the first approximation in Eq. (7.11) holds for $2G^2X^2/B^2 \ll 1$ and the second one for $G^2X_0^2/B^2 \ll 1$. The corresponding range of validity is illustrated in Fig. 7.2: For a Ioffe field strength of $B = 1\,\mathrm{G}$, the above approximations hold for gradients up to $10\,\mathrm{Tm}^{-1}$; at higher B even larger gradients are eligible.

7.3 Trapping Potentials

In this section we are going to discuss the calculated electronic potential energy surfaces for the nS, nP, and nD states of the ^{87}Rb atom in detail. In particular, the range of validity of the above derived analytic expression Eq. (7.10) is demonstrated. As a general example, we address in the following the magnetic field configuration $B = 1\,\mathrm{G}$, $G = 2.5\,\mathrm{Tm}^{-1}$, which yields a trap frequency of $\omega = 2\pi \times 319$ Hz. A similar field configuration is also found in current experiments [112].

In Figure 7.3 the electronic potential energy surfaces $E_\kappa(\mathbf{R})$ of the $40S_{1/2}$, $40P_{1/2}$, $40P_{3/2}$, $40D_{3/2}$, and $40D_{5/2}$ states with $m_j = j$ are illustrated. In addition, also sections along $X = Y$ of these surfaces are provided. On a first glance, the energy surfaces originating from different electronic states seem to differ quite substantially. However, qualitatively they are very similar, as we are going to argue in the following. For all surfaces presented in Fig. 7.3, the contribution of the composite character of the Rydberg atom, i.e., $E_\kappa^{(2)}(\mathbf{R})$ changes the continuous azimuthal symmetry of $E_\kappa^{(0)}(\mathbf{R})$ into a four-fold one. Moreover, the interplay between the harmonic confinement $E_\kappa^{(0)}(\mathbf{R})$ and the unbounded contribution $E_\kappa^{(2)}(\mathbf{R})$ gives rise to a finite trap depth along the diagonal $X = Y$; see second row of Fig. 7.3. Since the coefficient C_z of $E_\kappa^{(2)}(\mathbf{R})$ is approximately of the same magnitude for all states considered, cf. Tab. 7.1, the shape of the resulting energy surface – and the trap depth in particular – is characterized by the magnitude of the magnetic moment $\boldsymbol{\mu} \propto g_j \mathbf{J}$ that couples to the magnetic field. Consequently, the $j = m_j = l + 1/2$ electronic states show a deeper confinement than their $j = m_j = l - 1/2$ counterparts and the depth increases further with increasing orbital angular momentum l.[3] For the examples given in Fig. 7.3 this means that the quadratic approximation to the trapping potential for the $40S_{1/2}$ state is already violated at about two oscillator energies, while for the $40D_{5/2}$ it is fine up to $10\,\omega$. This trend is confirmed in the third row of Fig. 7.3 where the depth of the potential as a function of the field configuration is displayed: For the $40D_{5/2}$ state, the trap depth easily exceeds $100\,\omega$ within the given parameter range, while in the case of the $40S_{1/2}$ state there is a substantial regime of field strengths where not a single center of mass state can be confined, i.e., the trap depth being $< 1\,\omega$. Nevertheless, also for the $40S_{1/2}$ Rydberg state the field parameters B and G can be adjusted such that stable trapping is possible, i.e., the trap depth being much larger than

[3] Of course, this argumentation only holds as long as the magnetic field configuration is fixed.

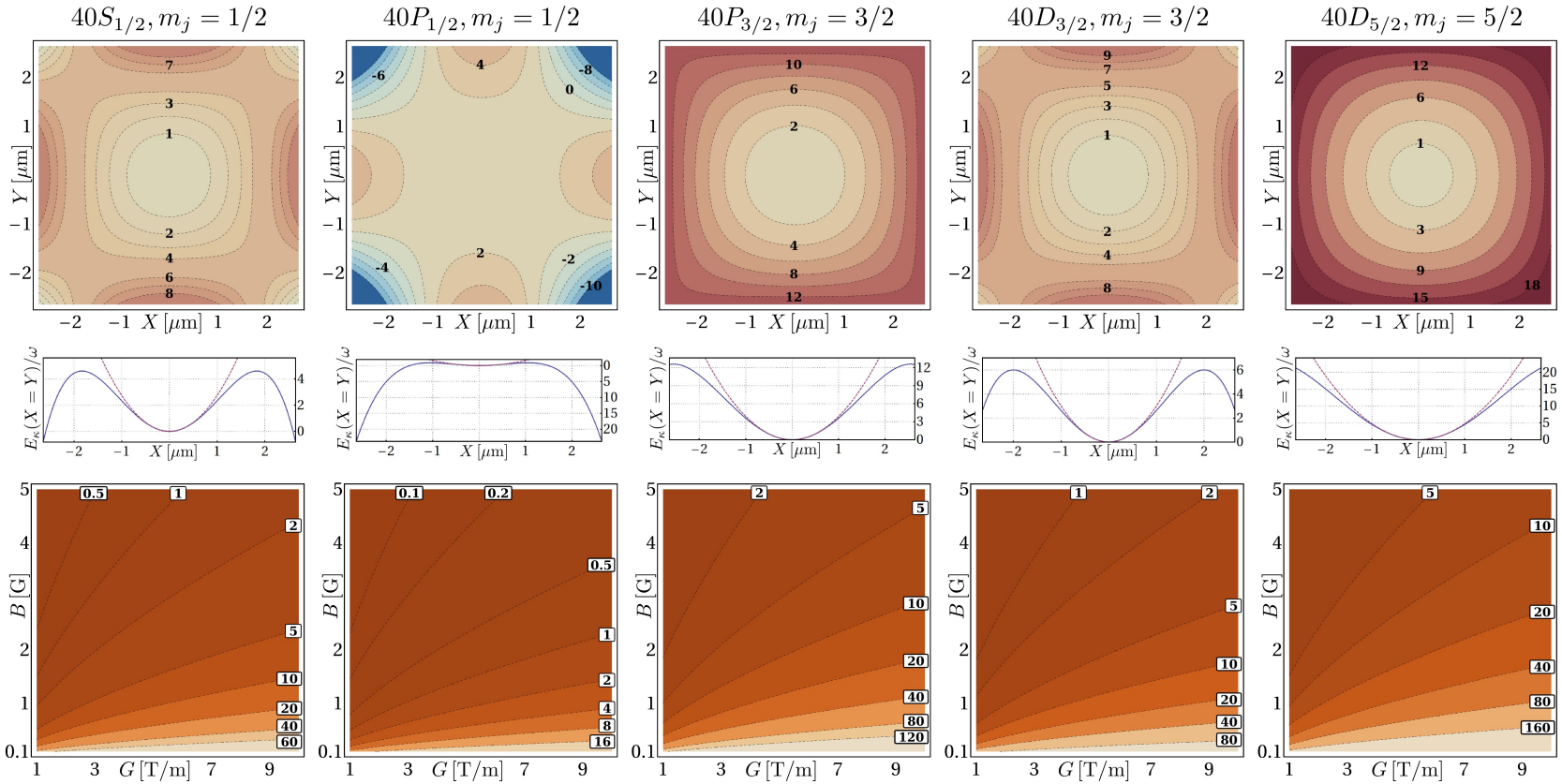

Figure 7.3: First Row: Contour plots of the electronic potential energy surfaces $E_\kappa(\mathbf{R})$ of the $40S_{1/2}$ (first column), $40P_{1/2}$ (second column), $40P_{3/2}$ (third column), $40D_{3/2}$ (fourth column), and $40D_{5/2}$ (fifth column) states with $m_j = j$ for the magnetic field configuration $B = 1\,\mathrm{G}$, $G = 2.5\,\mathrm{Tm}^{-1}$. Second Row: Section along $X = Y$ of the same energy surfaces; the contribution of $E_\kappa^{(0)}(\mathbf{R})$ (dashed lines) is shown in addition. Third Row: Depth of the potentials as given by Eq. (7.12) as a function of the magnetic field configuration. For all subfigures, the energy scale is given in terms of the trap frequency $\omega = G\sqrt{g_j m_j/2MB}$.

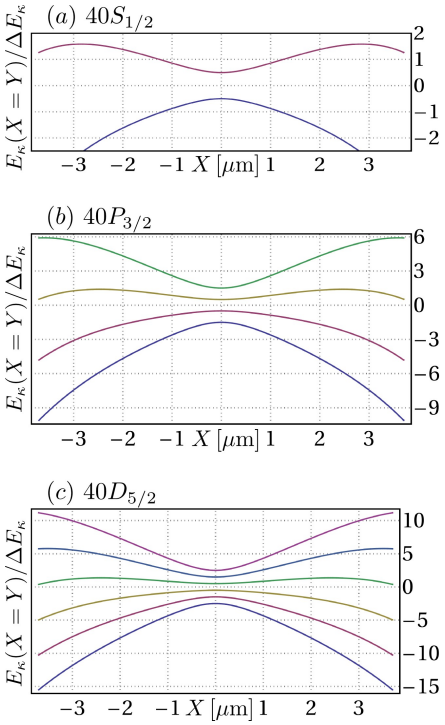

Figure 7.4: Sections along $X = Y$ of the energy surfaces of the (a) $40S_{1/2}$, (b) $40P_{3/2}$, and (c) $40D_{5/2}$ multiplets for the field configuration $B = 0.1\,\mathrm{G}$ and $G = 10\,\mathrm{Tm}^{-1}$, which yields a trap frequency of $\omega/\sqrt{g_j m_j} = 2\pi \times 4$ kHz.

the trap frequency. Similarly, the trapping potential of the $40D_{5/2}$ Rydberg state can be chosen very shallow by going to sufficiently strong Ioffe fields. We remark that the results presented in Fig. 7.3 are given in units of the trap frequency $\omega = G\sqrt{g_j m_j/2MB}$; the latter is, of course, only exact near the origin. For larger radii, the contribution $E_\kappa^{(2)}(\mathbf{R})$ flattens the potential resulting in smaller trap frequency and hence in a higher number of center of mass states that can be confined.

As can be deduced from the third row of Fig. 7.3, increasing the relative strength of the field gradient, i.e., either increasing G directly or decreasing the offset field B for fixed G, leads to a larger number of bound center of mass states – independently of the state under consideration. However, since the anti-trapping contribution $E_\kappa^{(2)}(\mathbf{R})$ quadratically increases with the field gradient G, we expect this trend to reverse for sufficiently high gradients. Indeed, for a Ioffe field of $B = 1\,\mathrm{G}$ the trap depth starts to decrease for field gradients $G \gtrsim 200\,\mathrm{Tm}^{-1}$; for $B = 0.1\,\mathrm{G}$ this trend already starts at $G \gtrsim 5\,\mathrm{Tm}^{-1}$. Similarly, for a fixed field gradient together with a decreasing offset field B we find a decrease of the trap depth if $B \lesssim 0.15\,\mathrm{G}$ or $B \lesssim 0.03\,\mathrm{G}$ for $G = 10\,\mathrm{Tm}^{-1}$ and $G = 1\,\mathrm{Tm}^{-1}$, respectively.

Let us now investigate the question if electronic energy surfaces belonging to different states intersect each other. In Chapter 6 and Refs. [64, 65], where high angular momentum states are considered, this issue is essential: there, the high level of degeneracy of the system leads to non-adiabatic crossings of the surfaces. As a consequence, only the circular electronic state ($m_l = l = n - 1$) provides stable trapping. For the low angular momentum states of

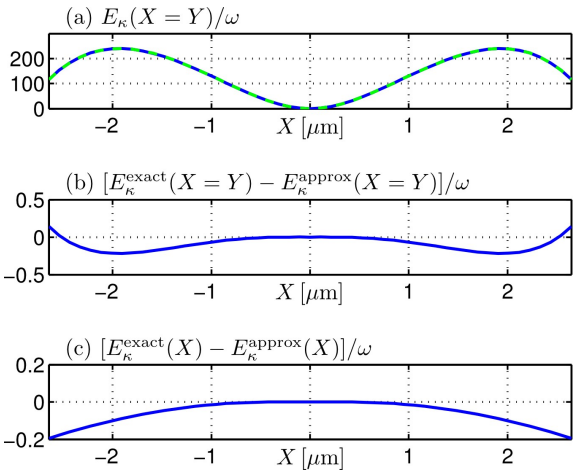

Figure 7.5: (a) Section along $X = Y$ of the energy surface of the $40D_{5/2}, m_j = 5/2$ state for the field configuration $B = 1\,\mathrm{G}$ and $G = 100\,\mathrm{Tm}^{-1}$ which yields a trap frequency of $\omega = 2\pi \times 22.1$ kHz near the origin. The solid line is obtained by the numerical diagonalization of Hamiltonian (7.2), the dashed one by Eq. (7.10). The surfaces have been offset to zero at the origin. (b) Difference (in terms of the trap frequency ω) between the analytic expression Eq. (7.10) and the result of the numerical diagonalization of Hamiltonian (7.2). (c) Same as (b) but for $Y = 0$ rather than $X = Y$.

^{87}Rb we are considering here, however, the fine structure splitting for different j and the varying quantum defect for different l separate the energy surfaces by lifting the degeneracy, therefore preventing their crossing. As a result, it is sufficient in our case to investigate the energy surface spectrum for fixed j, i.e., only as a function of the magnetic quantum number m_j. In Figure 7.4, sections along the diagonal of the energy surfaces of the multiplets of the $40S_{1/2}$, $40P_{3/2}$, and $40D_{5/2}$ states are presented. In order to show a strong spatial dependence, we chose an extreme case concerning the ratio of the Ioffe field compared to the gradient field, namely, $B = 0.1\,\mathrm{G}$, $G = 10\,\mathrm{Tm}^{-1}$ (of course, much higher gradients can be achieved on atom chips). Even for such a high gradient, the energy surfaces remain well separated with a minimum distance of $\frac{1}{2}g_j B$ at the trap center. Hence, each surface can be considered separately for trapping and our adiabatic approach is not limited by non-adiabatic interactions. Note that the anti-trapping of $m_j < 0$ states is even enhanced by the contribution $E_\kappa^{(2)}(\mathbf{R})$.

The above investigations employ the analytical expression Eq. (7.10) rather than the exact numerical solutions of Hamiltonian (7.2). Hence an estimation of the range of validity of our results is necessary. To this end, we provide in Fig. 7.5(a) a comparison between the analytical expression according to Eq. (7.10) and the numerical diagonalization of Hamiltonian (7.2) for the extreme field configuration of $B = 1\,\mathrm{G}$, $G = 100\,\mathrm{Tm}^{-1}$ (the quantitative agreement improves for smaller gradients / larger Ioffe fields). As one can observe, even for such a strong gradient Eq. (7.10) yields satisfactory results: The deviation within the spatial range considered is less than $0.2\,\omega$, cf. Fig. 7.5(b), ω being the splitting of the center of mass states and representing the smallest energy scale of the system. We remark that Fig. 7.5(b) shows results along the diagonals $X = Y$ of the surfaces where the deviation is at maximum. However, even along the axes, where $E_\kappa^{(2)}(\mathbf{R})$ vanishes, a perfect agreement cannot be found, cf. Fig. 7.5(c). This residual deviation is due to the purely electronic terms H'' of Hamiltonian

Table 7.2: Parameters for determining the radiative lifetime $\tau = \tau'(n-\delta_\kappa)^\gamma$ of low angular momentum Rydberg states. Adapted from Ref. [75]. The quantum defect δ can be determined using Eq. (2.3) and the parameters provided in Tab. 2.2.

l	τ' [ns]	γ
0	1.43	2.94
1	2.76	3.02
2	2.09	2.85

(7.2) that have been neglected in deriving Eq. (7.10). Although H'' does not explicitly depend on the center of mass coordinate $\mathbf{R}$, it introduces an implicit center of mass dependence by changing the electronic state. This can be easily understood in the rotated frame of reference, i.e., after applying the unitary transformation U_r: There, one has to consider $U_r H'' U_r^\dagger$ which introduces a center of mass dependence explicitly. We stress that for gradients weaker and/or Ioffe fields stronger than in Fig. 7.5, U_r is closer to unity and therefore the contribution of H'' becomes even less important in these cases and hence can be neglected.

7.4 Center of Mass Wave Functions

In the previous section, we determined the adiabatic electronic surfaces that arise for low angular momentum Rydberg atoms in a Ioffe-Pritchard trap. Within our adiabatic approach, these surfaces serve as trapping potentials for the center of mass motion of the Rydberg atom, cf. Section 3.4. In this section, we use the previously calculated potentials $E_\kappa(\mathbf{R})$ to determine the eigenfunctions $\chi(\mathbf{R})$ of the center of mass Hamiltonian

$$H_{cm} = \frac{\mathbf{P}^2}{2M} + E_\kappa(\mathbf{R})\,. \tag{7.13}$$

In particular, we are going to elucidate the differences to the harmonic oscillator eigenstates that are obtained by considering solely the 'unperturbed' potential $E_\kappa^{(0)}(\mathbf{R})$ [throughout this section, the harmonic approximation Eq. (7.6) for the potential $E_\kappa^{(0)}(\mathbf{R})$ is assumed]. The energies and eigenstates are computed using second order perturbation theory. We remark that the validity of the harmonic approximation together with the use of perturbation theory has been ensured by comparing with the results obtained by the numerical diagonalization of Hamiltonian (7.13).

Before presenting our results, let us comment on the issue of the finite radiative lifetime of Rydberg atoms that might spoil the experimental observation of the center of mass motion. The lifetime of Rydberg atoms in low angular momentum electronic states can be parameterized as $\tau = \tau'(n-\delta_\kappa)^\gamma$; actual values of τ' and γ for the ^{87}Rb atom are listed in Tab. 7.2, see also Section 2.2. For the $40S_{1/2}$ Rydberg state, this yields a radiative lifetime of $\tau = 58\,\mu$s. If we compare this to the typical time scale $\tau_\omega = 2\pi/\omega$ of the center of mass motion, one finds that for the envisaged field configuration ($B = 1\,\mathrm{G}$, $G = 2.5\,\mathrm{Tm}^{-1}$) $\tau_\omega = 3\,$ms is orders of magnitudes larger than the radiative lifetime which renders the resolution of the center of mass motion experimentally impossible. This drawback can be alleviated by several means. First of all, one can consider higher principal quantum numbers n which increases the life-

Table 7.3: Character table for the symmetry group $\boldsymbol{C}_{4v}$. For our system, the principal (4-fold) rotation axis is the Z-axis. The symmetry elements are as follows: We have the rotations C_{2Z}, C_{4Z}, and C_{4Z}^3 corresponding to a rotation through $\pi/2$, $\pi/4$, and $3\pi/4$ radians about the Z-axis, respectively. The latter two belong to the same symmetry class and are summarized as $2C_4$ in the table below. In addition to the rotational symmetry operations, we have two *vertical* mirror planes that contain the principal axis, namely, the XZ and the YZ planes. Both belong to the same reflection symmetry class, denoted as $2\sigma_v$ below. Besides the vertical mirror planes, we also have *dihedral* (diagonal) ones that contain the principal axis and bisect two σ_v or C_2 symmetry elements. Here, they bisect the two σ_v planes, i.e., they are defined by the diagonals $X = Y$ and $X = -Y$, respectively, in conjunction with the Z-axis. They are labeled as $2\sigma_d$. Finally, there is the identity operation E whose character determines the dimensionality of the irreducible representation.

$\boldsymbol{C}_{4v}$	E	C_2	$2C_4$	$2\sigma_v$	$2\sigma_d$
A_1	$+1$	$+1$	$+1$	$+1$	$+1$
A_2	$+1$	$+1$	$+1$	-1	-1
B_1	$+1$	-1	$+1$	$+1$	-1
B_2	$+1$	-1	$+1$	-1	$+1$
E	$+2$	0	-2	0	0

time substantially. For example, the $60S_{1/2}$ state already possesses a radiative lifetime of $\tau = 206\,\mu$s. The changes in the trapping potential, on the other hand, are marginal as can be seen from the weak n-dependence of the C_z coefficient, cf. Tab. 7.1; note that $E_\kappa^{(0)}(\mathbf{R})$ is n-independent. Additionally to increasing n, one can augment the trap frequency by increasing the gradient field and/or decreasing the Ioffe field.[4] As an example, the field configuration $B = 0.1\,\mathrm{G}$ and $G = 50\,\mathrm{Tm}^{-1}$ yields $\tau_\omega = 50\,\mu$s. Furthermore, one might also employ the $nP_{3/2}$ Rydberg states which possess a longer lifetime ($\tau = 155\,\mu$s and $\tau = 0.5$ ms for $n = 40$ and $n = 60$, respectively) and at the same time cause a higher trap frequency ($\tau_\omega = 2$ ms and $\tau_\omega = 35\,\mu$s for $B = 1\,\mathrm{G}$, $G = 2.5\,\mathrm{Tm}^{-1}$ and $B = 0.1\,\mathrm{G}$, $G = 50\,\mathrm{Tm}^{-1}$, respectively).

As an illustrative example, let us investigate again the $40S_{1/2}$ Rydberg state combined with the magnetic field parameters $B = 1$ G and $G = 2.5\,\mathrm{Tm}^{-1}$, despite the above mentioned restrictions. In this case, the resulting trapping potential $E_\kappa(\mathbf{R})$ confines only a very limited number of center of mass states, namely, twelve.[5] Consequently, already low center of mass excitations show an appreciable deviation from the harmonic behavior, which makes the influence of the perturbative effects of $E_\kappa^{(2)}(\mathbf{R})$ particularly visible. In Figure 7.6, the 3rd to 9th excited center of mass eigenstates of Hamiltonian (7.13) are illustrated using the potential $E_\kappa^{(0)}(\mathbf{R})$ (upper row) and $E_\kappa^{(0)}(\mathbf{R}) + E_\kappa^{(2)}(\mathbf{R})$ (lower row), respectively. For the case of $E_\kappa^{(0)}(\mathbf{R})$ and small radii $\rho = \sqrt{X^2 + Y^2}$ one yields a harmonic potential $\sim \frac{1}{2}M\omega^2\rho^2$. In this case, the Hamiltonian (7.13) decouples in X and Y, i.e., the total center of mass wave function can be written as a product of two independent harmonic oscillator states in X and Y:

$$\chi(\mathbf{R}) \equiv \chi_{\nu_x\nu_y}(\mathbf{R}) = \chi_{\nu_x}(X) \cdot \chi_{\nu_y}(Y)\,.$$

As a consequence, the corresponding energies only depend on the sum of the individual center of mass excitations $\nu = \nu_x + \nu_y$ and show a $\nu + 1$-fold degeneracy.

[4] Note that this might necessitate atom chip traps [83, 113].
[5] Throughout this section, κ stands for $n = 40$, $j = m_j = 1/2$, $l = 0$.

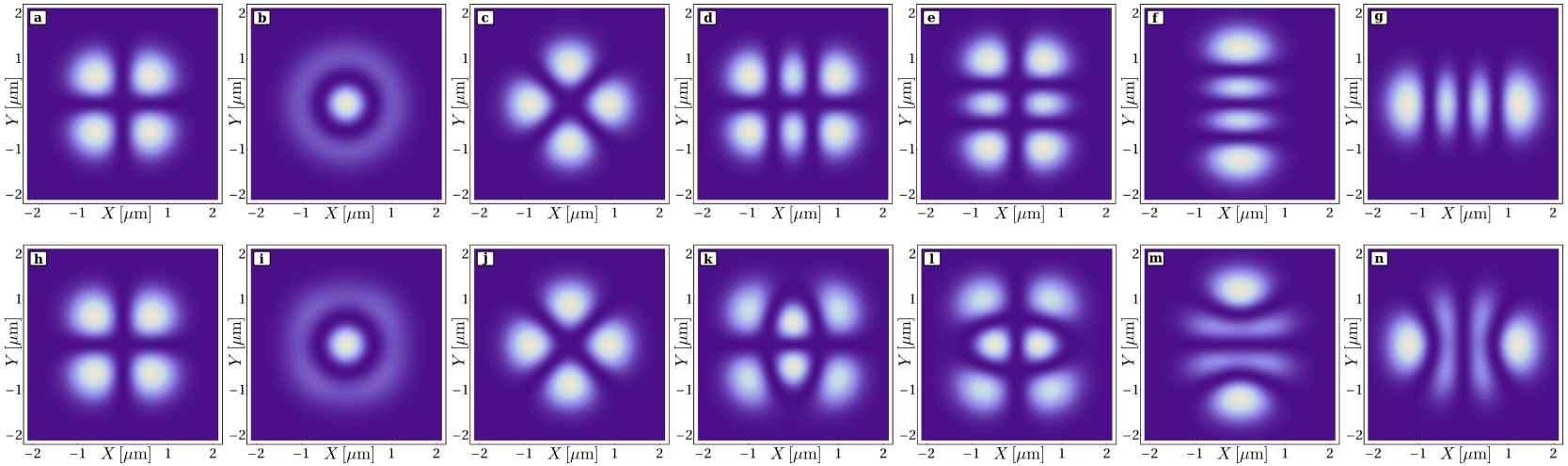

Figure 7.6: Probability density plots of the $\nu = 2$ [(a) – (c) and (h) – (j)] and $\nu = 3$ [(d) – (g) and (k) – (n)] center of mass wave functions. (h) – (n) The contribution of $E_\kappa^{(2)}(\mathbf{R})$ is included. (a) – (g) Only $E_\kappa^{(0)}(\mathbf{R})$ is considered. The electronic state is $40S_{1/2}$ and the magnetic field parameters are $B = 1\,\mathrm{G}$, $G = 2.5\,\mathrm{Tm}^{-1}$.

In anticipation of considering $E_\kappa^{(2)}(\mathbf{R})$ as well, it is advisable to employ adapted eigenstates that account for the $\boldsymbol{C}_{4v}$ symmetry of Hamiltonian (7.13) (including $E_\kappa^{(2)}(\mathbf{R})$, of course). Such symmetry adapted eigenstates are shown in Fig. 7.6. Their decomposition in terms of the product states $\chi_{\nu_x\nu_y}(\mathbf{R})$ can be found in the fourth column of Tab. 7.4 together with their corresponding symmetry label given in the second column. The character table for the $\boldsymbol{C}_{4v}$ symmetry group – along with the definition of the symmetry elements for our system – is reproduced in Tab. 7.3. Note that the symmetry adapted states are still degenerate in case of the harmonic potential $E_\kappa^{(0)}(\mathbf{R})$, cf. third column of Tab. 7.4. The inclusion of $E_\kappa^{(2)}(\mathbf{R})$ lifts this degeneracy by mixing states of equal symmetry according to the vanishing integral rule [114]: since $E_\kappa^{(2)}(\mathbf{R})$ is of A_1 symmetry, i.e., being totally symmetric the center of mass matrix element $\langle\chi'|E_\kappa^{(2)}|\chi\rangle$ is non-vanishing only if $|\chi\rangle$ and $|\chi'\rangle$ possess the same symmetry. Besides the symmetry constraints, the perturbation of the form $\sim X^2Y^2$ yields the selection rules $\Delta\nu_x \in \{0, \pm 2\}$ and $\Delta\nu_y \in \{0, \pm 2\}$.[6] Inspecting the wave functions as obtained by diagonalizing Hamiltonian (7.13) within a formerly degenerate ν-manifold, both the symmetry constraints as well as the selection rules become apparent; see sixth column of Tab. 7.4.

The energies $E_{\kappa,i}^{cm}$ of the first 12 eigenstates are tabulated in Tab. 7.4 for both potentials $E_\kappa^{(0)}(\mathbf{R})$ ("Harmonic Oscillator", third column) and $E_\kappa^{(0)}(\mathbf{R}) + E_\kappa^{(2)}(\mathbf{R})$ ("Perturbed", fifth column). While $E_\kappa^{(0)}(\mathbf{R})$ yields energies $E_\nu = (\nu+1)\omega$ with $\nu = 0, 1, 2, \ldots$[7], the eigenenergies belonging to $E_\kappa^{(0)}(\mathbf{R}) + E_\kappa^{(2)}(\mathbf{R})$ deviate from this rule: since the harmonic potential is flattened by the contribution $E_\kappa^{(2)}(\mathbf{R})$, the energies are below the harmonic ones. The remaining degeneracies which appear for odd ν (e.g., states 6–9) can be explained by the symmetry properties of the involved states: in such cases, only E symmetry is encountered. The two-dimensional irreducible representation of the latter then gives rise to the appearance of $(\nu + 1)/2$ degenerate pairs.

Finally, let us briefly comment on the issue of tunneling. States that are confined within the potentials shown in Section 7.3 may escape the trap by tunneling through the potential barrier along the diagonals. While this process most certainly plays no role for configurations where the time scale of the trap frequency is large compared to the radiative lifetime, *a priori* it is not clear if tunneling becomes crucial for tighter traps. For this reason, we estimated the lifetime associated with the tunneling process by investigating the transmission probability for the i^{th} excited center of mass state in one dimension,

$$P_t = \exp\left\{-2\int_a^b \sqrt{2M[E_\kappa(X=Y) - E_{\kappa,i}^{cm}]}\,\mathrm{d}X\right\}, \tag{7.14}$$

where the integration limits a and b are determined by the condition $E_\kappa(X = Y) = E_{\kappa,i}^{cm}$. Since the Rydberg atom 'hits' the potential barriers twice per trapping period, the loss rate can be roughly estimated by $2\omega P_t$. Actual values of P_t for the states discussed in this section

[6] Using the recurrence relation $X\,|\chi_{\nu_x}\rangle = \sqrt{\hbar/2M\omega}\,(\sqrt{\nu_x}\,|\chi_{\nu_x-1}\rangle + \sqrt{\nu_x+1}\,|\chi_{\nu_x+1}\rangle)$, we get

$$\langle\chi_{\nu_x}|X^2|\chi_{\nu_x'}\rangle = \frac{\hbar}{2M\omega}\left[\sqrt{\nu_x'(\nu_x'-1)}\,\delta_{\nu_x\nu_x'-2} + (2\nu_x'+1)\,\delta_{\nu_x\nu_x'} + \sqrt{(\nu_x'+1)(\nu_x'+2)}\,\delta_{\nu_x'\nu_x'+2}\right]$$

and analogously for the y-component of the two-dimensional harmonic oscillator.

[7] As mentioned before, we assume a perfectly harmonic potential $E_\kappa^{(0)}(\rho) \sim \frac{1}{2}M\omega^2\rho^2$.

Table 7.4: Properties of the center of mass states arising for the $40S_{1/2}$ Rydberg atom and the field configuration $B = 1$ G and $G = 2.5\,\mathrm{Tm}^{-1}$. Third Column: Energies of the center of mass Hamiltonian (7.13) for the harmonic potential $E_\kappa^{(0)}(\mathbf{R})$. Fourth Column: Corresponding symmetry adapted eigenstates. Fifth Column: Second order perturbation theory energies of Hamiltonian (7.13) including the contribution $E_\kappa^{(2)}(\mathbf{R})$. Sixth Column: Corresponding zero order perturbation theory wave functions. The symmetries of the states encountered are listed in the second column. Seventh column: Tunneling probability P_t according to Eq. (7.14) for the center of mass energies given in the fifth column.

State no.	Symmetry	Harmonic Oscillator Energies	Symmetry Adapted Eigenstates	Perturbed Energies	Zero Order Eigenstates	Tunneling Probability
ground	A_1	ω	χ_{00}	$0.9859\,\omega$	χ_{00}	3.19×10^{-6}
1	$\{E\}$	$2\,\omega$	χ_{01}	$1.9566\,\omega$	χ_{01}	1.35×10^{-4}
2		$2\,\omega$	χ_{10}	$1.9566\,\omega$	χ_{10}	1.35×10^{-4}
3	B_2	$3\,\omega$	χ_{11}	$2.8665\,\omega$	χ_{11}	3.38×10^{-3}
4	A_1	$3\,\omega$	$(\chi_{02} + \chi_{20})/\sqrt{2}$	$2.8942\,\omega$	$(\chi_{02} + \chi_{20})/\sqrt{2}$	3.71×10^{-3}
5	B_1	$3\,\omega$	$(\chi_{02} - \chi_{20})/\sqrt{2}$	$2.9572\,\omega$	$(\chi_{02} - \chi_{20})/\sqrt{2}$	4.60×10^{-3}
6	$\{E\}$	$4\,\omega$	χ_{12}	$3.7490\,\omega$	$0.937\chi_{12} + 0.349\chi_{30}$	6.44×10^{-2}
7		$4\,\omega$	χ_{21}	$3.7490\,\omega$	$0.937\chi_{21} + 0.349\chi_{03}$	6.44×10^{-2}
8	$\{E\}$	$4\,\omega$	χ_{03}	$3.9156\,\omega$	$0.937\chi_{30} - 0.349\chi_{12}$	0.11
9		$4\,\omega$	χ_{30}	$3.9156\,\omega$	$0.937\chi_{03} - 0.349\chi_{21}$	0.11
10	A_1	$5\,\omega$	χ_{22}	$4.5616\,\omega$	$0.937\chi_{22} + 0.257(\chi_{40} + \chi_{04})$	0.87
11	B_2	$5\,\omega$	$(\chi_{13} + \chi_{31})/\sqrt{2}$	$4.5684\,\omega$	$(\chi_{13} + \chi_{31})/\sqrt{2}$	0.89
12	A_2	$5\,\omega$	$(\chi_{13} - \chi_{31})/\sqrt{2}$	$> \Delta E_\kappa$	$(\chi_{13} - \chi_{31})/\sqrt{2}$	–
12	B_1	$5\,\omega$	$(\chi_{04} - \chi_{40})/\sqrt{2}$	$> \Delta E_\kappa$	$(\chi_{04} - \chi_{40})/\sqrt{2}$	–
12	A_1	$5\,\omega$	$(\chi_{04} + \chi_{40})/\sqrt{2}$	$> \Delta E_\kappa$	$0.663(\chi_{04} + \chi_{40}) - 0.349\chi_{22}$	–

are given in the last column of Tab. 7.4. For tighter magnetic traps, where more center of mass states can be confined, P_t substantially decreases further. Hence, tunneling has only to be considered for very high center of mass excitations close to the top of the barrier.

7.5 Parametric Heating

Utilizing state-dependent (Rydberg-Rydberg) interactions for quantum information protocols necessitates the excitation of trapped ground state atoms to a Rydberg state by a π-pulse [33, 34]. When the excitation process is much shorter than the timescale of the external motion, such an excitation effectively causes a sudden change of the trapping potential. This couples and thus redistributes the initial center of mass quantum state to neighboring levels, which – in general – increases the center of mass energy (hence we will denote this process as "parametric heating" in the following). In this section, we investigate this effect and calculate the corresponding heating rates.

Suppose we have a ^{87}Rb atom in its $5S_{1/2}, F = m_F = 2$ electronic ground state which is at $t = 0$ instantaneously excited to the Rydberg state $40S_{1/2}, m_j = 1/2$ and after a short period of time t' again de-excited to its electronic ground state. Furthermore, we assume the atom to reside in a well defined center of mass state at $t = 0$, i.e., $\chi(\mathbf{R}, t = 0) = \chi_{\nu_x\nu_y}(\mathbf{R})$; note that $\chi_{\nu_x\nu_y}(\mathbf{R})$ denote the center of mass eigenfunctions of the ground state atom rather than the Rydberg atom. Except for the contribution $E_\kappa^{(2)}(\mathbf{R})$, both electronic states give rise to the same trapping potential $E_\kappa^{(0)}(\mathbf{R})$, i.e., in the simplest approximation [which is neglecting $E_\kappa^{(2)}(\mathbf{R})$ completely] the external state is not affected by the excitation to the Rydberg level.[8] If we account for the extra term $E_\kappa^{(2)}(\mathbf{R})$, on the other hand, the situation changes substantially. We consider the sequence *ground state* $\rightarrow$ *Rydberg state* $\rightarrow$ *ground state*, where all transitions are carried out by fast π-pulses. $E_\kappa^{(2)}(\mathbf{R})$ can then be considered as a perturbation of the ground state trapping potential which acts for the time interval during which the atom resides in the Rydberg level, i.e., $0 < t < t'$. As shown in the previous section, $E_\kappa^{(2)}(\mathbf{R})$ mixes center of mass states according to the selection rules $\Delta\nu_{x/y} = 0$ and $\Delta\nu_{x/y} = \pm 2$; hence the Rydberg excitation leads for the ground state atom to the admixture of lower- and higher-lying center of mass levels with $\nu' = \nu$, $\nu' = \nu \pm 2$, and $\nu' = \nu \pm 4$, where $\nu = \nu_x + \nu_y$. Note that we adopt here again the approximation of a purely harmonic potential $E_\kappa^{(0)}(\mathbf{R}) \propto \frac{1}{2}M\omega^2(X^2 + Y^2)$.

Within time-dependent perturbation theory, the probability of a transition $|\nu_x\nu_y\rangle \rightarrow |\nu'_x\nu'_y\rangle$ of the center of mass state of a ground state atom due to its short-time Rydberg excitation, i.e., the acting of the perturbing potential $E_\kappa^{(2)}(\mathbf{R})$, is given by

$$W_{\nu_x\nu_y\rightarrow\nu'_x\nu'_y} = \left|\langle\nu'_x\nu'_y|E_\kappa^{(2)}(\mathbf{R})|\nu_x\nu_y\rangle\right|^2 f(t', \tilde{\omega})$$

with $f(t', \tilde{\omega}) = \frac{\sin^2(\tilde{\omega}t'/2)}{(\tilde{\omega}/2)^2}$ and $\tilde{\omega} = (\nu' - \nu) \cdot \omega = \Delta\nu \cdot \omega$ [73]. The average rate to make a

[8] We remark that for the Rydberg state the hyperfine interaction can be treated perturbatively and does not alter the trapping potentials for the regime of field strengths we are considering, cf. Section 3.1.

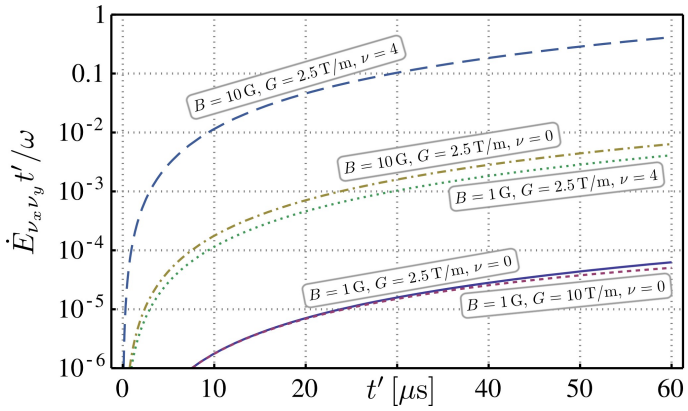

Figure 7.7: Parametric heating $\dot{E}_{\nu_x\nu_y} t'/\omega$ of a trapped ground state atom as a function of the time being excited to the Rydberg level $40S_{1/2}$. Several initial center of mass states and magnetic field configurations are considered: $B = 1\,\mathrm{G}$, $G = 2.5\,\mathrm{Tm}^{-1}$ (solid), $B = 1\,\mathrm{G}$, $G = 10\,\mathrm{Tm}^{-1}$ (short-dashed), and $B = 10\,\mathrm{G}$, $G = 2.5\,\mathrm{Tm}^{-1}$ (dashed-dotted) for $\nu_x = \nu_y = 0$ as well as $B = 1\,\mathrm{G}$, $G = 2.5\,\mathrm{Tm}^{-1}$ (dotted) and $B = 10\,\mathrm{G}$, $G = 2.5\,\mathrm{Tm}^{-1}$ (long-dashed) for $\nu_x = \nu_y = 2$.

transition to state $|\nu_x'\nu_y'\rangle$ within the time interval t' consequently reads

$$R_{\nu_x\nu_y\to\nu_x'\nu_y'} = \frac{1}{t'}\, W_{\nu_x\nu_y\to\nu_x'\nu_y'}\,. \tag{7.15}$$

This allows us to define a heating rate as

$$\dot{E}_{\nu_x\nu_y} = \sum_{\nu_x'\nu_y'} \tilde{\omega} R_{\nu_x\nu_y\to\nu_x'\nu_y'}\,.$$

Employing the recurrence relation $X\,|\chi_{\nu_x}\rangle = \sqrt{1/2M\omega}\,(\sqrt{\nu_x}\,|\chi_{\nu_x-1}\rangle + \sqrt{\nu_x+1}\,|\chi_{\nu_x+1}\rangle)$ of the harmonic oscillator eigenfunctions and accordingly

$$\langle\nu_x'|X^2|\nu_x\rangle = \frac{1}{2M\omega}\Big[\sqrt{\nu_x(\nu_x-1)}\,\delta_{\nu_x'\nu_x-2} + (2\nu_x+1)\,\delta_{\nu_x'\nu_x} + \sqrt{(\nu_x+1)(\nu_x+2)}\,\delta_{\nu_x'\nu_x+2}\Big]\,,$$

we yield

$$\begin{aligned}\dot{E}_{\nu_x\nu_y} = \frac{C_z^2 G^4}{M^4\omega^4}\,\frac{\omega}{t'}\Big\{&2\frac{\sin^2(\omega t')}{\omega^2}(\nu_x+\nu_y+1)(\nu_x+\tfrac{1}{2})(\nu_y+\tfrac{1}{2}) \\ &+ \frac{\sin^2(2\omega t')}{4\omega^2}(\nu_x+\nu_y+1)\big[(\nu_x+\tfrac{1}{2})(\nu_y+\tfrac{1}{2})+\tfrac{3}{4}\big]\Big\}\,.\end{aligned} \tag{7.16}$$

Here, we assumed $E_\kappa^{(2)}(\mathbf{R}) = C_z G^2 X^2 Y^2$. Note that $\dot{E}_{\nu_x\nu_y} > 0$ independent of the initial state, i.e., cooling is not possible. For short times $t' \ll 1/\omega$, one can approximate $\frac{\sin^2(\omega t')}{\omega^2} \approx t'^2$ which gives an overall linear increase of the heating rate in time.

In Figure 7.7, the parametric heating $\dot{E}_{\nu_x\nu_y} t'$ in terms of the trap frequency ω and as a function of the Rydberg excitation period t' is illustrated for several center of mass initial states and magnetic field configurations; throughout, the Rydberg state $40S_{1/2}$ is considered.

As one can observe, the heating mainly depends on the Ioffe field strength B rather than on the magnetic field gradient G. An increase of the latter barely changes $\dot{E}_{\nu_x\nu_y}t'/\omega$ while a stronger Ioffe field results in a substantial increase. As expected from Eq. (7.16), $\dot{E}_{\nu_x\nu_y}t'/\omega$ also significantly increases if the ground state atom is initially in an excited center of mass state. However, for the given examples the overall heating within the radiative lifetime of the Rydberg atom turns out to be very moderate with $\dot{E}_{\nu_x\nu_y}t' < 1\,\omega$ (for $B = 1$ G and $G = 2.5$ Tm^{-1}, $\dot{E}_{\nu_x\nu_y}t' = 1\,\omega$ corresponds to 15 nK). Hence, only for high center of mass levels $\nu = \nu_x + \nu_y$ and long times t' the above described excitation of the external motion of an ultracold sample of Rb atoms due to the Rydberg excitation is expected to become an issue.

Finally, let us briefly comment on what is expected for a thermal atom where the external state is not well-defined but rather distributed according to the Boltzmann statistics $f_\nu(T) = g_\nu e^{-(\nu+1)\omega/k_bT}/Z(T)$, $Z(T) = \sum_{\nu=0}^{\infty} g_\nu e^{-(\nu+1)\omega/k_bT}$ being the partition function and $g_\nu = \nu+1$ the degeneracy of the ν^{th} excited center of mass state. In this case, the heating rate reads

$$\dot{E}(T) = \sum_{\nu_x,\nu_y=0}^{\infty} f_\nu \dot{E}_{\nu_x\nu_y} \approx \frac{3}{2}\frac{C_z^2 G^4}{M^4\omega^3} t' \coth^3\left(\frac{1}{2}\frac{\omega}{k_bT}\right) . \tag{7.17}$$

Equation (7.17) is obtained by approximating $\frac{\sin^2(\omega t')}{\omega^2} \approx t'^2$ for short times $t' \ll 1/\omega$. Assuming high enough temperatures such that $k_bT \gg \omega$ simplifies Eq. (7.17) further to

$$\dot{E}(T) \approx \frac{12 C_z^2 G^4}{M^4\omega^3} t' \left(\frac{k_bT}{\omega}\right)^3 .$$

As expected from Eq. (7.16), $\dot{E}(T)$ rapidly increases with the temperature T since higher center of mass excitations are populated.

7.6 Dephasing

Besides the parametric heating due to the short-time Rydberg excitation of a ground state atom – as discussed in the previous section – the dephasing of the external motion of the Rydberg and the ground state atom might become an issue for experimental schemes realizing quantum information protocols. Let us consider the situation as described in Ref. [33], i.e., we have two ground states denoted by $|0\rangle$ and $|1\rangle$ where only the latter is coupled to a Rydberg state $|r\rangle$ by a laser transition. The density operator of the internal degree of freedom, i.e., only considering the electronic state, of such a two state system can generally be written as

$$\rho_{\text{int}} = a\,|0\rangle\langle 0| + (1-a)\,|1\rangle\langle 1| + b\,|1\rangle\langle 0| + b^*\,|0\rangle\langle 1|$$

giving rise to the density matrix

$$\rho_{\text{int}} = \begin{pmatrix} a & b^* \\ b & 1-a \end{pmatrix} . \tag{7.18}$$

If we assume furthermore that both ground states are identically prepared with respect to their external, i.e., center of mass motion the total density matrix factorizes into an internal

and external contribution,

$$\rho_{\mathrm{tot}} = \rho_{\mathrm{int}} \otimes \rho_{\mathrm{ext}} \,,$$

where $\rho_{\mathrm{ext}} = \sum_{\nu_y\nu_y} p_{\nu_x\nu_y} |\nu_x\nu_y\rangle\langle\nu_x\nu_y|$.

For various implementations of quantum information protocols, now the Rydberg state $|r\rangle$ comes into play. Suppose that state $|1\rangle$ is excited to $|r\rangle$ for a given time t'. As pointed out in Section 7.5, this will influence its center of mass motion by causing transitions $|\nu_x\nu_y\rangle \rightarrow |\tilde{\chi}\rangle$ where

$$|\tilde{\chi}\rangle \equiv \sum_{\nu'_x\nu'_y} C^{\nu'_x\nu'_y}_{\nu_x\nu_y}(t') \, |\nu'_x\nu'_y\rangle \,;$$

$C^{\nu'_x\nu'_y}_{\nu_x\nu_y}(t')$ denotes the amplitude for being at time t' in state $|\nu'_x\nu'_y\rangle$ if initially residing in state $|\nu_x\nu_y\rangle$. Hence, after the short-time Rydberg excitation of solely state $|1\rangle$, the density matrix does not decouple anymore and consequently reads

$$\begin{aligned}\rho_{\mathrm{tot}} = \sum_{\nu_x\nu_y} p_{\nu_x\nu_y} \Big[& a \, |0\rangle\langle 0| \otimes |\nu_x\nu_y\rangle\langle\nu_x\nu_y| + (1-a) \, |1\rangle\langle 1| \otimes |\tilde{\chi}\rangle\langle\tilde{\chi}| \\ & + b \, |1\rangle\langle 0| \otimes |\tilde{\chi}\rangle\langle\nu_x\nu_y| + b^* \, |0\rangle\langle 1| \otimes |\nu_x\nu_y\rangle\langle\tilde{\chi}| \Big] .\end{aligned}$$

Any qubit-related measurement, however, only acts on the internal degrees of freedom, i.e., the electronic states. As a consequence, the physically relevant object in this case is the reduced density matrix where the center of mass degree of freedom is traced out. Defining $\beta = \sum_{\nu_x\nu_y} p_{\nu_x\nu_y} \langle\nu_x\nu_y|\tilde{\chi}\rangle$, one eventually yields

$$\mathrm{Tr}_{\mathrm{ext}}\rho_{\mathrm{tot}} = \begin{pmatrix} a & b^*\beta^* \\ b\beta & 1-a \end{pmatrix} . \tag{7.19}$$

Comparing this result to the case where the internal and external degree of freedom factorize, $\mathrm{Tr}_{\mathrm{ext}}(\rho_{\mathrm{int}} \otimes \rho_{\mathrm{ext}}) = \rho_{\mathrm{int}}$, it is clear that the short-time Rydberg excitation will inevitably influence the properties of our system. In order to quantify this effect, we consider the purity $\mathcal{P}(\rho) = \mathrm{Tr}\rho^2$ of the reduced density matrix,

$$\mathcal{P}(\mathrm{Tr}_{\mathrm{ext}}\rho_{\mathrm{tot}}) = a^2 + (1-a)^2 + 2|b|^2|\beta|^2 \,.$$

In particular, if the system is initially prepared in a pure internal state (as for example the state $(|0\rangle \pm |1\rangle)/\sqrt{2}$, which is envisaged for the realization of a two qubit CNOT gate [43]) the above described process is expected to decrease its purity. Defining $\mathcal{P}_{\mathrm{int}} = a^2 + (1-a)^2 + 2|b|^2$ as the purity of the system only considering the internal degree of freedom, one indeed yields

$$\mathcal{P}(\mathrm{Tr}_{\mathrm{ext}}\rho_{\mathrm{tot}}) = \mathcal{P}_{\mathrm{int}} - 2|b|^2(1-|\beta|^2) \,.$$

Note that for any pure state $\mathcal{P}_{\mathrm{int}} = 1$ is found. Hence, the reduction of the purity is determined by the magnitude of $|\beta|^2$ and therefore by the overlap integrals $\langle\nu_x\nu_y|\tilde{\chi}\rangle$ of the center of mass wave function after the Rydberg excitation.

A particularly illustrative situation arises, if the atom is initially prepared in its center of mass ground state, i.e., $p_{\nu_x\nu_y} = \delta_{0\nu_x}\delta_{0\nu_y}$ and $|\beta|^2 = |\langle 00|\tilde{\chi}\rangle|^2$ correspondingly. In this case, $|\beta|^2$ is given by the probability of finding the atom still in the center of mass ground state

after being excited to the Rydberg state for the time t'. According to Section 7.5 we find

$$\begin{aligned}|\beta|^2 &= 1 - \sum_{\nu_x\nu_y\neq 00} W_{00\to\nu_x\nu_y} \\ &= 1 - \frac{C_z^2 G^4}{4M^4\omega^4}\left(\frac{\sin^2(\omega t')}{\omega^2} + \frac{\sin^2(2\omega t')}{4\omega^2}\right) \\ &\approx 1 - \frac{C_z^2 G^4}{2M^4\omega^4}\, t'^2\end{aligned}$$

and therefore

$$\mathcal{P}(\mathrm{Tr}_{\mathrm{ext}}\rho_{\mathrm{tot}}) \approx \mathcal{P}_{\mathrm{int}} - 2|b|^2 \frac{C_z^2 G^4}{2M^4\omega^4} t'^2 \,.$$

As expected, the decrease of the purity depends explicitly (for short times t' even quadratically) on the time t' of being excited to the Rydberg level.

Chapter 8

Mapping the Composite Character of Magnetically Trapped Rydberg Atoms

One major drawback of Rydberg atoms is their finite lifetimes due to spontaneous radiative decays. Although being denoted as *long-lived* for the purpose of many experiments, lifetimes in the range of microseconds up to milliseconds can still be insufficient. For example, the atomic motion in the ultracold regime is hard to resolve within this timescale. Also in the context of quantum information, coherence times exceeding the typical lifetime of Rydberg atoms are desirable. A remedy of this issue is to combine the huge amount of control known from ultracold physics with the exceptional properties of Rydberg atoms by *dressing* ground state atoms with Rydberg states. This can be achieved by off-resonantly coupling the ground and Rydberg state by an appropriate laser transition (which is usually of two-photon character), resulting in dressed states where the Rydberg level becomes weakly admixed to the ground state and vice versa. In this manner, Rydberg atoms have the potential to become useful tools in many areas of ultracold atomic physics. Employing trapped Rydberg ions, a similar scheme has been proposed recently for the realization of fast two-qubit quantum gates [115].

In this chapter, we illuminate the question of how the external, i.e., center of mass motion of magnetically trapped ^{87}Rb atoms is affected by the dressing with Rydberg atoms. The issue of trapping Rydberg atoms in a magnetic Ioffe-Pritchard trap has been studied extensively in the previous chapters. In particular, we demonstrated in Chapter 7 that the trapping potentials of Rydberg atoms in low angular momentum electronic states (here: $l \leq 2$) considerably deviate from the behavior known from ground state atoms. This effect is due to the *composite* nature of Rydberg atoms, i.e., the fact that they consist of an outer valence electron far apart from the ionic core. Because of the finite lifetimes of Rydberg atoms and the long timescales of the external motion at ultracold temperatures, the experimental observation of the particular trapping properties of the Rydberg atom is a difficult task. As mentioned above, this issue can be resolved by employing an off-resonant two-photon laser coupling scheme that maps the features of the Rydberg trapping potential onto the dressed ground state atom. Here, we thoroughly discuss this coupling scheme and systematically study the resulting dressed trapping potentials. In particular, we demonstrate how the delicate interplay between the spatially varying quantization axis of the Ioffe-Pritchard field and the fixed polarizations of the laser transitions determines the actual shape of the trapping potentials.

In detail, we proceed as follows. For the sake of completeness, Section 8.1 briefly reviews the Rydberg trapping potentials, including now the hyperfine structure. Section 8.2 then introduces the off-resonant two-photon laser coupling scheme that dresses the ground state

with the Rydberg state. In Section 8.3 we establish a simplified three-level scheme (opposed to the 32-level scheme that is needed to fully describe the excitation dynamics) that allows us to derive analytical expressions of the dressed potentials. Section 8.4 finally contains a thorough discussion of the dressed ground trapping potentials for a variety of field and laser configurations.

The results presented in this chapter are partially published in Ref. [110].

8.1 Rydberg Trapping Potentials

In this section, we provide a brief review of the trapping potentials emerging for a low angular momentum Rydberg atom in a Ioffe-Pritchard trap. For more details on this issue, we refer the reader to Chapter 7. As it will become necessary for the description of the laser coupling scheme, we also comment on the role of the hyperfine structure in this section. Moreover, the trapping potentials arising for a ground state atom are introduced.

As outlined in the previous chapter and thoroughly discussed in Chapter 3, the Hamiltonian describing a Rydberg atom in a magnetic Ioffe-Pritchard trap reads

$$\begin{aligned} U^\dagger H U = \frac{\mathbf{P}^2}{2M} + H_A + \tfrac{1}{2}[\mathbf{L}+2\mathbf{S}]\cdot\mathbf{B}_c - \boldsymbol{\mu}_e\cdot\mathbf{B}_l(\mathbf{R}+\mathbf{r}) - \boldsymbol{\mu}_c\cdot\mathbf{B}(\mathbf{R}) \\ + \mathbf{A}_l(\mathbf{R}+\mathbf{r})\cdot\mathbf{p} + \tfrac{1}{2}\mathbf{A}_c(\mathbf{r})^2 + H_{\text{corr}}\,, \end{aligned} \tag{8.1}$$

cf. Eq. 7.2. Here, $H_A = \mathbf{p}^2/2 + V_l(r) + V_{so}(\mathbf{L},\mathbf{S})$ is the field-free Hamiltonian of the valence electron whose core penetration, scattering, and polarization effects are accounted for by the l-dependent model potential $V_l(r)$ while $\mathbf{L}$ and $\mathbf{S}$ denote its orbital angular momentum and spin, respectively. $V_{so}(\mathbf{L},\mathbf{S})$ denotes the spin-orbit interaction that couples $\mathbf{L}$ and $\mathbf{S}$ to the total electronic angular momentum $\mathbf{J} = \mathbf{L}+\mathbf{S}$. H_{corr} are small corrections that are neglected in the parameter regime we are focusing on. In order to solve the resulting coupled Schrödinger equation, we employ a Born-Oppenheimer separation of the center of mass motion and the electronic degrees of freedom, cf. Section 3.4. We are thereby led to an electronic Hamiltonian for fixed center of mass position of the atom whose eigenvalues $E_\kappa(\mathbf{R})$ depend parametrically on the center of mass coordinates. These adiabatic electronic surfaces serve as trapping potentials for the quantized center of mass motion and are discussed extensively in Chapter 7.

For fixed total electronic angular momentum $\mathbf{J} = \mathbf{L} + \mathbf{S}$, approximate expressions for the adiabatic electronic energy surfaces can be derived by applying the spatially dependent transformation $U_r = e^{-i\gamma(L_x+S_x)}e^{-i\beta(L_y+S_y)}$ that rotates the local magnetic field vector into the z-direction of the laboratory frame of reference, see Chapter 4. In second order perturbation theory, the adiabatic electronic energy surfaces read

$$E_\kappa(\mathbf{R}) = E_\kappa^{(0)}(\mathbf{R}) + E_\kappa^{(2)}(\mathbf{R}), \tag{8.2}$$

where

$$E_\kappa^{(0)}(\mathbf{R}) = E_\kappa^{el} + \tfrac{1}{2}g_j m_j\sqrt{B^2 + G^2(X^2+Y^2)} \tag{8.3}$$

represents the coupling of a point-like particle to the magnetic field via its magnetic moment $\mu = \frac{1}{2}\mathbf{L} + \mathbf{S}$; κ represents the electronic state under investigation, i.e., $|\kappa\rangle = |njm_jls\rangle$ and

$g_j = \frac{3}{2} + \frac{s(s+1)-l(l+1)}{2j(j+1)}$ its Landé g-factor. $E_\kappa^{(0)}(\mathbf{R})$ is rotationally symmetric around the Z-axis and confining for $m_j > 0$. For small radii ($\rho = \sqrt{X^2+Y^2} \ll B/G$) an expansion up to second order yields a harmonic potential

$$E_\kappa^{(0)}(\rho) \approx E_\kappa^{el} + \tfrac{1}{2} g_j m_j B + \frac{1}{2} M\omega^2 \rho^2$$

with the trap frequency defined by $\omega = G\sqrt{\frac{g_j m_j}{2MB}}$ while we find a linear behavior $E_\kappa^{(0)}(\rho) \approx E_\kappa^{el} + \frac{1}{2} g_j m_j G\rho$ when the center of mass is far from the Z-axis ($\rho \gg B/G$).

The second order contribution $E_\kappa^{(2)}(\mathbf{R})$ stems from the composite nature of the Rydberg atom, i.e., the fact that it consists of an outer Rydberg electron far apart from the ionic core. It reads

$$E_\kappa^{(2)}(\mathbf{R}) = C \cdot G^2 X^2 Y^2$$

where the coefficient C depends on the electronic state κ under investigation. Since C is generally negative (see previous chapter), a de-confining behavior of the energy surface for large center of mass coordinates close to the diagonal ($X = Y$) is found.

At this point, let us comment on the role of the hyperfine interaction. As pointed out in Section 3.1, for a wide range of field strengths, the hyperfine interaction can be treated perturbatively, giving rise to a mere splitting of the trapping potentials according to $H_{\text{hfs}} = hAm_i m_j$, cf. Eq. (3.13). In this chapter, however, we are not only interested in the adiabatic energy surfaces *per se* but also in transitions between different electronic states of a trapped atom. Since for ground state alkali atoms the good magnetic quantum numbers are the ones belonging to the total angular momentum $\mathbf{F} = \mathbf{J} + \mathbf{I}$ ($\mathbf{I}$ being the nuclear spin), it is advisable to incorporate the hyperfine interaction fully also for Rydberg atoms. That is, for the Rydberg states we diagonalize the Hamiltonian

$$H = E_\kappa^{el} + hA\mathbf{I}\cdot\mathbf{J} + \frac{1}{2} g_j J_z |\mathbf{B}(\mathbf{R})| + E_\kappa^{(2)}(\mathbf{R}) \tag{8.4}$$

within a given j-manifold.[1] Similar to the spin-orbit coupling case, we employ the basis of angular momentum coupled eigenfunctions $|nFm_F jls\rangle$ for which the contribution $hA\mathbf{I}\cdot\mathbf{J}$ is diagonal. For actual values of the hyperfine constant A, we refer the reader to Section 3.1.

For ground state atoms, the hyperfine interaction easily overcomes the Zeeman splitting. Consequently, we need to consider the atom to couple via its total angular momentum $\mathbf{F}$ to the magnetic field. After rotating into the local magnetic field direction via the unitary transformation $U_r = e^{-i\gamma F_x} e^{-i\beta F_y}$, we yield for the trapping potentials

$$E_\kappa(\mathbf{R}) = E_\kappa^{el} + \frac{1}{2} g_F m_F |\mathbf{B}(\mathbf{R})|\,,$$

[1] More precisely, we should introduce the interaction term $hA\mathbf{I}\cdot\mathbf{J}$ at the very beginning of our theoretical treatment. The first unitary transformation employed in Chapter 7, $U = \exp\left\{\frac{i}{2}(\mathbf{B}_c \times \mathbf{r})\cdot\mathbf{R}\right\}$, leads to small corrections $U^\dagger \mathbf{I}\cdot\mathbf{J} U = \mathbf{I}\cdot\mathbf{J} - \mathbf{I}\cdot[\mathbf{r}\times\mathbf{A}_c(\mathbf{R})]$ for the hyperfine interaction that can be neglected. Including the nuclear spin degree of freedom, the second transformation that rotates into the local field direction reads $U_r = e^{-i\gamma(L_x+S_x+I_x)} e^{-i\beta(L_y+S_y+I_y)} = e^{-i\gamma F_x} e^{-i\beta F_y}$. Since $2\mathbf{I}\cdot\mathbf{J} = \mathbf{F}^2 - \mathbf{I}^2 - \mathbf{J}^2$ and $[\mathbf{F}^2, \mathbf{F}] = [\mathbf{I}^2, \mathbf{I}] = [\mathbf{J}^2, \mathbf{J}] = 0$, the coupling term $hA\mathbf{I}\cdot\mathbf{J}$ is invariant under this transformation. As in the rest of this thesis, we neglected in Hamiltonian (8.4) the direct coupling of the nuclear magnetic moment to the magnetic field.

where E_κ^{el} includes the hyperfine as well as spin-orbit effects, and

$$g_F = g_j \frac{F(F+1) + j(j+1) - I(I+1)}{2F(F+1)} .$$

The rotation angles β and γ are defined in Eqs. (4.14). Note that – except for the electronic energy offset E_κ^{el} – the $E^{(0)}_{nS_{1/2},m_j=1/2}(\mathbf{R})$ Rydberg and the $5S_{1/2}$ ground state energy surface are identical for $F = m_F = 2$.

8.2 Off-resonant Coupling Scheme

In this section, we discuss the coupling scheme of the ground- and Rydberg state that arises for a two-photon off-resonant laser excitation in the presence of the Ioffe-Pritchard trap. Such a scheme can be particularly useful since the direct experimental observation of the Rydberg trapping potentials Eq. (8.2) might be a difficult task due to the finite lifetime of Rydberg atoms and their strong susceptibility to external perturbations (stray electric fields, mutual interactions etc.). The off-resonant coupling results in a dressed ground state atom to which the Rydberg state is weakly admixed. In this manner, the ground state atom gains properties that are specific for the Rydberg atom. In particular, the trapping potential of the dressed ground state atom becomes effectively altered by the admixture of the Rydberg surface.

We investigate the excitation scheme that is frequently encountered in experiments [40,41]: Laser 1, which is σ^+ polarized, drives the transition $s \rightarrow p$ detuned by Δ_1 while a second, σ^- polarized laser then couples to the Rydberg state $n \equiv nS_{1/2}, m_j = 1/2, M_I = 3/2$, with s denoting the ground state $5S_{1/2}, F = m_F = 2$ and p the intermediate state $5P_{3/2}, F = m_F = 3$. The complete two-photon transition is supposed to be off-resonant by Δ_2. A sketch of the whole scheme is provided in Fig. 8.1(a). In a Ioffe-Pritchard trap, however, the quantization axis is spatially dependent and the polarization vectors of the two excitation lasers are only well defined as σ^+ and σ^- at the trap center. As we are going to show in the following, in the rotated frame of reference, i.e., after applying the unitary transformation $U_r H_{\mathrm{AF}} U_r^\dagger$, contributions of all polarizations emerge and the excitation scheme becomes more involved.

In the dipole approximation, the interaction of the atom with the laser field is given by

$$H_{\mathrm{AF}} = -\mathbf{d} \cdot \mathbf{E}(t) = \mathbf{r} \cdot \mathbf{E}(t) . \tag{8.5}$$

The electric field vector $\mathbf{E}(t)$ can be decomposed into its positive- and negative-rotating components according to $\mathbf{E}^{(+)}(t)$ and $\mathbf{E}^{(-)}(t)$,

$$\begin{aligned} \mathbf{E}(t) &= \frac{E_0}{2}\left(\boldsymbol{\epsilon} e^{-i\omega t} + \boldsymbol{\epsilon}^* e^{i\omega t}\right) \\ &\equiv \mathbf{E}^{(+)}(t) + \mathbf{E}^{(-)}(t) , \end{aligned}$$

i.e., $\mathbf{E}^{(\pm)} \sim e^{-i(\pm\omega)t}$ [117]. The electric field amplitude E_0 is connected to the intensity I of the laser via $E_0 = \sqrt{2I/c\varepsilon_0}$. We distinguish three different polarization vectors $\boldsymbol{\epsilon}$ of the excitation lasers, namely, $\boldsymbol{\epsilon}_\pm = (\hat{\mathbf{x}} \pm i\hat{\mathbf{y}})/\sqrt{2}$ and $\boldsymbol{\epsilon}_0 = \hat{\mathbf{z}}$ for $\sigma^\pm$- and π-polarized light, respectively.

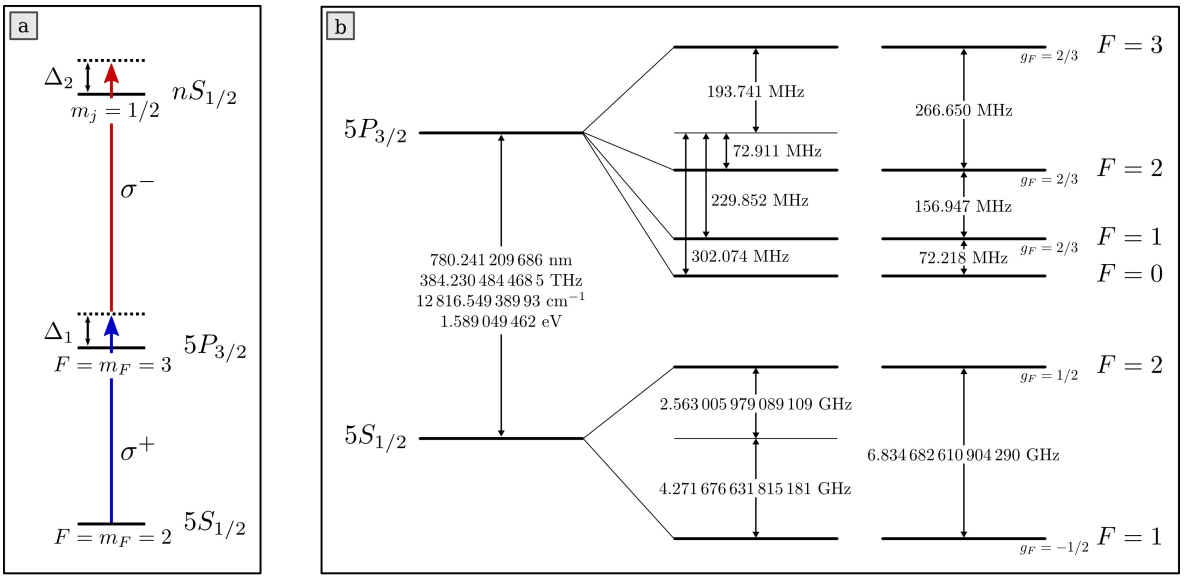

Figure 8.1: (a) Idealized level scheme for an off-resonant two photon coupling of the ground- and Rydberg state of ^{87}Rb. In a Ioffe-Pritchard trap, additional atomic levels and polarizations contribute away from the trap center, see text. Note that the hyperfine splittings of the Rydberg level are included in the calculation although not shown in this figure. (b) Atomic energy level scheme of the $5S_{1/2}$ and $5P_{3/2}$ states of ^{87}Rb including the hyperfine splittings; adapted from Ref. [116].

In order to solve the time-dependent Schrödinger equation, the Hamiltonian for the atom in the Ioffe-Pritchard trap, Eq. (8.4), and the laser interaction Hamiltonian (8.5) must be expressed in the same frame of reference. Hence, the unitary transformations of the previous section must be applied to H_{AF} as well. The first one, $U = \exp\left\{\frac{i}{2}(\mathbf{B}_c \times \mathbf{r}) \cdot \mathbf{R}\right\}$, leaves the interaction Hamiltonian (8.5) of the atom with the lasers unchanged. The transformation $U_r = e^{-i\gamma F_x} e^{-i\beta F_y}$ into the rotated frame of reference, on the other hand, yields

$$U_r \mathbf{r} U_r^\dagger = \begin{pmatrix} x\cos\beta + y\sin\gamma\sin\beta - z\cos\gamma\sin\beta \\ y\cos\gamma + z\sin\gamma \\ x\sin\beta - y\sin\gamma\cos\beta + z\cos\gamma\cos\beta \end{pmatrix},$$

cf. Chapter 4. That is, the σ^+ and σ^- laser transitions that are depicted in Fig. 8.1(a) become

$$\boldsymbol{\epsilon}_\pm \cdot U_r \mathbf{r} U_r^\dagger = \frac{1}{\sqrt{2}}\left[x\cos\beta + y\sin\gamma\sin\beta - z\cos\gamma\sin\beta \pm i(y\cos\gamma + z\sin\gamma)\right]. \tag{8.6}$$

Equation (8.6) can be rewritten in terms of the polarization vectors $\tilde{\boldsymbol{\epsilon}}_\pm$ and $\tilde{\boldsymbol{\epsilon}}_0$ defined in the rotated frame of reference. To this end, we rotate the polarization vector $\boldsymbol{\epsilon}$ and leave the position operator $\mathbf{r}$ unchanged: $\boldsymbol{\epsilon} \cdot U_r \mathbf{r} U_r^\dagger \to (\mathcal{R}\boldsymbol{\epsilon}) \cdot \mathbf{r}$ with $\mathcal{R}$ denoting the rotation matrix associated with the transformation U_r. $\mathcal{R}\boldsymbol{\epsilon}$ can then be decomposed into the components $\tilde{\boldsymbol{\epsilon}}_\pm$ and $\tilde{\boldsymbol{\epsilon}}_0$, i.e., $\mathcal{R}\boldsymbol{\epsilon} = \sum_{i=\pm,0} c_i \tilde{\boldsymbol{\epsilon}}_i$ with $c_i = \tilde{\boldsymbol{\epsilon}}_i^* \cdot \mathcal{R}\boldsymbol{\epsilon}$. Employing

$$\mathcal{R}\boldsymbol{\epsilon}_\pm = \frac{1}{\sqrt{2}} \begin{pmatrix} \cos\beta \\ \sin\gamma\sin\beta \pm i\cos\gamma \\ -\cos\gamma\sin\beta \pm i\sin\gamma \end{pmatrix}$$

finally yields

$$\boldsymbol{\epsilon}_+ \cdot U_r \mathbf{r} U_r^\dagger = \Big[\frac{1}{2}(\cos\gamma + \cos\beta - i\sin\gamma\sin\beta)\tilde{\boldsymbol{\epsilon}}_+ - \frac{1}{2}(\cos\gamma - \cos\beta - i\sin\gamma\sin\beta)\tilde{\boldsymbol{\epsilon}}_- - \frac{1}{\sqrt{2}}(\cos\gamma\sin\beta - i\sin\gamma)\tilde{\boldsymbol{\epsilon}}_0\Big] \cdot \mathbf{r}\,, \tag{8.7}$$

$$\boldsymbol{\epsilon}_- \cdot U_r \mathbf{r} U_r^\dagger = \Big[\frac{1}{2}(\cos\gamma + \cos\beta + i\sin\gamma\sin\beta)\tilde{\boldsymbol{\epsilon}}_- - \frac{1}{2}(\cos\gamma - \cos\beta + i\sin\gamma\sin\beta)\tilde{\boldsymbol{\epsilon}}_+ - \frac{1}{\sqrt{2}}(\cos\gamma\sin\beta + i\sin\gamma)\tilde{\boldsymbol{\epsilon}}_0\Big] \cdot \mathbf{r}\,. \tag{8.8}$$

Thus, in a Ioffe-Pritchard trap contributions of all polarizations emerge away from the trap center. In particular, the $5S_{1/2}, F = m_F = 2$ ground state can also couple to $m_F < 3$ magnetic sublevels of the $5P_{3/2}$ intermediate state. Moreover, two-photon couplings between the $5S_{1/2}, F = m_F = 2$ and $5S_{1/2}, F = 2, m_F < 2$ levels via the hyperfine levels of the $5P_{3/2}$ intermediate state emerge if the first excitation laser gains a significant contribution of the σ^-- or π-polarization in the rotated frame of reference. On the Rydberg side, also $m_j = -1/2$ states become accessible. As a results, the simple three-level excitation scheme $s \leftrightarrow p \leftrightarrow n$ is in general not sufficient and all relevant hyperfine levels must be included in the theoretical treatment.[2] For this reason, the field-free energy level scheme of the $5S_{1/2}$ and $5P_{3/2}$ states of ^{87}Rb is illustrated in Fig. 8.1(b). Note that the intermediate $5P_{3/2}, F < 3$ states are splitted considerably below the $5P_{3/2}, F = 3$ levels because of the hyperfine interaction. An even stronger splitting is found for the $F = 1$ and $F = 2$ hyperfine levels of the $5S_{1/2}$ electronic state. The hyperfine structure effects for the Rydberg state are discussed in the previous section, cf. Eq. 8.4.

The resulting multi-level excitation scheme is solved by employing the rotating wave approximation while adiabatically eliminating the intermediate states by a strong off-resonance condition. This procedure results in an effective coupling matrix for the ground and Rydberg states whose diagonalization yields a dressed electronic potential energy surface for the center of mass motion of the ground state atom. In the next section, we derive the coupling matrix for the illustrative example of a simplified three-level system. The generalization to the full level scheme is straightforward, although laborious.

8.3 Simplified Three-Level Scheme

In this section, we restrict ourselves to the three-level system $s \leftrightarrow p \leftrightarrow n$, i.e., including from the transformed dipole interaction Eqs. (8.7-8.8) only the σ^+ and σ^- part for the first and second laser, respectively. Such a simplification allows us to derive analytical solutions of the time-dependent Schrödinger equation and therefore constitutes a particularly illustrative example. It is expected to be valid for large Ioffe fields B and/or small gradients G when the quantization axis only shows a weak spatial dependence and the $nS_{1/2}, m_j = 1/2, M_I = 3/2$

[2] In detail, these are the $F = 1$ and $F = 2$ hyperfine levels of the $5S_{1/2}$ ground and the $nS_{1/2}$ Rydberg state. For the intermediate $5P_{3/2}$ state we have $F \in \{0, 1, 2, 3\}$. Of course, for each F there are in addition $2F+1$ magnetic sublevels with $|m_F| \leq F$. In total, this yields 32 states that must be considered. Other electronic states are far off-resonant and thus do not contribute in the excitation dynamics.

Rydberg state is predominantly addressed via the $5P_{3/2}, F = m_F = 3$ intermediate state. For higher gradients, the polarization vector significantly changes its character throughout the excitation area such that the contributions of other states cannot be neglected anymore.

Within the simplified 3-level picture, our initial Hamiltonian matrix reads

$$\mathcal{H}_{3l} = \mathcal{H}_{\mathrm{A}} + \mathcal{H}_{\mathrm{AF}}$$

where

$$\mathcal{H}_{\mathrm{A}} = \begin{pmatrix} E_n & 0 & 0 \\ 0 & E_p & 0 \\ 0 & 0 & E_s \end{pmatrix}$$

is the matrix representation of the atomic Hamiltonian including the interaction with the magnetic Ioffe-Pritchard field, i.e., $E_n \equiv E^{el}_{nS_{1/2},m_j=1/2} + \tilde{E}_n$, $E_s \equiv E^{el}_{5S_{1/2},F=m_F=2} + \tilde{E}_s$, and $E_p \equiv E^{el}_{5P_{3/2},F=m_F=3} + \tilde{E}_p$; E^{el}_{κ} are the field-free atomic energy levels while $\tilde{E}_n \equiv \frac{1}{2}|\mathbf{B}(\mathbf{R})| + C \cdot G^2X^2Y^2$, $\tilde{E}_s \equiv \frac{1}{2}|\mathbf{B}(\mathbf{R})|$, and $\tilde{E}_p \equiv |\mathbf{B}(\mathbf{R})|$ are the corresponding trapping potentials. Note that the Rydberg state n experiences the same potential energy surface as the ground state s, plus the perturbation $E^{(2)}_{nS_{1/2}}(\mathbf{R})$ due to its non-pointlike character. Defining $\omega_1^{(\pm)} = \langle p|\mathbf{E}_1^{(\pm)}(t)\, U_r \mathbf{r} U_r^\dagger|s\rangle$ as well as $\omega_2^{(\pm)} = \langle n|\mathbf{E}_2^{(\pm)}(t)\, U_r \mathbf{r} U_r^\dagger|p\rangle$, the interaction $\mathcal{H}_{\mathrm{AF}}$ of the atom with the laser field reads

$$\mathcal{H}_{\mathrm{AF}} = \begin{pmatrix} 0 & \omega_2^{(+)} + \omega_2^{(-)} & 0 \\ \left[\omega_2^{(+)} + \omega_2^{(-)}\right]^* & 0 & \omega_1^{(+)} + \omega_1^{(-)} \\ 0 & \left[\omega_1^{(+)} + \omega_1^{(-)}\right]^* & 0 \end{pmatrix}. \tag{8.9}$$

Rotating Wave Approximation

In order to remove the time-dependence of Hamiltonian (8.9), we transform into a frame of reference that rotates along with the positive components of $\mathbf{E}_i(t)$. This is achieved by applying the unitary transformation

$$\mathcal{U}_{\mathrm{rf}} = \begin{pmatrix} e^{-i(\omega_1+\omega_2)t} & 0 & 0 \\ 0 & e^{-i\omega_1 t} & 0 \\ 0 & 0 & 1 \end{pmatrix}. \tag{8.10}$$

In the rotating frame of reference, the Schrödinger equation reads

$$i[\mathcal{U}_{\mathrm{rf}}^\dagger \partial_t \mathcal{U}_{\mathrm{rf}}]\varphi = [\mathcal{U}_{\mathrm{rf}}^\dagger \mathcal{H}_{3l} \mathcal{U}_{\mathrm{rf}}]\varphi\,.$$

Expanding the time derivative, $\mathcal{U}_{\mathrm{rf}}^\dagger \partial_t (\mathcal{U}_{\mathrm{rf}}\varphi) = [\mathcal{U}_{\mathrm{rf}}^\dagger \mathcal{U}_{\mathrm{rf}} \partial_t + \mathcal{U}_{\mathrm{rf}}^\dagger (\partial_t \mathcal{U}_{\mathrm{rf}})]\varphi$, and noting that $\mathcal{U}_{\mathrm{rf}}^\dagger \mathcal{U}_{\mathrm{rf}} = 1$, we get

$$i\partial_t \varphi = [-i\mathcal{U}_{\mathrm{rf}}^\dagger (\partial_t \mathcal{U}_{\mathrm{rf}}) + \mathcal{U}_{\mathrm{rf}}^\dagger \mathcal{H}_{3l} \mathcal{U}_{\mathrm{rf}}]\varphi\,.$$

Comparing this to the Schrödinger equation in the transformed variables, $i\partial_t\varphi = \mathcal{H}_{\mathrm{rf}}\varphi$, we can identify the transformed Hamiltonian as

$$\mathcal{H}_{\mathrm{rf}} = -i\mathcal{U}_{\mathrm{rf}}^\dagger (\partial_t \mathcal{U}_{\mathrm{rf}}) + \mathcal{U}_{\mathrm{rf}}^\dagger \mathcal{H}_{3l} \mathcal{U}_{\mathrm{rf}}\,.$$

Employing

$$-i\mathcal{U}_{\mathrm{rf}}^{\dagger}(\partial_t\mathcal{U}_{\mathrm{rf}}) = \begin{pmatrix} -\omega_1-\omega_2 & 0 & 0 \\ 0 & -\omega_1 & 0 \\ 0 & 0 & 0 \end{pmatrix}$$

we get

$$\begin{aligned}\mathcal{H}_{\mathrm{rf}} = &\begin{pmatrix} E_n-\omega_1-\omega_2 & 0 & 0 \\ 0 & E_p-\omega_1 & 0 \\ 0 & 0 & E_s \end{pmatrix} \\ &+ \begin{pmatrix} 0 & \left[\omega_2^{(+)}+\omega_2^{(-)}\right]e^{i\omega_2 t} & 0 \\ \left\{\left[\omega_2^{(+)}+\omega_2^{(-)}\right]e^{i\omega_2 t}\right\}^* & 0 & \left[\omega_1^{(+)}+\omega_1^{(-)}\right]e^{i\omega_1 t} \\ 0 & \left\{\left[\omega_1^{(+)}+\omega_1^{(-)}\right]e^{i\omega_1 t}\right\}^* & 0 \end{pmatrix}.\end{aligned} \tag{8.11}$$

For this Hamiltonian, we can apply the *Rotating Wave Approximation* (RWA) which goes as follows. Expanding the products in Eq. (8.11), terms of the form $\mathbf{E}_i^{(\pm)}(t)e^{i\omega_i t}$ are encountered. Having in mind that $\mathbf{E}_i^{(\pm)}(t) \sim e^{-i(\pm\omega_i)t}$, the time-dependence of the positive-rotating component cancels while we get for the negative-rotating ones $\mathbf{E}_i^{(-)}(t)e^{i\omega_i t} \sim e^{2i\omega_i t}$. The rotating wave approximation consists in replacing such fast rotating terms by their zero average value. For our optical frequencies ω_1 and ω_2, this corresponds to focusing on slow dynamics and coarse-graining on femtoseconds time scales. We remark that in the non-rotating, i.e., the laboratory frame of reference the slow dynamics are determined by $e^{\pm i\Delta_i t}$, which allows for the same reasoning.

In the following, let us rearrange the Hamiltonian matrix (8.11) by switching $n \leftrightarrow s$, anticipating that we are interested in the two-photon excitation dynamics between the ground and Rydberg state. Introducing furthermore an energy offset such that $E_s = 0$ at the origin, the time-independent RWA Hamiltonian

$$\mathcal{H}_{\mathrm{rwa}} = \begin{pmatrix} \Delta_1+\tilde{E}_p & \frac{\omega_{pn}}{2} & \frac{\omega_{ps}}{2} \\ \frac{\omega_{np}}{2} & \Delta_2+\tilde{E}_n & 0 \\ \frac{\omega_{sp}}{2} & 0 & \tilde{E}_s \end{pmatrix} \tag{8.12}$$

is found. The laser detunings are defined by $\Delta_1 = E_p - E_s - \omega_1$ and $\Delta_2 = E_n - E_s - \omega_1 - \omega_2$, again at the origin $X = Y = 0$ and for $B = 0$. To be consistent with the usual notation, we introduced the single-photon Rabi frequencies ω_{ps} and ω_{np} of the first and second transition, respectively:

$$\omega_{ps} = \tfrac{1}{2}(\cos\gamma + \cos\beta - i\sin\gamma\sin\beta)\cdot\omega_{ps}^{(0)} = \omega_{sp}^{*}\,, \tag{8.13}$$

$$\omega_{np} = \tfrac{1}{2}(\cos\gamma + \cos\beta + i\sin\gamma\sin\beta)\cdot\omega_{np}^{(0)} = \omega_{pn}^{*}\,. \tag{8.14}$$

$\omega_{ps}^{(0)} = E_{1,0}\langle p|\tilde{\boldsymbol{\epsilon}}_+\cdot\mathbf{r}|s\rangle$ and $\omega_{np}^{(0)} = E_{2,0}\langle n|\tilde{\boldsymbol{\epsilon}}_-\cdot\mathbf{r}|p\rangle$ denote the single-photon Rabi frequency at the trap center. Note that within the simplified three-level scheme, only the contributions of the 'original' polarization vectors $\boldsymbol{\epsilon}_+$ and $\boldsymbol{\epsilon}_-$ for the first and second laser, respectively, are kept from the transformed laser interaction $\boldsymbol{\epsilon}_\pm U_r\mathbf{r}U_r^{\dagger}$. We remark that in the regime of strong Ioffe fields, where the simplified three-level scheme is valid, the spatial dependencies

of Eqs. (8.13-8.13) are largely negligible. Hence, the single-photon Rabi frequencies are to a good approximation given by their values $\omega_{ps}^{(0)}$ and $\omega_{np}^{(0)}$ at the origin.

Adiabatic Elimination of the Intermediate State

We are considering the regime where the intermediate level p is only weakly coupled to both the ground state s and the Rydberg level n. Such a scenario allows us to adiabatically eliminate the intermediate state p from the excitation dynamics, as we are going to show in the following. To begin with, let us rewrite Hamiltonian (8.12) as

$$\mathcal{H}_{\mathrm{rwa}} = \underbrace{\begin{pmatrix} \Delta_1 + \tilde{E}_p & 0 & 0 \\ 0 & \Delta_2 + \tilde{E}_n & 0 \\ 0 & 0 & \tilde{E}_s \end{pmatrix}}_{\equiv \mathcal{H}_0} + \underbrace{\begin{pmatrix} 0 & \frac{\omega_{pn}}{2} & \frac{\omega_{ps}}{2} \\ \frac{\omega_{np}}{2} & 0 & 0 \\ \frac{\omega_{sp}}{2} & 0 & 0 \end{pmatrix}}_{\equiv \mathcal{V}} . \tag{8.15}$$

In this picture, $\mathcal{V}$ represents a perturbation that couples the "model space" $\{n, s\}$ to the one-dimensional orthogonal subspace $\{p\}$. If $|\Delta_1| \gg \omega_{ps}$ and $|\Delta_1 - \Delta_2| \gg \omega_{np}$, quasidegenerate van Vleck perturbation theory allows us to introduce a unitary transformation e^{-G} that block diagonalizes $\mathcal{H}_{\mathrm{rwa}}$. In this manner, the subspace $\{p\}$ is decoupled from the dynamics of the model space $\{n, s\}$, yielding an effective Hamiltonian $H_{2l} = H_0 + W$ for the latter. Our goal is to determine the unitary transformation e^{-G} and hence the effective interaction W within the model space $\{n, s\}$.

The formalism to calculate G and accordingly W is derived in Ref. [118], which we are going to briefly summarize in the following. We consider a general Hamiltonian H that can be divided into a zero-order part H_0 and a perturbation V, i.e., $H = H_0 + V$, with zero-order eigenfunctions $H_0|t\rangle = \varepsilon_t|t\rangle$. The set of eigensolutions of H_0 can then be partitioned into two subsets

$$\{t, u, \dots\} = \{\alpha, \beta, \dots\} \cup \{i, j, \dots\}$$

defining the model space $\{\alpha, \beta, \dots\}$ and its orthogonal complement. The projection operator into the model space and its orthogonal complement read $P = \sum_\alpha |\alpha\rangle\langle\alpha|$ and $Q = 1 - P = \sum_i |i\rangle\langle i|$, respectively. Any operator A can be partitioned into a block diagonal part A_D and a block off-diagonal part A_X, $A = A_D + A_X$, where $A_D = PAP + QAQ$ and $A_X = PAQ + QAP$. For a product of two operators we find $(AB)_D = A_D B_D + A_X B_X$ and $(AB)_X = A_D B_X + A_X B_D$. Since H_0 is diagonal, we have for the Hamiltonian in general

$$\begin{aligned} H_D &= H_0 + V_D \,, \\ H_X &= V_X \,. \end{aligned}$$

Within the canonical form of van Vleck perturbation theory, we require $G = G_X$, i.e., $G_D = 0$ for the operator determining the unitary transformation e^{-G}. Moreover, G is an anti-Hermitian operator, $G = -G^\dagger$. It is defined order by order via

$$\begin{aligned} [H_0, G^{(1)}] &= -V_X \,, \\ [H_0, G^{(2)}] &= -[V_D, G^{(1)}] \,, \\ [H_0, G^{(3)}] &= -[V_D, G^{(2)}] - \tfrac{1}{3}[[V_x, G^{(1)}], G^{(1)}] \,. \end{aligned} \tag{8.16}$$

For higher orders, see Ref. [118]; the zeroth order contribution vanishes, i.e., $G^{(0)} = 0$. The order-by-order computation of the effective interaction W follows as

$$\begin{aligned} W^{(1)} &= V_D\,, \\ W^{(2)} &= \tfrac{1}{2}[V_X, G^{(1)}]\,, \\ W^{(3)} &= \tfrac{1}{2}[V_X, G^{(2)}]\,. \end{aligned} \tag{8.17}$$

Explicit equations for the $G^{(n)}$ can be gained from Eqs. (8.16) using the resolvent formalism. The resolvent operator $R_\alpha^{(0)}$ is defined as

$$R_\alpha^{(0)} = \frac{Q}{\varepsilon_\alpha - H_0} = \sum_i \frac{|i\rangle\langle i|}{\varepsilon_\alpha - \varepsilon_i}\,.$$

Employing $G|\alpha\rangle = G_X|\alpha\rangle = (PGQ + QGP)|\alpha\rangle = \sum_i |i\rangle\langle i|G|\alpha\rangle$, we find

$$-R_\alpha^{(0)}[H_0, G]|\alpha\rangle = -\sum_i \frac{|i\rangle\langle i|}{\varepsilon_\alpha - \varepsilon_i}[H_0, G]|\alpha\rangle = \sum_i |i\rangle\langle i|G|\alpha\rangle = G|\alpha\rangle\,. \tag{8.18}$$

Equating Eq. (8.18) order by order and utilizing Eq. (8.16) yields for $G^{(1)}$ the matrix representation

$$\begin{aligned} \mathcal{G}_{j\alpha}^{(1)} &= \langle j|G^{(1)}|\alpha\rangle \\ &= \langle j|\big\{ - R_\alpha^{(0)}[H_0, G^{(1)}]|\alpha\rangle\big\} \\ &= \langle j| \sum_i \frac{\langle i|V_X|\alpha\rangle}{\varepsilon_\alpha - \varepsilon_i}|i\rangle \\ &= \frac{\mathcal{V}_{j\alpha}}{\varepsilon_\alpha - \varepsilon_j}\,. \end{aligned} \tag{8.19}$$

Note that per definition there are no block diagonal contributions to $\mathcal{G}$. The second order matrix elements of the effective interaction W correspondingly read

$$\begin{aligned} \mathcal{W}_{\beta\alpha}^{(2)} &= \langle\beta|\tfrac{1}{2}[V_X, G^{(1)}]|\alpha\rangle \\ &= \tfrac{1}{2}\Big[\langle\beta|V_X G^{(1)}|\alpha\rangle + \langle\alpha|V_X^\dagger G^{(1)}|\beta\rangle^*\Big] \\ &= \tfrac{1}{2}\sum_i \mathcal{V}_{\beta i}\mathcal{V}_{i\alpha}\Big(\frac{1}{\varepsilon_\alpha - \varepsilon_i} + \frac{1}{\varepsilon_\beta - \varepsilon_i}\Big)\,, \end{aligned} \tag{8.20}$$

where we made use of Eqs. (8.16) and (8.18) as well as $G^\dagger = -G$, and assumed $V_X^\dagger = V_X$.

Now, we are in a position to treat our initial three-level problem Eq. (8.15). The model space is constituted by the ground- and Rydberg state, i.e., $\{\alpha, \beta, \dots\} = \{s, n\}$, and its orthogonal complement is defined by the intermediate level p. The zero-order energies read $\varepsilon_p = \tilde{E}_p + \Delta_1$, $\varepsilon_n = \tilde{E}_n + \Delta_2$, and $\varepsilon_s = \tilde{E}_s$. The perturbation V only possesses block off-diagonal matrix elements, i.e., $V_D = 0$ and $\mathcal{V}_{i\alpha} = \omega_{i\alpha}/2$. Hence, the first order of the effective interaction vanishes, $W^{(1)} = 0$, cf. Eq. (8.17). The first non-vanishing order is the second

one, whose matrix representation within the model space reads according to Eq. (8.20)

$$\mathcal{W}^{(2)}_{\beta\alpha} = \tfrac{1}{8}\omega_{\beta p}\omega_{p\alpha}\Big(\frac{1}{\varepsilon_\alpha - \varepsilon_p} + \frac{1}{\varepsilon_\beta - \varepsilon_p}\Big)\,. \tag{8.21}$$

Two-Level Hamiltonian

After all, the above described procedure provides us an effective two-level system whose excitation dynamics are determined up to second order by the Hamiltonian

$$\mathcal{H}_{2l} = \mathcal{H}_0 + \mathcal{W}^{(2)} = \begin{pmatrix} \Delta_2 + \tilde{E}_n + V_n & \Omega/2 \\ \Omega^*/2 & \tilde{E}_s + V_s \end{pmatrix}. \tag{8.22}$$

The interaction between the ground- and Rydberg state s and n is given by the two-photon Rabi frequency

$$\Omega = \frac{\omega_{ps}\omega_{np}}{4}\left[\frac{1}{\tilde{E}_s - \tilde{E}_p - \Delta_1} + \frac{1}{\tilde{E}_n - \tilde{E}_p + \Delta_2 - \Delta_1}\right]. \tag{8.23}$$

Moreover, the effective interaction W yields the diagonal elements

$$V_n = -\frac{1}{4}\frac{|\omega_{np}|^2}{\tilde{E}_p - \tilde{E}_n + \Delta_1 - \Delta_2}\,, \tag{8.24}$$

$$V_s = -\frac{1}{4}\frac{|\omega_{ps}|^2}{\tilde{E}_p - \tilde{E}_s + \Delta_1} \tag{8.25}$$

which are the so-called *light shifts* of the Rydberg and ground state, respectively. In the limit $\Delta_1 \gg \Delta_2$ and neglecting the energy surfaces $\tilde{E}_i$ – which means looking at the trap center – one recovers $\Omega = -\omega_{ps}\omega_{np}/2\Delta_1$, $V_n = -|\omega_{np}|^2/4\Delta_1$, and $V_s = -|\omega_{ps}|^2/4\Delta_1$.

The diagonalization of Hamiltonian (8.22) yields the *dressed* Rydberg (+) and ground state energy surfaces (−)

$$E_\pm(\mathbf{R}) = \frac{1}{2}\left[\tilde{E}_s + V_s + \tilde{E}_n + V_n + \Delta_2 \pm \sqrt{(\tilde{E}_n + V_n - \tilde{E}_s - V_s + \Delta_2)^2 + \Omega^2}\right] \tag{8.26}$$

that serve as trapping potential for the external motion. Here, we are mainly interested in the dressed potential for the ground state. For large detunings $\Delta_2 \gg \Omega$ one can approximate

$$E_-(\mathbf{R}) \approx \tilde{E}_s + V_s - \frac{\Omega^2}{4\Delta_2} + \frac{\Omega^2}{4\Delta_2^2}(\tilde{E}_n + V_n - \tilde{E}_s - V_s)\,, \tag{8.27}$$

i.e., the contribution of the Rydberg surface $\tilde{E}_n$ to the dressed ground state trapping potential $E_-(\mathbf{R})$ is suppressed by the factor $(\Omega/\Delta_2)^2$. Note that any spatial variation in the light shift V_s and in the Rabi frequency Ω will effectively alter the trapping potential experienced by the dressed ground state atom.

8.4 Dressed Ground State Trapping Potentials

In this section, we investigate the dressed ground state trapping potentials arising from the two-photon coupling described in Section 8.2. Since the actual shape of these energy surfaces is determined by the interplay of the various parameters belonging to the field configuration (B and G) as well as to the laser couplings ($\omega_{ps}^{(0)}$, $\omega_{np}^{(0)}$, Δ_1, and Δ_2), there is a plethora of possible configurations. Nevertheless, one can distinguish basically two relevant regimes based on the magnetic field parameters. First of all, there is the regime where the ground state trapping potential is substantially influenced by the admixture of the Rydberg surface. This regime is usually encountered for a Ioffe dominated magnetic field configuration combined with a relatively strong laser coupling. In contrast, the second regime is obtained for strong gradient fields. In this case, the resulting spatially inhomogeneous light shift determines the characteristics of the ground state trapping potential and the contribution of the Rydberg surface is of minor importance. Exemplary dressed energy surfaces belonging to both regimes are discussed in the following. We stress that for determining the dressed trapping potentials the full 32-level scheme is solved. Comparisons with the analytically obtained result Eq. (8.26) are provided. As in the previous chapter, a Rydberg state of $n = 40$ is considered throughout this section.

In Figures 8.2(a)-(b) the trapping potential of the dressed ground state atom is illustrated for the configuration $B = 10\,\mathrm{G}$, $G = 2.5\,\mathrm{Tm}^{-1}$, $\omega_{ps}^{(0)} = \omega_{np}^{(0)} = 2\pi\times 30\,\mathrm{MHz}$, $\Delta_1 = -2\pi\times 1\,\mathrm{GHz}$, and $\Delta_2 = -2\pi \times 2.5\,\mathrm{MHz}$. In this Ioffe field dominated case, the contribution $E_{40S}^{(2)}(\mathbf{R})$ to the Rydberg trapping potential $E_{40S}(\mathbf{R})$ is very strong, cf. Eq. (8.2). As a result, the Rydberg potential energy surface is extremely shallow and does not confine even a single center of mass state.[3] According to Eq. (8.27), this strong deviation from the harmonic confinement of the ground state, $E_{5S}(\mathbf{R}) \propto \frac{1}{2}M\omega^2\rho^2$, is consequently mirrored in the dressed ground state potential: Along the diagonal ($X = Y$), where the effect of $E_{40S}^{(2)}(\mathbf{R})$ is most pronounced, the trapping potential is gradually lowered compared to the harmonic confinement of the non-dressed ground state, cf. Fig. 8.2(b). Along the axes ($X = 0$ or $Y = 0$), on the other hand, $E_{\kappa}^{(2)}(\mathbf{R})$ vanishes and the non-dressed Rydberg and ground state energy surfaces coincide. As a consequence, the continuous azimuthal symmetry of the two-dimensional ground state trapping potential is reduced to a four-fold one, see Fig. 8.2(a).

In addition to the full numerical solution, in Fig. 8.2(b) the results of the simplified three-level scheme according to Eq. (8.26) are illustrated as well (dotted line). Since in the Ioffe-field dominated regime the spatial variation of the quantization axis is minor, Eq. (8.26) agrees very well with the solution of the full 32-level problem (solid line). This allows us to recapitulate the above made observations on grounds of the analytical expressions available within the reduced level scheme. For this reason, let us first consider the single photon Rabi frequencies as given by Eqs. (8.13-8.14). Because of the strong Ioffe field, they experience only a weak spatial dependence and are therefore essentially defined by their values $\omega_{ps}^{(0)}$ and $\omega_{np}^{(0)}$ at the origin. As a consequence, also the light shifts V_n and V_s [cf. Eqs. (8.24-8.25)] as well as the effective two-photon Rabi frequency Ω [cf. Eq. (8.23)], can be approximated by their values at the origin. Hence, these quantities are not contributing to the particular shape of the dressed ground state energy surface. Omitting in this manner all contributions from Eq. (8.27) that

[3] For a detailed discussion of the Rydberg trapping potentials, see Chapter 7.

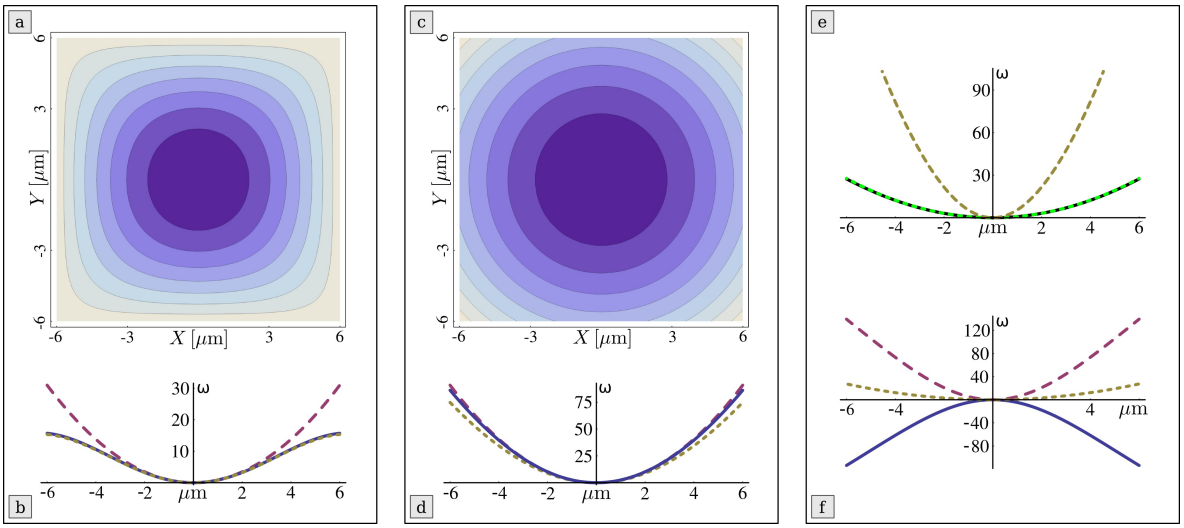

Figure 8.2: (a) Contour plot of the dressed ground state trapping potential for $B = 10\,\mathrm{G}$, $G = 2.5\,\mathrm{Tm}^{-1}$, $\omega_{ps}^{(0)} = \omega_{np}^{(0)} = 2\pi \times 30\,\mathrm{MHz}$, $\Delta_1 = -2\pi \times 1\,\mathrm{GHz}$, and $\Delta_2 = -2\pi \times 2.5\,\mathrm{MHz}$. (b) Cut along the diagonal $X = Y$ of the same surface (solid line); the dotted line corresponds to the analytical solution Eq. (8.26) of the simplified three level system. For comparison, the cut along the axis $X = 0$ – where $E_{40S}^{(2)}(\mathbf{R})$ does not contribute – is also illustrated, which corresponds to the trapping potential $E_{5S}(\mathbf{R})$ of the ground state (dashed line). (c) and (d) Same as in subfigures (a) and (b), respectively, but for $B = 1\,\mathrm{G}$. (e) Cut along the diagonal of the dressed ground state trapping potential for $B = 0.25\,\mathrm{G}$, $G = 2.5\,\mathrm{Tm}^{-1}$, $\omega_{ps}^{(0)} = 2\pi \times 500\,\mathrm{MHz}$, $\omega_{np}^{(0)} = 2\pi \times 30\,\mathrm{MHz}$, $\Delta_1 = -2\pi \times 10\,\mathrm{GHz}$, and $\Delta_2 = -2\pi \times 5\,\mathrm{MHz}$. Note that in this strong gradient regime the trapping potential shows a continuous azimuthal symmetry, hence the corresponding contour plot is not provided. The trap frequency of the dressed surface (solid line) is greatly reduced compared to the trapping potential $E_{5S}(\mathbf{R})$ of the ground state (dashed line). Turning of the second laser, i.e., setting $\omega_{np}^{(0)} = 0$ hardly changes the shape of the potential surface (dotted line). (f) Spatially dependent light shift (solid line) that in combination with the energy surface of the ground state (dashed line) leads to the trapping potential presented in subfigure (e) (dotted line). The energy scale of all subfigures is given by the ground state trap frequency $\omega = \sqrt{G^2/MB}$.

merely yield a constant energy offset, one arrives at

$$E_-(\mathbf{R}) = \tilde{E}_{5S}(\mathbf{R}) + \frac{\Omega^2}{4\Delta_2^2} E_{40S}^{(2)}(\mathbf{R}) + \text{const.} \tag{8.28}$$

That is, the deviation of the dressed ground state surface from its non-dressed counterpart is given by

$$E_-(\mathbf{R}) - E_{5S}(\mathbf{R}) = \frac{\Omega^2}{4\Delta_2^2} E_{40S}^{(2)}(\mathbf{R})\,.$$

This complies with the observations made before: $E_\kappa^{(2)}(\mathbf{R})$ possesses the envisaged $\boldsymbol{C}_{4v}$ symmetry and contributes mostly close to the diagonals of the two-dimensional trapping surface while vanishing on the axes. Moreover, $E_{40S}^{(2)}(\mathbf{R}) < 0$ which agrees with the lowering of the energy surface. Hence, the regime of strong Ioffe fields in combination with a strong laser coupling allows us to map the specific features of the Rydberg trapping potential onto the ground state.

In Figure 8.2(c)-(d) the same dressed trapping potential as before is illustrated, but now for $B = 1\,\mathrm{G}$. The reduction of the Ioffe field strength has basically two effects. First of all, considering the same spatial range as before the variation of the quantization axis is stronger. Consequently, the simplified three-level approach starts to deviate from the exact solution, as can be observed in Fig. 8.2(d). Secondly, decreasing the Ioffe field influences the dressed potential by altering the Rydberg surface. For $B = 1\,\mathrm{G}$, $G = 2.5\,\mathrm{Tm}^{-1}$, the Rydberg trapping potential is not quite as shallow as for $B = 10\,G$, $G = 2.5\,\mathrm{Tm}^{-1}$ and now supports a few confined center of mass states, see Chapter (7). Consequently, the deviation between the Rydberg and the ground state surface is not as strong as in the previous case, resulting in a reduced lowering of the energy surface along the diagonal. Considering the two-dimensional trapping potential, the azimuthal symmetry is thus nearly recovered. In view of Eq. (8.28) this can be understood as follows. While the contribution $E^{(2)}_{40S}(\mathbf{R})$ is identical for both cases (it depends only on the magnetic field gradient G rather than on the Ioffe field strength B), the spatial dependence of $E_{5S}(\mathbf{R})$ is stronger in the case of the weaker Ioffe field. Hence, for a decreasing Ioffe field the importance of $E^{(2)}_{40S}(\mathbf{R})$ is diminished and the original behavior of the ground state trapping potential $E_{5S}(\mathbf{R})$ is more and more recovered. Note that this does *not* imply a weaker contribution of the Rydberg level to the dressed state. This regime is thus particularly useful if any change of the trapping surface due to the Rydberg dressing is not desirable but the admixture of the Rydberg character is still wanted. Utilizing state-dependent Rydberg-Rydberg interactions for quantum information protocols might be a possible application for such a scenario: As shown in Section 7.6 of the previous chapter, the dephasing of the external motion of Rydberg and ground state atoms reduces the purity of an initially prepared pure state. This issue can be avoided by employing dressed ground state atoms in the just described regime where the trapping potential is only marginally influenced. The Rydberg admixture to the atomic wave function of the dressed atom then provides the desired properties specific for Rydberg atoms, as for example a strong mutual interaction.

Regarding the magnetic field parameters, the previous example represents the intermediate regime between the Ioffe dominated and the gradient dominated case; the latter let us investigate in the following. To achieve a strong gradient Ioffe-Pritchard configuration, we further reduce the Ioffe field to $B = 0.25\,\mathrm{G}$ and leave the magnetic field gradient $G = 2.5\,\mathrm{Tm}^{-1}$ unchanged. An important aspect of the strong gradient regime is the contribution of $E^{(2)}_{40S}(\mathbf{R})$ to the dressed ground state energy surface. Already in the case of Figs. 8.2(b)-(d) it was indicated that the influence of $E^{(2)}_{40S}(\mathbf{R})$ is diminished if the gradient field becomes more important. Indeed, for the present field parameters the deviation of the Rydberg trapping potential from the ground state potential is minor and many center of mass states can be confined. Thus in the spatial domain we are considering, the continuous azimuthal symmetry of the ground state trapping potential is conserved and we present in Fig. 8.2(e)-(f) only cuts along the diagonal of the dressed ground state energy surface. The parameters of the lasers are $\omega^{(0)}_{ps} = 2\pi \times 500\,\mathrm{MHz}$, $\omega^{(0)}_{np} = 2\pi \times 30\,\mathrm{MHz}$, $\Delta_1 = -2\pi \times 10\,\mathrm{GHz}$, and $\Delta_2 = -2\pi \times 5\,\mathrm{MHz}$.

The dashed line in Fig. 8.2(e) represents the non-dressed ground state trapping potential, $E_{5S}(\mathbf{R})$. As one can observe, the two-photon dressing (solid line) substantially alters this surface by significantly reducing the trap frequency, namely, from 638 Hz to 239 Hz. Although the simplified three-level system derived in Section 8.3 is not able to reproduce this result quantitatively, it nevertheless provides us a qualitative understanding of the underlying physics, as we shall demonstrate in the following. In the case of a strong gradient field, the

light shift V_s experienced by the ground state atom, Eq. (8.25), shows a strong spatial dependence and therefore cannot be omitted in Eq. (8.27). Specifically, it can be approximated for small center of mass coordinates by

$$V_s \approx V_s^{(0)} \cdot \left(1 - \frac{1}{2}\frac{G^2\rho^2}{B^2}\right),$$

where $V_s^{(0)} = -\frac{1}{4}\frac{|\omega_{ps}^{(0)}|^2}{\tilde{E}_p - \tilde{E}_s + \Delta_1}$ denotes the light shift at the origin. Except for constant contributions, the dressed ground state surface then reads

$$\begin{aligned} E_-(\mathbf{R}) &\propto E_{5S}(\mathbf{R}) - \frac{1}{2}\frac{G^2\rho^2}{B^2}V_s^{(0)} \\ &= \frac{1}{2}M(\omega^2 - \frac{G^2}{MB^2}V_s^{(0)})\rho^2, \end{aligned} \tag{8.29}$$

i.e., one encounters a reduced trap frequency $\tilde{\omega}^2 \equiv \omega^2 - \frac{G^2}{MB^2}V_s^{(0)}$. Note that the azimuthal symmetry of $E_-(\mathbf{R})$ is conserved; hence the dressed trapping potentials experienced in this regime are qualitatively different from the one of Figs. 8.2(a)-(b). We stress that Eq. (8.29) only serves for our qualitative understanding of the underlying physics. In the given regime, it fails to quantitatively reproduce the dressed potentials. The actual spatial dependence of the light shift is illustrated as the solid line in Fig. 8.2(f). It has been calculated by solving the full 32-level system but without the contribution of the Ioffe-Pritchard trapping potentials. The combination with the confinement $E_{5S}(\mathbf{R})$ (dashed line) finally yields the surface of reduced trap frequency (dotted line).

The dotted line in Fig. 8.2(e) represents the trapping potential for $\omega_{np}^{(0)} = 0$, i.e., in absence of the second laser that couples to the Rydberg state. Remarkably, turning off the second laser hardly changes the dressed potential. Hence, for the given example it is the interplay between the spatially varying quantization axis of the Ioffe-Pritchard field and the fixed polarization of the first laser that determines the spatially dependent light shift. As in the case of Figs. 8.2(c)-(d), this does not mean that the Rydberg state does not contribute to the dressed state even if the second laser is turned on. Hence, in the strong gradient regime we have two means to manipulate a ground state atom: With the first laser, one can alter the trapping potential experienced by the dressed atom and with the second laser we can in addition admix some Rydberg character to the atomic wave function.

Dressed Trapping Potentials of the $m_F = 0$ State

In the discussion above, we focused on the dressed ground state arising from the $m_F = 2$ magnetic sublevel of the $5S_{1/2}, F = 2$ electronic state. Since ultracold samples of ground state atoms can nowadays routinely prepared in this state, this is the most natural and sensible choice. Nevertheless, intriguing physics is also found for different states. As an example, we consider in the following dressed states of the $m_F = 0$ sublevel. Note that the latter is untrapped in a pure Ioffe-Pritchard trap, i.e., without the coupling lasers. Therefore, one can expect that the influence of the specific features of the Rydberg trapping potential on the shape of the dressed surface is much more pronounced than in the case of the $m_F = 2$ dressed state. Both examples that are presented in the following belong to the strong gradient regime

where the simplified three-level scheme is not valid anymore and the full 32-level system must be considered.

In Figures 8.3(a)-(b) the trapping potential of the dressed $m_F = 0$ ground state atom is illustrated for the configuration $B = 1\,\mathrm{G}$, $G = 10\,\mathrm{Tm}^{-1}$, $\omega_{ps}^{(0)} = 2\pi \times 100\,\mathrm{MHz}$, $\omega_{np}^{(0)} = 2\pi \times 35\,\mathrm{MHz}$, $\Delta_1 = -2\pi \times 4\,\mathrm{GHz}$, and $\Delta_2 = -2\pi \times 10\,\mathrm{MHz}$.[4] The first thing to note is that – in contrast to the non-dressed $m_F = 0$ state – the atom experiences a confining potential that is due to the spatially dependent light shift of the off-resonant laser coupling. Moreover, Figure 8.3(a) reveals the four-fold symmetry known from the Rydberg trapping potential $E_{40S}(\mathbf{R})$. Because the admixed Rydberg surface has not to compete against a strong magnetic confinement of the ground state according to $\boldsymbol{\mu}_F \cdot \mathbf{B}(\mathbf{R})$, the anti-trapping effect of $E_{40S}^{(2)}(\mathbf{R})$ becomes particularly visible in the dressed potential of the $m_F = 0$ state. In Figure 8.3(b) once more the cut along the diagonal of the dressed potential is illustrated (solid line). As expected, the admixture of the Rydberg surface eventually changes the character of the trapping potential from confining to de-confining when going to larger center of mass coordinates. However, for very large coordinates a weak confining behavior is recovered that can be explained as follows. For such large center of mass coordinates, the contribution $E_{40S}^{(2)}(\mathbf{R})$ shifts the Rydberg state far off-resonant and thereby diminishes the contribution of the Rydberg level to the dressed state. The slightly confining character of the dressed potential in this regime is reminiscent of the spatially dependent light shift. Note that the azimuthally symmetric dressed potential arising in absence of the second laser (dotted line) coincides very well with the two-photon dressed potential along the axes (dashed line). Hence, the first laser can be used to trap and prepare the atoms in the $m_F = 0$ ground state. By switching on the second laser, the Rydberg state gets admixed, resulting in the above described significant change of the trapping potential in the vicinity of the diagonals ($X = Y$). Overall, the influence of the Rydberg surface is much more distinct than in the case of the $m_F = 2$ dressed states, cf. Fig. 8.2.

For a comparison, we show in Figs. 8.3(c)-(d) the dressed trapping potentials of the $m_F = 0$ state for a more dominant gradient field and a red-detuned first laser. The actual parameters are $B = 0.5\,\mathrm{G}$, $G = 10\,\mathrm{Tm}^{-1}$, $\omega_{ps}^{(0)} = 2\pi \times 100\,\mathrm{MHz}$, $\omega_{np}^{(0)} = 2\pi \times 50\,\mathrm{MHz}$, $\Delta_1 = 2\pi \times 2\,\mathrm{GHz}$, and $\Delta_2 = -2\pi \times 10\,\mathrm{MHz}$. This configuration results in a much tighter confinement ($\omega = 2\pi \times 718\,\mathrm{Hz}$ compared to $\omega = 2\pi \times 78\,\mathrm{Hz}$ for the previous example) and a deeper trap along the diagonals. On the other hand, the revival of the weak trapping character as previously observed in Fig. 8.3(b) for large center of mass coordinates along the diagonal is lost since the light shift of the first laser already reached a constant asymptotic behavior in this regime.[5] As discussed for the previous example, the contribution $E_{40S}^{(2)}(\mathbf{R})$ shifts the Rydberg state far off-resonant and thereby diminishes the influence of the second laser on the excitation dynamics. Consequently, for large center of mass coordinates close to the diagonal the dressed surface approaches the asymptotic of the single-photon dressing of the first laser [dotted line in Fig. 8.3(d)]. In contrast, along the axes (dashed line) the potential does not reach

[4] Note that the laser parameters, i.e., the single-photon Rabi frequencies and the detunings are defined in exactly the same way as in Sections 8.2 and 8.3.

[5] For such large center of mass coordinates and such a strong gradient field, the magnetic field direction is solely determined by the gradient field vector, i.e., $\mathbf{B} \propto (X, -Y, 0)^T$. As a consequence, we find a constant quantization axis along the diagonals in this regime. Similarly, the spatial variance of the polarization vector vanishes, resulting in a constant light shift.

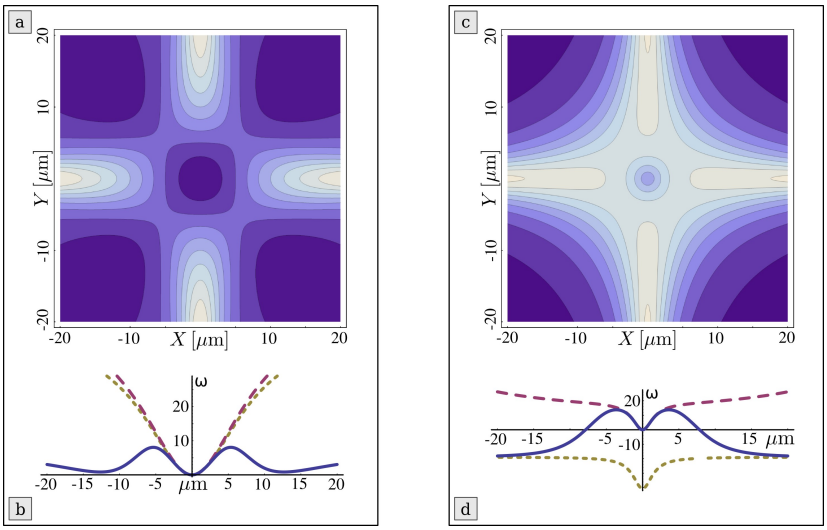

Figure 8.3: (a) Contour plot of the dressed ground state trapping potential for the $5S_{1/2}, m_F = 0$ state. The parameters are $B = 1\,\mathrm{G}$, $G = 10\,\mathrm{Tm}^{-1}$, $\omega_{ps}^{(0)} = 2\pi \times 100\,\mathrm{MHz}$, $\omega_{np}^{(0)} = 2\pi \times 35\,\mathrm{MHz}$, $\Delta_1 = -2\pi \times 4\,\mathrm{GHz}$, and $\Delta_2 = -2\pi \times 10\,\mathrm{MHz}$. (b) Cut along the diagonal $X = Y$ (solid line) and along the axis with $X = 0$ (dashed line) of the same surface; the dotted line corresponds to the single-photon dressing, i.e., $\omega_{np}^{(0)} = 0$. For comparison, all curves are offset to zero at the origin. (c) and (d) Same as in subfigures (a) and (b), respectively, but for $B = 0.5\,\mathrm{G}$, $G = 10\,\mathrm{Tm}^{-1}$, $\omega_{ps}^{(0)} = 2\pi \times 100\,\mathrm{MHz}$, $\omega_{np}^{(0)} = 2\pi \times 50\,\mathrm{MHz}$, $\Delta_1 = 2\pi \times 2\,\mathrm{GHz}$, and $\Delta_2 = -2\pi \times 10\,\mathrm{MHz}$. In subfigure (d) we refrained from offsetting all curves to zero at the origin but rather applied a common offset such that the joint asymptote of the solid and dotted line becomes evident. Note that the detunings are defined in the same way as for the $5S_{1/2}, m_F = 2$ case. The energy scale in all subfigures is given in terms of the trap frequency. The latter has been gained by a harmonic fit around the origin, yielding $\omega = 2\pi \times 78\,\mathrm{Hz}$ and $\omega = 2\pi \times 718\,\mathrm{Hz}$ for the first and second configuration, respectively.

a constant asymptote but maintains a weak confining behavior. The latter is due to the admixture of predominantly $m_j = 1/2$ Rydberg states: Since we assumed the two-photon transition to be blue-detuned, the magnetic field interaction $\sim m_j|\mathbf{B}(\mathbf{R})|$ pushes the $m_j = 1/2$ Rydberg state closer to resonance and in the same manner repels its $m_j = -1/2$ counterpart. Hence, the dressed state shows a stronger admixture of trapped than anti-trapped Rydberg states, giving rise to a confining energy surface. We remark that the dressed state not only shows contributions of the Rydberg state. In fact, the first laser slightly mixes the $5S_{1/2}, F = 2, m_F = 0$ state with $m_F \neq 0$ states of the same hyperfine level. However, the $m_F < 0$ states are admixed in the same degree as their $m_F > 0$ counterparts such that their confining and de-confining character cancels.

Experimental Issues

At this point, let us comment on the experimental feasibility of the above discussed scheme. The proposed dressed states possess a finite effective lifetime that can be estimated by

$$\tau = \frac{\tau_n}{|c_n|^2}\,, \tag{8.30}$$

c_n being the admixture coefficient of the Rydberg state; within the simplified three-level scheme it evaluates to $|c_{n,3l}|^2 = (\Omega/2\Delta_2)^2$. τ_n denotes the radiative lifetime of the $nS_{1/2}$

Table 8.1: Effective lifetimes of the dressed states considered in this section. The lifetimes are determined according to Eq. (8.30) using the Rydberg admixture coefficient c_n of the full 32-level system. When applicable, the admixture coefficient $c_{n,3l}$ of the simplified three-level system is provided for comparison.

Configuration	$\lvert c_{n,3l}\rvert^2$	$\lvert c_n\rvert^2$	τ_n(ms)
Fig. 8.2(a)	0.009 835	0.009 812	5.91
Fig. 8.2(c)	0.010 000	0.009 729	5.96
Fig. 8.2(e)	–	0.001 162	49.92
Fig. 8.3(a)	–	0.002 318	250.237
Fig. 8.3(c)	–	0.002 532	22.9108

Rydberg atom and can be parameterized as $\tau_n = \tau'(n-\delta)^\gamma$, cf. Eq. 2.4; for $n = 40$ we get $\tau_n = 58\,\mu$s. In Table 8.1, the effective lifetimes for the examples presented in this section are tabulated. Because the Rydberg state is only weakly admixed ($|c_n|^2 < 10^{-2}$ for all examples), very long effective lifetimes greater than one millisecond are obtained.

Similarly, the van der Waals interaction of two Rydberg atoms is suppressed by $|c_n|^4$. The latter interaction results in an energy shift δ that depends on the interparticle distance and effectively alters the detuning of the two-photon transition. In order to avoid any such effects, δ should be well below the the excitation detuning Δ_2. Taking $c_n = 0.1$ and $\delta < 2\pi \times 0.1\,$MHz as an (quite restrictive) example yields a minimum interparticle distance of $\sim 1\,\mu$m.

Dressed Rydberg Surfaces

Let us finish this chapter by commenting on the influence of the two-photon dressing on the Rydberg trapping potentials. Similarly to Eq. (8.27), for large detunings $\Delta_2 \gg \Omega$ the Rydberg surface is given by

$$E_+(\mathbf{R}) \approx \tilde{E}_n + V_n + \Delta_2 + \frac{\Omega^2}{4\Delta_2} - \frac{\Omega^2}{4\Delta_2^2}(\tilde{E}_n + V_n - \tilde{E}_s - V_s) \tag{8.31}$$

within the simplified three-level scheme. In the Ioffe field dominated regime, the spatial dependence of the light shift and the Rabi frequencies are marginal. Omitting like for Eq. (8.28) all contributions from Eq. (8.31) that merely yield a constant energy offset, we get

$$E_+(\mathbf{R}) = \tilde{E}_{5S}(\mathbf{R}) + \Big(1 - \frac{\Omega^2}{4\Delta_2^2}\Big) E^{(2)}_{40S}(\mathbf{R}) + \text{const.} \tag{8.32}$$

Comparing Eq. (8.32) with Eq. (8.28) reveals the key difference between the dressed Rydberg and ground state surfaces: Because for the latter the contribution $E^{(2)}_{40S}(\mathbf{R})$ is absent in the non-dressed case, its inclusion – although suppressed by $\Omega^2/4\Delta_2^2$ – can change the character of the trapping potential considerably, cf. Fig. 8.2(a) for example. For the Rydberg surface, however, $E^{(2)}_{40S}(\mathbf{R})$ fully contributes already in the non-dressed case. Consequently, the two-photon coupling only result in a small correction, $E^{(2)}_{40S}(\mathbf{R}) \to (1 - \Omega^2/4\Delta_2^2) E^{(2)}_{40S}(\mathbf{R})$, in the expression of the Rydberg trapping potential.

Going to the opposite limit, i.e., a strong gradient field, the spatial dependence of the light shift determined in Fig. 8.2(e) the particular shape of the dressed surface. Since the

high energy-level density of Rydberg states does not allow for a large detuning Δ_2 of the two-photon process, the light shift Eq. (8.24) of the Rydberg state can be approximated by[6]

$$V_n \approx -\frac{1}{4}\frac{|\omega_{np}|^2}{\Delta_1}\,.$$

Hence, for single-photon Rabi frequencies $\omega_{np}^{(0)}$ as considered in Figs. 8.2 and 8.3 the spatial variance of the light shift is strongly suppressed by the large detuning Δ_1. As a consequence, also in the strong gradient regime the Rydberg surface is hardly altered due to the two-photon dressing.

[6]Note that, in order to adiabatically eliminate the intermediate state, a large detuning Δ_1 of the first laser is indispensable, i.e., $\Delta_2 \ll \Delta_1$.

Chapter 9

Conclusion and Outlook

Let us finish this thesis by summarizing our findings and providing a brief outlook on further research directions in the field of ultracold Rydberg physics. The footing of this work is constituted by the thorough derivation of the theory of ultracold Rydberg atoms in a Ioffe-Pritchard trap. In particular, the working Hamiltonian in a two-particle picture (Rydberg electron and remaining ionic core) was derived, including a detailed examination of all ingredients necessary to adequately describe the low angular momentum Rydberg states of an alkali atom. Introducing center of mass and relative coordinates as well as a suitable unitary transformation allowed us to simplify the initial Hamiltonian considerably. The remaining couplings between the relative and center of mass motion were finally treated by an adiabatic approach reminiscent of the Born-Oppenheimer separation in molecular dynamics. The initial problem of coupled center of mass and electronic dynamics was thereby reduced to the determination of the adiabatic electronic energy surfaces that serve as trapping potentials for the center of mass motion. An analytical approach was introduced for gaining the adiabatic energy surfaces of a Rydberg atom in a Ioffe-Pritchard trap. While this approach relies on further approximations, it provided us nevertheless accurate results and a profound understanding of the underlying physics. For in principle arbitrarily exact results, we introduced a numerical method that employs an adapted basis set for the low angular momentum states of alkali atoms.

One-Dimensional Rydberg Gas

Before turning to the discussion of our results concerning Rydberg atoms in low angular momentum electronic states, we used the Ioffe-Pritchard configuration as a key ingredient in order to prepare and study a one-dimensional Rydberg gas consisting of long lived *circular* states. In detail, we demonstrated that in a Ioffe-Pritchard trap, which is superimposed by a homogeneous electric field, Rydberg states can be tightly confined in electronic states exhibiting a permanent electric dipole moment of hundreds of Debyes. The resulting strong repulsion between neighboring Rydberg atoms in conjunction with the tight transverse confinement was demonstrated to entail an effectively one-dimensional Rydberg gas with macroscopic interparticle distances. Analytical expressions for the density that is required to enter the one-dimensional regime were calculated. Moreover, we pointed out that the lifetime of the Rydberg states is sufficiently long to probe the dynamics of the interacting gas. This regime is complementary to the well-studied frozen Rydberg gases where mechanical atom-atom interaction effects can hardly be probed. The potential of the proposed magneto-electric trap

is by far not entirely exhausted, e.g., one could think of using the double-well structure that arises for non-circular Rydberg states in order to realize two coupled dipolar Rydberg chains.

Magnetic Trapping of Rydberg Atoms

In a next step, we theoretically investigated the electronic properties and the center of mass dynamics of the low angular momentum nS, nP, and nD states of ^{87}Rb in a Ioffe-Pritchard trap. It turned out that the composite nature of Rydberg atoms, i.e., the fact that they consists of an outer electron far away from a compact ionic core, significantly alters the coupling of the electronic motion to the inhomogeneous magnetic field of the Ioffe-Pritchard trap. We demonstrated that this leads to qualitative changes in the trapping potentials, namely, the appearance of a de-confining contribution which reduces the azimuthal symmetry to $\boldsymbol{C}_{4v}$. As a consequence, the resulting energy surfaces possess a finite depth. Analytical expressions describing the surfaces were derived and the applicability of the applied perturbative treatment has been verified for experimentally relevant field strengths by comparison with numerical solutions of the underlying Schrödinger equation. Exemplary energy surfaces of the fully polarized $n = 40$, $l = 0, 1, 2$, $m_j = j$ states were provided. A clear deviation from the harmonic confinement of a point-like particle with a trap depth of only a few vibrational quanta could be observed. Choosing different magnetic field parameters, on the other hand, stable trapping can be achieved with trap depths in the micro-Kelvin regime. The non-harmonicity of the Rydberg trapping potential becomes also apparent in the resulting center of mass dynamics: The additional contribution due to the two-body character of the Rydberg atom mixes the "unperturbed" harmonic eigenstates and thereby partially lifts their degeneracy. For an atom in its electronic ground state that is excited to a Rydberg state only for a short period of time, this provides a mechanism for parametric heating by populating excited center of mass states. The corresponding heating rate as a function of the initial center of mass state of the ground state atom has been derived. In the framework of quantum information protocols involving the short-time population of Rydberg atoms, it has been demonstrated that the same mechanism can lead to a decrease of the purity of the involved qubit states.

Mapping the Composite Character of Rydberg Atoms

In the last part of this thesis, we investigated a magnetically trapped rubidium atom that is coupled to its nS Rydberg state via a two-photon laser transition. We studied the off-resonant case where the ground state atom becomes *dressed* by the Rydberg state and vice versa. By this procedure, properties specific for the Rydberg atom become accessible also for the ground state atom. In particular, we investigated how the trapping potential experienced by a ground state atom in a magnetic Ioffe-Pritchard trap is altered because of such an off-resonant laser coupling. We demonstrated that in the limit of a strong Ioffe-field the four-fold azimuthal symmetry, which is inherent for the trapping potential of the Rydberg atom, is mirrored in the dressed ground state trapping potential. In this regime, we derived a simplified three-level scheme that facilitates the interpretation of the observed results. In the opposite regime of strong gradient fields, on the other hand, the influence of the Rydberg trapping potential is marginal. Instead, the delicate interplay between the spatially varying quantization axis of the Ioffe-Pritchard field and the fixed polarizations of the laser transitions determined the actual shape of the dressed trapping potentials.

Outlook

A rather natural extension of the present work would be the investigation of other magnetic field configurations than the Ioffe-Pritchard trap. For example, it is expected also in the case of a three-dimensional quadrupole field that similar terms associated with the composite nature of the Rydberg atom arise, significantly altering the trapping potential compared to the point-like particle description. Moreover, it would be very interesting to see to what extend inhomogeneous magnetic fields influence the trilobite and butterfly states of giant Rydberg molecules [46–49]. In particular, we envisage the regime where the composite nature of Rydberg atoms significantly alters the trap properties and a two-particle description of the Rydberg atom is indispensable.

Another very promising direction of research is the study of collective phenomena in the Rydberg excitation of an ultracold gas of ground state atoms. Besides the nowadays well-studied dipole blockade effect [33–44], first works have shown that – amongst others – also antiblockade can be achieved [119] and that on a ring lattice collective fermionic excitations can be created [120]. An extension of these works would be for example the study of finite one- or two-dimensional systems, the inclusion of unequally distributed Rabi frequencies, or going beyond nearest neighbor interactions.

Appendix A

Atomic Units

Quantity	Atomic Unit	Système International d'Unités
mass	$m_e = 1$	$9.109\,382\,15 \times 10^{-31}$ kg
charge	$e = 1$	$1.602\,176\,487 \times 10^{-19}$ C
length	$a_0 = 1$	$0.529\,177\,208\,59 \times 10^{-10}$ m
angular momentum	$\hbar = 1$	$1.054\,571\,628 \times 10^{-34}$ Js
energy	$E_h = \hbar^2/m_e a_0^2 = 1$	$4.359\,743\,94 \times 10^{-18}$ J
velocity	$a_0 E_h/\hbar = 1$	$2.187\,691\,254\,1 \times 10^{6}$ ms^{-1}
momentum	$\hbar/a_0$=1	$1.992\,851\,565 \times 10^{-24}$ kg ms^{-1}
magnetic field strength	$\hbar/ea_0^2 = 1$	$2.350\,517\,382 \times 10^{5}$ T
magnetic field gradient	$\hbar/ea_0^3 = 1$	$4.441\,834 \times 10^{15}$ Tm^{-1}
magnetic dipole moment	$\hbar e/m_e = 1$	$1.854\,801\,830 \times 10^{-23}$ JT^{-1} $= 2\mu_B$
electric dipole moment	$ea_0 = 1$	$8.478\,352\,81 \times 10^{-30}$ Cm
electric field	$E_h/ea_0 = 1$	$5.142\,206\,32 \times 10^{11}$ Vm^{-1}
time	$\hbar/E_h = 1$	$2.418\,884\,326\,505 \times 10^{-17}$ s
speed of light	$1/\alpha = 137.035\,999\,67$	$2.997\,924\,58 \times 10^{8}$ ms^{-1}

Appendix B

Center of Mass and Relative Coordinates

In this part of the Appendix, the terms involving the vector potential $\mathbf{A}(\mathbf{x})$ are derived in center of mass and relative coordinates. The latter are given by

$$\begin{aligned}
&\mathbf{r} = \mathbf{r}_e - \mathbf{r}_c && \mathbf{R} = \frac{m_e\mathbf{r}_e + M_c\mathbf{r}_c}{m_e + M_c} && M = m_e + M_c \\
&\mathbf{p} = \frac{M_c\mathbf{p}_e - m_e\mathbf{p}_c}{m_e + M_c} && \mathbf{P} = \mathbf{p}_e + \mathbf{p}_c && m = \frac{m_e M_c}{m_e + M_c} \approx m_e \,.
\end{aligned}$$

The inverse relations read correspondingly $\mathbf{r}_e = \mathbf{R} + \frac{M_c}{M}\mathbf{r}$ and $\mathbf{r}_c = \mathbf{R} - \frac{m_e}{M}\mathbf{r}$, as well as $\mathbf{p}_e = \frac{m_e}{M}\mathbf{P} + \mathbf{p}$ and $\mathbf{p}_c = \frac{M_c}{M}\mathbf{P} - \mathbf{p}$.

B.1 Paramagnetic Contributions

Let us start with the linear terms of Hamiltonian (3.2) involving the constant part $\mathbf{A}_c(\mathbf{x})$ of the vector potential:

$$\begin{aligned}
&\frac{\mathbf{A}_c(\mathbf{r}_e)\cdot\mathbf{p}_e}{m_e} - \frac{\mathbf{A}_c(\mathbf{r}_c)\cdot\mathbf{p}_c}{M_c} \\
&= \frac{B}{2}\Big\{\frac{1}{m_e}\Big[\Big(X + \frac{M_c}{M}x\Big)\Big(\frac{m_e}{M}P_y + p_y\Big) - \Big(Y + \frac{M_c}{M}y\Big)\Big(\frac{m_e}{M}P_x + p_x\Big)\Big] \\
&\quad - \frac{1}{M_c}\Big[\Big(X - \frac{m_e}{M}x\Big)\Big(\frac{M_c}{M}P_y - p_y\Big) - \Big(Y - \frac{m_e}{M}y\Big)\Big(\frac{M_c}{M}P_x - p_x\Big)\Big]\Big\} \\
&= \frac{B}{2}\Big[\Big(\frac{1}{m_e} + \frac{1}{M_c}\Big)Xp_y - \Big(\frac{1}{m_e} + \frac{1}{M_c}\Big)Yp_x + \Big(\frac{M_c}{M^2} + \frac{m_e}{M^2}\Big)xP_y - \Big(\frac{M_c}{M^2} + \frac{m_e}{M^2}\Big)yP_x \\
&\quad + \Big(\frac{M_c}{m_eM} - \frac{m_e}{M_cM}\Big)xp_y - \Big(\frac{M_c}{m_eM} - \frac{m_e}{M_cM}\Big)yp_x\Big] \\
&= \frac{B}{2}\Big[\Big(\frac{1}{m_e} + \frac{1}{M_c}\Big)(Xp_y - Yp_x) + \Big(\frac{M_c^2 - m_e^2}{m_eM_cM}\Big)(xp_y - yp_x) + \Big(\frac{M_c + m_e}{M^2}\Big)(xP_y - yP_x)\Big] \\
&= \frac{1}{m}\mathbf{A}_c(\mathbf{R})\cdot\mathbf{p} + \underbrace{\Big(\frac{1}{m_e} - \frac{1}{M_c}\Big)}_{=\frac{1}{m}-\frac{2}{M_c}}\mathbf{A}_c(\mathbf{r})\cdot\mathbf{p} + \frac{1}{M}\mathbf{A}_c(\mathbf{r})\cdot\mathbf{P}\,. \qquad \text{(B.1)}
\end{aligned}$$

Performing a similar calculation for the linear part of the vector potential $\mathbf{A}_l(\mathbf{x})$, we get

$$\begin{aligned}
&\frac{\mathbf{A}_l(\mathbf{r}_e)\cdot\mathbf{p}_e}{m_e} - \frac{\mathbf{A}_l(\mathbf{r}_c)\cdot\mathbf{p}_c}{M_c} \\
&= G\Big[\frac{1}{m_e}\Big(X+\frac{M_c}{M}x\Big)\Big(Y+\frac{M_c}{M}y\Big)\Big(\frac{m_e}{M}P_z+p_z\Big) - \frac{1}{M_c}\Big(X-\frac{m_e}{M}x\Big)\Big(Y-\frac{m_e}{M}y\Big)\Big(\frac{M_c}{M}P_z-p_z\Big)\Big] \\
&= Gp_z\Big[\Big(\frac{1}{m_e}+\frac{1}{M_c}\Big)XY + \Big(\frac{M_c}{m_eM}+\frac{m_e^2}{m_eM_cM}\Big)(Xy+xY) + \Big(\frac{M_c^2}{m_eM^2}+\frac{m_e^2}{M_cM^2}\Big)xy\Big] \\
&\quad + GP_z\Big[\Big(\frac{M_c}{M^2}+\frac{m_e}{M^2}\Big)(Xy+xY) + \frac{1}{M}\Big(\frac{M_c^2}{M^2}-\frac{m_e^2}{M^2}\Big)xy\Big] \\
&= Gp_z\Big[\frac{1}{m}XY + \Big(\frac{1}{m}-\frac{2}{M}\Big)(Xy+xY) + \Big(\frac{1}{m}-\frac{3}{M}\Big)xy\Big] \\
&\quad + GP_z\Big[\frac{1}{M}(Xy+xY) + \Big(\frac{1}{M}-2\frac{m_e}{M^2}\Big)xy\Big] \qquad \text{(B.2)} \\
&\approx G\frac{p_z}{m}\Big[XY+Xy+xY+xy\Big] + G\frac{P_z}{M}\Big[Xy+xY+xy\Big] \qquad \text{(B.3)} \\
&= \frac{G}{m}XYp_z + G\Big(\frac{p_z}{m}+\frac{P_z}{M}\Big)(xY+Xy+xy) \\
&\approx \frac{G}{m}XYp_z + \frac{G}{m}(xY+Xy+xy)p_z = \frac{1}{m}\mathbf{A}_l(\mathbf{R}+\mathbf{r})\cdot\mathbf{p}\,, \qquad \text{(B.4)}
\end{aligned}$$

where we approximated $\frac{1}{m}-\frac{2}{M}\approx\frac{1}{m}-\frac{3}{M}\approx m^{-1}$ and $\frac{1}{M}-2\frac{m_e}{M^2}\approx M^{-1}$ in Eq. (B.3) due to the large mass of the ionic core, i.e., $m/M\ll 1$. Equation (B.4) is obtained by approximating $\langle\mathbf{P}/M\rangle\ll\langle\mathbf{p}/m\rangle$ for ultracold temperatures.

B.2 Diamagnetic Contributions

Next, we consider the diamagnetic contributions arising from Hamiltonian (3.2), i.e., all terms quadratic in the vector potential $\mathbf{A}(\mathbf{x})$. Before doing so, we recognize that $\mathbf{A}_c(\mathbf{x})$ and $\mathbf{A}_l(\mathbf{x})$ are perpendicular to each other, $\mathbf{A}_c(\mathbf{x})\cdot\mathbf{A}_l(\mathbf{x})=0$, and therefore get

$$\frac{\mathbf{A}(\mathbf{r}_e)^2}{2m_e}+\frac{\mathbf{A}(\mathbf{r}_c)^2}{2M_c} = \frac{1}{2m_e}\Big[\mathbf{A}_c(\mathbf{r}_e)^2+\mathbf{A}_l(\mathbf{r}_e)^2\Big] + \frac{1}{2M_c}\Big[\mathbf{A}_c(\mathbf{r}_c)^2+\mathbf{A}_l(\mathbf{r}_c)^2\Big]. \qquad \text{(B.5)}$$

Employing furthermore that $\mathbf{A}_c(\mathbf{x})$ is linear, i.e., $\mathbf{A}_c(\mathbf{x}+\alpha\mathbf{x}')=\mathbf{A}_c(\mathbf{x})+\alpha\mathbf{A}_c(\mathbf{x}')$, yields

$$\begin{aligned}
\frac{\mathbf{A}(\mathbf{r}_e)^2}{2m_e}+\frac{\mathbf{A}(\mathbf{r}_c)^2}{2M_c} &= \frac{1}{2m_e}\Big[\mathbf{A}_c(\mathbf{R})^2+2\frac{M_c}{M}\mathbf{A}_c(\mathbf{R})\cdot\mathbf{A}_c(\mathbf{r})+\frac{M_c^2}{M^2}\mathbf{A}_c(\mathbf{r})^2+\mathbf{A}_l(\mathbf{R}+\tfrac{M_c}{M}\mathbf{r})^2\Big] \\
&\quad + \frac{1}{2M_c}\Big[\mathbf{A}_c(\mathbf{R})^2-2\frac{m_e}{M}\mathbf{A}_c(\mathbf{R})\cdot\mathbf{A}_c(\mathbf{r})+\frac{m_e^2}{M^2}\mathbf{A}_c(\mathbf{r})^2+\mathbf{A}_l(\mathbf{R}-\tfrac{m_e}{M}\mathbf{r})^2\Big]
\end{aligned} \qquad \text{(B.6)}$$

$$
\begin{aligned}
&\frac{\mathbf{A}(\mathbf{r}_e)^2}{2m_e} + \frac{\mathbf{A}(\mathbf{r}_c)^2}{2M_c} \\
&= \frac{1}{2}\Big[\Big(\frac{1}{m_e}+\frac{1}{M_c}\Big)\mathbf{A}_c(\mathbf{R})^2 + 2\Big(\frac{M_c}{m_e M}+\frac{m_e}{M_c M}\Big)\mathbf{A}_c(\mathbf{R})\cdot\mathbf{A}_c(\mathbf{r}) + \Big(\frac{M_c^2}{m_e M^2}+\frac{m_e^2}{M_c M^2}\Big)\mathbf{A}_c(\mathbf{r})^2\Big] \\
&\quad + \frac{1}{2m_e}\mathbf{A}_l(\mathbf{R}+\tfrac{M_c}{M}\mathbf{r})^2 + \frac{1}{2M_c}\mathbf{A}_l(\mathbf{R}-\tfrac{m_e}{M}\mathbf{r})^2 \\
&= \frac{1}{2m}\mathbf{A}_c(\mathbf{R})^2 + \Big(\frac{1}{m}-\frac{2}{M}\Big)\mathbf{A}_c(\mathbf{R})\cdot\mathbf{A}_c(\mathbf{r}) + \frac{1}{2}\Big(\frac{1}{m}-\frac{3}{M}\Big)\mathbf{A}_c(\mathbf{r})^2 \\
&\quad + \frac{1}{2m_e}\mathbf{A}_l(\mathbf{R}+\tfrac{M_c}{M}\mathbf{r})^2 + \frac{1}{2M_c}\mathbf{A}_l(\mathbf{R}-\tfrac{m_e}{M}\mathbf{r})^2\,. \qquad \text{(B.7)}
\end{aligned}
$$

As before, one might approximate $\frac{1}{m}-\frac{2}{M} \approx \frac{1}{m}-\frac{3}{M} \approx m^{-1}$ in Eq. (B.7). However, in anticipation of the unitary transformation that still is to be applied for these terms, we refrain from performing such an approximation at this point. We are left with the investigation of the diamagnetic terms in Eq. (B.7) involving the linear part of the vector potential. Unfortunately, $\mathbf{A}_l(\mathbf{x})$ is not linear in $\mathbf{x}$. Nevertheless, we can establish the following relation:

$$
\mathbf{A}_l(\mathbf{R}+\alpha\mathbf{r}) = \mathbf{A}_l(\mathbf{R}) + \alpha^2\mathbf{A}_l(\mathbf{r}) + \alpha\,\underbrace{G(Xy+xY)\mathbf{e}_3}_{\equiv\tilde{\mathbf{A}}}\,,
$$

Using this relation and employing similar mass-related approximations as above[1], eventually yields

$$
\begin{aligned}
&\frac{\mathbf{A}_l(\mathbf{R}+\frac{M_c}{M}\mathbf{r})^2}{2m_e} + \frac{\mathbf{A}_l(\mathbf{R}-\frac{m_e}{M}\mathbf{r})^2}{2M_c} \\
&= \frac{1}{2}\Big[\frac{1}{m}\mathbf{A}_l(\mathbf{R})^2 + 2\Big(\frac{1}{m}-\frac{3}{M}\Big)\mathbf{A}_l(\mathbf{R})\cdot\mathbf{A}_l(\mathbf{r}) + 2\Big(\frac{1}{m}-\frac{2}{M_c}\Big)\mathbf{A}_l(\mathbf{R})\cdot\tilde{\mathbf{A}} \\
&\quad + \Big(\frac{1}{m}-\frac{5}{M}+5\frac{m}{M^2}\Big)\mathbf{A}_l(\mathbf{r})^2 + 2\Big(\frac{1}{m}-\frac{4}{M}-2\frac{m_e}{M}-2\frac{m_e^2}{M_c M^2}\Big)\mathbf{A}_l(\mathbf{r})\cdot\tilde{\mathbf{A}} + \Big(\frac{1}{m}-\frac{3}{M}\Big)\tilde{\mathbf{A}}^2\Big] \\
&\approx \frac{1}{2m}\Big[\mathbf{A}_l(\mathbf{R})^2 + 2\mathbf{A}_l(\mathbf{R})\cdot\mathbf{A}_l(\mathbf{r}) + 2\mathbf{A}_l(\mathbf{R})\cdot\tilde{\mathbf{A}} + \mathbf{A}_l(\mathbf{r})^2 + 2\mathbf{A}_l(\mathbf{r})\cdot\tilde{\mathbf{A}} + \tilde{\mathbf{A}}^2\Big] \\
&= \frac{1}{2m}\mathbf{A}_l(\mathbf{R}+\mathbf{r})^2\,. \qquad \text{(B.8)}
\end{aligned}
$$

Putting all together leaves us with

$$
\begin{aligned}
\frac{\mathbf{A}(\mathbf{r}_e)^2}{2m_e} + \frac{\mathbf{A}(\mathbf{r}_c)^2}{2M_c} &\approx \frac{1}{2m}\mathbf{A}_c(\mathbf{R})^2 + \Big(\frac{1}{m}-\frac{2}{M}\Big)\mathbf{A}_c(\mathbf{R})\cdot\mathbf{A}_c(\mathbf{r}) + \frac{1}{2}\Big(\frac{1}{m}-\frac{3}{M}\Big)\mathbf{A}_c(\mathbf{r})^2 \\
&\quad + \frac{1}{2m}\mathbf{A}_l(\mathbf{R}+\mathbf{r})^2\,. \qquad \text{(B.9)}
\end{aligned}
$$

[1] We do not refrain from performing the heavy nuclear mass approximation for the terms involving $\mathbf{A}_l(\mathbf{x})$ since the latter are invariant under the unitary transformation we have in mind.

Appendix C

Unitary Transformation

In this part of the Appendix, we derive the transformation laws and the transformed Hamiltonian as given in Section 3.3. The unitary transformation that we need to apply reads

$$U = \exp\left\{ i\frac{e}{2}(\mathbf{B}_c \times \mathbf{r}) \cdot \mathbf{R} \right\} . \tag{C.1}$$

The behavior of a given operator O under such an unitary transformation can be calculated using the so-called *Baker-Campbell-Hausdorff* formula,

$$e^X O e^{-X} = \sum_{n=0}^{\infty} \frac{1}{n!}[X, O]_n \,, \tag{C.2}$$

with $[X, O]_n = [X, [X, O]_{n-1}]$, $[X, O]_0 = B$, and $X = -i\frac{e}{2}(\mathbf{B}_c \times \mathbf{r}) \cdot \mathbf{R}$ in our case. As pointed out in Section 3.3, any operator that commutes with $\mathbf{R}$ and $\mathbf{r}$ is invariant under the transformation U.

C.1 Transformation of the Momentum Operators

For the momentum operators, we find

$$\begin{aligned}
[-i\frac{e}{2}(\mathbf{B}_c \times \mathbf{r}) \cdot \mathbf{R}, \mathbf{p}] &= -i\frac{e}{2}[(\mathbf{R} \times \mathbf{B}_c) \cdot \mathbf{r}, \mathbf{p}] = -i\frac{e}{2}(\mathbf{R} \times \mathbf{B}_c) \cdot i\hbar = -\frac{e\hbar}{2}(\mathbf{B}_c \times \mathbf{R}) \\
[-i\frac{e}{2}(\mathbf{B}_c \times \mathbf{r}) \cdot \mathbf{R}, \mathbf{P}] &= -i\frac{e}{2}(\mathbf{B}_c \times \mathbf{r}) \cdot i\hbar = \frac{e\hbar}{2}(\mathbf{B}_c \times \mathbf{r}) \\
[-i\frac{e}{2}(\mathbf{B}_c \times \mathbf{r}) \cdot \mathbf{R}, \mathbf{p}]_2 &= [-i\frac{e}{2}(\mathbf{B}_c \times \mathbf{r}) \cdot \mathbf{R}, -\frac{e\hbar}{2}(\mathbf{B}_c \times \mathbf{R})] = 0 \\
[-i\frac{e}{2}(\mathbf{B}_c \times \mathbf{r}) \cdot \mathbf{R}, \mathbf{P}]_2 &= [-i\frac{e}{2}(\mathbf{B}_c \times \mathbf{r}) \cdot \mathbf{R}, \frac{e\hbar}{2}(\mathbf{B}_c \times \mathbf{r})] = 0 \,.
\end{aligned}$$

Employing $\mathbf{A}_c(\mathbf{x}) = \frac{1}{2}\mathbf{B}_c \times \mathbf{x}$ then yields for the transformed momenta[1]

$$U^\dagger \mathbf{p} U = \mathbf{p} - \frac{e\hbar}{2}(\mathbf{B}_c \times \mathbf{R}) = \mathbf{p} - \mathbf{A}_c(\mathbf{R}) \tag{C.3}$$

$$U^\dagger \mathbf{P} U = \mathbf{P} + \frac{e\hbar}{2}(\mathbf{B}_c \times \mathbf{r}) = \mathbf{P} + \mathbf{A}_c(\mathbf{r}) \tag{C.4}$$

[1] Note that the last expression of each equation is given in atomic units: $\frac{e\hbar}{2}\mathbf{B}_c \times \mathbf{x} = \mathbf{A}_c(\mathbf{x})$ a.u. We will make use of this relation throughout this chapter.

$$U^\dagger \mathbf{p}^2 U = (U^\dagger \mathbf{p} U)(U^\dagger \mathbf{p} U) = (\mathbf{p} - \frac{e\hbar}{2}(\mathbf{B}_c \times \mathbf{R}))^2$$
$$= \mathbf{p}^2 - e\hbar(\mathbf{B}_c \times \mathbf{R}) \cdot \mathbf{p} + \frac{e^2\hbar^2}{4}(\mathbf{B}_c \times \mathbf{R})^2 = \mathbf{p}^2 - 2\mathbf{A}_c(\mathbf{R}) \cdot \mathbf{p} + \mathbf{A}_c(\mathbf{R})^2 \qquad \text{(C.5)}$$
$$U^\dagger \mathbf{P}^2 U = (U^\dagger \mathbf{P} U)(U^\dagger \mathbf{P} U) = (\mathbf{P} + \frac{e\hbar}{2}(\mathbf{B}_c \times \mathbf{r}))^2$$
$$= \mathbf{P}^2 + e\hbar(\mathbf{B}_c \times \mathbf{r}) \cdot \mathbf{P} + \frac{e^2\hbar^2}{4}(\mathbf{B}_c \times \mathbf{r})^2 = \mathbf{P}^2 + 2\mathbf{A}_c(\mathbf{r}) \cdot \mathbf{P} + \mathbf{A}_c(\mathbf{r})^2 \,. \qquad \text{(C.6)}$$

C.2 Transformation of the Spin-Orbit Interaction

In the expression for the spin-orbit interaction potential, we have to account for two contributions that are not invariant under the unitary transformation U, namely, the electronic angular momentum $\mathbf{L}$ and the model potential $V_l(r)$. The latter, however, only leads to minor correction as pointed out in Section 3.3. Consequently, we assume $V_l(r)$ to be invariant under U in the following. We get

$$U^\dagger V_{so}(\mathbf{L}, \mathbf{S}) U = \frac{\alpha^2}{2} \frac{1}{r} \frac{\mathrm{d}V(r)}{\mathrm{d}r} (U^\dagger \mathbf{L} U) \cdot \mathbf{S} = \frac{\alpha^2}{2} \frac{1}{r} \frac{\mathrm{d}V_l(r)}{\mathrm{d}r} \sum_{i=1}^{3} (U^\dagger L_i U) S_i \,.$$

That is, we have to calculate the commutators involving $L_i = (\mathbf{r} \times \mathbf{p})_i$,

$$\begin{aligned}
[-i\frac{e}{2}(\mathbf{B}_c \times \mathbf{r}) \cdot \mathbf{R}, (\mathbf{r} \times \mathbf{p})_i] &= -\frac{ie}{2}[\epsilon_{lmn} R_m B_n r_l, \epsilon_{ijk} r_j p_k] = -\frac{ie}{2}\epsilon_{lmn}\epsilon_{ijk}[R_m B_n r_l, r_j p_k] \\
&= -\frac{ie}{2}\epsilon_{lmn}\epsilon_{ijk}\Big\{ \underbrace{[R_m B_n r_l, r_j]}_{=0} p_k + r_j \underbrace{[R_m B_n r_l, p_k]}_{=R_m B_l i\hbar\delta_{lk}} \Big\} \\
&= \frac{e\hbar}{2}\epsilon_{lmn}\epsilon_{ijl} R_m B_n r_j = \frac{e\hbar}{2}\epsilon_{ijl} r_j (\mathbf{R} \times \mathbf{B}_c)_l \\
&= -\frac{e\hbar}{2}\big(\mathbf{r} \times (\mathbf{B}_c \times \mathbf{R})\big)_i = -\big(\mathbf{r} \times \mathbf{A}_c(\mathbf{R})\big)_i \\
[-i\frac{e}{2}(\mathbf{B}_c \times \mathbf{r}) \cdot \mathbf{R}, \mathbf{L}]_{n>1} &= 0 \,.
\end{aligned}$$

Equivalently, we can write $[-i\frac{e}{2}(\mathbf{B}_c \times \mathbf{r}) \cdot \mathbf{R}, \mathbf{L}] = -\mathbf{r} \times \mathbf{A}_c(\mathbf{R})$. Hence, the spin-orbit coupling potential $V_{so}(\mathbf{L}, \mathbf{S})$ is transformed by replacing $\mathbf{p} \mapsto \mathbf{p} - \frac{e\hbar}{2}(\mathbf{B}_c \times \mathbf{R})$ and we get

$$\begin{aligned}
U^\dagger V_{so}(\mathbf{L}, \mathbf{S}) U &= V_{so}(\mathbf{L}, \mathbf{S}) - \frac{\alpha^2}{2r}\frac{\mathrm{d}V_l(r)}{\mathrm{d}r}\frac{e\hbar}{2}\big[\mathbf{r} \times (\mathbf{B}_c \times \mathbf{R})\big] \cdot \mathbf{S} \\
&= V_{so}(\mathbf{L}, \mathbf{S}) - \frac{\alpha^2}{2r}\frac{\mathrm{d}V_l(r)}{\mathrm{d}r}\big[\mathbf{r} \times \mathbf{A}_c(\mathbf{R})\big] \cdot \mathbf{S} \,.
\end{aligned} \qquad \text{(C.7)}$$

C.3 Transformation of the Field Interaction Terms

For transforming the magnetic field interaction terms, we rewrite the unitary transformation as

$$U = \exp\Big\{ ie\mathbf{A}_c(\mathbf{r}) \cdot \mathbf{R} \Big\} = \exp\Big\{ -ie\mathbf{A}_c(\mathbf{R}) \cdot \mathbf{r} \Big\} \,.$$

Because of the particular choice of the vector potentials, the terms involving $\mathbf{A}_l(\mathbf{x})$ are invariant:

$$[ie\mathbf{A}_c(\mathbf{R})\cdot\mathbf{r}, \mathbf{A}_l(\mathbf{x})\cdot\mathbf{p}] = ie[B(-Yx+Xy), Gxyp_z] = 0$$

since $[x, p_z] = [y, p_z] = 0$. Similarly,

$$[-ie\mathbf{A}_c(\mathbf{r})\cdot\mathbf{R}, \mathbf{A}_l(\mathbf{x})\cdot\mathbf{P}] = 0\,.$$

For the terms involving the constant magnetic field, we get

$$\begin{aligned}
[ie\mathbf{A}_c(\mathbf{R})\cdot\mathbf{r}, \mathbf{A}_c(\mathbf{R})\cdot\mathbf{p}] &= ie\cdot i\hbar\mathbf{A}_c(\mathbf{R})^2 = -e\hbar\mathbf{A}_c(\mathbf{R})^2 = -\mathbf{A}_c(\mathbf{R})^2\\
[-ie\mathbf{A}_c(\mathbf{r})\cdot\mathbf{R}, \mathbf{A}_c(\mathbf{r})\cdot\mathbf{P}] &= e\hbar\mathbf{A}_c(\mathbf{r})^2 = \mathbf{A}_c(\mathbf{r})^2\\
[ie\mathbf{A}_c(\mathbf{R})\cdot\mathbf{r}, \mathbf{L}_r\cdot\mathbf{B}_c] &= ie[\mathbf{A}_c(\mathbf{R})\cdot\mathbf{r}, 2\mathbf{A}_c(\mathbf{r})\cdot\mathbf{p}] = -2e\hbar\mathbf{A}_c(\mathbf{R})\cdot\mathbf{A}_c(\mathbf{r})\\
&= -2\mathbf{A}_c(\mathbf{R})\cdot\mathbf{A}_c(\mathbf{r})\,.
\end{aligned}$$

The diamagnetic terms commute with U since they possess only a coordinate dependence. That is, the only magnetic field interaction terms not being invariant under the unitary transformation are

$$U^\dagger\big[\mathbf{A}_c(\mathbf{R})\cdot\mathbf{p}\big]U = \mathbf{A}_c(\mathbf{R})\cdot\mathbf{p} - \mathbf{A}_c(\mathbf{R})^2 \tag{C.8}$$

$$U^\dagger\big[\mathbf{A}_c(\mathbf{r})\cdot\mathbf{P}\big]U = \mathbf{A}_c(\mathbf{r})\cdot\mathbf{P} + \mathbf{A}_c(\mathbf{r})^2 \tag{C.9}$$

$$U^\dagger\big[\mathbf{A}_c(\mathbf{r})\cdot\mathbf{p}\big]U = \mathbf{A}_c(\mathbf{r})\cdot\mathbf{p} - \mathbf{A}_c(\mathbf{R})\cdot\mathbf{A}_c(\mathbf{r}) \tag{C.10}$$

$$U^\dagger\big[\mathbf{L}_r\cdot\mathbf{B}_c\big]U = \mathbf{L}_r\cdot\mathbf{B}_c - 2\mathbf{A}_c(\mathbf{R})\cdot\mathbf{A}_c(\mathbf{r})\,. \tag{C.11}$$

C.4 Final Hamiltonian

Applying the unitary transformation $U = \exp\left\{i\frac{e}{2}(\mathbf{B}_c \times \mathbf{r}) \cdot \mathbf{R}\right\}$ on the Hamiltonian (3.15) while employing the results from above, yields (in atomic units)

$$
\begin{aligned}
U^\dagger H U = {} & \frac{\mathbf{P}^2}{2M} + \frac{\mathbf{p}^2}{2m} + V_l(r) + V_{so}(\mathbf{L},\mathbf{S}) - \boldsymbol{\mu}_e \cdot \big[\mathbf{B}_c + \mathbf{B}_l(\mathbf{R}+\mathbf{r})\big] \\
& + \frac{1}{m}\mathbf{A}_c(\mathbf{R}) \cdot \mathbf{p} + \big(\frac{1}{m} - \frac{2}{M_c}\big)\mathbf{A}_c(\mathbf{r}) \cdot \mathbf{p} + \frac{1}{M}\mathbf{A}_c(\mathbf{r}) \cdot \mathbf{P} \\
& + \frac{1}{2m}\mathbf{A}_c(\mathbf{R})^2 + \big(\frac{1}{m} - \frac{2}{M_c}\big)\mathbf{A}_c(\mathbf{R}) \cdot \mathbf{A}_c(\mathbf{r}) + \frac{1}{2}\big(\frac{1}{m} - \frac{3}{M}\big)\mathbf{A}_c(\mathbf{r})^2 \\
& + \frac{1}{m}\mathbf{A}_l(\mathbf{R}+\mathbf{r}) \cdot \mathbf{p} + \frac{1}{2m}\mathbf{A}_l(\mathbf{R}+\mathbf{r})^2 \\
& + \underbrace{\frac{1}{M}\mathbf{A}_c(\mathbf{r}) \cdot \mathbf{P} + \frac{1}{2M}\mathbf{A}_c(\mathbf{r})^2}_{\text{from } \frac{1}{2M}U^\dagger \mathbf{P}^2 U} \underbrace{-\frac{1}{m}\mathbf{A}_c(\mathbf{R}) \cdot \mathbf{p} + \frac{1}{2m}\mathbf{A}_c(\mathbf{R})^2}_{\text{from } \frac{1}{2m}U^\dagger \mathbf{p}^2 U} \underbrace{+\frac{1}{M}\mathbf{A}_c(\mathbf{r})^2}_{\frac{1}{M}U^\dagger(\mathbf{A}_c(\mathbf{r})\cdot\mathbf{P})U} \\
& \underbrace{-\frac{1}{m}\mathbf{A}_c(\mathbf{R})^2}_{\frac{1}{m}U^\dagger(\mathbf{A}_c(\mathbf{R})\cdot\mathbf{p})U} \underbrace{-\big(\frac{1}{m} - \frac{2}{M_c}\big)\mathbf{A}_c(\mathbf{R}) \cdot \mathbf{A}_c(\mathbf{r})}_{\left(\frac{1}{m}-\frac{2}{M_c}\right)U^\dagger(\mathbf{A}_c(\mathbf{r})\cdot\mathbf{p})U} \underbrace{-\frac{\alpha^2}{2r}\frac{\mathrm{d}V_l(r)}{\mathrm{d}r}\big[\mathbf{r} \times \mathbf{A}_c(\mathbf{R})\big] \cdot \mathbf{S}}_{U^\dagger V_{so} U} \\
= {} & \frac{\mathbf{P}^2}{2M} + \frac{\mathbf{p}^2}{2m} + V_l(r) + V_{so}(\mathbf{L},\mathbf{S}) - \boldsymbol{\mu}_e \cdot \big[\mathbf{B}_c + \mathbf{B}_l(\mathbf{R}+\mathbf{r})\big] \\
& + \big(\frac{1}{m} - \frac{2}{M_c}\big)\mathbf{A}_c(\mathbf{r}) \cdot \mathbf{p} + \frac{2}{M}\mathbf{A}_c(\mathbf{r}) \cdot \mathbf{P} + \frac{1}{2m}\mathbf{A}_c(\mathbf{r})^2 \\
& + \frac{1}{m}\mathbf{A}_l(\mathbf{R}+\mathbf{r}) \cdot \mathbf{p} + \frac{1}{2m}\mathbf{A}_l(\mathbf{R}+\mathbf{r})^2 - \frac{\alpha^2}{2r}\frac{\mathrm{d}V_l(r)}{\mathrm{d}r}\big[\mathbf{r} \times \mathbf{A}_c(\mathbf{R})\big] \cdot \mathbf{S} \\
= {} & \frac{\mathbf{P}^2}{2M} + \frac{\mathbf{p}^2}{2m} + V_l(r) + V_{so}(\mathbf{L},\mathbf{S}) - \boldsymbol{\mu}_e \cdot \big[\mathbf{B}_c + \mathbf{B}_l(\mathbf{R}+\mathbf{r})\big] + \frac{1}{2m}\big(1 - \tfrac{2m}{M_c}\big)\mathbf{L} \cdot \mathbf{B}_c \\
& + \frac{1}{m}\mathbf{A}_l(\mathbf{R}+\mathbf{r}) \cdot \mathbf{p} + \frac{1}{2m}\mathbf{A}_c(\mathbf{r})^2 + \frac{1}{2m}\mathbf{A}_l(\mathbf{R}+\mathbf{r})^2 \\
& + \underbrace{\frac{2}{M}\mathbf{A}_c(\mathbf{r}) \cdot \mathbf{P}}_{=\frac{1}{M}\mathbf{B}_c \cdot \left[\mathbf{r}\times\mathbf{P}\right]} - \frac{\alpha^2}{2r}\frac{\mathrm{d}V_l(r)}{\mathrm{d}r}\big[\mathbf{r} \times \mathbf{A}_c(\mathbf{R})\big] \cdot \mathbf{S}\,. \qquad \text{(C.12)}
\end{aligned}
$$

We remark once more that we approximated $U^\dagger V_l(r) U \approx V_l(r)$ at this point already. Also, we utilized the heavy mass approximation $(\frac{1}{m} - \frac{1}{M}) \approx m^{-1}$ for terms involving $\mathbf{A}_l(\mathbf{x})$ when appropriate. For our final Hamiltonian (3.20), we furthermore approximated $\frac{1}{2m}\big(1 - 2\frac{m}{M_c}\big) \approx \frac{1}{2m}$.

Appendix D

Transition Matrix Elements of Hydrogen

In this part of the Appendix, we provide analytic expressions for the dipole transition matrix elements between hydrogenic eigenstates, i.e.,

$$\langle nlm|\mathbf{r}|n'l'm'\rangle = \langle nlm|x\mathbf{e}_x + y\mathbf{e}_y + z\mathbf{e}_z|n'l'm'\rangle\,.$$

The wave function of the state $|nlm\rangle$ in the position representation is given by (cf. Section 5.3)

$$\psi_{nlm}(r,\theta,\phi) = R_{nl}(r)Y_{lm}(\theta,\phi)\,,$$

i.e., the integration of the matrix element can be separated in a radial and an angular part,

$$\langle nlm|\mathbf{r}|n'l'm'\rangle = \langle nl|r|n'l'\rangle_r\langle lm|\hat{\mathbf{r}}|l'm'\rangle_\Omega\,,$$

with

$$\langle nl|r|n'l'\rangle_r = \int_0^\infty R_{nl}(r)\,r R_{n'l'}(r)\,r^2\mathrm{d}r$$
$$\langle lm|\hat{\mathbf{r}}|l'm'\rangle_\Omega = \int_0^{2\pi}\int_0^\pi Y^*_{lm}(\theta,\phi)\,\hat{\mathbf{r}}Y_{l'm'}(\theta,\phi)\,\sin\theta\,\mathrm{d}\theta\,\mathrm{d}\phi$$

and $\hat{\mathbf{r}} = \mathbf{r}/r$ being the angular part of the position operator. In the following, we are going to omit the indices r and Ω denoting the radial and angular integration, respectively, as it will be clear from the context.

D.1 Angular Matrix Elements

The spherical harmonics $Y_{lm}(\theta,\phi)$ are defined as

$$Y_{lm}(\theta,\phi) = (-1)^m\sqrt{\frac{2l+1}{4\pi}\frac{(l-m)!}{(l+m)!}}\,P_l^m(\cos\theta)\,e^{im\phi}\,,$$

cf. Section 5.3. Employing the recurrence relations of the associated Legendre functions $P_l^m(\cos\theta)$,

$$(2l+1)\cos\theta\,P_l^m(\cos\theta) = (l+m)P_{l-1}^m(\cos\theta) + (l-m+1)P_{l+1}^m(\cos\theta)\,,$$

$$
\begin{aligned}
(2l+1)\sin\theta\, P_l^m(\cos\theta) &= P_{l+1}^{m+1}(\cos\theta) - P_{l-1}^{m+1}(\cos\theta) \\
&= (l+m)(l+m-1)P_{l-1}^{m-1}(\cos\theta) \\
&\quad + (l-m+1)(l-m+2)P_{l+1}^{m-1}(\cos\theta)\,,
\end{aligned}
$$

the angular matrix elements evaluate to

$$
\begin{aligned}
\langle lm|\sin\theta\,\cos\phi|l'm'\rangle &= \frac{1}{2}\Big[\langle lm|\sin\theta\, e^{i\phi}|l'm'\rangle + \langle lm|\sin\theta\, e^{i\phi}|l'm'\rangle\Big] \\
&= \frac{1}{2}\Bigg[\sqrt{\frac{(l'-m')(l'-m'-1)}{4l'^2-1}}\,\delta_{ll'-1}\delta_{mm'+1} \\
&\qquad + \sqrt{\frac{(l'+m'+2)(2l'+1)}{(2l'+3)(l'+m'+1)}}\left(\frac{l'-m'}{2l'+1}-1\right)\delta_{ll'+1}\delta_{mm'+1}\Bigg] \\
&\qquad - \sqrt{\frac{(l'+m')(l'+m'-1)}{4l'^2-1}}\,\delta_{ll'-1}\delta_{mm'-1} \\
&\qquad - \sqrt{\frac{(l'-m'+2)(2l'+1)}{(2l'+3)(l'-m'+1)}}\left(\frac{l'+m'}{2l'+1}-1\right)\delta_{ll'+1}\delta_{mm'-1}\Bigg]\,, \\
\langle lm|\sin\theta\,\sin\phi|l'm'\rangle &= \frac{1}{2i}\Big[\langle lm|\sin\theta\, e^{i\phi}|l'm'\rangle - \langle lm|\sin\theta\, e^{i\phi}|l'm'\rangle\Big] \\
&= \frac{1}{2i}\Bigg[\sqrt{\frac{(l'-m')(l'-m'-1)}{4l'^2-1}}\,\delta_{ll'-1}\delta_{mm'+1} \\
&\qquad + \sqrt{\frac{(l'+m'+2)(2l'+1)}{(2l'+3)(l'+m'+1)}}\left(\frac{l'-m'}{2l'+1}-1\right)\delta_{ll'+1}\delta_{mm'+1}\Bigg] \\
&\qquad + \sqrt{\frac{(l'+m')(l'+m'-1)}{4l'^2-1}}\,\delta_{ll'-1}\delta_{mm'-1}\,, \\
&\qquad + \sqrt{\frac{(l'-m'+2)(2l'+1)}{(2l'+3)(l'-m'+1)}}\left(\frac{l'+m'}{2l'+1}-1\right)\delta_{ll'+1}\delta_{mm'-1}\Bigg] \\
\langle lm|\cos\theta|l'm'\rangle &= \sqrt{\frac{(l'+m')(l'-m')}{4l'^2-1}}\,\delta_{ll'-1}\delta_{mm'} \\
&\qquad + \sqrt{\frac{(l'+m'+1)(l'-m'+1)}{(2l'+1)(2l'+3)}}\,\delta_{ll'+1}\delta_{mm'}\,.
\end{aligned}
$$

D.2 Radial Matrix Elements

For the scope of this chapter, we adopt the definition

$$
R_{nl}(r) = 2^{l+1}e^{-\frac{r}{n}}n^{-l-2}r^l\sqrt{\frac{(n-l-1)!}{(n+l)!}}\,L_{n-l-1}^{2l+1}(\tfrac{2r}{n})
$$

for the radial part of the hydrogen wave functions. The spatial integral needed is then given by

$$\langle nl|r|n'l'\rangle = 2^{l+l'+2} n^{-l-2} n'^{-l'-2} \sqrt{\frac{(n-l-1)!(n'-l'-1)!}{(n+l)!(n'+l')!}} \times \int_0^\infty \mathrm{d}r\, r^{3+l+l'} e^{-\frac{r}{n}-\frac{r}{n'}} L_{n-l-1}^{2l+1}(\tfrac{2r}{n}) L_{n'-l'-1}^{2l'+1}(\tfrac{2r}{n'})\,.$$

For the calculation of this integral, we use the following property of the generalized Laguerre polynomials:

$$L_{n-l-1}^{2l+1}(\tfrac{2r}{n}) L_{n'-l'-1}^{2l'+1}(\tfrac{2r}{n'}) = \sum_{m=0}^{n-l-1} \sum_{m'=0}^{n'-l'-1} (-1)^{m+m'} \binom{n+l}{n-l-1-m} \times \binom{n'+l'}{n'-l'-1-m'} \frac{2^{m+m'}}{m!m'!} \frac{1}{n^m n'^{m'}}\, r^{m+m'}\,.$$

Thus, the only integration we need is

$$\int_0^\infty \mathrm{d}r\, r^{3+l+l'+m+m'} e^{-r(\frac{1}{n}-\frac{1}{n'})} = \frac{(3+l+l'+m+m')!}{(\frac{1}{n}+\frac{1}{n'})^{4+l+l'+m+m'}}\,.$$

Putting all together, we obtain for the radial part of the dipole transition matrix element

$$\langle nl|r|n'l'\rangle = 2^{l+l'+2} n^{-l-2} n'^{-l'-2} \sqrt{\frac{(n-l-1)!(n'-l'-1)!}{(n+l)!(n'+l')!}} \times \sum_{m=0}^{n-l-1} \sum_{m'=0}^{n'-l'-1} (-1)^{m+m'} \binom{n+l}{n-l-1-m} \binom{n'+l'}{n'-l'-1-m'} \times \frac{2^{m+m'}}{m!m'!} \frac{1}{n^m n'^{m'}} \frac{(3+l+l'+m+m')!}{(\frac{1}{n}+\frac{1}{n'})^{4+l+l'+m+m'}}\,.$$

Bibliography

[1] M. H. Anderson, J. R. Ensher, M. R. Matthews, C. E. Wieman, and E. A. Cornell, *Observation of Bose-Einstein Condensation in a Dilute Atomic Vapor*, Science **269**, 198 (1995).

[2] S. N. Bose, *Plancks Gesetz und Lichtquantenhypothese*, Z. Phys. **26**, 178 (1924).

[3] A. Einstein, Sitz. K. Preuss. Akad. Wiss. 1924, 261 (1924).

[4] A. Einstein, Sitz. K. Preuss. Akad. Wiss. 1925, 3 (1925).

[5] K. B. Davis, M. O. Mewes, M. R. Andrews, N. J. van Druten, D. S. Durfee, D. M. Kurn, and W. Ketterle, *Bose-Einstein Condensation in a Gas of Sodium Atoms*, Phys. Rev. Lett. **75**, 3969 (1995).

[6] B. DeMarco and D. S. Jin, *Onset of Fermi Degeneracy in a Trapped Atomic Gas*, Science **285**, 1703 (1999).

[7] L. P. Pitaevskii, Zh. Eksp. Teor. Fys. **40**, 646 (1961).

[8] L. P. Pitaevskii, Sov. Phys. JETP **13**, 451 (1961).

[9] E. Gross, *Structure of a quantized vortex in boson systems*, Il Nuovo Cimento **20**, 454 (1961).

[10] E. P. Gross, *Hydrodynamics of a Superfluid Condensate*, J. Math. Phys. **4**, 195 (1963).

[11] G. Baym and C. J. Pethick, *Ground-State Properties of Magnetically Trapped Bose-Condensed Rubidium Gas*, Phys. Rev. Lett. **76**, 6 (1996).

[12] C. J. Pethik and H. Smith, *Bose-Einstein Condensation in Dilute Gases*, Cambridge University Press, 2002.

[13] K.-K. Ni, S. Ospelkaus, M. H. G. de Miranda, A. Pe'er, B. Neyenhuis, J. J. Zirbel, S. Kotochigova, P. S. Julienne, D. S. Jin, and J. Ye, *A High Phase-Space-Density Gas of Polar Molecules*, Science **322**, 231 (2008).

[14] S. Wildermuth, S. Hofferberth, I. Lesanovsky, E. Haller, L. M. Andersson, S. Groth, I. Bar-Joseph, P. Krüger, and J. Schmiedmayer, *Bose-Einstein condensates Microscopic magnetic-field imaging*, Nature **435**, 440 (2005).

[15] R. Krems, *Cold controlled chemistry*, Phys. Chem. Chem. Phys. **10**, 4079 (2008).

[16] M. A. Nielsen and I. L. Chuang, *Quantum Computation and Quantum Information*, Cambridge University Press, 2000.

[17] M. Greiner, O. Mandel, T. Esslinger, T. W. Hansch, and I. Bloch, *Quantum phase transition from a superfluid to a Mott insulator in a gas of ultracold atoms*, Nature **415**, 39 (2002).

[18] C. Chin, M. Bartenstein, A. Altmeyer, S. Riedl, S. Jochim, J. H. Denschlag, and R. Grimm, *Observation of the Pairing Gap in a Strongly Interacting Fermi Gas*, Science **305**, 1128 (2004).

[19] Z. Hadzibabic, P. Krüger, M. Cheneau, B. Battelier, and J. Dalibard, *Berezinskii-Kosterlitz-Thouless crossover in a trapped atomic gas*, Nature **441**, 1118 (2006).

[20] M. Girardeau, *Relationship between Systems of Impenetrable Bosons and Fermions in One Dimension*, J. Math. Phys. **1**, 516 (1960).

[21] B. Paredes, A. Widera, V. Murg, O. Mandel, S. Folling, I. Cirac, G. V. Shlyapnikov, T. W. Hansch, and I. Bloch, *Tonks-Girardeau gas of ultracold atoms in an optical lattice*, Nature **429**, 277 (2004).

[22] R. González-Férez and P. Schmelcher, *Rovibrational spectra of diatomic molecules in strong electric fields: The adiabatic regime*, Phys. Rev. A **69**, 023402 (2004).

[23] R. González-Férez and P. Schmelcher, *Electric-field-induced adiabaticity in the rovibrational motion of heteronuclear diatomic molecules*, Phys. Rev. A **71**, 033416 (2005).

[24] R. González-Férez, M. Mayle, and P. Schmelcher, *Rovibrational Dynamics of LiCs Dimers in Strong Electric Fields*, Chem. Phys. **329**, 203 (2006).

[25] M. Mayle, R. González-Férez, and P. Schmelcher, *Controlling molecular orientation through radiative rotational transitions in strong static electric fields*, Phys. Rev. A **75**, 013421 (2007), see also Phys. Rev. A **77**, 029901(E) (2008).

[26] R. González-Férez, M. Mayle, and P. Schmelcher, *Formation of ultracold heteronuclear dimers in electric fields*, Europhys. Lett. **78**, 53001 (2007).

[27] R. González-Férez, M. Mayle, P. Sánchez-Moreno, and P. Schmelcher, *Comparative study of the rovibrational properties of heteronuclear alkali dimers in electric fields*, Europhys. Lett. **83**, 43001 (2008).

[28] T. Lahaye, T. Koch, B. Frohlich, M. Fattori, J. Metz, A. Griesmaier, S. Giovanazzi, and T. Pfau, *Strong dipolar effects in a quantum ferrofluid*, Nature **448**, 672 (2007).

[29] T. Köhler, K. Goral, and P. S. Julienne, *Production of cold molecules via magnetically tunable Feshbach resonances*, Rev. Mod. Phys. **78**, 1311 (2006).

[30] W. D. Phillips, *Nobel Lecture: Laser cooling and trapping of neutral atoms*, Rev. Mod. Phys. **70**, 721 (1998).

[31] W. Ketterle and N. J. van Druten, *Evaporative Cooling*, Adv. At. Mol. Opt. Phys. **37**, 181 (1996).

[32] T. F. Gallagher, *Rydberg Atoms*, Cambridge University Press, 1994.

[33] D. Jaksch, J. I. Cirac, P. Zoller, S. L. Rolston, R. Côté, and M. D. Lukin, *Fast Quantum Gates for Neutral Atoms*, Phys. Rev. Lett. **85**, 2208 (2000).

[34] M. D. Lukin, M. Fleischhauer, R. Côté, L. M. Duan, D. Jaksch, J. I. Cirac, and P. Zoller, *Dipole Blockade and Quantum Information Processing in Mesoscopic Atomic Ensembles*, Phys. Rev. Lett. **87**, 037901 (2001).

[35] D. Tong, S. M. Farooqi, J. Stanojevic, S. Krishnan, Y. P. Zhang, R. Côté, E. E. Eyler, and P. L. Gould, *Local Blockade of Rydberg Excitation in an Ultracold Gas*, Phys. Rev. Lett. **93**, 063001 (2004).

[36] K. Singer, M. Reetz-Lamour, T. Amthor, L. G. Marcassa, and M. Weidemüller, *Suppression of Excitation and Spectral Broadening Induced by Interactions in a Cold Gas of Rydberg Atoms*, Phys. Rev. Lett. **93**, 163001 (2004).

[37] T. Cubel Liebisch, A. Reinhard, P. R. Berman, and G. Raithel, *Atom Counting Statistics in Ensembles of Interacting Rydberg Atoms*, Phys. Rev. Lett. **95**, 253002 (2005).

[38] T. Vogt, M. Viteau, A. Chotia, J. Zhao, D. Comparat, and P. Pillet, *Electric-Field Induced Dipole Blockade with Rydberg Atoms*, Phys. Rev. Lett. **99**, 073002 (2007).

[39] C. S. E. van Ditzhuijzen, A. F. Koenderink, J. V. Hernández, F. Robicheaux, L. D. Noordam, and H. B. van Linden van den Heuvell, *Spatially Resolved Observation of Dipole-Dipole Interaction between Rydberg Atoms*, Phys. Rev. Lett. **100**, 243201 (2008).

[40] R. Heidemann, U. Raitzsch, V. Bendkowsky, B. Butscher, R. Löw, L. Santos, and T. Pfau, *Evidence for Coherent Collective Rydberg Excitation in the Strong Blockade Regime*, Phys. Rev. Lett. **99**, 163601 (2007).

[41] M. Reetz-Lamour, T. Amthor, J. Deiglmayr, and M. Weidemüller, *Rabi Oscillations and Excitation Trapping in the Coherent Excitation of a Mesoscopic Frozen Rydberg Gas*, Phys. Rev. Lett. **100**, 253001 (2008).

[42] T. A. Johnson, E. Urban, T. Henage, L. Isenhower, D. D. Yavuz, T. G. Walker, and M. Saffman, *Rabi Oscillations between Ground and Rydberg States with Dipole-Dipole Atomic Interactions*, Phys. Rev. Lett. **100**, 113003 (2008).

[43] E. Urban, T. A. Johnson, T. Henage, L. Isenhower, D. D. Yavuz, T. G. Walker, and M. Saffman, *Observation of Rydberg blockade between two atoms*, Nat. Phys. **5**, 110 (2009).

[44] A. Gaëtan, Y. Miroshnychenko, T. Wilk, A. Chotia, M. Viteau, D. Comparat, P. Pillet, A. Browaeys, and P. Grangier, *Observation of collective excitation of two individual atoms in the Rydberg blockade regime*, Nat. Phys. **5**, 115 (2009).

[45] M. Saffman and K. Mølmer, *Efficient Multiparticle Entanglement via Asymmetric Rydberg Blockade*, Phys. Rev. Lett. **102**, 240502 (2009).

[46] C. H. Greene, A. S. Dickinson, and H. R. Sadeghpour, *Creation of Polar and Nonpolar Ultra-Long-Range Rydberg Molecules*, Phys. Rev. Lett. **85**, 2458 (2000).

[47] E. L. Hamilton, C. H. Greene, and H. R. Sadeghpour, *Shape-resonance-induced long-range molecular Rydberg states*, J. Phys. B **35**, L199 (2002).

[48] A. A. Khuskivadze, M. I. Chibisov, and I. I. Fabrikant, *Adiabatic energy levels and electric dipole moments of Rydberg states of Rb_2 and Cs_2 dimers*, Phys. Rev. A **66**, 042709 (2002).

[49] I. Lesanovsky, P. Schmelcher, and H. R. Sadeghpour, *Ultra-long-range Rydberg molecules exposed to a magnetic field*, J. Phys. B **39**, L69 (2006).

[50] V. Bendkowsky, B. Butscher, J. Nipper, J. P. Shaffer, R. Low, and T. Pfau, *Observation of ultralong-range Rydberg molecules*, Nature **458**, 1005 (2009).

[51] P. Hyafil, J. Mozley, A. Perrin, J. Tailleur, G. Nogues, M. Brune, J. M. Raimond, and S. Haroche, *Coherence-Preserving Trap Architecture for Long-Term Control of Giant Ryberg Atoms*, Phys. Rev. Lett. **93**, 103001 (2004).

[52] S. D. Hogan and F. Merkt, *Demonstration of Three-Dimensional Electrostatic Trapping of State-Selected Rydberg Atoms*, Phys. Rev. Lett. **100**, 043001 (2008).

[53] S. K. Dutta, J. R. Guest, D. Feldbaum, A. Walz-Flannigan, and G. Raithel, *Ponderomotive Optical Lattice for Rydberg Atoms*, Phys. Rev. Lett. **85**, 5551 (2000).

[54] J.-H. Choi, J. R. Guest, A. P. Povilus, E. Hansis, and G. Raithel, *Magnetic Trapping of Long-Lived Cold Rydberg Atoms*, Phys. Rev. Lett. **95**, 243001 (2005).

[55] R. Gerritsma, S. Whitlock, T. Fernholz, H. Schlatter, J. A. Luigjes, J.-U. Thiele, J. B. Goedkoop, and R. J. C. Spreeuw, *Lattice of microtraps for ultracold atoms based on patterned magnetic films*, Phys. Rev. A **76**, 033408 (2007).

[56] S. Whitlock, R. Gerritsma, T. Fernholz, and R. J. C. Spreeuw, *Two-dimensional array of microtraps with atomic shift register on a chip*, New J. Phys. **11**, 023021 (2009).

[57] I. Lesanovsky, J. Schmiedmayer, and P. Schmelcher, *Rydberg atoms in magnetic quadrupole traps*, Europhys. Lett. **65**, 478 (2004).

[58] I. Lesanovsky and P. Schmelcher, *Selected aspects of the quantum dynamics and electronic structure of atoms in magnetic microtraps*, Eur. Phys. J. D **35**, 31 (2005).

[59] I. Lesanovsky, J. Schmiedmayer, and P. Schmelcher, *Electronic structure of atoms in magnetic quadrupole traps*, Phys. Rev. A **69**, 053405 (2004).

[60] I. Lesanovsky, J. Schmiedmayer, and P. Schmelcher, *Rydberg atoms in a magnetic quadrupole field*, J. Phys. B **38**, S151 (2005).

[61] I. Lesanovsky and P. Schmelcher, *Magnetic Trapping of Ultracold Rydberg Atoms*, Phys. Rev. Lett. **95**, 053001 (2005).

[62] I. Lesanovsky and P. Schmelcher, *Quantum states of ultracold electronically excited atoms in a magnetic quadrupole trap*, Phys. Rev. A **72**, 053410 (2005).

[63] T. H. Bergeman, P. McNicholl, J. Kycia, H. Metcalf, and N. L. Balazs, *Quantized motion of atoms in a quadrupole magnetostatic trap*, J. Opt. Soc. Am. B **6**, 2249 (1989).

[64] B. Hezel, I. Lesanovsky, and P. Schmelcher, *Controlling Ultracold Rydberg Atoms in the Quantum Regime*, Phys. Rev. Lett. **97**, 223001 (2006).

[65] B. Hezel, I. Lesanovsky, and P. Schmelcher, *Ultracold Rydberg atoms in a Ioffe-Pritchard trap*, Phys. Rev. A **76**, 053417 (2007).

[66] J. J. Balmer, *Notiz über die Spectrallinien des Wasserstoffs*, Ann. Phys. Chem. **25**, 80 (1885).

[67] J. R. Rydberg, Phil. Mag. 5^{th} Ser. **29**, 331 (1890).

[68] H. A. Bethe and E. E. Salpeter, *Quantum Mechanics of One- and Two-Electron Systems*, Springer, 1957.

[69] C.-J. Lorenzen and K. Niemax, *Quantum Defects of the $n^2P_{1/2,3/2}$ Levels in ^{39}K I and ^{85}Rb I*, Phys. Scr. **27**, 300 (1983).

[70] W. Li, I. Mourachko, M. W. Noel, and T. F. Gallagher, *Millimeter-wave spectroscopy of cold Rb Rydberg atoms in a magneto-optical trap: Quantum defects of the ns, np, and nd series*, Phys. Rev. A **67**, 052502 (2003).

[71] Y. Ralchenko, A. Kramida, J. Reader, and NIST ASD Team, NIST Atomic Spectra Database (version 3.1.5), http://physics.nist.gov/asd3 [2009, August 19]. National Institute of Standards and Technology, Gaithersburg, MD.

[72] M. Marinescu, H. R. Sadeghpour, and A. Dalgarno, *Dispersion coefficients for alkali-metal dimers*, Phys. Rev. A **49**, 982 (1994).

[73] H. Friedrich, *Theoretical Atomic Physics*, Springer, 2nd edition, 1998.

[74] C. E. Theodosiou, *Lifetimes of alkali-metal–atom Rydberg states*, Phys. Rev. A **30**, 2881 (1984).

[75] A. L. de Oliveira, M. W. Mancini, V. S. Bagnato, and L. G. Marcassa, *Measurement of Rydberg-state lifetimes using cold trapped atoms*, Phys. Rev. A **65**, 031401(R) (2002).

[76] V. A. Nascimento, L. L. Caliri, A. L. de Oliveira, V. S. Bagnato, and L. G. Marcassa, *Measurement of the lifetimes of S and D states below n = 31 using cold Rydberg gas*, Phys. Rev. A **74**, 054501 (2006).

[77] F. Gounand, *Calculation of radial matrix elements and radiative lifetimes for highly excited states of alkali atoms using the Coulomb approximation*, J. Phys. (Paris) **40**, 457 (1979).

[78] E. Arimondo, M. Inguscio, and P. Violino, *Experimental determinations of the hyperfine structure in the alkali atoms*, Rev. Mod. Phys. **49**, 31 (1977).

[79] C. V. Sukumar and D. M. Brink, *Spin-flip transitions in a magnetic trap*, Phys. Rev. A **56**, 2451 (1997).

[80] D. E. Pritchard, *Cooling Neutral Atoms in a Magnetic Trap for Precision Spectroscopy*, Phys. Rev. Lett. **51**, 1336 (1983).

[81] T. Esslinger, I. Bloch, and T. W. Hänsch, *Bose-Einstein condensation in a quadrupole-Ioffe-configuration trap*, Phys. Rev. A **58**, R2664 (1998).

[82] M.-O. Mewes, M. R. Andrews, N. J. van Druten, D. M. Kurn, D. S. Durfee, and W. Ketterle, *Bose-Einstein Condensation in a Tightly Confining dc Magnetic Trap*, Phys. Rev. Lett. **77**, 416 (1996).

[83] J. Fortagh and C. Zimmermann, *Magnetic microtraps for ultracold atoms*, Rev. Mod. Phys. **79**, 235 (2007).

[84] K. Gottfried and T.-M. Yan, *Quantum Mechanics: Fundamentals*, Springer, 2nd edition, 2004.

[85] M. Mayle, B. Hezel, I. Lesanovsky, and P. Schmelcher, *One-Dimensional Rydberg Gas in a Magnetoelectric Trap*, Phys. Rev. Lett. **99**, 113004 (2007).

[86] C. Bahrim, U. Thumm, A. A. Khuskivadze, and I. I. Fabrikant, *Near-threshold photodetachment of heavy alkali-metal anions*, Phys. Rev. A **66**, 052712 (2002).

[87] E. U. Condon and G. H. Shortley, *The Theory of Atomic Spectra*, Cambridge University Press, 1935.

[88] L. Armstrong, Jr., *Theory of the Hyperfine Structure of Free Atoms*, Wiley-Interscience, 1971.

[89] C. Cohen-Tannoudji, B. Diu, and F. Laloë, *Quantenmechanik 1 & 2*, de Gruyter, 1999.

[90] J. E. Avron, I. W. Herbst, and B. Simon, *Separation of Center of Mass in Homogeneous Magnetic Fields*, Ann. Phys. **114**, 431 (1978).

[91] B. R. Johnson, J. O. Hirschfelder, and K.-H. Yang, *Interaction of atoms, molecules, and ions with constant electric and magnetic fields*, Rev. Mod. Phys. **55**, 109 (1983).

[92] H. Ruder, G. Wunner, H. Herold, and F. Geyer, *Atoms in Strong Magnetic Fields*, Springer, 1994.

[93] M. Bouten, *On the rotation operators in quantum mechanics*, Physica **42**, 572 (1969).

[94] W. J. Thompson, *Angular Momentum*, Wiley-Interscience, 1994.

[95] A. Messiah, *Quantum Mechanics*, Dover, 1999.

[96] A. Szabo and N. S. Ostlund, *Modern Quantum Chemistry*, Dover, 1996.

[97] E. Anderson, Z. Bai, C. Bischof, S. Blackford, J. Demmel, J. Dongarra, J. D. Croz, A. Greenbaum, S. Hammarling, A. McKenney, and D. Sorensen, *LAPACK Users' Guide*, SIAM, 1999.

[98] D. C. Sorensen, *Implicit application of polynomial filters in a k-step Arnoldi method*, SIAM J. Matrix Analysis and Applications **13**, 357 (1992).

[99] R. B. Lehoucq, K. Maschhoff, D. C. Sorensen, and C. Yang, ARPACK Software Package, http://www.caam.rice.edu/software/ARPACK/, 1996.

[100] R. B. Lehoucq, D. C. Sorensen, and C. Yang, *ARPACK User's Guide*, SIAM, 1998.

[101] J. W. Demmel, S. C. Eisenstat, J. R. Gilbert, X. S. Li, and J. W. H. Liu, *A Supernodal Approach to Sparse Partial Pivoting*, SIAM J. Matrix Analysis and Applications **20**, 720 (1999).

[102] M. H. Beck, A. Jäckle, G. A. Worth, and H.-D. Meyer, *The multiconfiguration time-dependent Hartree (MCDTH) method: A highly efficient algorithm for propagating wavepackets*, Phys. Rep. **324**, 1 (2000).

[103] W. H. Press, S. A. Teukolsky, W. T. Vetterling, and B. P. Flannery, *Numerical Recipes*, Cambridge University Press, 2007.

[104] C. W. McCurdy, W. A. Isaacs, H.-D. Meyer, and T. N. Rescigno, *Resonant vibrational excitation of CO_2 by electron impact: Nuclear dynamics on the coupled components of the $^2\Pi_u$ resonance*, Phys. Rev. A **67**, 042708 (2003).

[105] E. H. Lieb and W. Liniger, *Exact Analysis of an Interacting Bose Gas. I. The General Solution and the Ground State*, Phys. Rev. **130**, 1605 (1963).

[106] E. H. Lieb, *Exact Analysis of an Interacting Bose Gas. II. The Excitation Spectrum*, Phys. Rev. **130**, 1616 (1963).

[107] U. Schmidt, I. Lesanovsky, and P. Schmelcher, *Ultracold Rydberg atoms in a magneto-electric trap*, J. Phys. B **40**, 1003 (2007).

[108] R. G. Hulet, E. S. Hilfer, and D. Kleppner, *Inhibited Spontaneous Emission by a Rydberg Atom*, Phys. Rev. Lett. **55**, 2137 (1985).

[109] R. Lutwak, J. Holley, P. P. Chang, S. Paine, D. Kleppner, and T. Ducas, *Circular states of atomic hydrogen*, Phys. Rev. A **56**, 1443 (1997).

[110] M. Mayle, I. Lesanovsky, and P. Schmelcher, *Exploiting the composite character of Rydberg atoms for cold-atom trapping*, Phys. Rev. A **79**, 041403(R) (2009), see also Phys. Rev. A **80**, 029903(E) (2009).

[111] M. Mayle, I. Lesanovsky, and P. Schmelcher, *Magnetic trapping of ultracold Rydberg atoms in low angular momentum states*, arXiv:0906.0946v1 [physics.atom-ph]; accepted for publication in Phys. Rev. A.

[112] R. Loew, U. Raitzsch, R. Heidemann, V. Bendkowsky, B. Butscher, A. Grabowski, and T. Pfau, *Apparatus for excitation and detection of Rydberg atoms in quantum gases*, arXiv:0706.2639v1 [quant-ph].

[113] R. Folman, P. Krüger, J. Schmiedmayer, J. Denschlag, and C. Henkel, *Microscopic atom optics: From wires to an atomchip*, Adv. At. Mol. Opt. Phys. **48**, 263 (2002).

[114] P. R. Bunker and P. Jensen, *Molecular Symmetry and Spectroscopy*, NRC Research Press, 2nd edition, 1998.

[115] M. Müller, L. Liang, I. Lesanovsky, and P. Zoller, *Trapped Rydberg ions: from spin chains to fast quantum gates*, New J. Phys. **10**, 093009 (2008).

[116] D. A. Steck, Rubidium 87 D Line Data, available online at http://steck.us/alkalidata, (revision 2.1.2, 12 August 2009).

[117] D. A. Steck, Quantum and Atom Optics, available online at http://steck.us/teaching, 2006.

[118] I. Shavitt and L. T. Redmon, *Quasidegenerate perturbation theories. A canonical van Vleck formalism and its relationship to other approaches*, J. Chem. Phys. **73**, 5711 (1980).

[119] T. Amthor, C. Giese, C. S. Hofmann, and M. Weidemüller, *Evidence of antiblockade in an ultracold Rydberg gas*, arXiv:0909.0837v1 [physics.atom-ph].

[120] B. Olmos, R. González-Férez, and I. Lesanovsky, *Fermionic collective excitations in a lattice gas of Rydberg atoms*, arXiv:0909.2716v1 [quant-ph].

Danksagung

Besonderer Dank gilt meinem Betreuer **Peter Schmelcher**, der meiner wissenschaftlichen Laufbahn seit meiner Diplomarbeit fördernd zur Seite steht.

Desweiteren möchte ich **Igor Lesanovsky** danken, der einerseits durch seine Vorarbeiten sowie andererseits durch stets neue Ideen zu der Arbeit beigetragen hat. In diesem Zusammenhang möchte ich auch ganz besonders **Bernd Hezel** danken; Referenz [85] über das eindimensionale Rydberg Gas, welches in Kapitel 6 behandelt wird, ist unser gemeinsames Werk.

Me gustaría dar las gracias a **Rosario González-Férez** por la preparación del informe sobre este trabajo. Fue siempre para mi un placer colaborar con Rosario, y poderla saludar a menudo en Heidelberg. Su hospitalidad durante las visitas a Granada quedará para siempre en mi recuerdo. Entschuldige, dass ich es in der ganzen Zeit nie geschafft habe Spanisch zu lernen.

Mein ausdrücklicher Dank gilt der **TC** in Heidelberg, die ich all die Jahre als ein überaus angenehmes Arbeitsumfeld zu schätzen gelernt habe. Insbesondere möchte ich mich bei **Michael Brill**, **Stephan Middelkamp** und all den anderen Doppelkopfkumpanen für die vielen gefangenen Füchse bedanken. Dass **Florian Lenz** die Doppelkopfrunde vor dem Aussterben aufgrund eines akuten Personalmangels gerettet hat, freut mich besonders.

Meiner **Familie** sowie meinen **Freunden** möchte ich für die Unterstützung während meiner gesamten Studienzeit danken. Insbesondere danke ich natürlich **Marion** für die vielen wunderbaren Jahre, auf die wir gemeinsam zurückblicken können, und freue mich auf die unzähligen, die da noch kommen mögen.